



Space engineering

Thermal design handbook - Part 4: Conductive Heat Transfer

**ECSS Secretariat
ESA-ESTEC
Requirements & Standards Division
Noordwijk, The Netherlands**

Foreword

This Handbook is one document of the series of ECSS Documents intended to be used as supporting material for ECSS Standards in space projects and applications. ECSS is a cooperative effort of the European Space Agency, national space agencies and European industry associations for the purpose of developing and maintaining common standards.

The material in this Handbook is a collection of data gathered from many projects and technical journals which provides the reader with description and recommendation on subjects to be considered when performing the work of Thermal design.

The material for the subjects has been collated from research spanning many years, therefore a subject may have been revisited or updated by science and industry.

The material is provided as good background on the subjects of thermal design, the reader is recommended to research whether a subject has been updated further, since the publication of the material contained herein.

This handbook has been prepared by ESA TEC-MT/QR division, reviewed by the ECSS Executive Secretariat and approved by the ECSS Technical Authority.

Disclaimer

ECSS does not provide any warranty whatsoever, whether expressed, implied, or statutory, including, but not limited to, any warranty of merchantability or fitness for a particular purpose or any warranty that the contents of the item are error-free. In no respect shall ECSS incur any liability for any damages, including, but not limited to, direct, indirect, special, or consequential damages arising out of, resulting from, or in any way connected to the use of this document, whether or not based upon warranty, business agreement, tort, or otherwise; whether or not injury was sustained by persons or property or otherwise; and whether or not loss was sustained from, or arose out of, the results of, the item, or any services that may be provided by ECSS.

Published by: ESA Requirements and Standards Division
ESTEC, P.O. Box 299,
2200 AG Noordwijk
The Netherlands

Copyright: 2011 © by the European Space Agency for the members of ECSS

Table of contents

1 Scope	11
2 References	12
3 Terms, definitions and symbols	13
3.1 Terms and definitions	13
3.2 Abbreviated terms	13
3.3 Symbols.....	13
4 Conductive shape factors	15
4.1 General.....	15
4.2 Planar-planar surfaces	16
4.2.1 Two-dimensional configurations	16
4.3 Planar surface-cylindrical surface	18
4.3.1 Two-dimensional configurations	18
4.3.2 Axisymmetrical configuration.....	21
4.4 Planar surface-spherical surface	23
4.4.1 Plane and sphere	23
4.5 Cylindrical-cylindrical surfaces	25
4.5.1 Two-dimensional configurations	25
4.6 Spherical-spherical surfaces	41
4.6.1 Two concentric spheres.....	41
5 Thermal joint conductance	43
5.1 General.....	43
5.1.1 Empirical correlations	44
5.1.2 Thermal interface materials	48
5.1.3 Joint geometries	50
5.2 Bare metallic joints	51
5.2.1 Metal-metal joints	62
5.2.2 Metal-composite joints.....	94
5.2.3 Composite-composite joints	96
5.3 Interfacial materials between metals	98

5.3.1	Metallic foils between metals.....	98
5.3.2	Metallic oxide powders between similar metals.....	109
5.3.3	Porous metallic materials between similar metals.....	109
5.3.4	Insulating spacers between similar metals	119
5.3.5	Fluids between metals.....	133
5.3.6	Elastomeric spacers between similar metals.....	143
5.4	Outgassing data	152
Bibliography.....		154

Figures

Figure 4-1:	Values of the conductive shape factor per unit length, S/L , vs. the dimensionless width of the strip, X . Calculated by the compiler.	17
Figure 4-2:	Values of the conductive shape factor per unit length, S/L , vs. X for different values of Y . Calculated by the compiler.....	19
Figure 4-3:	Values of the conductive shape factor per unit length, S/L , vs. dimensionless diameter of the cylinder cross section. Calculated by the compiler.	20
Figure 4-4:	Values of the dimensionless conductive shape factor, S/L , vs. cylinder diameter to length ratio, D/L . Calculated by the compiler.	22
Figure 4-5:	Values of the dimensionless conductive shape factor, S/D , vs. the dimensionless diameter of the sphere, Z . Calculated by the compiler.....	24
Figure 4-6:	Values of the conductive shape factor per unit length, S/L , vs. radius ratio, ρ ; for different values of the dimensionless distance between cylinder axes, ε . Calculated by the compiler.	26
Figure 4-7:	Values of the dimensionless conductive shape factors per unit length, S_i/L , vs. the eccentricity of one of the holes X_2 , for different values of the relevant geometrical parameters. From Faulkner & Andrews (1955) [13].	28
Figure 4-8:	Values of the conductive shape factors per unit length, S_i/L , vs. the diameter ratio d_3 , for different values of the relevant geometric parameters. From Faulkner & Andrews (1955) [13].	30
Figure 4-9:	Values of the conductive shape factor per unit length, S/L , vs. the dimensionless characteristic length of the holes, X . Calculated by the compiler.	32
Figure 4-10:	Values of the conductive shape factor per unit length, S/L , vs. the dimensionless diameter of the hole, X , for several values of the aspect ratio, Y , of the rectangular bar cross-section. Calculated by the compiler.....	34
Figure 4-11:	Values of the conductive shape factor per unit length, S/L , vs. the dimensionless diameter of the hole, X , for different values of the aspect ratio, Y , of the rectangular bar cross section. After Griggs, Pitts & Goyal (1973) [25].	36
Figure 4-12:	Values of the conductive shape factor per unit length, S/L , vs. the dimensionless diameter of the hole, X , for several values of the aspect ratio, Y , of the rectangular bar cross section. After Griggs, Pitts & Goyal (1973) [25].	38

Figure 4-13: Values of the conductive shape factor per unit length, S/L , vs. the dimensionless hole radius, ρ , for several values of n . Calculated by the compiler.	40
Figure 4-14: Values of the dimensionless conductive shape factor, S/r_1 , vs. radius ratio, ρ . Calculated by the compiler.	42
Figure 5-1: Estimation of the temperature drop at the interface.....	43
Figure 5-2: Variation of gap thickness parameter, δ_o , with contact surface parameter, d . After Fletcher & Gyorog (1970) [17].....	45
Figure 5-3: Variation of contact conductance with apparent interface pressure. After Fletcher & Gyorog (1970) [17].	46
Figure 5-4: Dimensionless conductance vs. dimensionless load. Stainless steel under vacuum conditions. From Thomas & Probert (1972) [47].	47
Figure 5-5: Dimensionless conductance vs. dimensionless load. Stainless steel under vacuum conditions. From Thomas & Probert (1972) [47].	48
Figure 5-6: Schematic representation of two surfaces in contact and heat flow across the interface.	48
Figure 5-7: Interface material compressed between two contacting surfaces.	49
Figure 5-8: Plots of contact conductance vs. contact pressure for two different surface finishes. From Fried & Kelley (1966) [24].	51
Figure 5-9: Plot of contact conductance vs. contact pressure for two different surface finishes. From Fried & Atkins (1965) [23].	52
Figure 5-10: Plots of contact conductance vs. contact pressure for two different surface finishes. From Fried (1966) [22] quoted by Scollon & Carpitella (1970) [43].	53
Figure 5-11: Plot of contact conductance vs. contact pressure for different ambient pressures. From Fried & Kelley (1966) [24].	54
Figure 5-12: Plots of contact conductance vs. contact pressure for different surface finishes and ambient pressures. Circle: From Fried & Atkins (1965) [23]. Square: From Fried (1966) [21] quoted by Scollon & Carpitella (1970) [43].	55
Figure 5-13: Plot of contact conductance vs. contact pressure for different surface finishes. From Clausing & Chao (1965) [7].	56
Figure 5-14: Plot of contact conductance vs. contact pressure for different surface finishes. From Fried & Atkins (1965) [23].	57
Figure 5-15: Plot of contact conductance vs. contact pressure for various surface finishes, mean temperatures and ambient pressures. Circle, square and rhombus: from Clausing & Chao (1965) [7]. Triangle: from Fried (1966) [21] quoted by Scollon & Carpitella (1970) [43].	58
Figure 5-16: Plot of contact conductance vs. contact pressure. Notice the directional effect on contact conductance. From Fried & Kelley (1966) [24].	59
Figure 5-17: Plot of contact conductance vs. contact pressure for different surface finishes. Circle and square: from Fried (1965) [21]. Rhombus and triangle: from Fried & Atkins (1965) [23]. Inverted triangle and right-oriented triangle: from Fried & Kelley (1966) [24].	60
Figure 5-18: Plot of contact conductance vs. contact pressure for different surface finishes. Circle: From Fried (1966) [22] quoted by Scollon & Carpitella (1970) [43]. Square: From Gyorog (1970) [26].	61

Figure 5-19: Plot of contact conductance vs. contact pressure for different surface finishes. From Fried (1966) [21] quoted by Scollon & Carpitella (1970) [43].	62
Figure 5-20: Plot of contact conductance vs. contact pressure for different surface finishes: smooth surfaces. White square: from Padgett & Fletcher (1982) [35]. Black square: from Padgett & Fletcher (1982) [35]. Black triangle: from Fletcher & Gyorg (1971) [17]. Circle: from Clausing & Chao (1963) [7].	63
Figure 5-21: Plot of contact conductance vs. contact pressure for different surface finishes: medium surfaces. White square: from Padgett & Fletcher (1982) [35]. Black square: from Padgett & Fletcher (1982) [35]. Black triangle: from Fletcher & Gyorg (1971) [17]. Circle: from Clausing & Chao (1963) [7].	64
Figure 5-22: Experimental values of thermal contact conductance vs. contact pressure. From Marchetti, Testa & Torrisi (1988) [31].	65
Figure 5-23: Experimental values of thermal contact conductance vs. contact pressure. From Marchetti, Testa & Torrisi (1988) [31].	66
Figure 5-24: 0,1 μm brass sample pair applied force comparison. Dashed line: 112 N; dashed-dotted line: 224 N; long-short dashed line: 336 N; long-double short dashed line: 448 N; dashed-triple dotted line: 560 N; solid line: 670 N.	67
Figure 5-25: 0,2 μm brass sample pair applied force comparison.	67
Figure 5-26: 0,4 μm brass sample pair applied force comparison.	68
Figure 5-27: 0,8 μm brass sample pair applied force comparison.	68
Figure 5-28: 1,6 μm brass sample pair applied force comparison.	69
Figure 5-29: Brass sample pairs, 4,2 K surface finish comparison. Short dashed line: 0,1 μm ; long dashed line: 0,2 μm ; dashed-dotted line: 0,4 μm ; long-short dashed line: 0,8 μm ; long-double short dashed line: 1,6 μm .	69
Figure 5-30: Brass sample pairs, 4,2 K surface finish comparison. Long-double short dashed line: 112 N; short dashed line: 224 N; dashed-dotted line: 336 N; dotted line: 448 N; long dashed line: 560 N; solid line: 670 N.	70
Figure 5-31: γ copper sample pairs, 4,2 K surface finish comparison. Key as in Figure 5-30.	71
Figure 5-32: Physical model of two rotating cylinders contacted to each other.	71
Figure 5-33: Contact thermal resistance after applied high contact pressure vs. rotating speed.	72
Figure 5-34: Contact thermal resistance after applied high contact pressure vs. rotating speed.	73
Figure 5-35: Thermal contact conductance as a function of position for: (a) 4 x 6 load array; (b) 5 x 7 load array; c) 6 x 8 load array. From Peterson and Fletcher (1992) [37].	75
Figure 5-36: Integrated thermal contact conductance. From Table 5-2.	76
Figure 5-37: Plot of contact conductance vs. contact pressure. Notice the directional effect on contact conductance. From Fried & Kelley (1966) [24].	77
Figure 5-38: Thermal contact conductance vs. interfacial pressure for Al 2024-T4/SS 304 contacts: experimental data and theoretical results.	78
Figure 5-39: Thermal contact conductance vs. interfacial pressure for Al 2024-T4/Zircaloy-2 contacts: experimental data and theoretical results.	79

Figure 5-40: Thermal contact conductance vs. interfacial pressure for SS 304/Zircaloy-2 contacts: experimental data and theoretical results.....	80
Figure 5-41: Thermal contact conductance vs. interfacial pressure for Mg AZ31B/zircaloy-2 contacts: experimental data and theoretical results.	81
Figure 5-42: Thermal contact conductance vs. interfacial pressure for Brass 271/Zircaloy-2 contacts: experimental data and theoretical results.	82
Figure 5-43: Variation of contact conductance with apparent interface pressure for Al 2024-T4/SS 304 metal surfaces at different mean junction temperatures.....	83
Figure 5-44: Thermal contact conductance vs. contact pressure. Theoretical curve: $h_c = KP^{0,93}$. (1) SS-Al, $K = 3,27 \times 10^{-11}$. (2) SS-Cu, $K = 1,84 \times 10^{-11}$	84
Figure 5-45: Comparison between experimental and theoretical values for SS/Al interface. Theoretical curve: $h_c = 3,65 \times 10^{-9} P^{0,66}$	84
Figure 5-46: Comparison between experimental and theoretical values for SS/Cu interface.	85
Figure 5-47: Comparison between experimental and theoretical values for SS/Al interface.	85
Figure 5-48: Thermal contact resistance vs. applied pressure for SS to Cu specimens (RMS roughness values as indicated).	86
Figure 5-49: Thermal contact resistance vs. applied pressure for Cu to SS (RMS roughness values as indicated).	87
Figure 5-50: Dimensionless correlation of contact resistances between machined SS specimens pressed against copper optical-flats (surface finishes of the SS specimens as indicated).	88
Figure 5-51: Dimensionless correlation as for Figure 5-50 but for different surface finishes of the SS specimens.....	89
Figure 5-52: Overall thermal conductance as a function of apparent contact pressure and mean junction temperature.	91
Figure 5-53: Joint Configuration.	92
Figure 5-54: Thermal contact conductance as a function of distance from center of bolt. From Peterson, Stanks & Fletcher (1991) [39].	92
Figure 5-55: Integrated thermal contact conductance. From Table 5-4.	93
Figure 5-56: Stainless-steel and Graphite-epoxi-laminate.	94
Figure 5-57: Stainless-steel and glass-epoxi-laminate.....	95
Figure 5-58: Experimental values of thermal transverse conductivity a) Graphite-epoxi-laminate. b) Glass-epoxi-laminate.	96
Figure 5-59: Graphite-epoxi-laminate and graphite-epoxi-laminate.	97
Figure 5-60: Glass-epoxi-laminate and glass-epoxi-laminate.	97
Figure 5-61: Plot of contact conductance vs. contact pressure. From Cunnington (1964) [9].....	98
Figure 5-62: Loading resistance with tin.....	99
Figure 5-63: Unloading resistance with tin.	99
Figure 5-64: Loading resistance with lead.....	100
Figure 5-65: Unloading resistance with lead.	100

Figure 5-66: Loading resistance with aluminium.	101
Figure 5-67: Unloading resistance with aluminium.	101
Figure 5-68: Loading resistance with copper.	102
Figure 5-69: Unloading resistance with copper.	102
Figure 5-70: Dimensionless minimum resistance to bare joint resistance.	103
Figure 5-71: Dimensionless thermal contact conductance for specimen sets 1, 2 and 3 as a function of the distance from a load point. $P_{\text{contact}} = 689,5 \times 10^3 \text{ Pa}$. Values for h_{uncoated} from Table 5-1 (clause 5.2.1.1). From Peterson and Fletcher (1992) [37].	104
Figure 5-72: Thermal contact conductance variation: a) 0,79 N.m; b) 1,92 N.m; c) 3,04 N.m. From Peterson & Fletcher (1991) [37].	107
Figure 5-73: Integrated thermal contact conductance. From Table 5-6.	108
Figure 5-74: Plot of contact conductance vs. contact pressure for different surface finishes and mean temperatures. From Miller & Fletcher (1973) [32].	110
Figure 5-75: Plot of contact conductance vs. contact pressure for different surface finishes and mean temperatures. From Miller & Fletcher (1973) [32].	111
Figure 5-76: Plot of contact conductance vs. contact pressure for different porosities. From Miller & Fletcher (1973) [32].	112
Figure 5-77: Plot of contact conductance vs. contact pressure. From Gyrog (1970) [26].	113
Figure 5-78: Plot of contact conductance vs. contact pressure. From Gyrog (1970) [26].	114
Figure 5-79: Comparison of thermal conductance of fiber metals with aluminium bare junction conductance, $T_m = 307 \text{ K}$	116
Figure 5-80: Comparison of thermal conductance of powder metals with aluminium bare junction conductance, $T_m = 342 \text{ K}$	116
Figure 5-81: Effect of surface finish on thermal conductance with a porous copper interstitial material.	117
Figure 5-82: Effect of mean junction temperature on thermal conductance with a porous copper interstitial material.	117
Figure 5-83: Dimensionless effectiveness parameter for porous metals and selected thermal control materials.	118
Figure 5-84: Effects of surface finish and temperature conductance with a porous nickel interstitial material.	118
Figure 5-85: Effects of mean junction temperature on thermal conductance with a porous copper interstitial material.	119
Figure 5-86: Plot of contact conductance vs. contact pressure. From Fletcher, Smuda & Gyrog (1969) [20].	120
Figure 5-87: Plot of contact conductance vs. contact pressure. From Fletcher, Smuda & Gyrog (1969) [20].	121
Figure 5-88: Plot of contact conductance vs. contact pressure. From Fletcher, Smuda & Gyrog (1969) [20].	122
Figure 5-89: Plot of contact conductance vs. contact pressure. From Fletcher, Smuda & Gyrog (1969) [20].	123

Figure 5-90: Plot of contact conductance vs. contact pressure. From Fletcher, Smuda & Gyorog (1969) [20].....	124
Figure 5-91: Plot of contact conductance vs. contact pressure. From Fletcher, Smuda & Gyorog (1969) [20].....	126
Figure 5-92: Plot of contact conductance vs. contact pressure. From Gyorog (1970) [26].....	127
Figure 5-93: Plot of contact conductance vs. contact pressure. From Fletcher, Smuda & Gyorog (1969) [20].....	128
Figure 5-94: Plot of contact conductance vs. contact pressure. From Fletcher, Smuda & Gyorog (1969) [20].....	129
Figure 5-95: Plot of contact conductance vs. contact pressure. From Fletcher, Smuda & Gyorog (1969) [20].....	130
Figure 5-96: Plot of contact conductance vs. contact pressure. From Fletcher, Smuda & Gyorog (1969) [20].....	131
Figure 5-97: Plot of contact conductance vs. contact pressure. From Gyorog (1970) [26].....	132
Figure 5-98: Plot of contact conductance vs. contact pressure. From Fletcher, Smuda & Gyorog (1969) [20].....	133
Figure 5-99: Plot of contact conductance vs. contact pressure. From Cunnington (1964) [9].....	134
Figure 5-100: Plot of contact conductance vs. contact pressure. From Cunnington (1964) [9].	135
Figure 5-101: Photograph of segmented surface test specimen.....	135
Figure 5-102: Thermal contact resistance values for Al 6061-T6 with and without segmented surface interstitial material (one atmosphere).....	136
Figure 5-103: Comparison between models and experimental results for SS1 and SS2. ...	138
Figure 5-104: Comparison between models and experimental results for SS1 and SS2. ...	139
Figure 5-105: Comparison between models and experimental results for SS3 and SS4. ...	140
Figure 5-106: Comparison between models and experimental results for SS3 and SS4. ...	140
Figure 5-107: Effect of variation of initial contact pressure on joint resistance for the edge tube/fin system. $h_o = 0$, $h_e = 0$, $P_i = 0$, $P_o = 0$, $T_i = 313$ K, $T_o = 293$ K, $T_i = 373$ K, $T_o = 293$ K.....	142
Figure 5-108: Plot of contact conductance vs. contact pressure for various elastomeric materials at two mean temperatures. From Fletcher & Miller (1973) [18].....	145

Tables

Table 5-1: Load configuration thermal contact conductance data.....	74
Table 5-2: Integrated load configuration test thermal contact conductance values	76
Table 5-3: Parameters of Samples Used in Tests Shown in Figure 5-43.	83
Table 5-4: Integrated thermal contact conductance values.....	93
Table 5-5: Thermal contact conductance data.	106
Table 5-6: Integrated thermal contact conductance values.....	108

Table 5-7: Values of contact conductance vs. contact pressure. 109

Table 5-8: Values of contact conductance as a function of contact pressure and mean temperature. 125

Table 5-9: Values of contact conductance as a function of contact pressure and mean temperature. 129

Table 5-10: Values of contact conductance as a function of contact pressure and mean temperature. 132

Table 5-11: Outgassing Data of Several Materials..... 152

1 Scope

This Part 4 of the spacecraft thermal control and design data handbooks, provides information on calculating the conductive heat transfer rate for a variety of two and three-dimensional configurations.

Calculations for the conductance of the interface between two surfaces (joints) require special consideration and are included as a separate clause.

The Thermal design handbook is published in 16 Parts

ECSS-E-HB-31-01 Part 1	Thermal design handbook – Part 1: View factors
ECSS-E-HB-31-01 Part 2	Thermal design handbook – Part 2: Holes, Grooves and Cavities
ECSS-E-HB-31-01 Part 3	Thermal design handbook – Part 3: Spacecraft Surface Temperature
ECSS-E-HB-31-01 Part 4	Thermal design handbook – Part 4: Conductive Heat Transfer
ECSS-E-HB-31-01 Part 5	Thermal design handbook – Part 5: Structural Materials: Metallic and Composite
ECSS-E-HB-31-01 Part 6	Thermal design handbook – Part 6: Thermal Control Surfaces
ECSS-E-HB-31-01 Part 7	Thermal design handbook – Part 7: Insulations
ECSS-E-HB-31-01 Part 8	Thermal design handbook – Part 8: Heat Pipes
ECSS-E-HB-31-01 Part 9	Thermal design handbook – Part 9: Radiators
ECSS-E-HB-31-01 Part 10	Thermal design handbook – Part 10: Phase – Change Capacitors
ECSS-E-HB-31-01 Part 11	Thermal design handbook – Part 11: Electrical Heating
ECSS-E-HB-31-01 Part 12	Thermal design handbook – Part 12: Louvers
ECSS-E-HB-31-01 Part 13	Thermal design handbook – Part 13: Fluid Loops
ECSS-E-HB-31-01 Part 14	Thermal design handbook – Part 14: Cryogenic Cooling
ECSS-E-HB-31-01 Part 15	Thermal design handbook – Part 15: Existing Satellites
ECSS-E-HB-31-01 Part 16	Thermal design handbook – Part 16: Thermal Protection System

2 References

ECSS-S-ST-00-01 ECSS System - Glossary of terms

All other references made to publications in this Part are listed, alphabetically, in the **Bibliography**.

Terms, definitions and symbols

3.1 Terms and definitions

For the purpose of this Standard, the terms and definitions given in ECSS-S-ST-00-01 apply.

3.2 Abbreviated terms

The following abbreviated terms are defined and used within this Standard.

FD	flatness deviation, [m]
RD	roughness deviation, [m]
TWL	total weight loss, percent
VCM	volatile condensable materials, percent by weight

Other symbols, mainly used to define the geometry of the configuration, are introduced when required.

3.3 Symbols

<i>A</i>	cross-sectional area normal to temperature gradient, [m ²]
<i>E</i>	modulus of elasticity, [Pa]
<i>L</i>	length normal to the plane of the figure in two-dimensional configurations, [m]
<i>M</i>	surface hardness, [Pa]
<i>P</i>	applied compressive load, also called contact pressure, [Pa]
<i>Q</i>	heat transfer rate, [W]

S	langmuir conductive shape factor, [m]
T	temperature, [K]
T_m	arithmetic mean temperature, [K]
b	Clause 2: radius of the specimen, [m]
d	surface parameter in Fletcher & Gyrog correlation, [m]
h_c	thermal joint conductance, [$\text{W}\cdot\text{m}^{-2}\cdot\text{K}^{-1}$]
h_f	interstitial contribution to thermal joint conductance, [$\text{W}\cdot\text{m}^{-2}\cdot\text{K}^{-1}$]
h_r	radiative contribution to thermal joint conductance, [$\text{W}\cdot\text{m}^{-2}\cdot\text{K}^{-1}$]
h_s	solid contribution to thermal joint conductance, [$\text{W}\cdot\text{m}^{-2}\cdot\text{K}^{-1}$]
k	thermal conductivity, [$\text{W}\cdot\text{m}^{-1}\cdot\text{K}^{-1}$]
k_m	mean thermal conductivity, [$\text{W}\cdot\text{m}^{-1}\cdot\text{K}^{-1}$]. $k_m = 2k_1k_2/(k_1+k_2)$
l	heat path length, [m]
p	ambient pressure, [Pa]
r	filter rating, [m]
t	thickness, [m]
ΔT	interfacial temperature drop, [K]
ϕ	porosity
β	coefficient of linear thermal expansion, [K^{-1}]
δ	gap thickness parameter in Fletcher & Gyrog correlation, [m]
ρ	density, [$\text{kg}\cdot\text{m}^{-3}$]
σ	rms surface roughness, [m]

4

Conductive shape factors

4.1 General

The conductive heat transfer rate through fairly complicated two-or-three dimensional configurations can be estimated on the basis of the so-called conductive shape factor, S .

In order to introduce the concept of conductive shape factor it is customary to start with the expression giving the one-dimensional conductive heat transfer rate, Q , between two parallel planer surfaces, 1 and 2, of cross-sectional area, A . Assuming that the thermal conductance k , of the space between the planes is constant, Fourier's law yields the following equation:

$$Q = k(A/l)(T_2 - T_1) = kS(T_2 - T_1),$$

l being the distance between the planes.

The factor S , known as Langmuir conductive shape factor, is, in this case, the ratio of the cross-sectional area, A , to the heat path length, l .

When two-or-three dimensional configurations are involved, the temperature field can be calculated by use of one of the methods available to solve Laplace differential equations. In many instances, however, only the overall heat transfer rate between arbitrary surfaces, 1 and 2, is required, and the above expression giving Q can be used, provided that S represents the ratio of the average cross-sectional area to the average heat path length. although the mathematical problem must be solved in full, in order to calculate S , the resulting values of S can be displayed in a very compact and useful way, as it is shown in this clause.

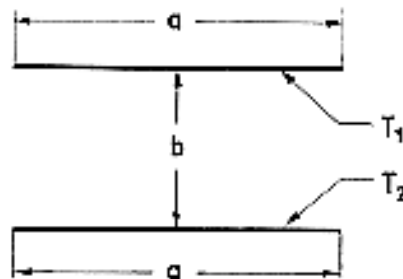
It should be mentioned that for two-dimensional configurations, that is to say, configurations which do not depend on the coordinate normal to the plane of the figure, the heat transfer rate is to be understood as that corresponding to the unit length normal to the mentioned plane. In order to keep unchanged the physical dimensions of S , the conductive shape factor for two-dimensional configurations is defined as S/L , which is a dimensionless magnitude.

4.2 Planar-planar surfaces

4.2.1 Two-dimensional configurations

4.2.1.1 Strips of equal width

Two parallel strips of equal width.



Formula:

$$S/L = a/b$$

Comments:

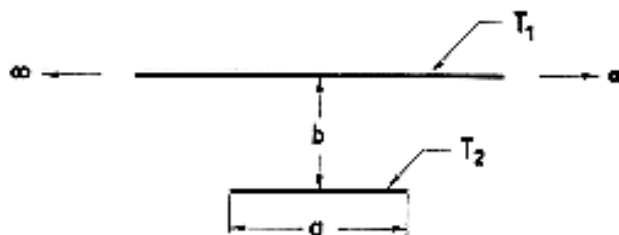
The configuration is two-dimensional.

S/L is the conductive shape factor per unit length normal to the plane of the figure.

References: Andrews (1955) [3], Sunderland & Johnson (1964) [46].

4.2.1.2 Strips of unequal width

Finite width strip and infinite parallel plane.



Formula:

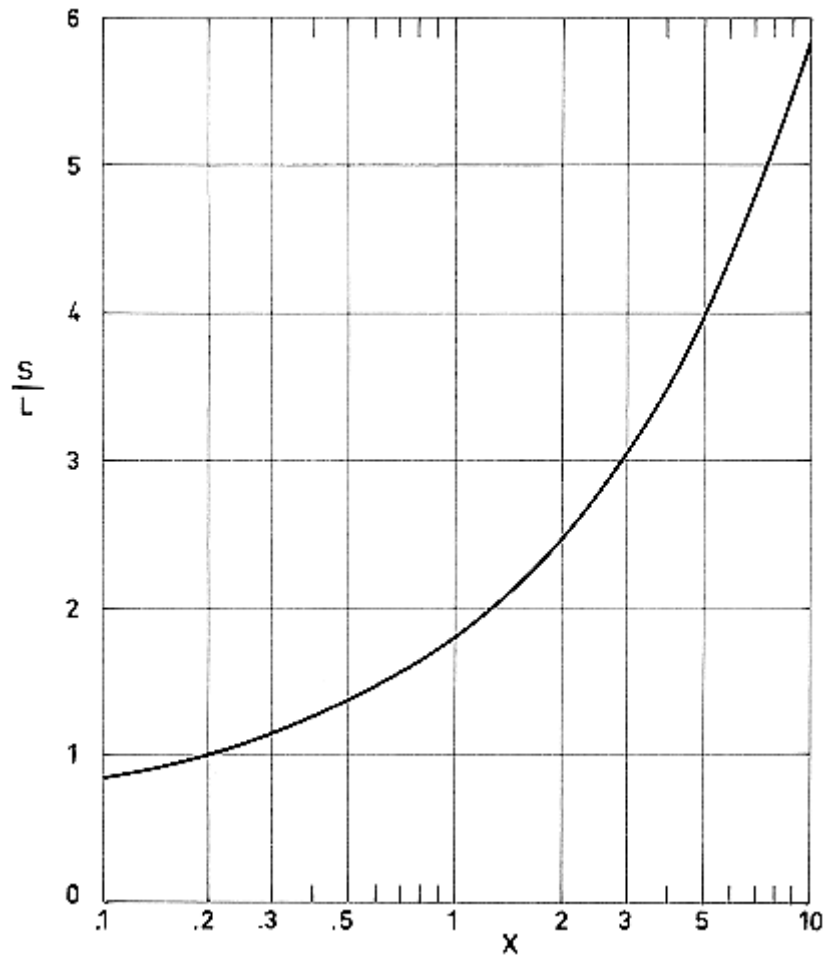
$$\frac{S}{L} = 1,45 \left[\ln \left(1 + \frac{1}{X} \right) \right]^{-0,59} \quad [4-1]$$

Comments:

The configuration is two-dimensional.

S/L is the conductive shape factor per unit length normal to the plane of the figure.

The results are given in Figure 4-1.



Note: non-si units are used in this figure

Figure 4-1: Values of the conductive shape factor per unit length, S/L , vs. the dimensionless width of the strip, X . Calculated by the compiler.

Reference: Andrews (1955) [3].

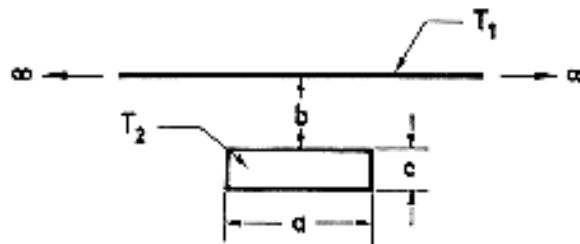
4.3 Planar surface-cylindrical surface

4.3.1 Two-dimensional configurations

4.3.1.1 Plane and cylinder of rectangular cross section

Plane and cylinder of rectangular cross section. The plane is parallel to the base of the rectangle.

The cylinder is assumed to be infinitely conductive.



Formula:

$$\frac{S}{L} = 1,685 \left[\ln \left(1 + \frac{1}{X} \right) \right]^{-0,59} \left[\frac{1}{Y} \right]^{-0,078} \quad [4-2]$$

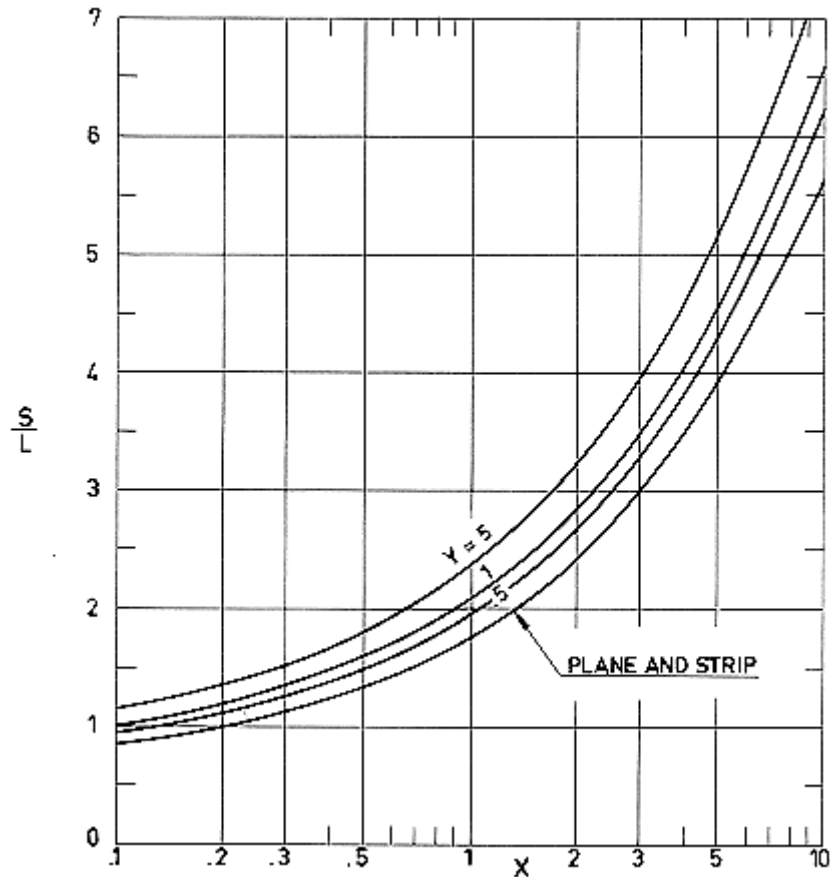
Comments:

The configuration is two-dimensional.

S/L is the conductive shape factor per unit length normal to the plane of the figure.

The above expression has been obtained by means of the electric analogy, using a conductive paper of finite dimensions (Andrews (1955) [3]). Since it is not stated in the reference how the point at infinity has been taken into account, results for small values of Y , which is presumably correspond to large values of b , are doubtful. In Figure 4-2 the finite strip case (see clause 4.2.1.2) has been taken to bound below the recommended values.

The results are given in Figure 4-2.



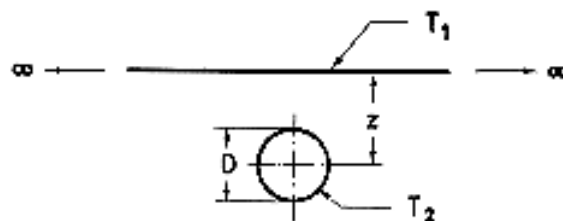
Note: non-si units are used in this figure

Figure 4-2: Values of the conductive shape factor per unit length, S/L , vs. X for different values of Y . Calculated by the compiler.

References: Andrews (1955) [3], Sunderland & Johnson (1964) [46].

4.3.1.2 Plane and circular cylinder

Plane and circular cylinder whose axis is parallel to the plane.



The cylinder is assumed to be infinitely conductive.

$$Z = D/z$$

Formula:

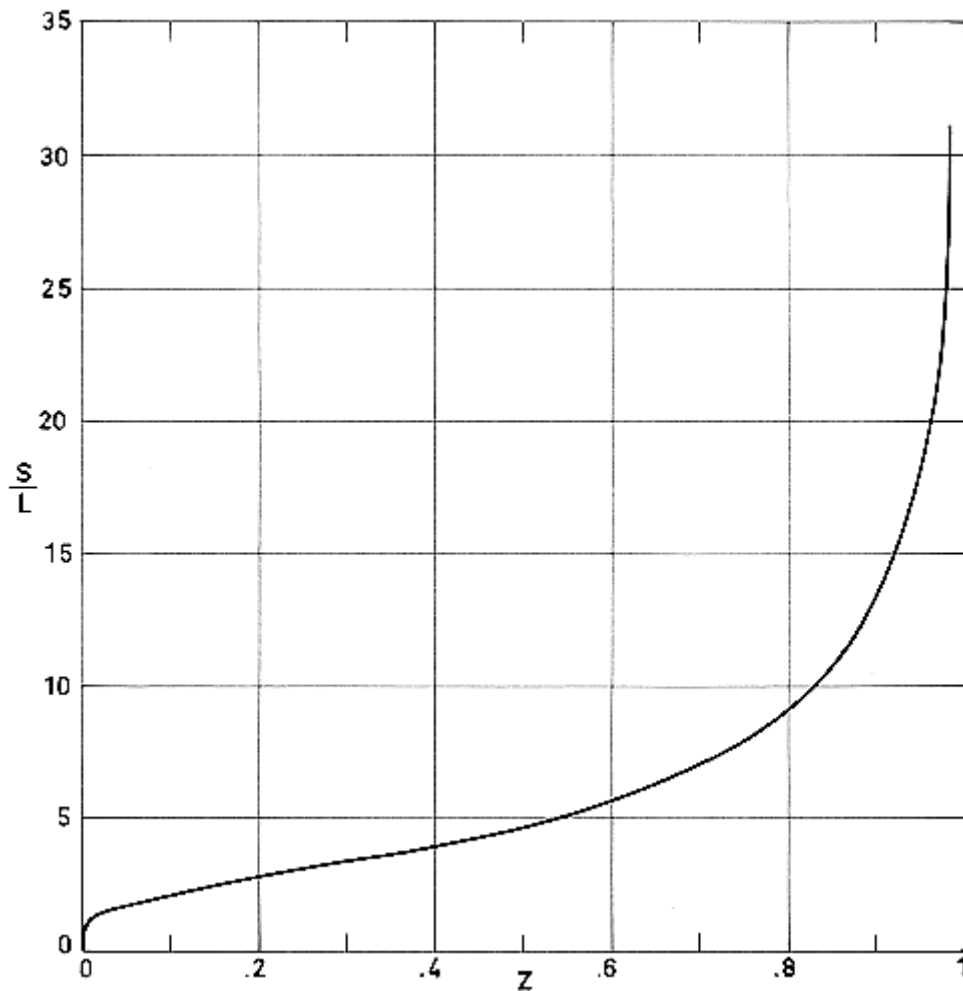
$$\frac{S}{L} = \frac{2\pi}{\cosh^{-1} \frac{2}{Z}} \quad [4-3]$$

Comments:

The configuration is two-dimensional.

S/L is the conductive shape factor per unit length normal to the plane of the figure.

The results are given in Figure 4-3.



Note: non-si units are used in this figure

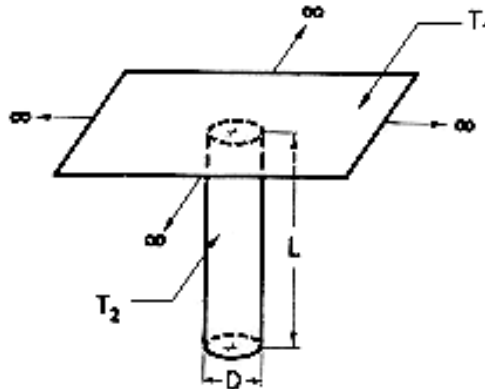
Figure 4-3: Values of the conductive shape factor per unit length, S/L , vs. dimensionless diameter of the cylinder cross section. Calculated by the compiler.

References: Sunderland & Johnson (1964) [46], Kutateladze & Borishanskii (1966) [28].

4.3.2 Axisymmetrical configuration

4.3.2.1 Plane and circular cylinder

Plane and circular cylinder of finite length with its base on the plane.



The cylinder is assumed to be infinitely conductive.

$$D \ll L$$

Formulae:

$$\frac{S}{L} = \frac{2\pi}{\ln \frac{4L}{D}} \quad (\text{a}) \quad [4-4]$$

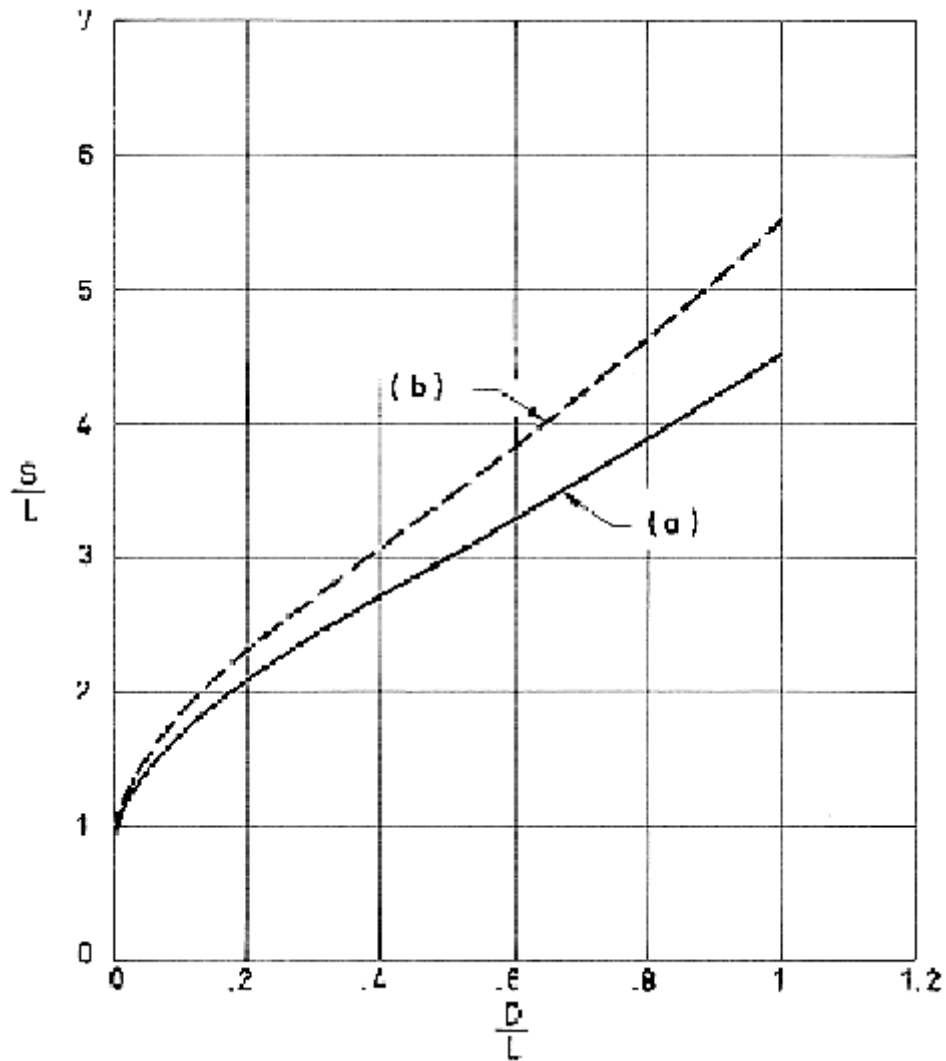
$$\frac{S}{L} = \frac{2\pi}{\ln \frac{4L}{D}} - \frac{2\pi(2\ln \sqrt{2} - 1)}{\left(\ln \frac{4L}{D}\right)^2} \quad (\text{b}) \quad [4-5]$$

Comments:

To obtain expression (a) the end effects corresponding to the free end of the cylinder have been neglected, so that this expression is only valid when the cylinder is slender enough.

Expression (b), which includes the second asymptotic term of the three-dimensional solution, has been obtained by the compiler.

The results are given in Figure 4-4.



Note: non-si units are used in this figure

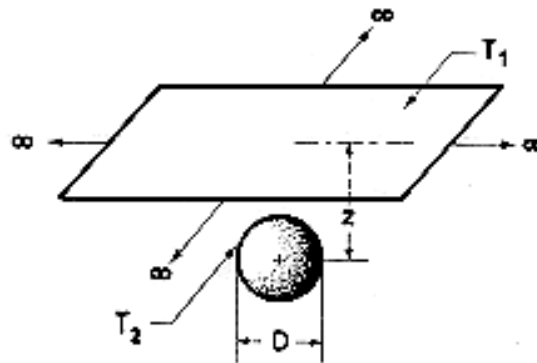
Figure 4-4: Values of the dimensionless conductive shape factor, S/L , vs. cylinder diameter to length ratio, D/L . Calculated by the compiler.

References: Sunderland & Johnson (1964) [46], Kutateladze & Borishanskii (1966) [28]; Parker, Boggs & Blick (1969) [36].

4.4 Planar surface-spherical surface

4.4.1 Plane and sphere

Plane and sphere.



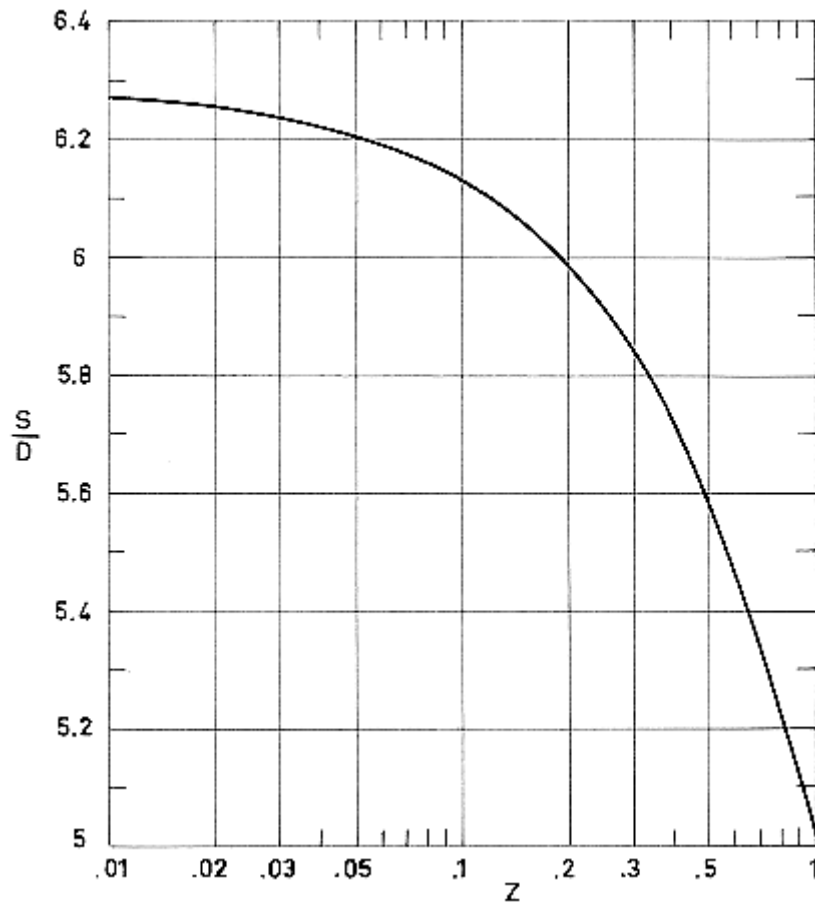
The sphere is assumed to be infinitely conductive.

$$Z = D/z$$

Formula:

$$\frac{S}{D} = \frac{2\pi}{1 + \frac{Z}{4}} \quad [4-6]$$

The results are given in Figure 4-5.



Note: non-si units are used in this figure

Figure 4-5: Values of the dimensionless conductive shape factor, S/D , vs. the dimensionless diameter of the sphere, Z . Calculated by the compiler.

References: Andrews (1955) [3], Sunderland & Johnson (1964) [46], Kutateladze & Borishanskii (1966) [28]; Parker, Boggs & Blick (1969) [36].

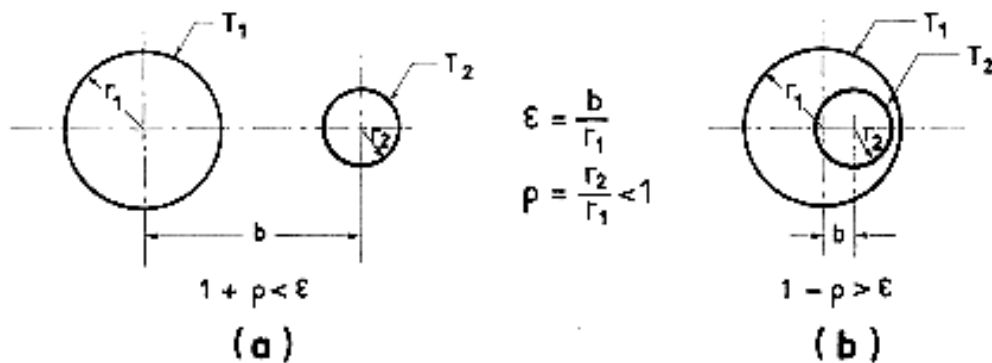
4.5 Cylindrical-cylindrical surfaces

4.5.1 Two-dimensional configurations

4.5.1.1 Circular cylinders

Parallel circular cylinders.

Both cylinders are assumed to be infinitely conductive.



Formula:

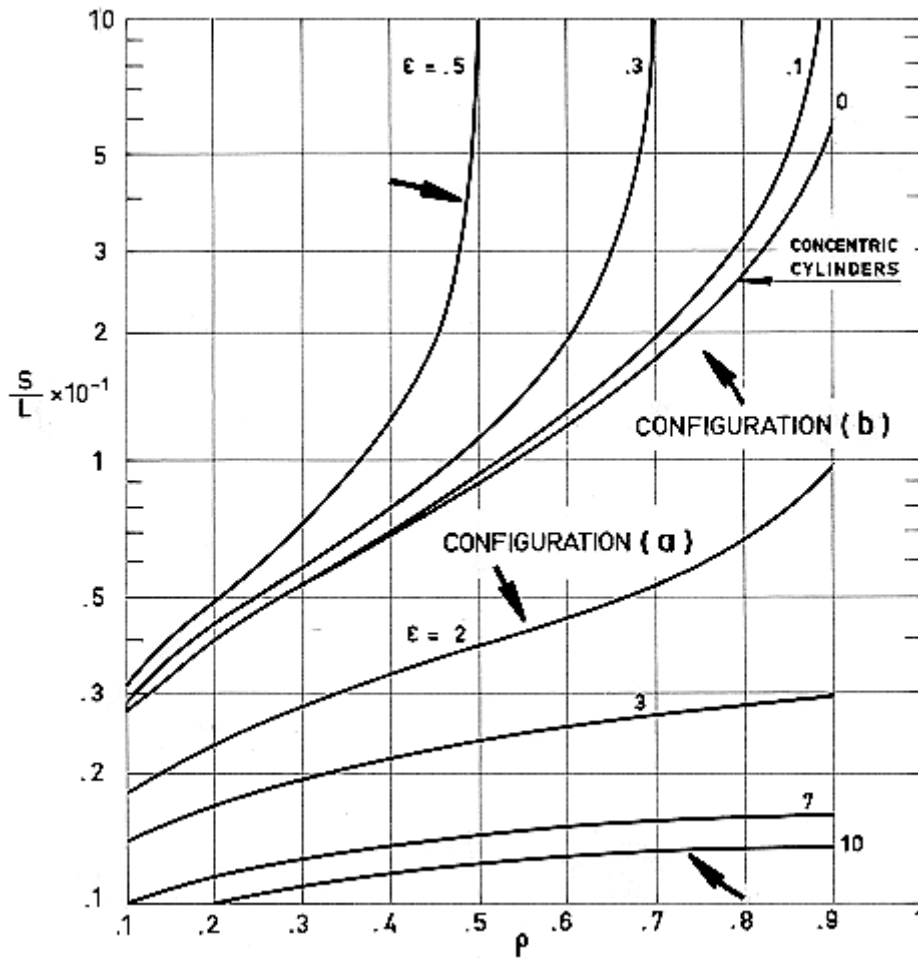
$$\frac{S}{L} = \frac{2\pi}{\cosh^{-1} \left[\frac{1 + \rho^2 - \epsilon^2}{2\rho} \right]} \quad [4-7]$$

Comments:

Both configurations are two-dimensional.

S/L is the conductive shape factor per unit length normal to the plane of the figure.

The results are given in Figure 4-6.



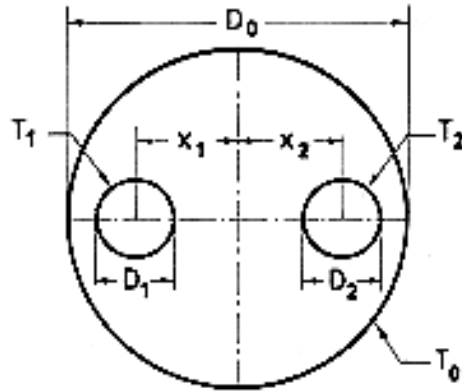
Note: non-si units are used in this figure

Figure 4-6: Values of the conductive shape factor per unit length, S/L , vs. radius ratio, ρ , for different values of the dimensionless distance between cylinder axes, ϵ . Calculated by the compiler.

References: Andrews (1955) [3], Sunderland & Johnson (1964) [46]; Parker, Boggs & Blick (1969) [36].

4.5.1.2 Circular rods with holes

Circular rod with two circular holes.



$$X_i = x_i/D_0$$

$$d_i = D_i/D_0$$

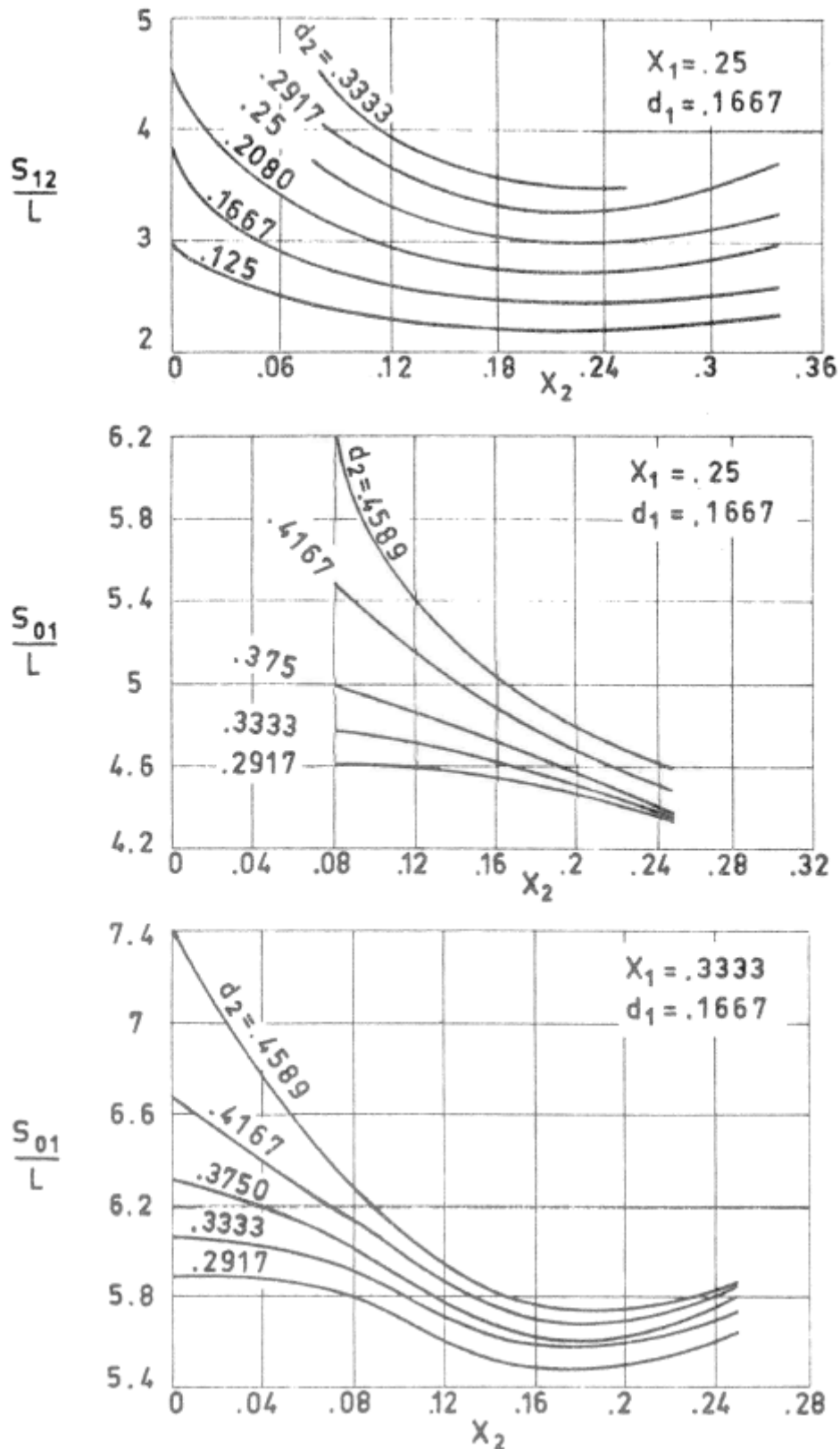
The results presented have been obtained by using an electrical analogue method.

Comments:

The configuration is two-dimensional.

S/L is the conductive shape factor per unit length normal to the plane of the figure.

The results are given in Figure 4-7.

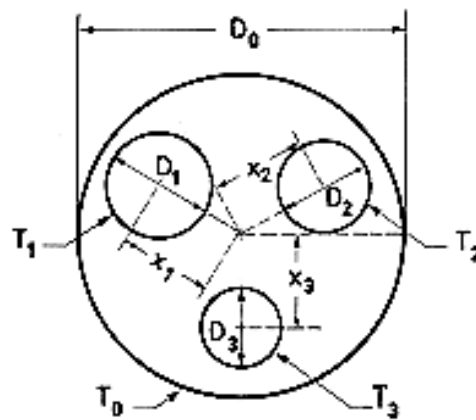


Note: non-si units are used in this figure

Figure 4-7: Values of the dimensionless conductive shape factors per unit length, S_{ij}/L , vs. the eccentricity of one of the holes X_2 , for different values of the relevant geometrical parameters. From Faulkner & Andrews (1955) [13].

Reference: Faulkner & Andrews (1955) [13].

Circular rod with three circular holes.



$$X_i = x_i/D_0$$

$$d_i = D_i/D_0$$

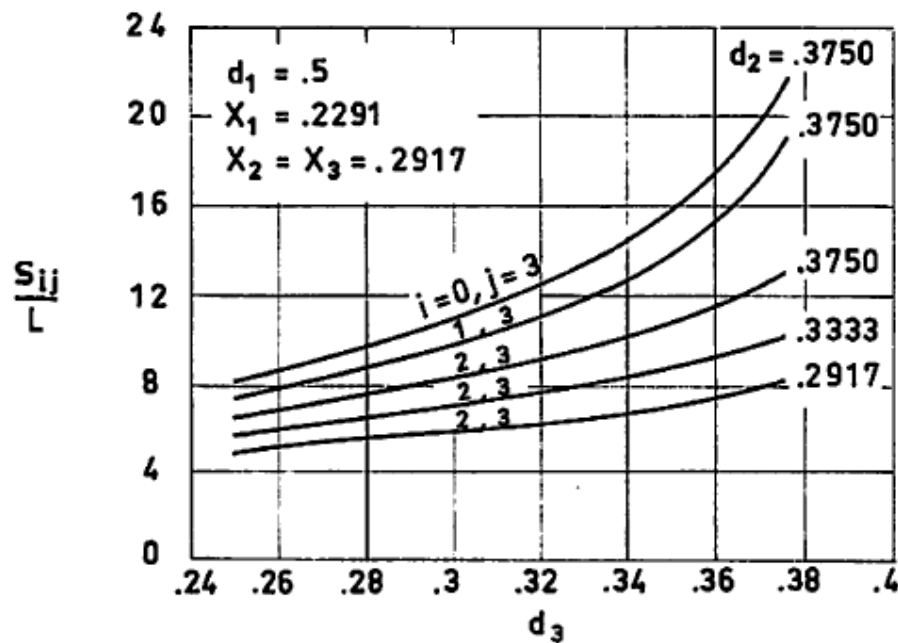
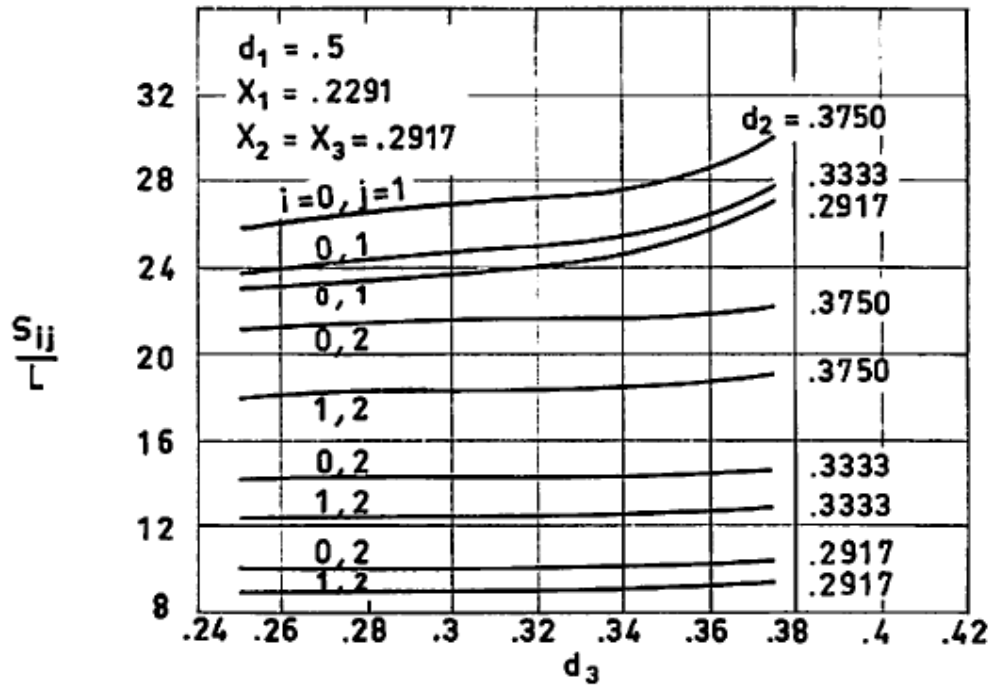
The results presented have been obtained by using an electrical analogue method.

Comments:

The configuration is two-dimensional.

S/L is the conductive shape factor per unit length normal to the plane of the figure.

The results are given in Figure 4-8.

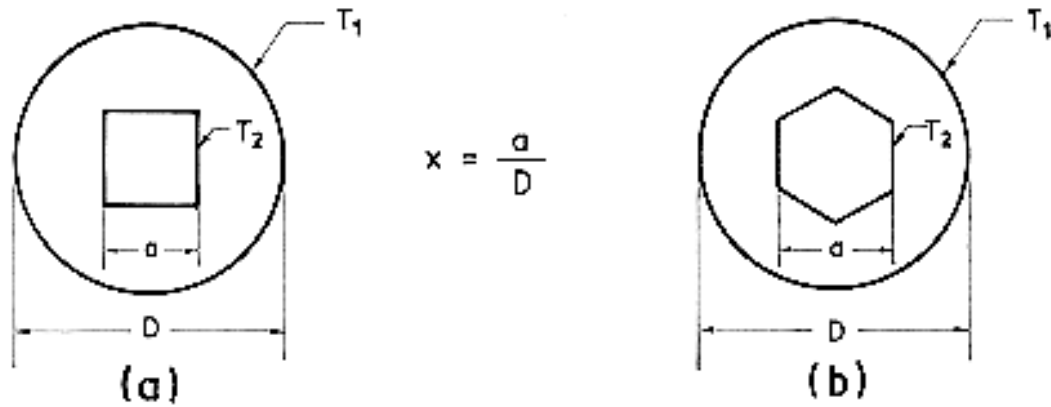


Note: non-si units are used in this figure

Figure 4-8: Values of the conductive shape factors per unit length, S_{ij}/L , vs. the diameter ratio d_3 , for different values of the relevant geometric parameters. From Faulkner & Andrews (1955) [13].

Reference: Faulkner & Andrews (1955) [13].

Circular rod with square or hexagonal concentric holes.



Formulae:

$$(a) \frac{S}{L} = \frac{6,533}{\ln \frac{1}{x} - 0,15921} \quad [4-8]$$

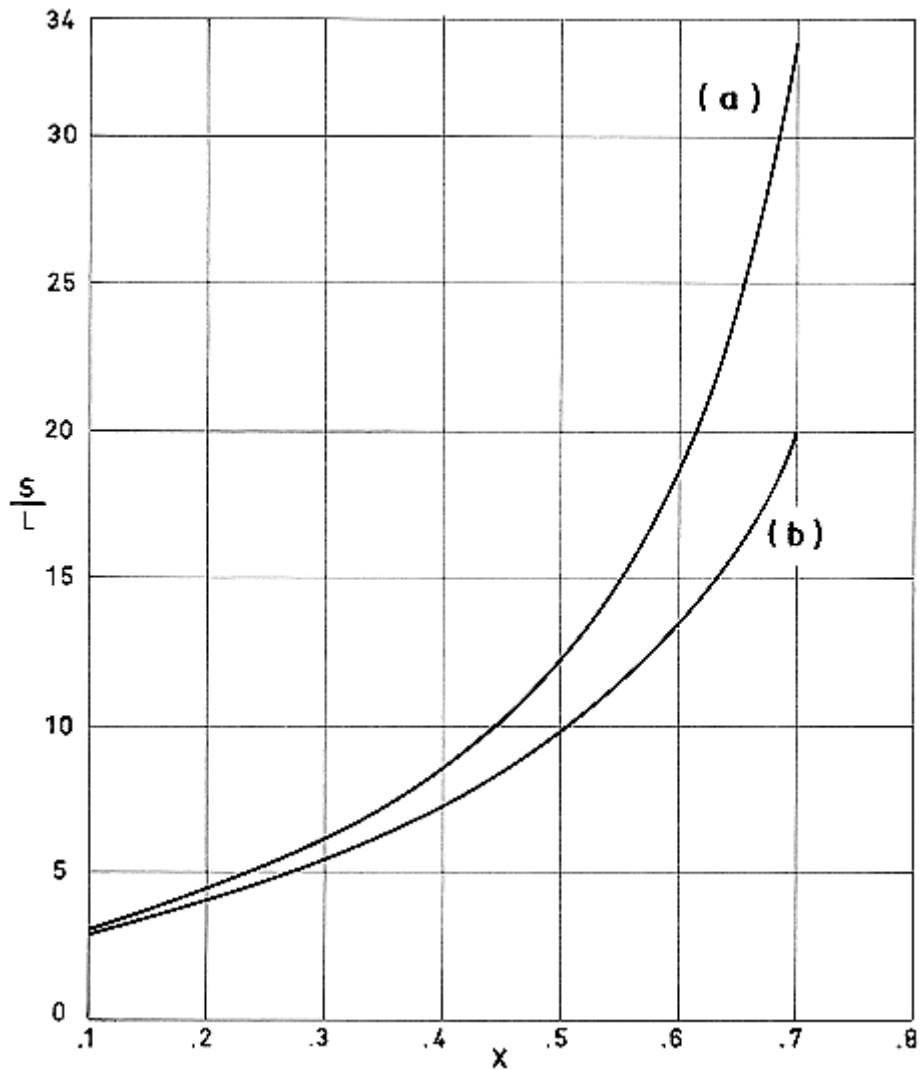
$$(b) \frac{S}{L} = \frac{6,46}{\ln \frac{1}{x} - 0,03147} \quad [4-9]$$

Comments:

The configuration is two-dimensional.

S/L is the conductive shape factor per unit length normal to the plane of the figure.

The results are given in Figure 4-9.



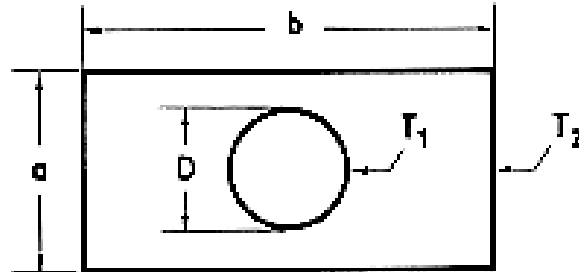
Note: non-si units are used in this figure

Figure 4-9: Values of the conductive shape factor per unit length, S/L , vs. the dimensionless characteristic length of the holes, X . Calculated by the compiler.

Reference: Ramachandra Murthy & Ramachandran (1967) [40].

4.5.1.3 Rectangular bars with holes

Rectangular bar with a concentric circular hole:



$$X = D/a$$

$$Y = b/a$$

Formula:

$$\frac{S}{L} = \frac{2\pi}{\ln \frac{4}{\pi X} - 2k} \quad [4-10]$$

where k is a coefficient which depends upon Y as indicated below

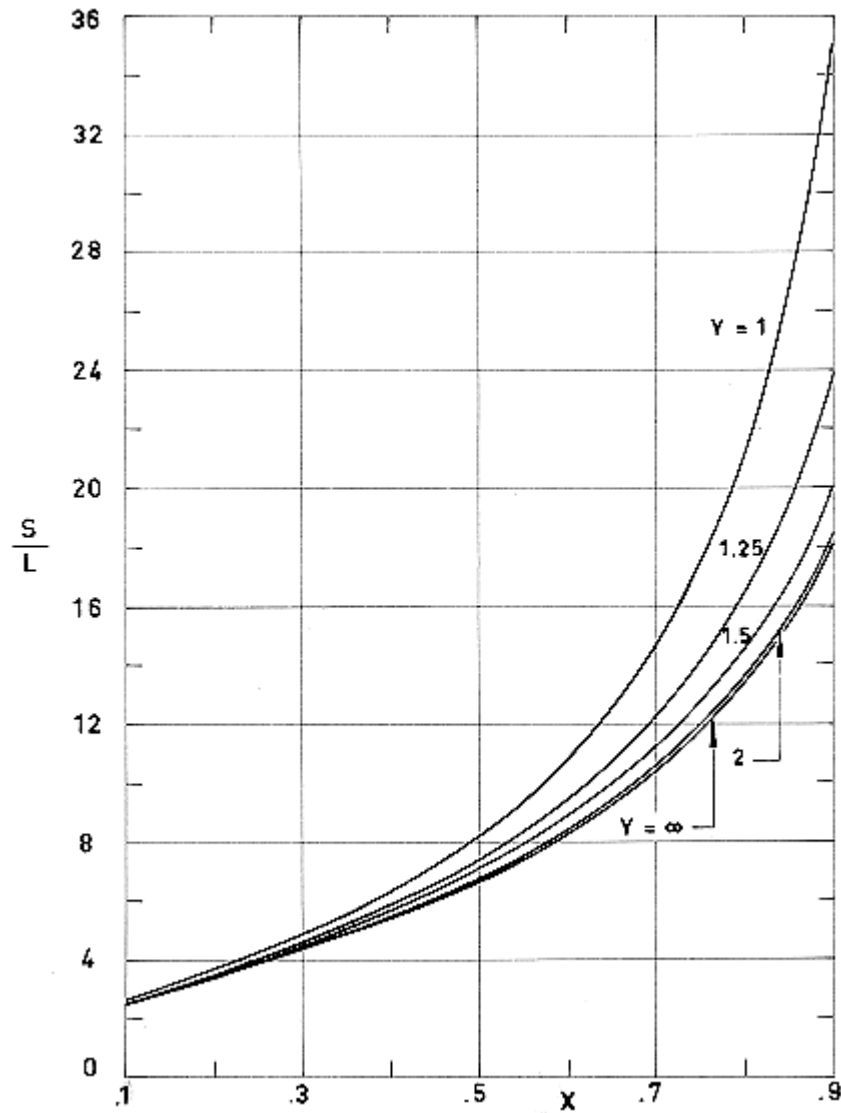
Y	k
1,00	0,08290
1,25	0,03963
1,50	0,01781
1,75	0,00816
2,00	0,00373
2,25	0,00170
2,50	0,00078
3,00	0,00016
4,00	$6,9748 \times 10^{-6}$
5,00	$3,0140 \times 10^{-7}$
10,00	$4,5422 \times 10^{-14}$
∞	0

Comments:

The configuration is two-dimensional.

S/L is the conductive shape factor per unit length normal to the plane of the figure.

The results are given in Figure 4-10.

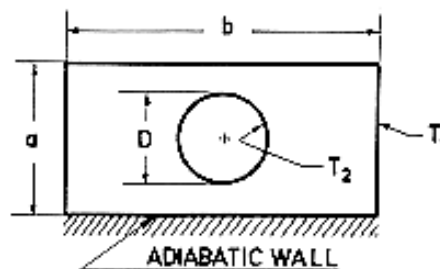


Note: non-si units are used in this figure

Figure 4-10: Values of the conductive shape factor per unit length, S/L , vs. the dimensionless diameter of the hole, X , for several values of the aspect ratio, Y , of the rectangular bar cross-section. Calculated by the compiler.

Reference: Sunderland & Johnson (1964) [46].

Rectangular bar having one adiabatic face and a concentric circular hole.



$$X = D/a$$

$$Y = b/a$$

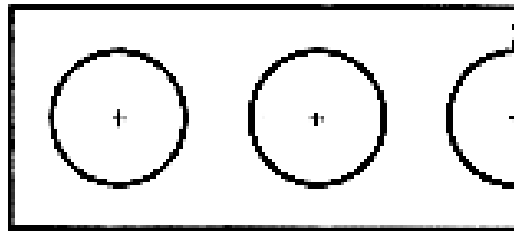
The results presented were obtained numerically.

Comments:

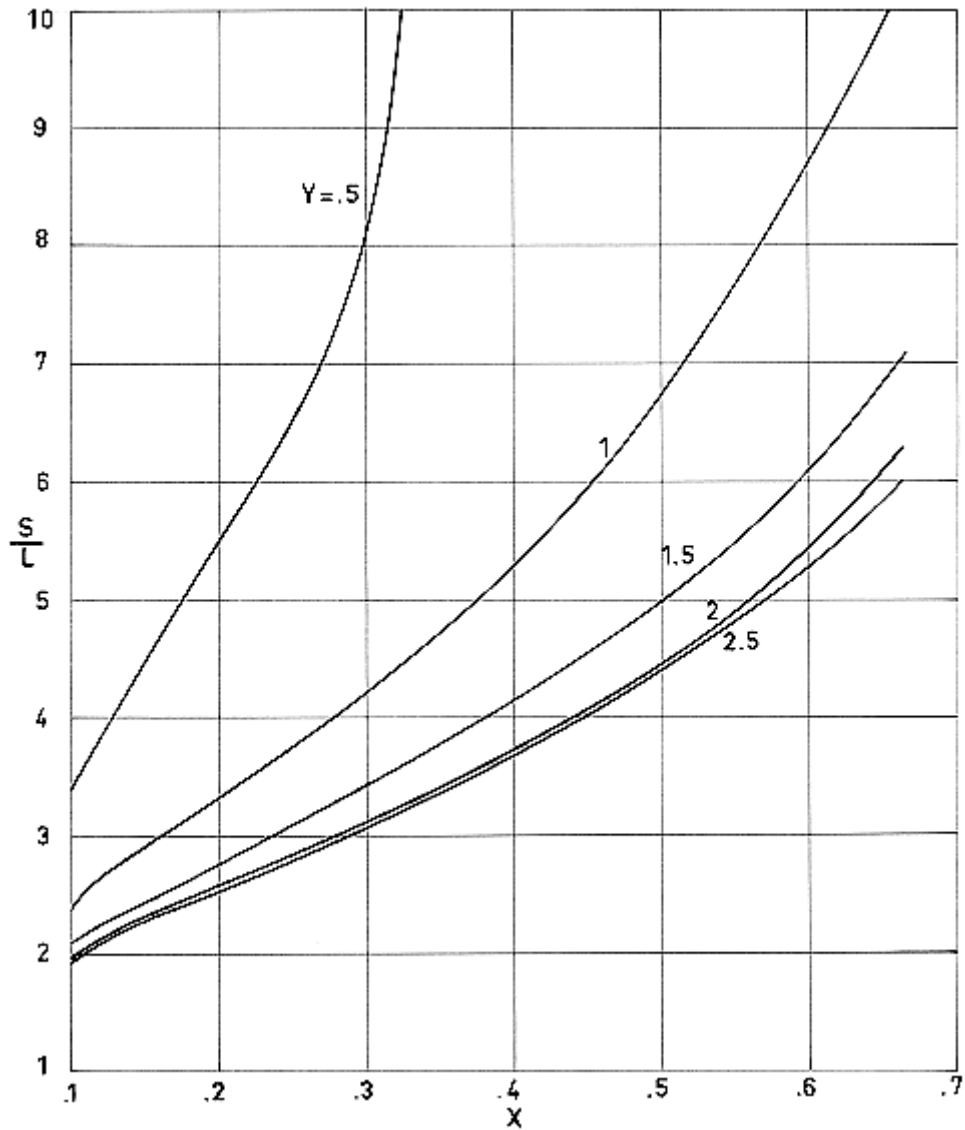
The configuration is two-dimensional.

S/L is the conductive shape factor per unit length normal to the plane of the figure.

These results can be used to study configurations similar to the one sketched below.



The results are given in Figure 4-11.

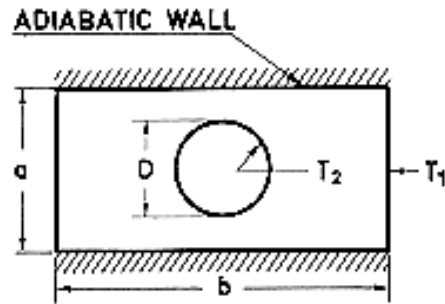


Note: non-si units are used in this figure

Figure 4-11: Values of the conductive shape factor per unit length, S/L , vs. the dimensionless diameter of the hole, X , for different values of the aspect ratio, Y , of the rectangular bar cross section. After Griggs, Pitts & Goyal (1973) [25].

Reference: Griggs, Pitts & Goyal (1973) [25].

Rectangular bar having two opposite adiabatic faces and a concentric circular hole.



$$X = D/a$$

$$Y = b/a$$

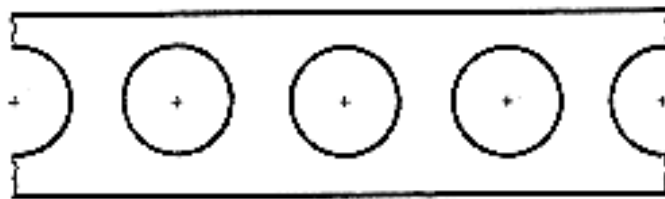
The results presented were obtained numerically.

Comments:

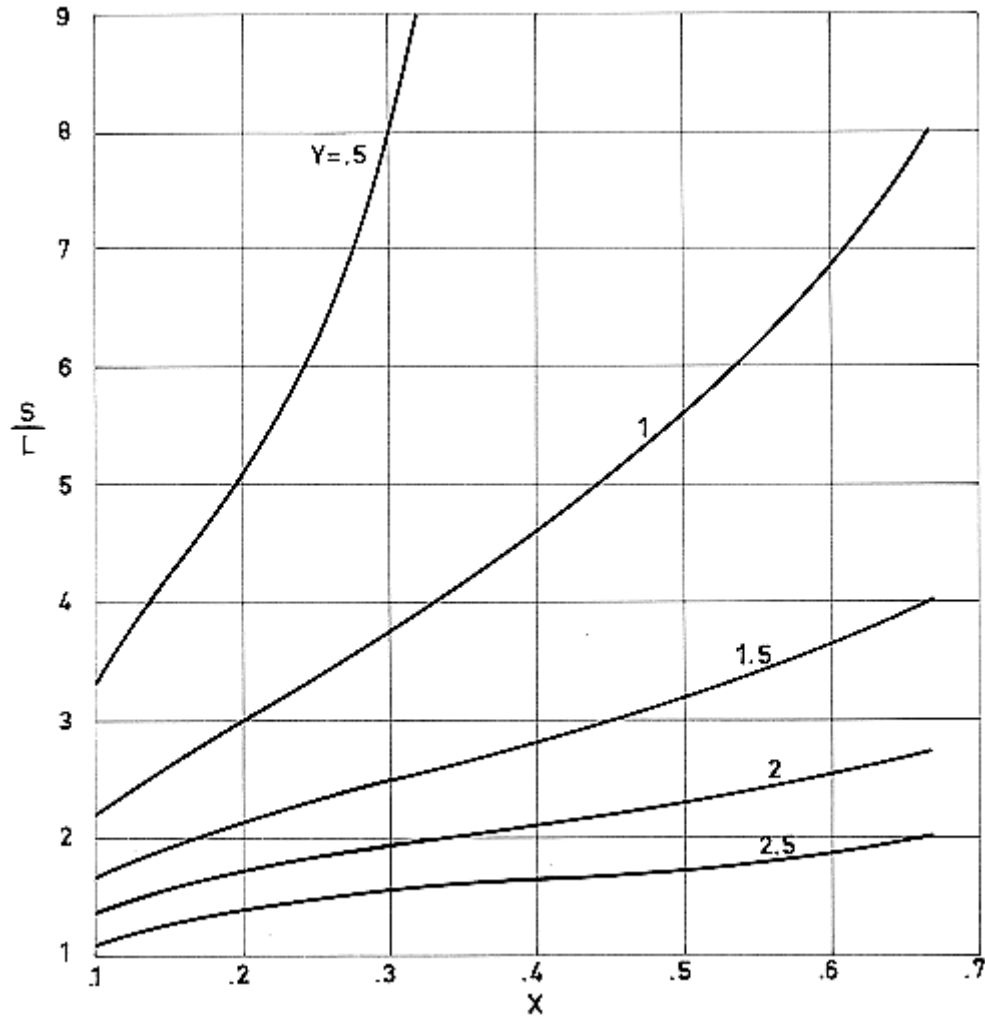
The configuration is two-dimensional.

S/L is the conductive shape factor per unit length normal to the plane of the figure.

These results can be used to study configurations similar to the one sketched below.



The results are given in Figure 4-12.



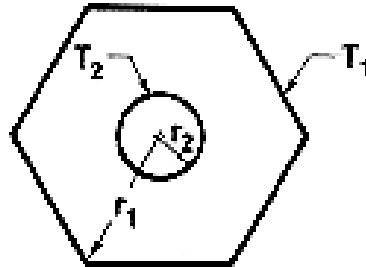
Note: non-si units are used in this figure

Figure 4-12: Values of the conductive shape factor per unit length, S/L , vs. the dimensionless diameter of the hole, X , for several values of the aspect ratio, Y , of the rectangular bar cross section. After Griggs, Pitts & Goyal (1973) [25].

Reference: Griggs, Pitts & Goyal (1973) [25].

4.5.1.4 Polygonal bars with holes

Cylinder with an n-sided regular cross section and a concentric circular hole:



$$\rho = r_2/r_1$$

Formula:

$$\frac{S}{L} = \frac{2\pi}{\ln\left(\frac{1}{\rho} - \frac{B}{2}\right)} \quad [4-11]$$

where B is a coefficient which depends upon n as indicated in the table below.

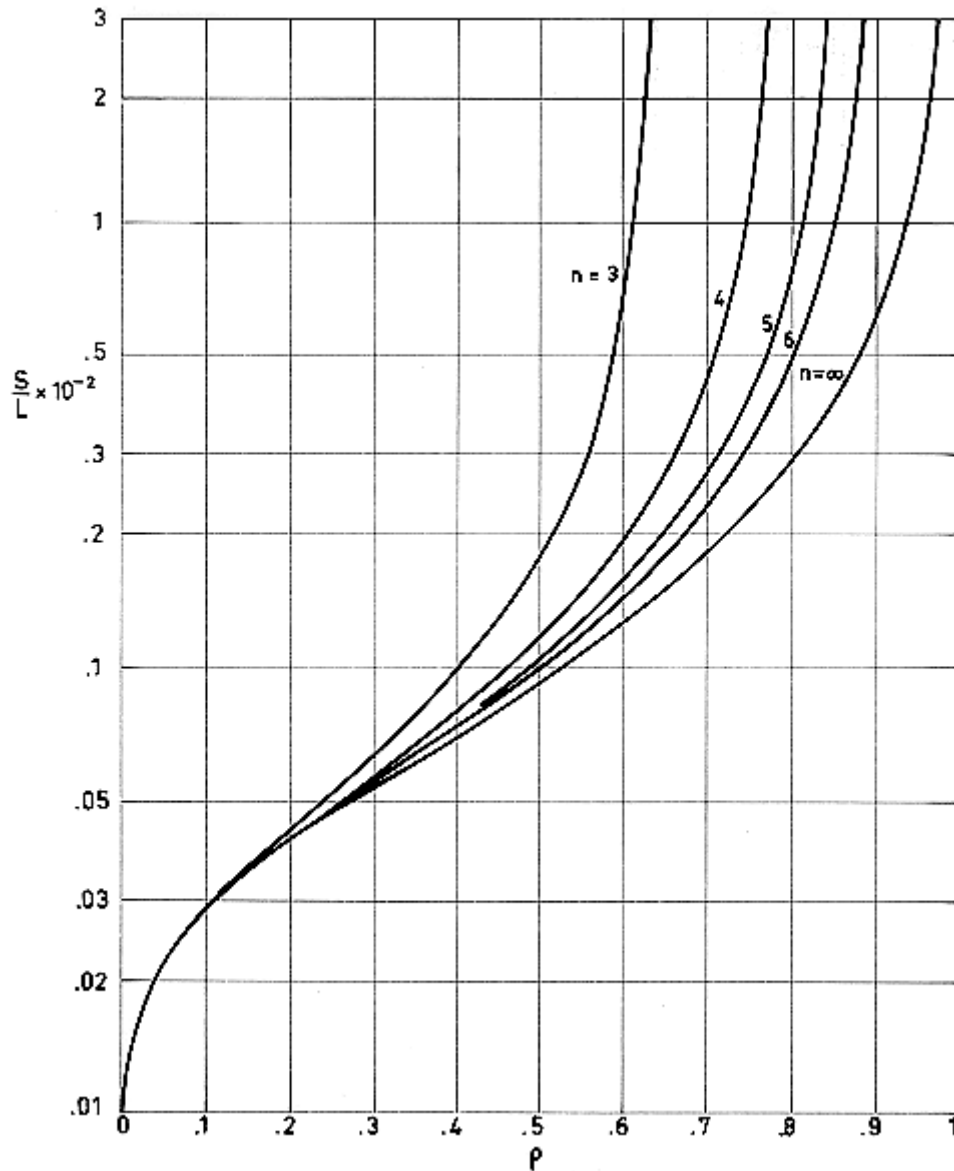
n	B
3	1,13916
4	0,54159
5	0,32131
6	0,21339
∞	0

Comments:

The configuration is two-dimensional.

S/L is the conductive shape factor per unit length normal to the plane of the figure.

The results are given in Figure 4-13.



Note: non-si units are used in this figure

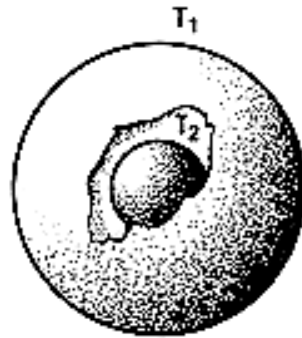
Figure 4-13: Values of the conductive shape factor per unit length, S/L , vs. the dimensionless hole radius, ρ , for several values of n . Calculated by the compiler.

Reference: Sunderland & Johnson (1964) [46].

4.6 Spherical-spherical surfaces

4.6.1 Two concentric spheres

Two concentric spheres.



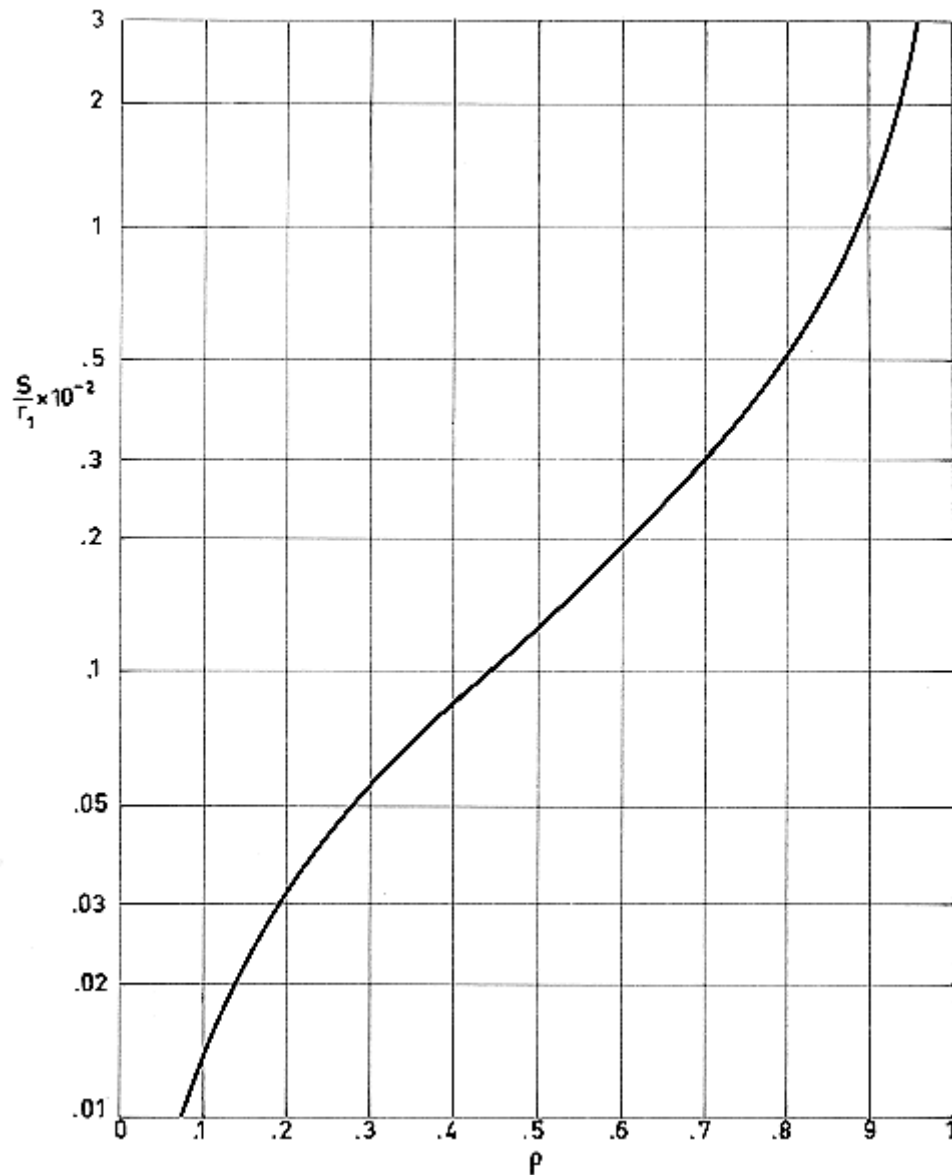
$$\rho = r_2/r_1$$

where r_1 and r_2 are the radii of the outer and inner sphere, respectively.

Formula:

$$\frac{S}{r_1} = \frac{4\pi}{\frac{1}{\rho} - 1} \quad [4-12]$$

The results are given in Figure 4-14.



Note: non-si units are used in this figure

Figure 4-14: Values of the dimensionless conductive shape factor, S/r_1 , vs. radius ratio, ρ . Calculated by the compiler.

Reference: Parker, Boggs & Blick (1969) [36].

5

Thermal joint conductance

5.1 General

The interface existing between two surfaces in contact introduces a resistance to heat transfer between the materials making up the contact. The thermal conductance, h_c , between these surfaces is given by:

$$h_c = (Q/A)/(\Delta T),$$

where:

Q/A , Heat flux across the interface. [$\text{W}\cdot\text{m}^{-2}$].

ΔT , Interfacial temperature drop, estimated as in Figure 5-1. [K].

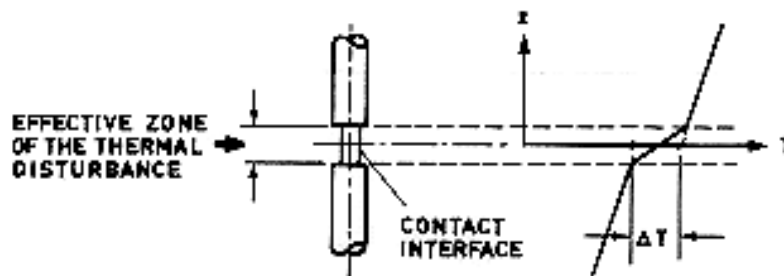


Figure 5-1: Estimation of the temperature drop at the interface.

The thermal conductance, h_c , which depends on the actual contact area and on the physical properties of the mating materials, can be split into three contributions, namely: the radiative, h_r , interstitial, h_f , and solid, h_s , contributions

$$h_c = h_r + h_f + h_s.$$

The radiative contribution, h_r , can be neglected for temperatures below 900 K, as shown by Fenech & Rohsenow (1959) [15] and by Clausing & Chao (1965) [7].

Concerning h_f , no generally valid method has been developed up to the moment to predict its contribution. The problem has been considered, among others, by Cetinkale & Fishended (1951) [6], Laming (1961) [29], Fenech & Rohsenow (1963) [14], and Henry & Fenech (1964) [27].

The contribution, h_s , of the solid contacting materials has been calculated, in the case of very simple geometrical configurations, by Roess (1949) [41], Laming (1961) [29], Clausing & Chao (1965) [7], Fenech & Rohsenow (1963) [15], and Henry & Fenech (1964) [27]. However, the direct application of these data is impeded by the impossibility of correctly defining the geometrical characteristics of the contact area under practical conditions.

Because of the difficulties which have been mentioned, the use of empirical correlations based on directly measurable parameters should be recommended. These correlations, which are based on dimensional considerations for the selection of the relevant dimensionless groups of parameters, include together the contributions of h_r , h_f , and h_s .

Unfortunately, only correlations for bare contacting metals have reached widespread use, thence, when information on the contact conductance between similar metals separated by a suitable spacer material is required, one must resort to the use of experimental data on systems which resemble as much as possible the configuration which is expected to be used in the real case.

Recently Al-Astrabadi et al. (1977) [2] correlated data on thermal contact conductance's for stacks of thin layers in high vacuum. Data from different sources, for both bare metals and plastic layers, correlate fairly in terms of appropriate dimensionless parameters.

5.1.1 Empirical correlations

5.1.1.1 Fletcher & Gyorog correlation

The following expression to predict the thermal conductance of contacting metal surfaces in a vacuum has been suggested by Fletcher & Gyorog (1970) [17].

$$h_c = \frac{km}{\delta_o} \left[5,22 \times 10^{-6} \frac{\delta_o}{b} + 0,036 \frac{P}{E} \beta Tm \right]^{0,56} \exp \left[170 \frac{\frac{P}{E} \beta Tm}{\delta_o / b} \right] \quad [5-1]$$

where:

E , Modulus of Elasticity. [Pa].

P , Applied Compressive Load. [Pa].

Tm , Mean Temperature. [K].

b , Specimen Radius. [m].

h_c , Thermal Contact Conductance. [$W \cdot m^{-2} \cdot K^{-1}$].

km , Mean Thermal Conductivity. [$W \cdot m^{-1} \cdot K^{-1}$].

$km = 2k_1k_2/(k_1+k_2)$. k_1 and k_2 are thermal conductivities of the mating materials.

β , Coefficient of Linear Thermal Expansion. [K^{-1}].

δ_o , Gap Thickness Parameter. [m].

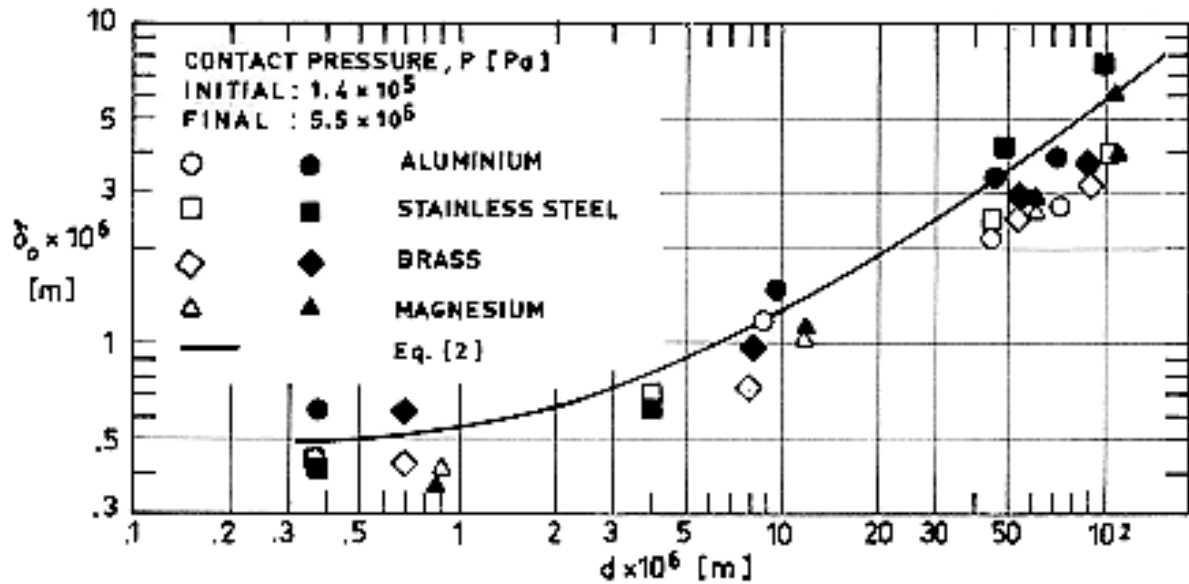
$$\delta_o = 0,519 \times 10^{-6} + 0,806 \times 10^{-1} d - 0,622 \times 10^3 d^2 + 0,211 \times 10^7 d^3 \quad [5-2]$$

$d = (FD + 2RD)_{\text{rough surface}}^{-1/2} (FD + 2RD)_{\text{smooth surface}}$. [m].

FD, Flatness Deviation. [m].

RD, Roughness Deviation. [m].

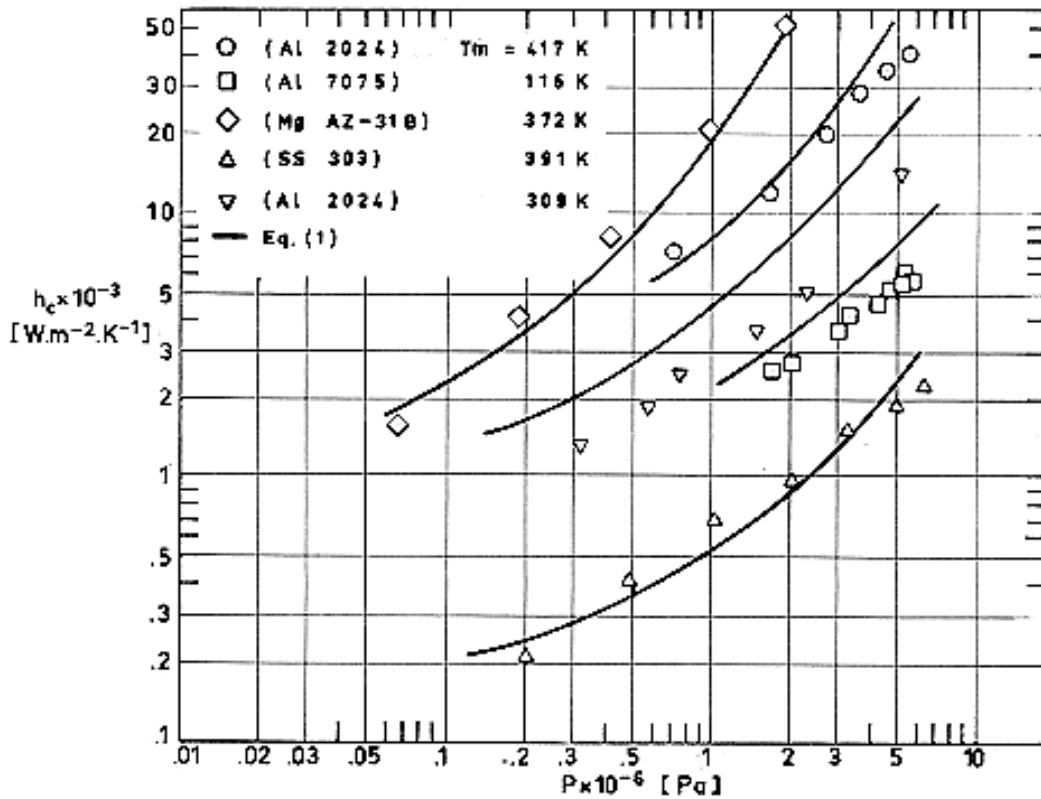
The gap thickness parameter, δ is represented as a function of d in Figure 5-2. Experimental data from different sources are included in this figure.



Note: non-si units are used in this figure

Figure 5-2: Variation of gap thickness parameter, δ_0 with contact surface parameter, d . After Fletcher & Gyrog (1970) [17].

The thermal conductance, h_c , is plotted vs. the load pressure, P , in Figure 5-3. Again the empirical correlation is compared with data from several sources. A mean error of 24% is reported by the authors.



Note: non-si units are used in this figure

**Figure 5-3: Variation of contact conductance with apparent interface pressure.
 After Fletcher & Gyorg (1970) [17].**

5.1.1.2 Thomas & Probert correlation

This correlation has been set forth by Thomas & Probert (1972) [47] and extensively verified, under conditions, both by the mentioned authors and by O'Callaghan & Probert (1973) [34].

$$\log \frac{h_c A}{\sigma k m} = C \log \frac{PA}{\sigma^2 M} + D \quad [5-3]$$

where:

A , Nominal Contact Area. [m²].

$C = 0,743 \pm 0,067$ for stainless steel.

$C = 0,720 \pm 0,044$ for aluminium.

$D = 2,26 \pm 0,88$ for stainless steel.

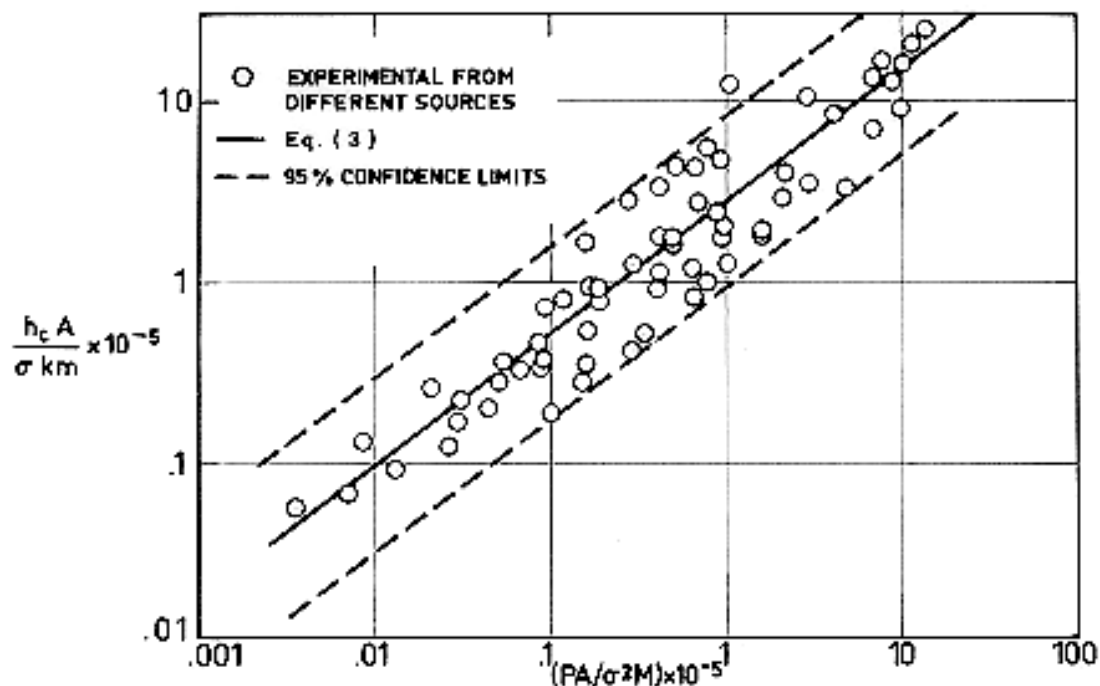
$D = 0,66 \pm 0,62$ for aluminium.

M , Surface Hardness. [Pa].

σ , *rms* Surface Roughness. [m].

$\sigma = ((RD)_1^2 + (RD)_2^2)^{1/2}$. $(RD)_1$ and $(RD)_2$ are the roughness deviations of the mating materials.

Figure 5-4 gives the dimensionless conductance vs. the dimensionless load for stainless steel contacts in a vacuum, while Figure 5-5 shows similar data when one or both surfaces are aluminium.



Note: non-si units are used in this figure

Figure 5-4: Dimensionless conductance vs. dimensionless load. Stainless steel under vacuum conditions. From Thomas & Probert (1972) [47].

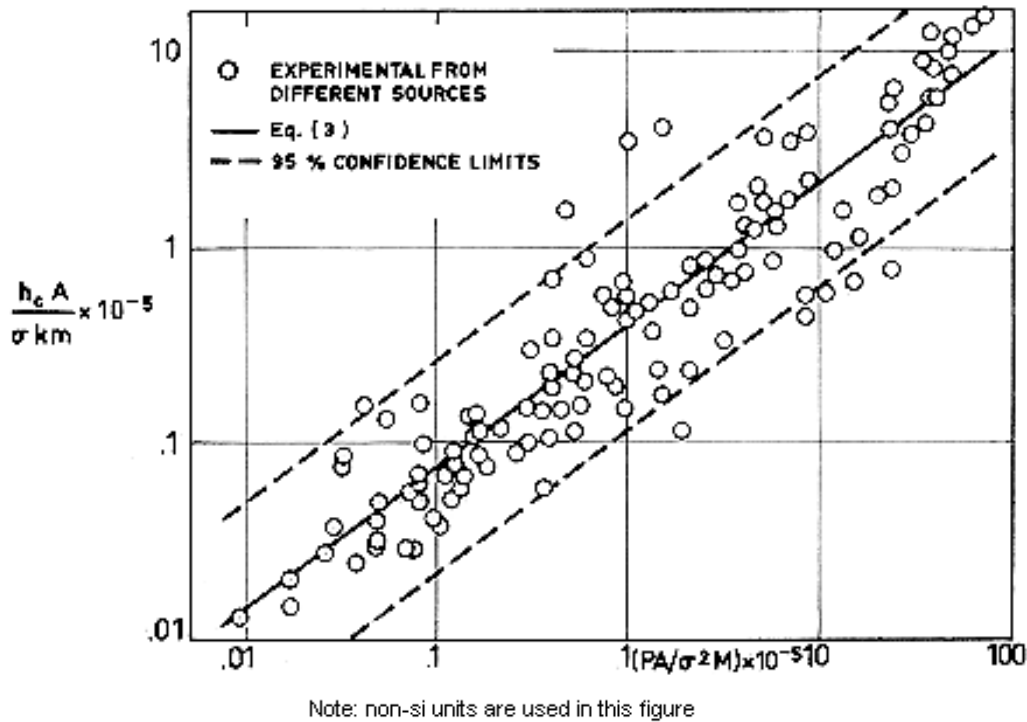


Figure 5-5: Dimensionless conductance vs. dimensionless load. Stainless steel under vacuum conditions. From Thomas & Probert (1972) [47].

5.1.2 Thermal interface materials

When two solids are brought into contact and heat is conducted from one into the other, the joint resistance is caused by inherent irregularities of the contacting surfaces. Each surface, no matter how well polished, consists of peaks and valleys as shown in Figure 5-6. The actual metal to metal contact area is a small fraction of the total contact area. Voids formed by valleys are filled with air and contribute little to the conduction of heat. The majority of the heat flow is constricted to the areas of metal to metal contact and gives rise to the observed temperature gradient across the interface.

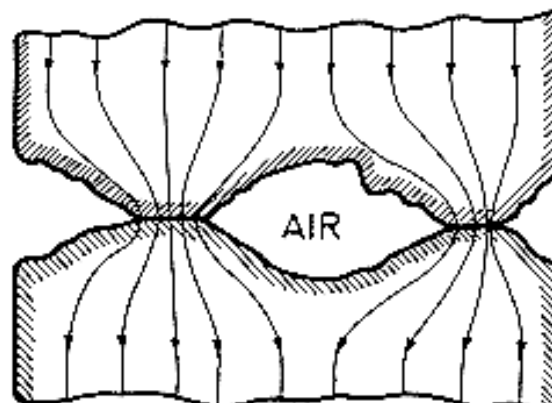


Figure 5-6: Schematic representation of two surfaces in contact and heat flow across the interface.

In many applications (e.g., removal of waste heat generated by semiconductor devices) the physical interfaces will offer minimum resistance to heat flow, and generally they will also provide electrical isolation. These requirements can be met by using conventional insulators coated with a thermal compound, or with one-component thermal interface materials (see clause 5.3.6.1). A thermal interface material is illustrated in Figure 5-7. Electrical isolation is achieved because the two metal surfaces are separated by the dielectric material. Thermal contact resistance has been minimized because the air gaps have been eliminated and replaced with a material whose thermal conductivity is much greater than that of air.

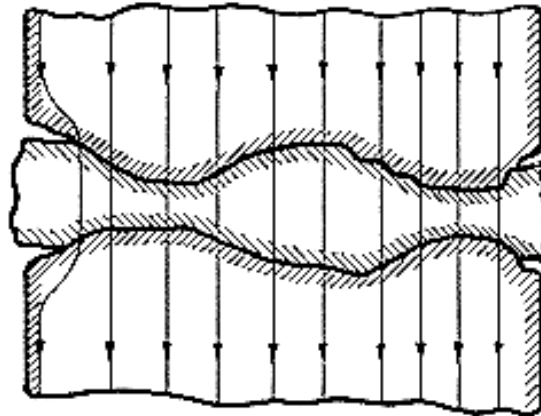






Figure 5-7: Interface material compressed between two contacting surfaces.

To perform successfully, thermal interface materials have high dielectric strength, high thermal conductivity and sufficient pliancy to conform to both microscopic and macroscopic surface irregularities. They are also sufficiently durable to survive a variety of assembly, use and environmental conditions.

5.1.3 Joint geometries

In the following the geometry of the joints most used in this clause are sketched. Other particular geometries will be explained in the text when required.

<p>Two cylinders (same diameter)</p>	
<p>Two different cylinders (different diameter)</p>	
<p>Two disks (can be off different thickness)</p>	
<p>Three cylinders (same diameter)</p>	

5.2 Bare metallic joints

SPECIMENS: Two cylinders, Al - 4,3 Cu - 1,5 Mg - 0,6 Mn. (Al 2024-T4).

Radius, $b = 2,54 \times 10^{-2}$ m.

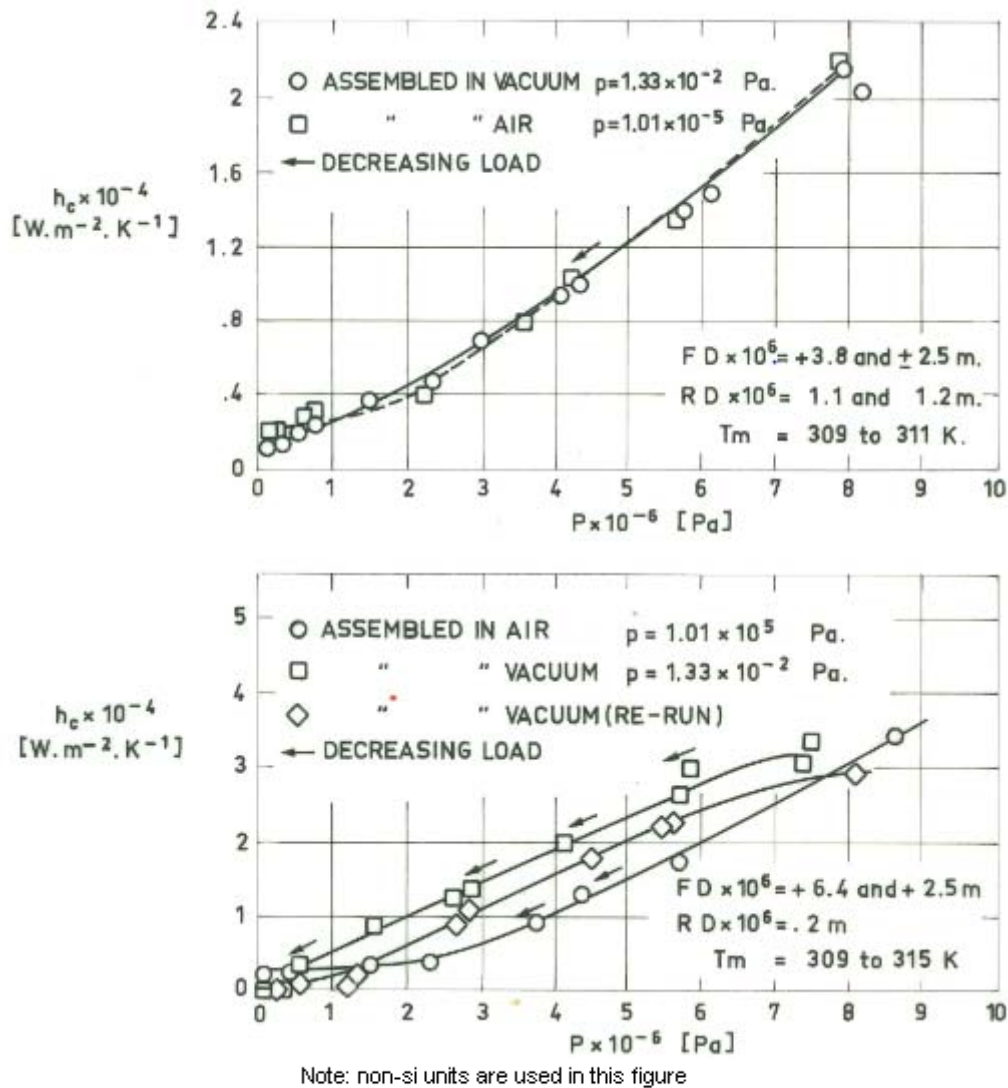


Figure 5-8: Plots of contact conductance vs. contact pressure for two different surface finishes. From Fried & Kelley (1966) [24].

SPECIMENS: Two cylinders, Al - 1 Mg - 0,6 Si. (Al 6061-T6).

Radius, $b = 2,54 \times 10^{-2}$ m.

Ambient Pressure, $p = 1,33 \times 10^{-2}$ Pa.

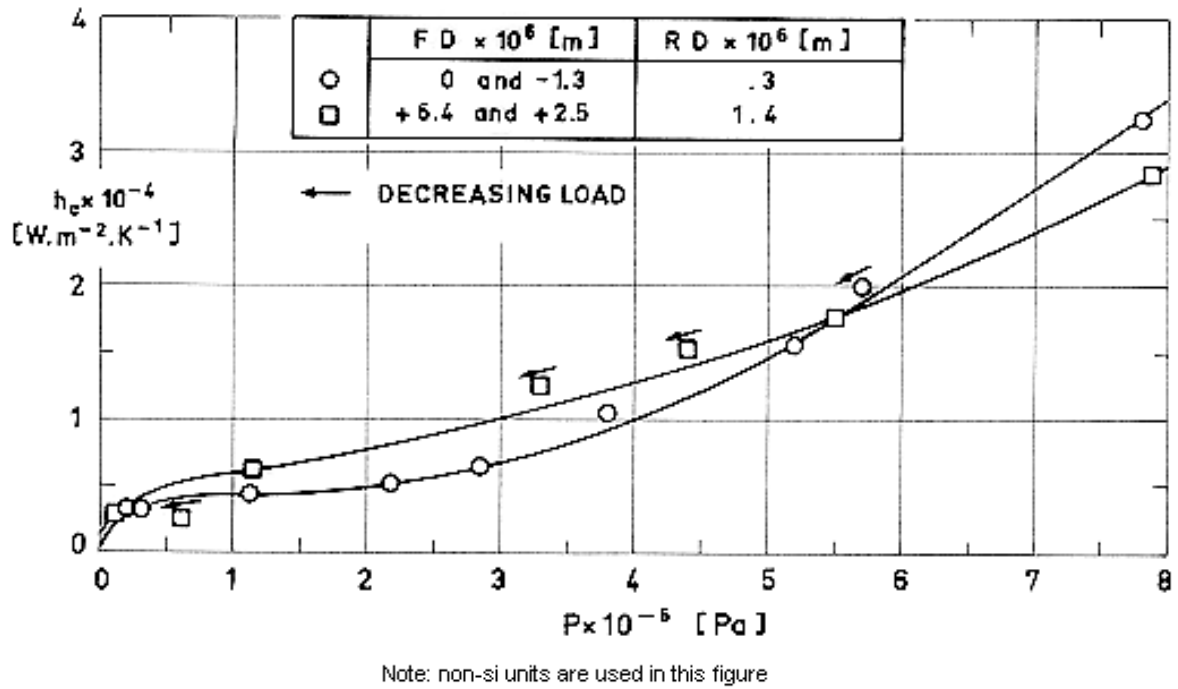
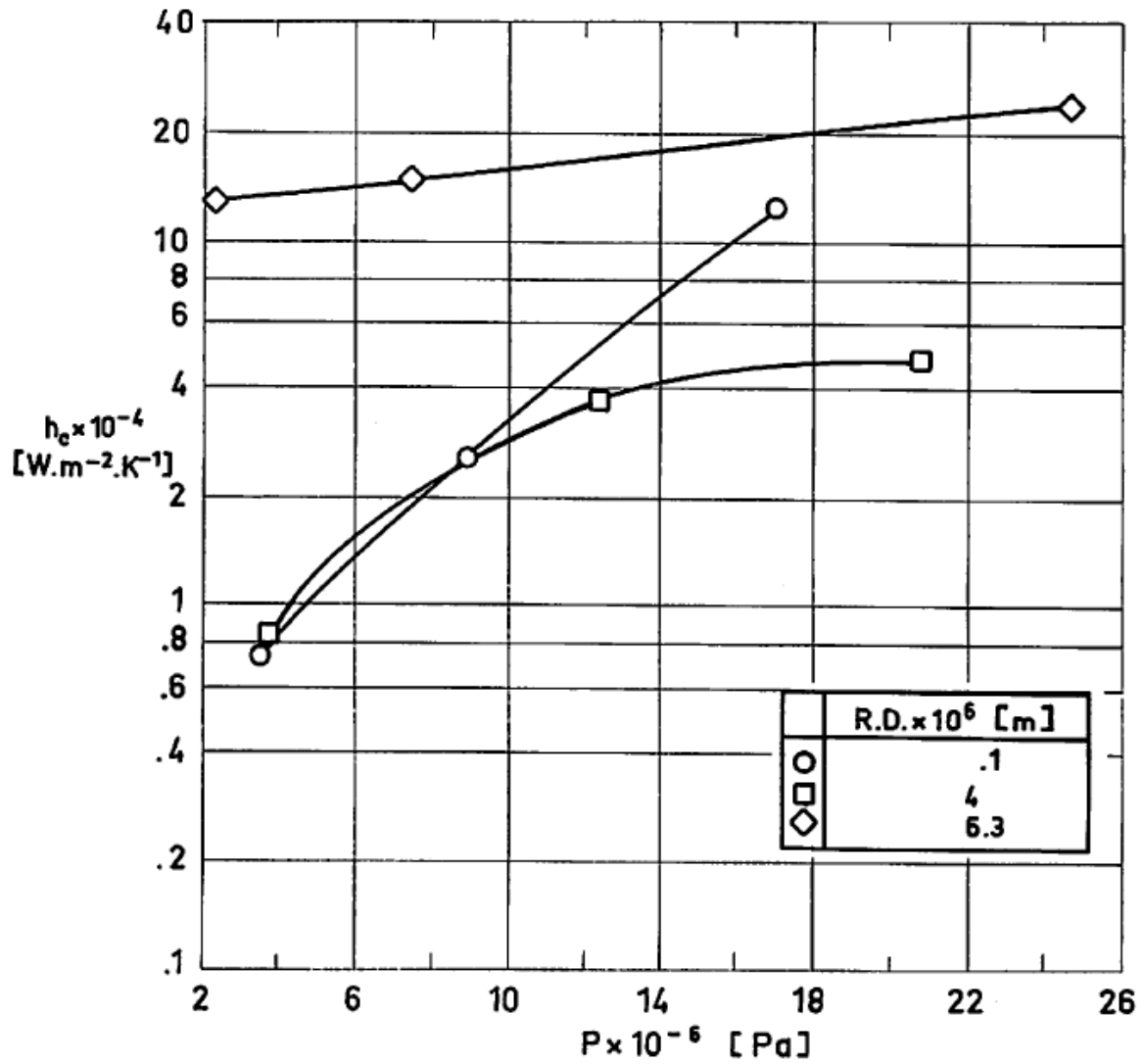


Figure 5-9: Plot of contact conductance vs. contact pressure for two different surface finishes. From Fried & Atkins (1965) [23].

SPECIMENS: Two cylinders, Al - 5,5 Zn - 2,5 Mg - 1,5 Cu. (Al 7075-T6).

Radius, $b = 1,27 \times 10^{-2}$ m.

Ambient Pressure, $p = 1,33 \times 10^{-3}$ Pa.



Note: non-si units are used in this figure

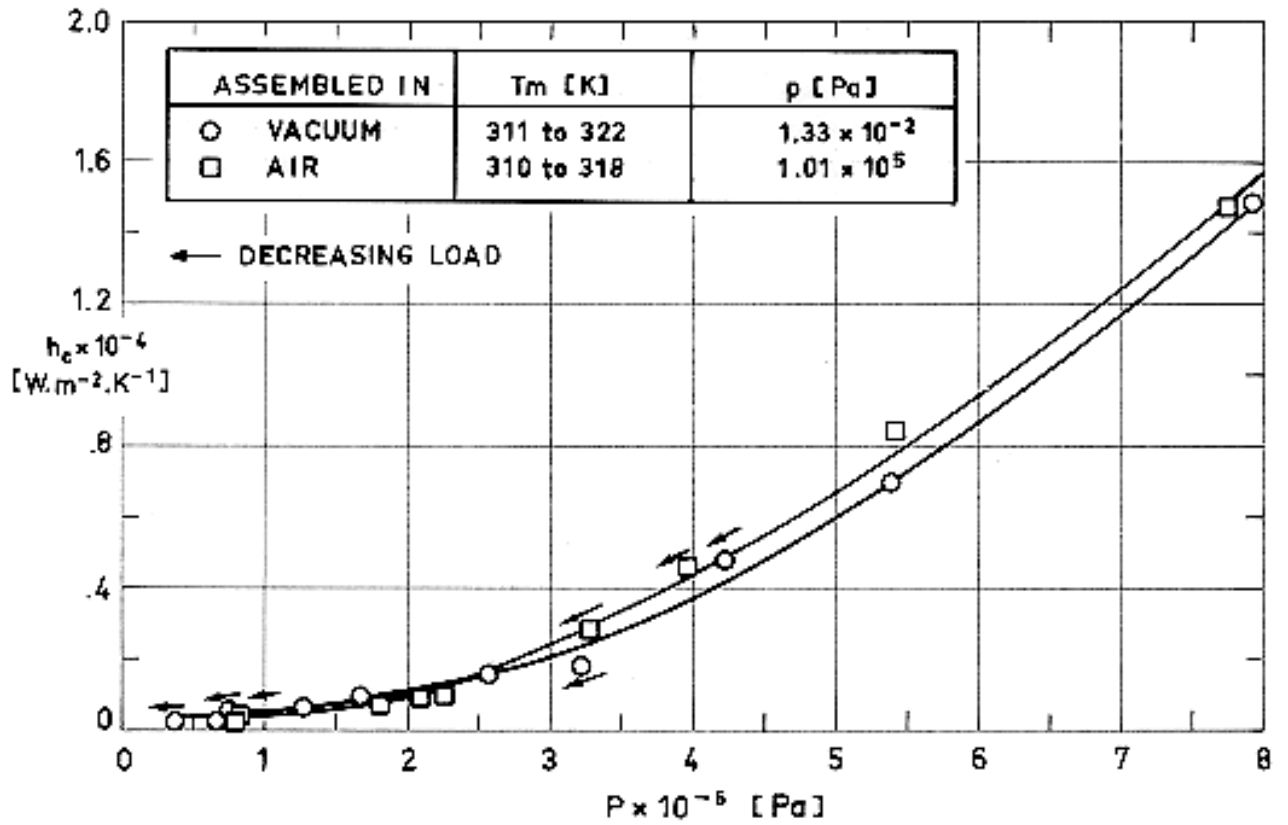
Figure 5-10: Plots of contact conductance vs. contact pressure for two different surface finishes. From Fried (1966) [22] quoted by Scollon & Carpitella (1970) [43].

SPECIMENS: Two cylinders, Be.

Radius, $b = 2,54 \times 10^{-2}$ m.

Flatness Deviation, $FD = +3,8 \times 10^{-6}$ and $+3 \times 10^{-6}$ m.

Roughness Deviation, $RD = 0,1 \times 10^{-6}$ m.

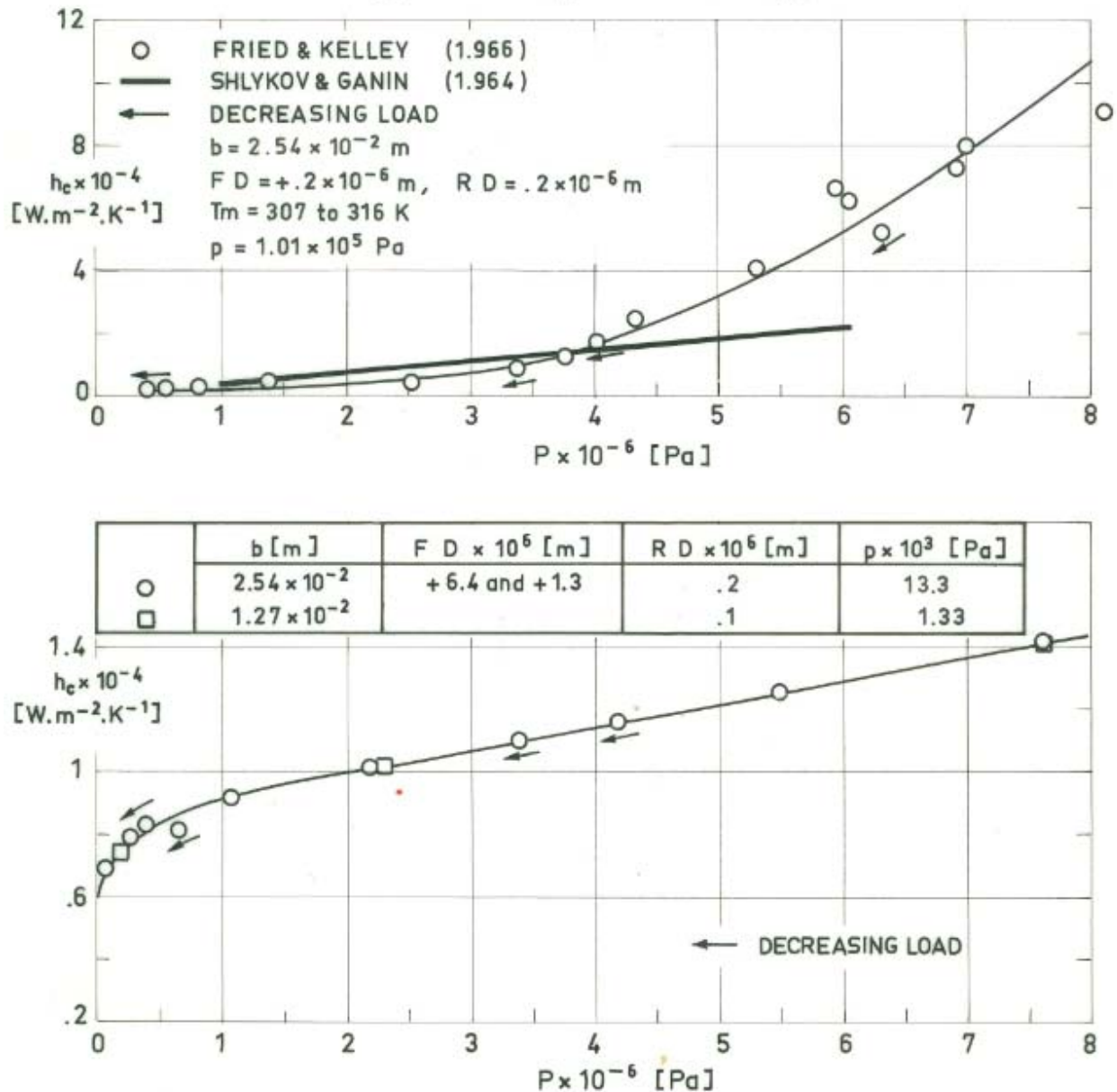


Note: non-si units are used in this figure

Figure 5-11: Plot of contact conductance vs. contact pressure for different ambient pressures. From Fried & Kelley (1966) [24].

SPECIMENS: Two cylinders, Cu OFHC.

(OFHC: Oxygen Free High Conductivity).



Note: non-si units are used in this figure

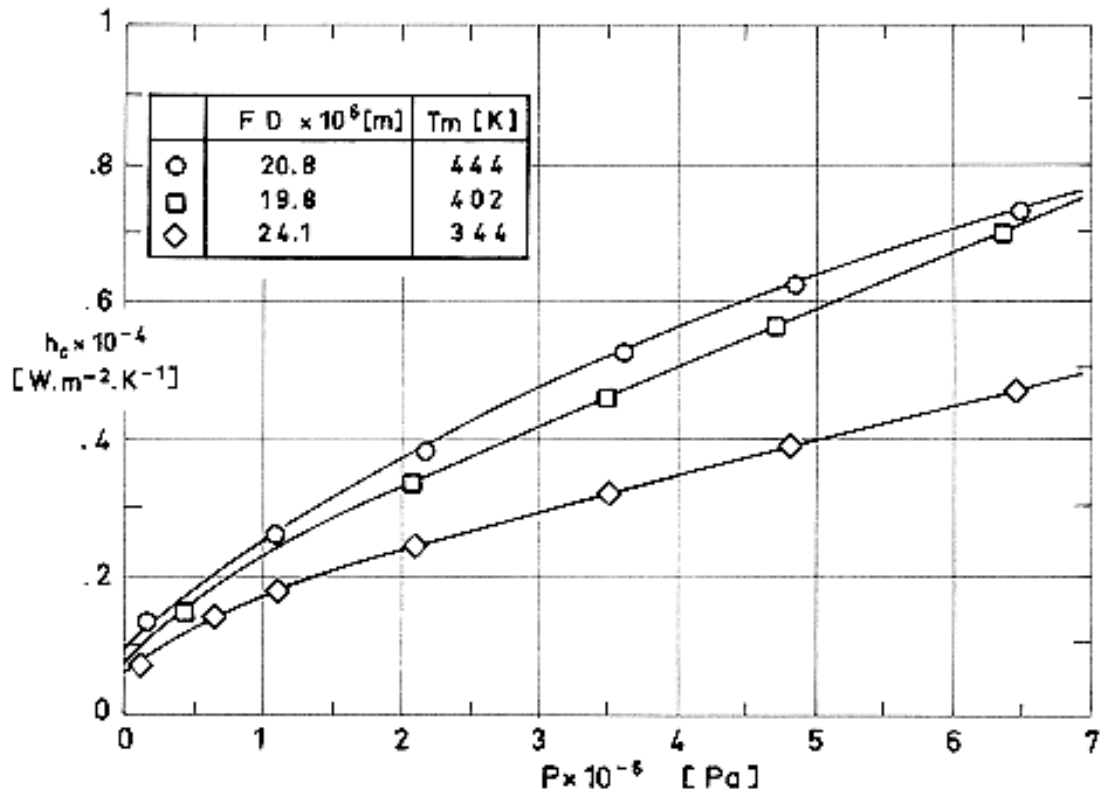
Figure 5-12: Plots of contact conductance vs. contact pressure for different surface finishes and ambient pressures. Circle: From Fried & Atkins (1965) [23]. Square: From Fried (1966) [21] quoted by Scollon & Carpitella (1970) [43].

SPECIMENS: Two cylinders, Cu - 35 Zn - 3 Pb (Brass, Anaconda alloy 271).

Radius, $b = 1,27 \times 10^{-2} \text{ m}$.

Roughness Deviation, $RD = 0,1 \times 10^{-6} \text{ m}$.

Ambient Pressure, $p = 0,66 \times 10^{-3} \text{ Pa}$.



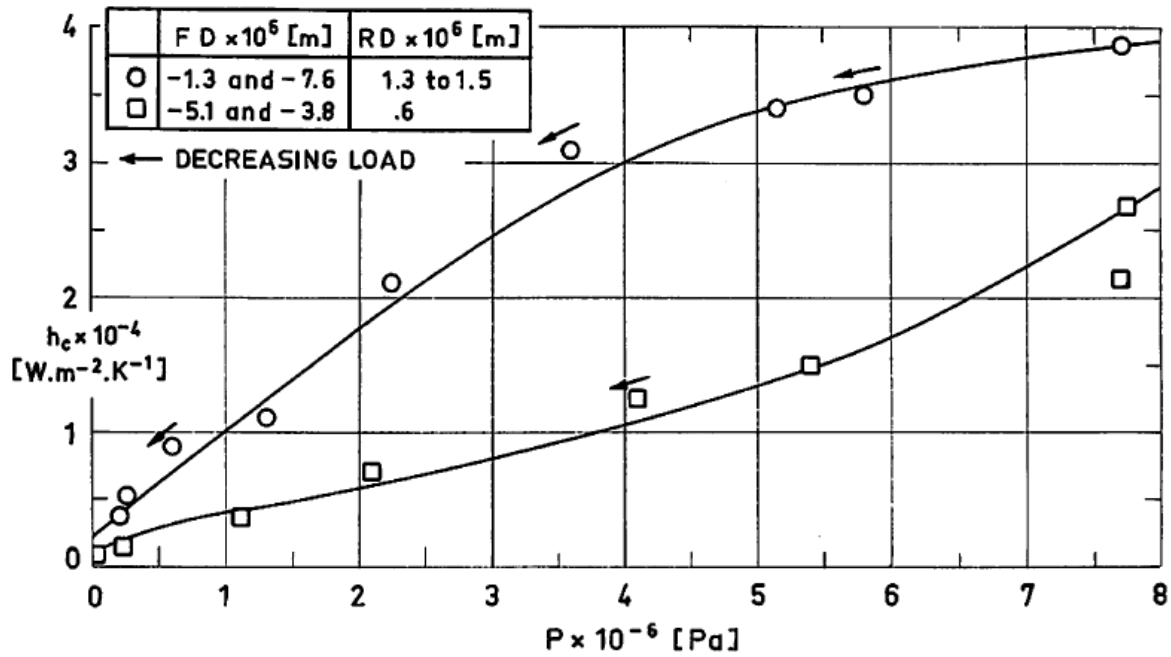
Note: non-si units are used in this figure

Figure 5-13: Plot of contact conductance vs. contact pressure for different surface finishes. From Clausing & Chao (1965) [7].

SPECIMENS: Two cylinders, Mg - 3 Al - 1 Zn - 0,2 Mn. (Mg AZ-31B).

Radius, $b = 2,54 \times 10^{-2}$ m.

Ambient Pressure, $p = 1,33 \times 10^{-2}$ Pa.



Note: non-si units are used in this figure

Figure 5-14: Plot of contact conductance vs. contact pressure for different surface finishes. From Fried & Atkins (1965) [23].

Comments: Oxide films were detected on both test surfaces. This could be the explanation on the higher conductance exhibited by the coarse finish.

SPECIMENS: Two cylinders, Mg - 3 Al - 1 Zn - 0,2 Mn. (Mg AZ-31B).

Radius, $b = 1,27 \times 10^{-2}$ m.

Roughness Deviation, $RD = 0,1 \times 10^{-6}$ m.

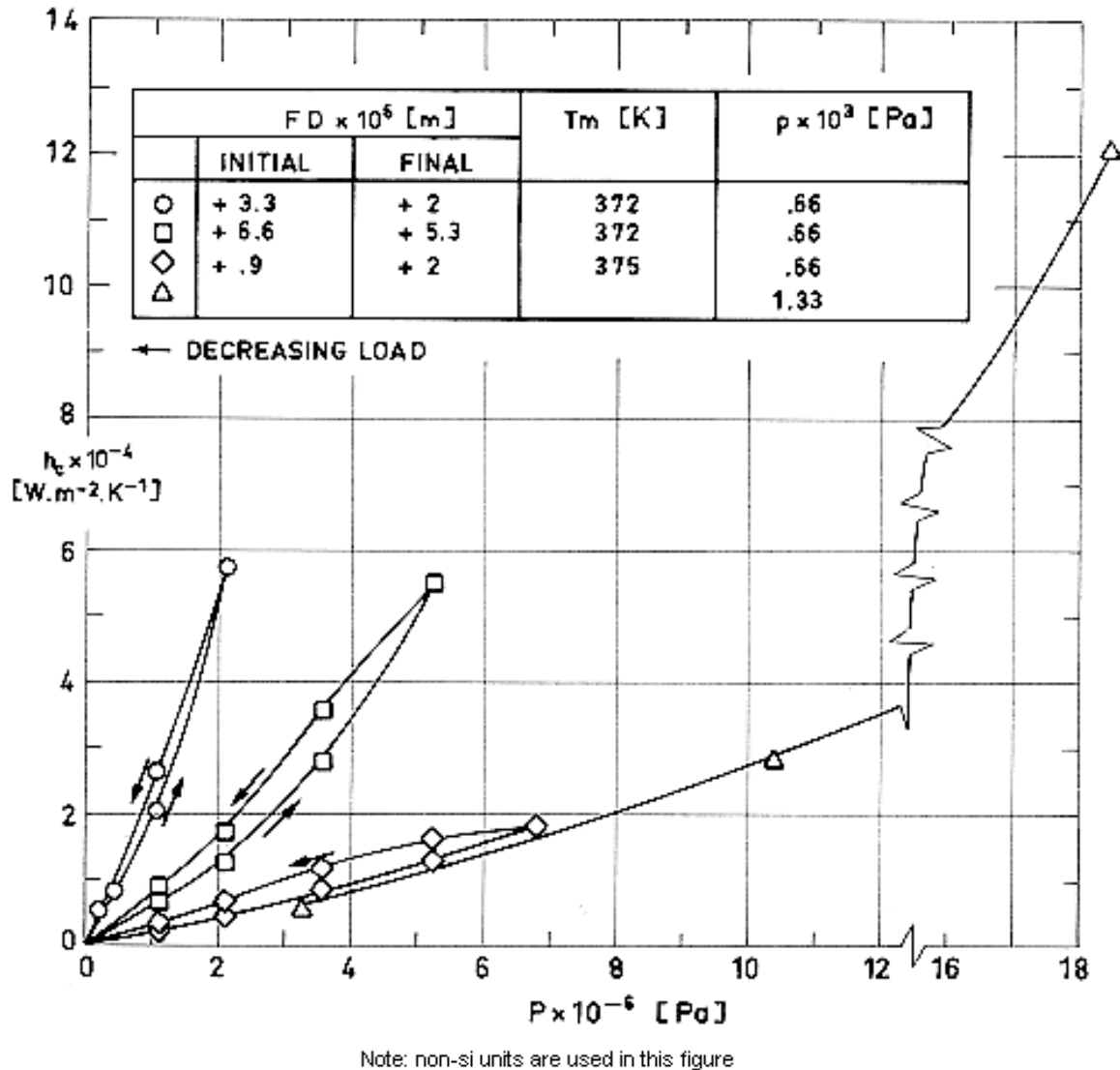


Figure 5-15: Plot of contact conductance vs. contact pressure for various surface finishes, mean temperatures and ambient pressures. Circle, square and rhombus: from Clausing & Chao (1965) [7]. Triangle: from Fried (1966) [21] quoted by Scollon & Carpitella (1970) [43].

Comments: Notice the effect of loading and unloading.

In the case of the curve of rhombus, a film was detected on both test surfaces.

SPECIMENS: Two cylinders, Fe - 19 Cr - 10 Ni (SS 304) and

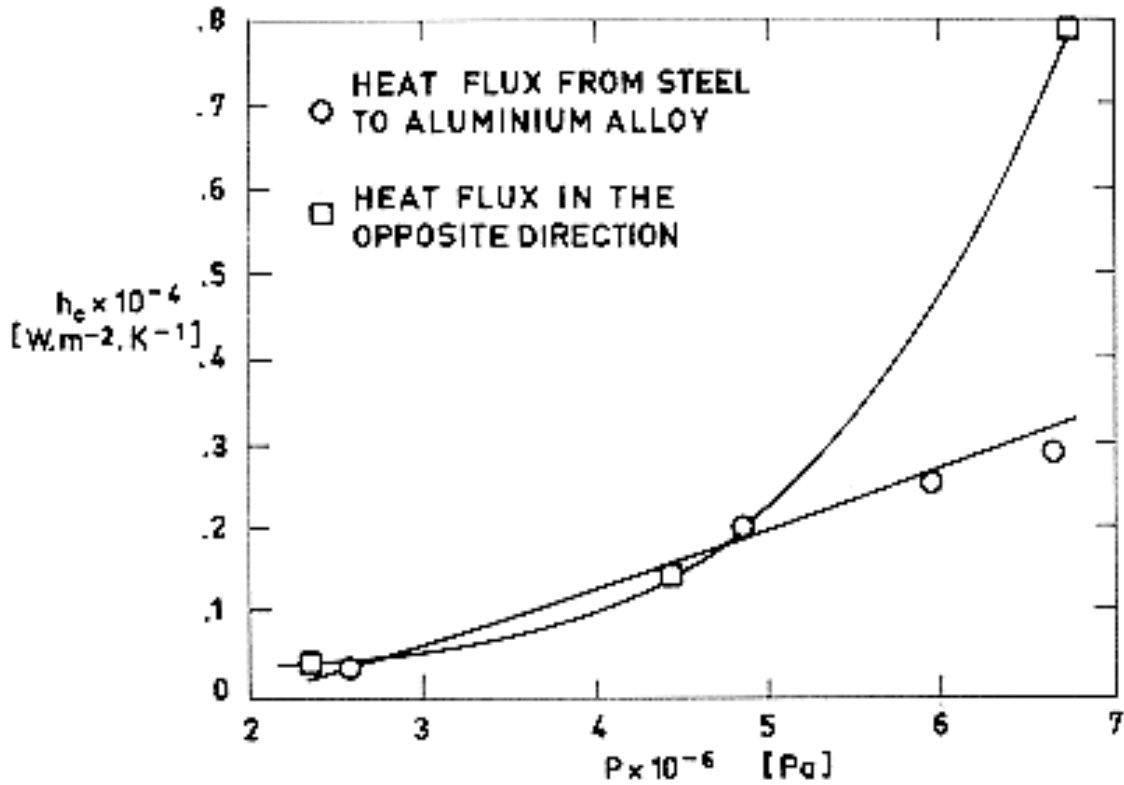
Al - 4,3 Cu - 1,5 Mg - 0,6 Mn (Al 2024-T4).

Radius, $b = 2,54 \times 10^{-2}$ m.

Flatness Deviation, $FD = -1,3 \times 10^{-6}$ and $+6,4 \times 10^{-6}$ m.

Roughness Deviation, $RD = 0,3 \times 10^{-6}$ and $0,2 \times 10^{-6}$ m.

Ambient Pressure, $p = 1,33 \times 10^{-2}$ Pa.



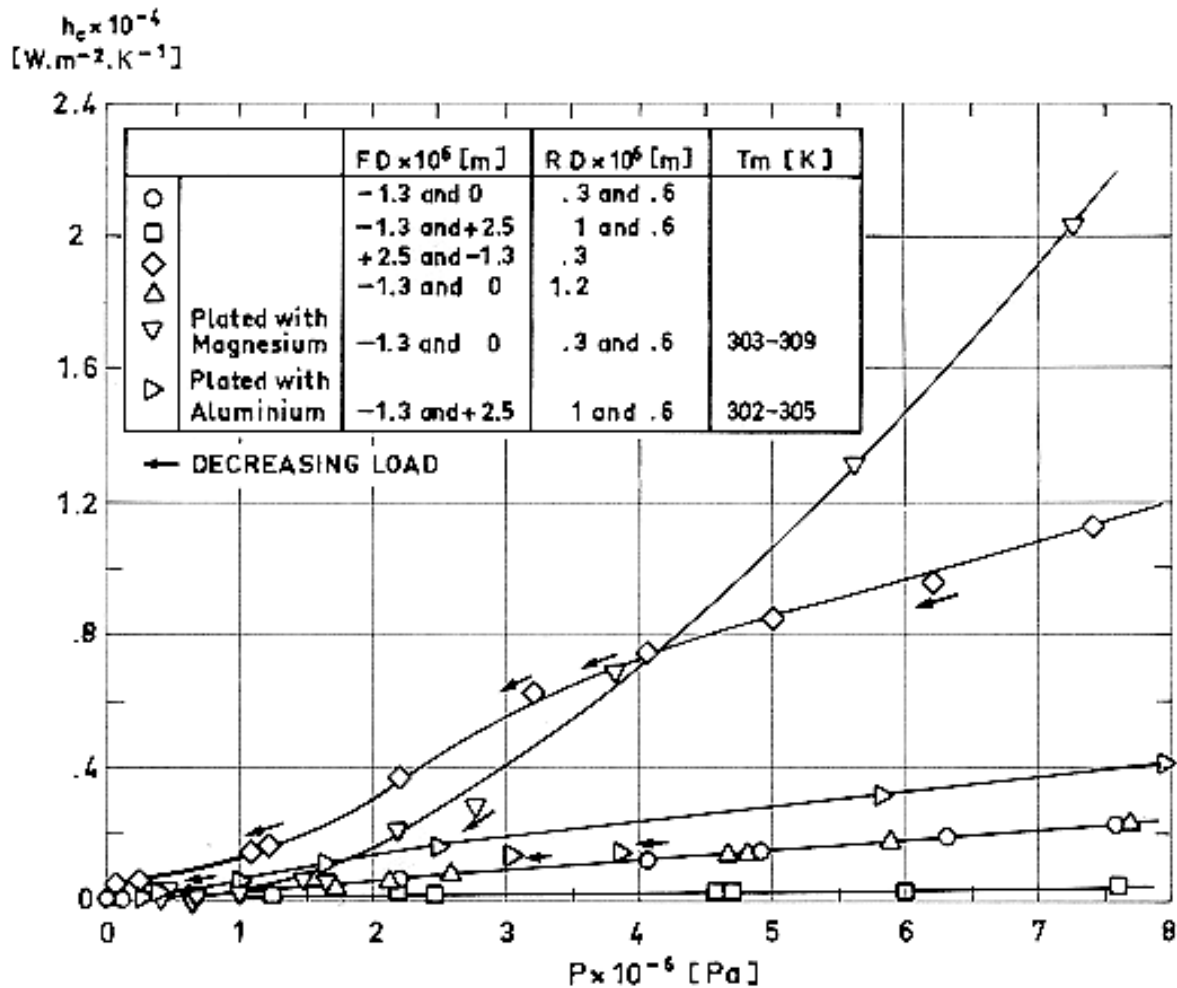
Note: non-si units are used in this figure

Figure 5-16: Plot of contact conductance vs. contact pressure. Notice the directional effect on contact conductance. From Fried & Kelley (1966) [24].

SPECIMENS: Two cylinders, Fe - 19 Cr - 10 Ni (SS 304).

Radius, $b = 2,54 \times 10^{-2}$ m.

Ambient Pressure, $p = 1,33 \times 10^{-2}$ Pa.



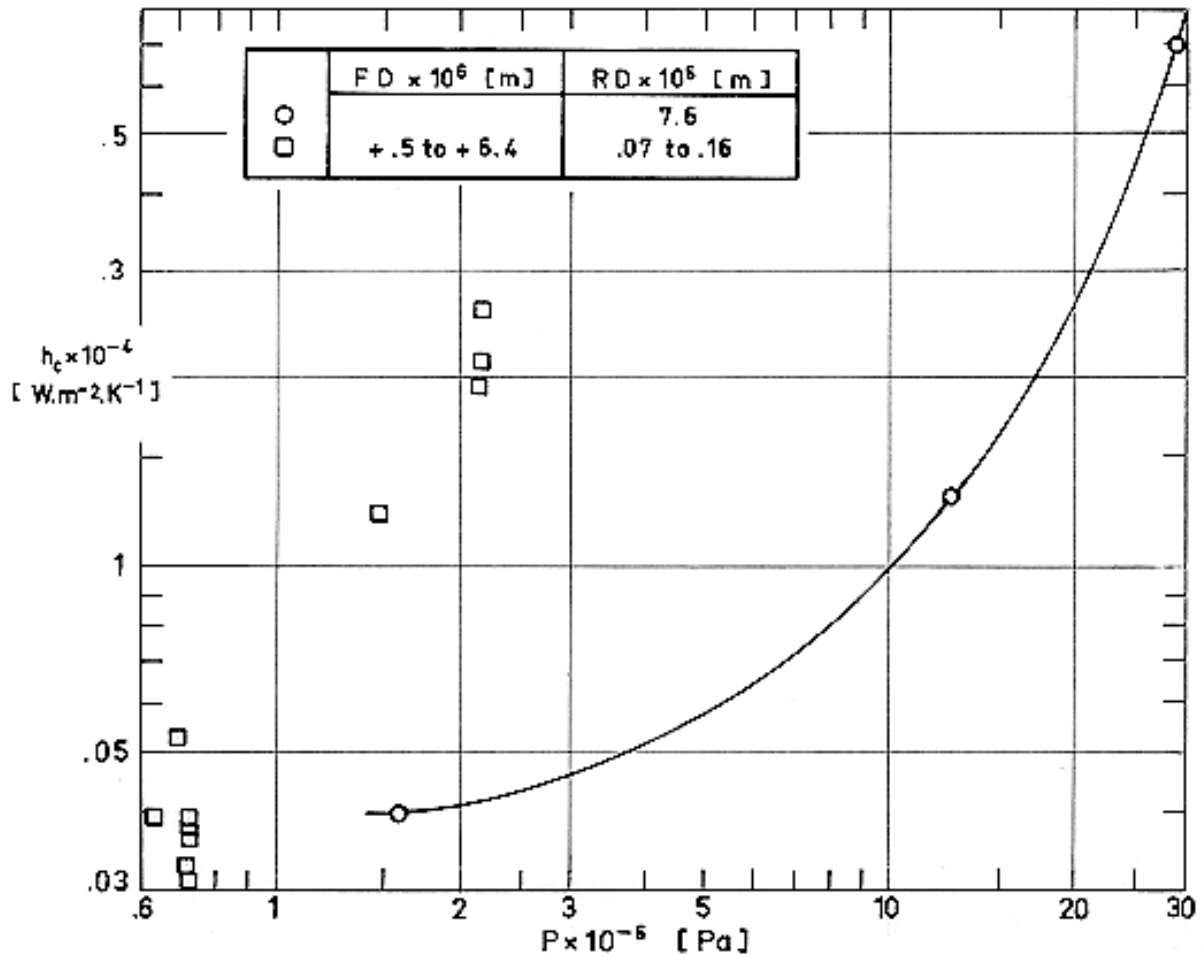
Note: non-si units are used in this figure

Figure 5-17: Plot of contact conductance vs. contact pressure for different surface finishes. Circle and square: from Fried (1965) [21]. Rhombus and triangle: from Fried & Atkins (1965) [23]. Inverted triangle and right-oriented triangle: from Fried & Kelley (1966) [24].

SPECIMENS: Two cylinders, Fe - 19 Cr - 10 Ni. (SS 304).

Radius, $b = 1,27 \times 10^{-2}$ m.

Ambient Pressure, $p = 1,33 \times 10^{-3}$ Pa.



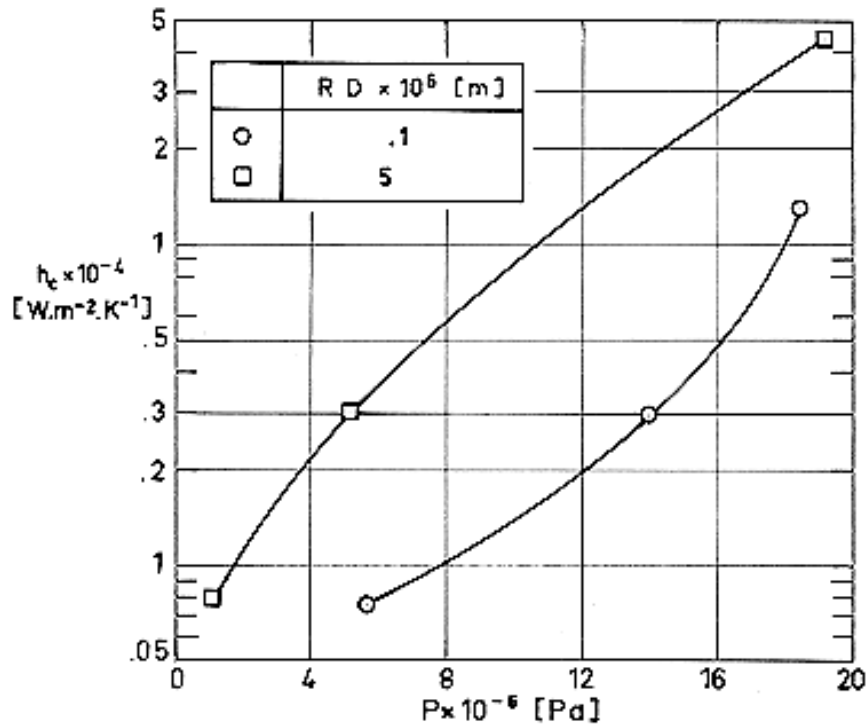
Note: non-si units are used in this figure

Figure 5-18: Plot of contact conductance vs. contact pressure for different surface finishes. Circle: From Fried (1966) [22] quoted by Scollon & Carpitella (1970) [43]. Square: From Gyorog (1970) [26].

SPECIMENS: Two cylinders, Ti - 6 Al - 4 V. (Ti 6 Al 4 V).

Radius, $b = 1,27 \times 10^{-2}$ m.

Ambient Pressure, $p = 1,33 \times 10^{-3}$ Pa.



Note: non-si units are used in this figure

Figure 5-19: Plot of contact conductance vs. contact pressure for different surface finishes. From Fried (1966) [21] quoted by Scollon & Carpitella (1970) [43].

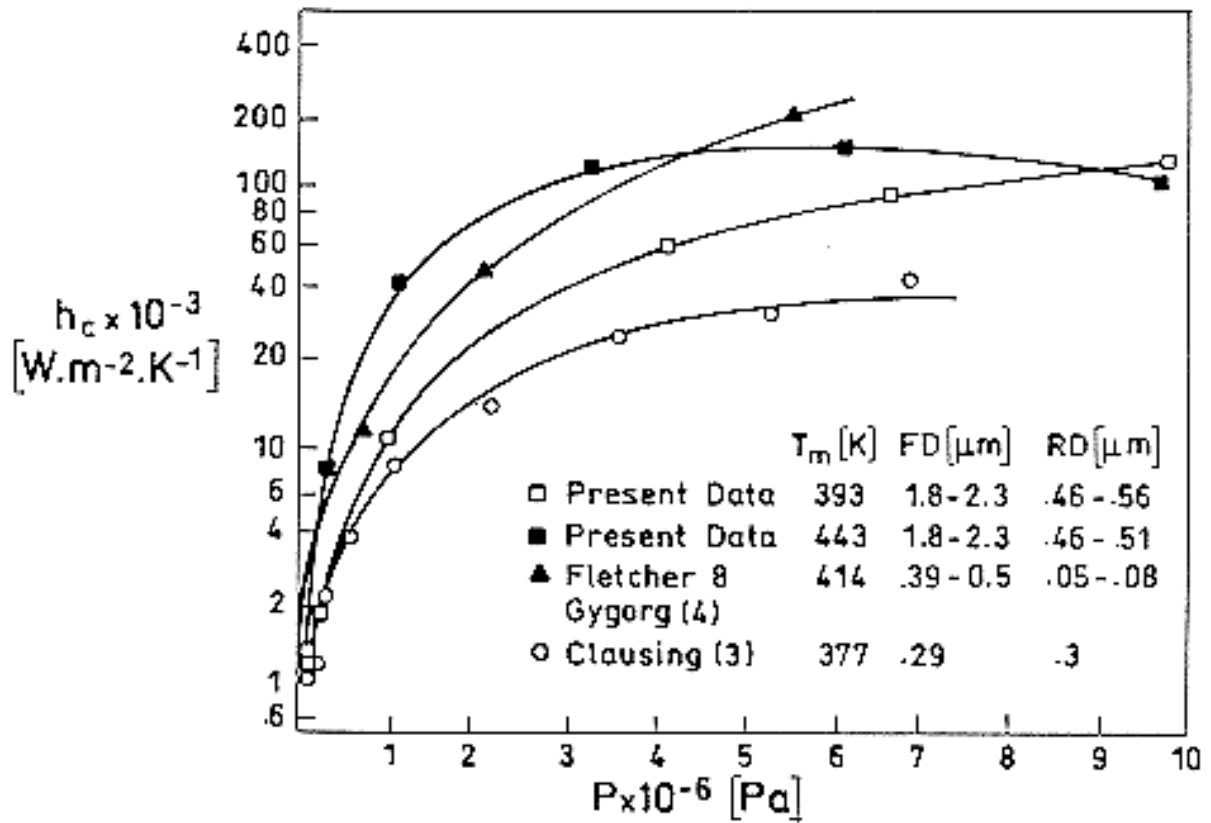
5.2.1 Metal-metal joints

5.2.1.1 Two equal materials

SPECIMENS: Two cylinders, Al 2024 - T4.

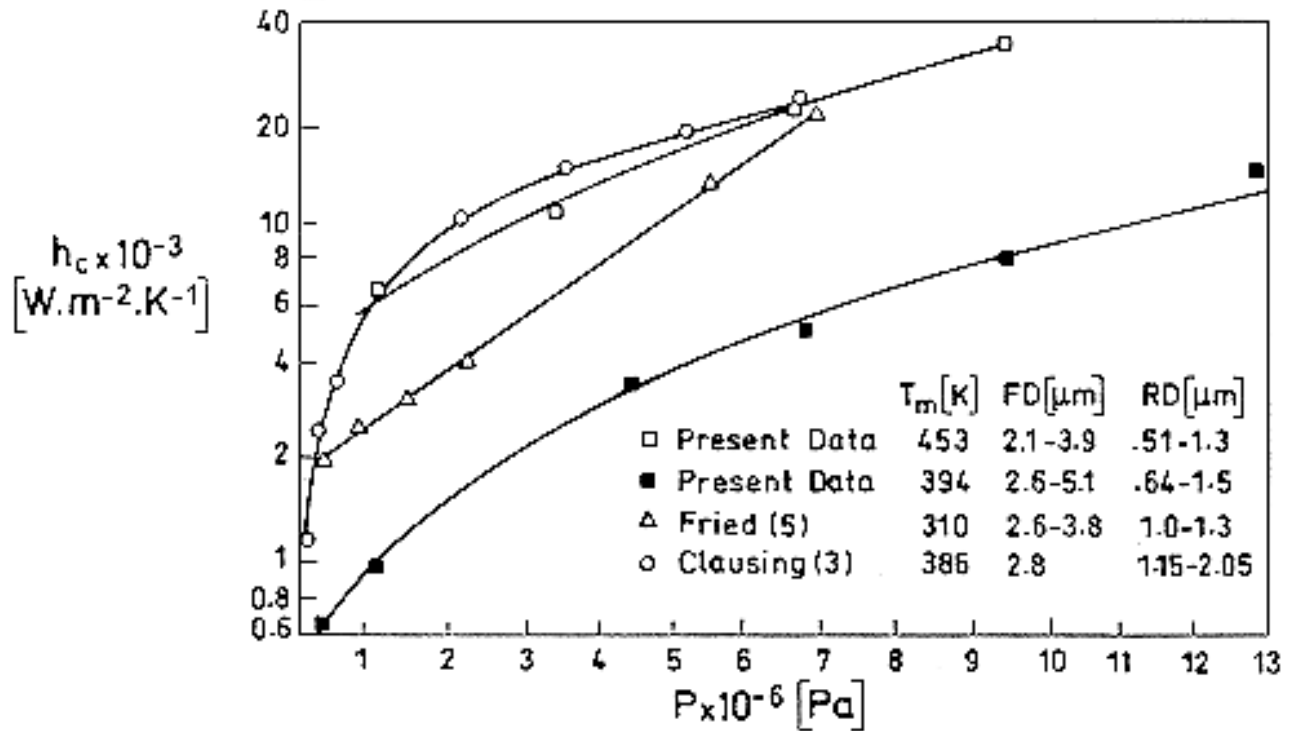
Radius, $1,27 \times 10^{-2}$ m

Ambient pressure, $1,33 \times 10^{-3}$ Pa



Note: non-si units are used in this figure

Figure 5-20: Plot of contact conductance vs. contact pressure for different surface finishes: smooth surfaces. White square: from Padgett & Fletcher (1982) [35]. Black square: from Padgett & Fletcher (1982) [35]. Black triangle: from Fletcher & Gyorg (1971) [17]. Circle: from Clausing & Chao (1963) [7].



Note: non-si units are used in this figure

Figure 5-21: Plot of contact conductance vs. contact pressure for different surface finishes: medium surfaces. White square: from Padgett & Fletcher (1982) [35]. Black square: from Padgett & Fletcher (1982) [35]. Black triangle: from Fletcher & Gyorg (1971) [17]. Circle: from Clausing & Chao (1963) [7].

SPECIMENS: Two cylinders, Al-alloy 6061 - T6.

Radius, $1,55 \times 10^{-2}$ m

Thickness, 10^{-3} m

Surface roughness, $\sim 3 \times 10^{-3}$ m

Vacuum

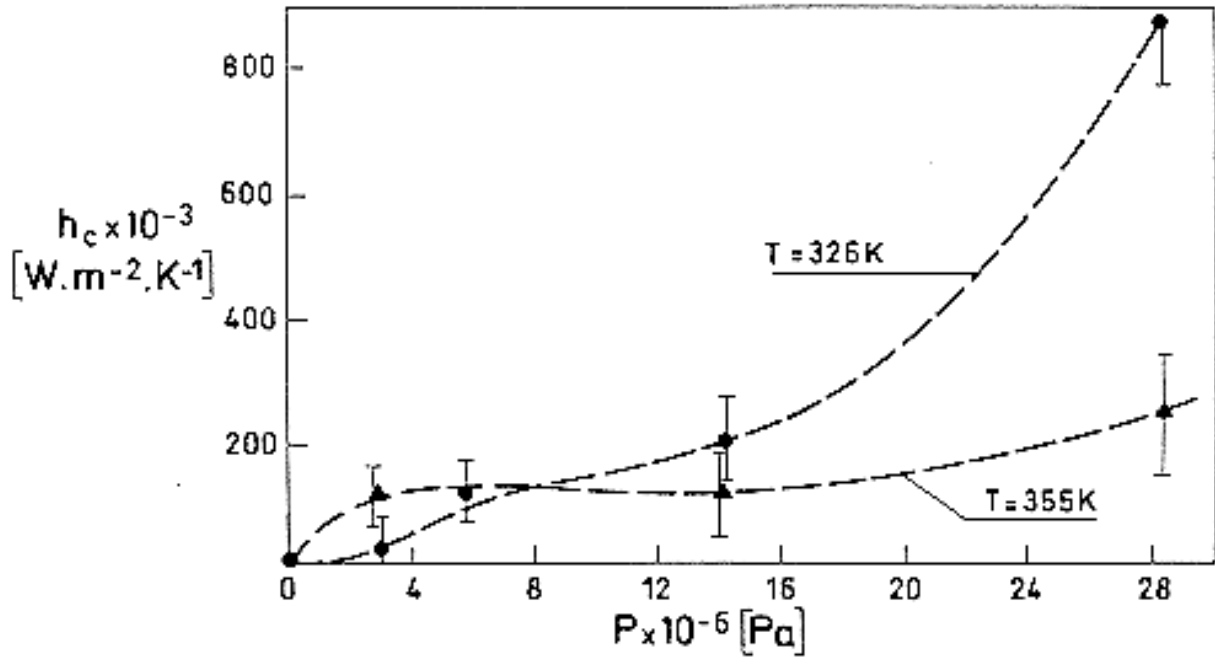


Figure 5-22: Experimental values of thermal contact conductance vs. contact pressure. From Marchetti, Testa & Torrisi (1988) [31].

SPECIMENS: Two cylinders, Cu UNI 2528.

Radius, $1,55 \times 10^{-2}$ m

Thickness, 10^{-3} m

Vacuum.

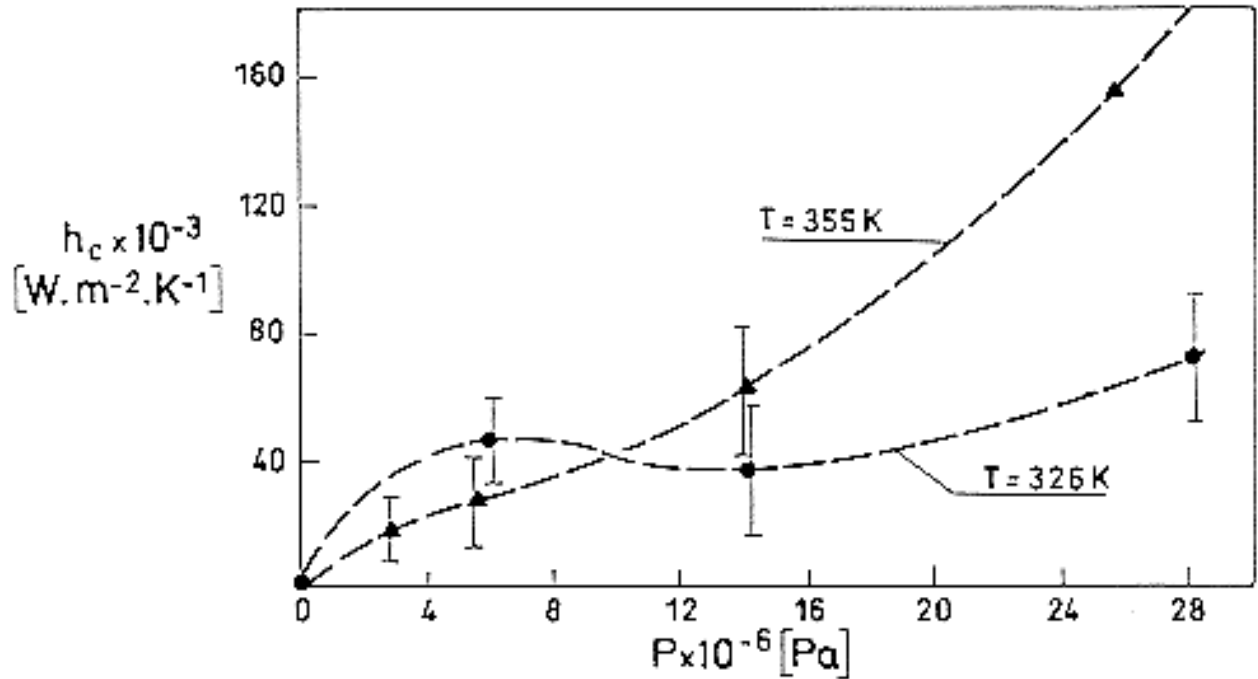


Figure 5-23: Experimental values of thermal contact conductance vs. contact pressure. From Marchetti, Testa & Torrisi (1988) [31].

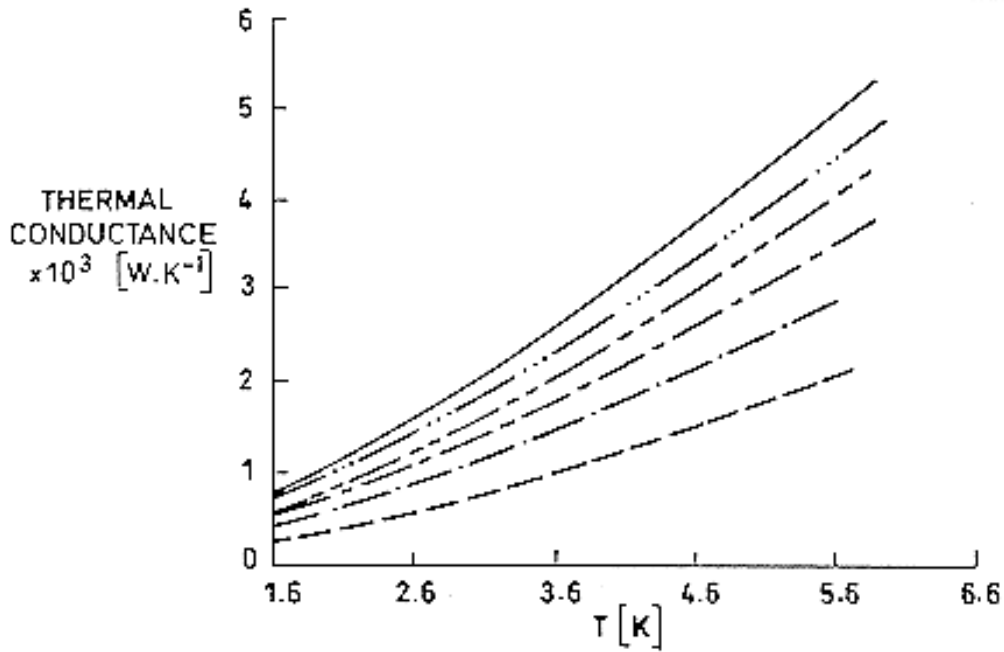
SPECIMENS: Two different cylinders, Brass.

Radius, $r_1 = 6,35 \times 10^{-3}$ m; $r_2 = 5,10 \times 10^{-3}$ m

Length, $L_1 = 8,89 \times 10^{-3}$ m; $L_2 = 10,2 \times 10^{-3}$ m

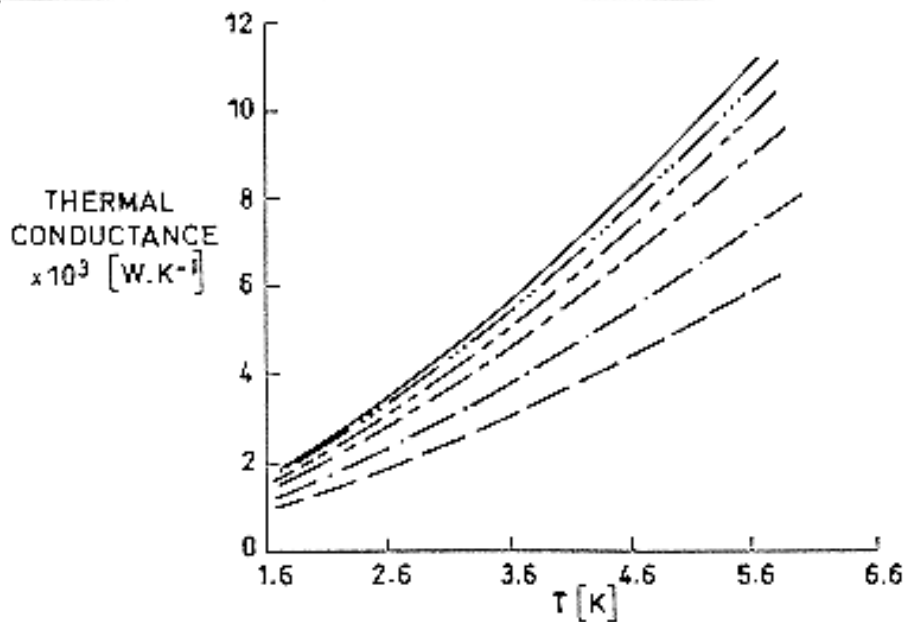
Ambient pressure, $< 7 \times 10^{-3}$ Pa.

Contact at liquid helium temperatures.



Note: non-si units are used in this figure

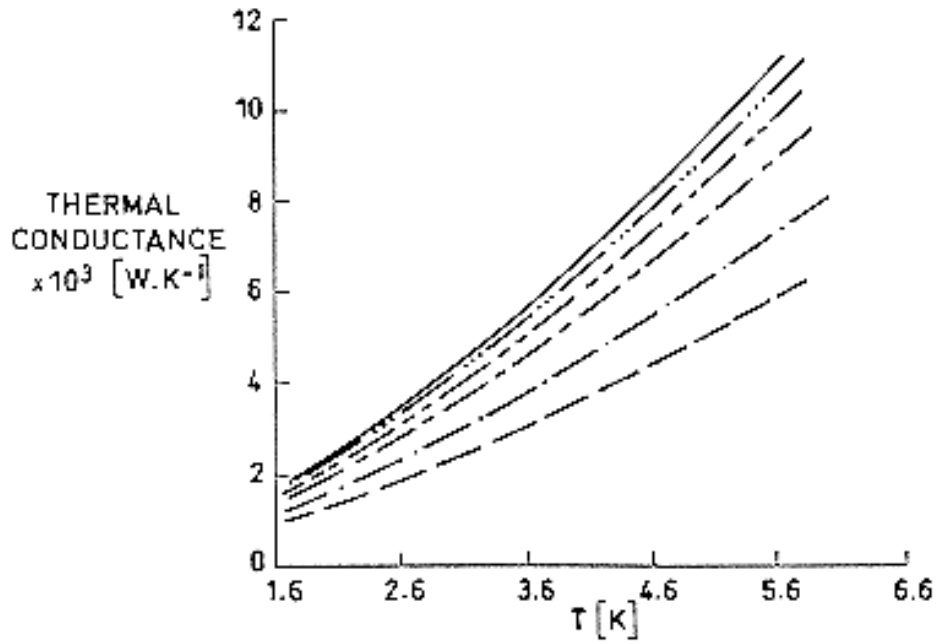
Figure 5-24: 0,1 μm brass sample pair applied force comparison. Dashed line: 112 N; dashed-dotted line: 224 N; long-short dashed line: 336 N; long-double short dashed line: 448 N; dashed-triple dotted line: 560 N; solid line: 670 N.



Note: non-si units are used in this figure

Figure 5-25: 0,2 μm brass sample pair applied force comparison.

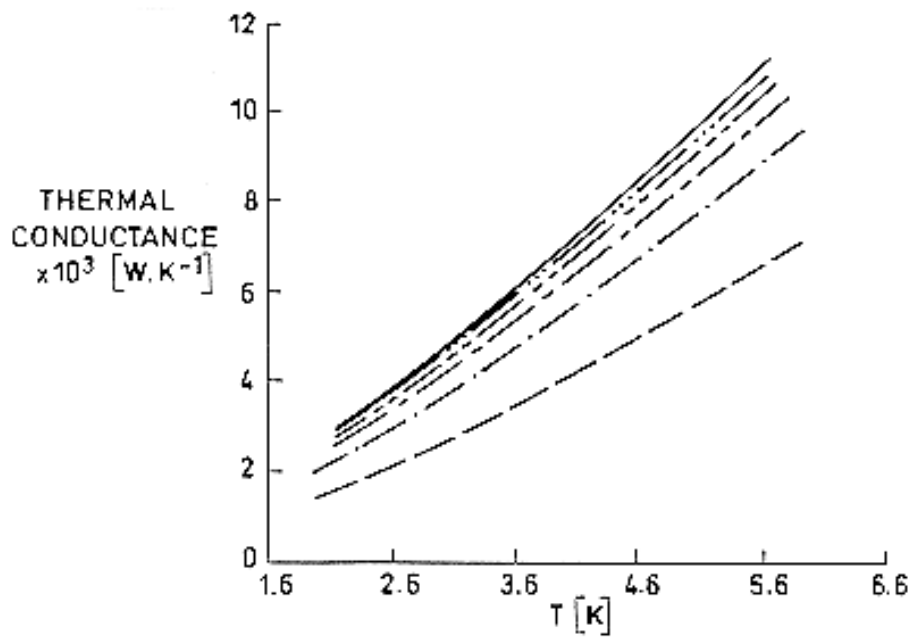
Key as in Figure 5-24.



Note: non-si units are used in this figure

Figure 5-26: 0,4 μm brass sample pair applied force comparison.

Key as in Figure 5-24.



Note: non-si units are used in this figure

Figure 5-27: 0,8 μm brass sample pair applied force comparison.

Key as in Figure 5-24.

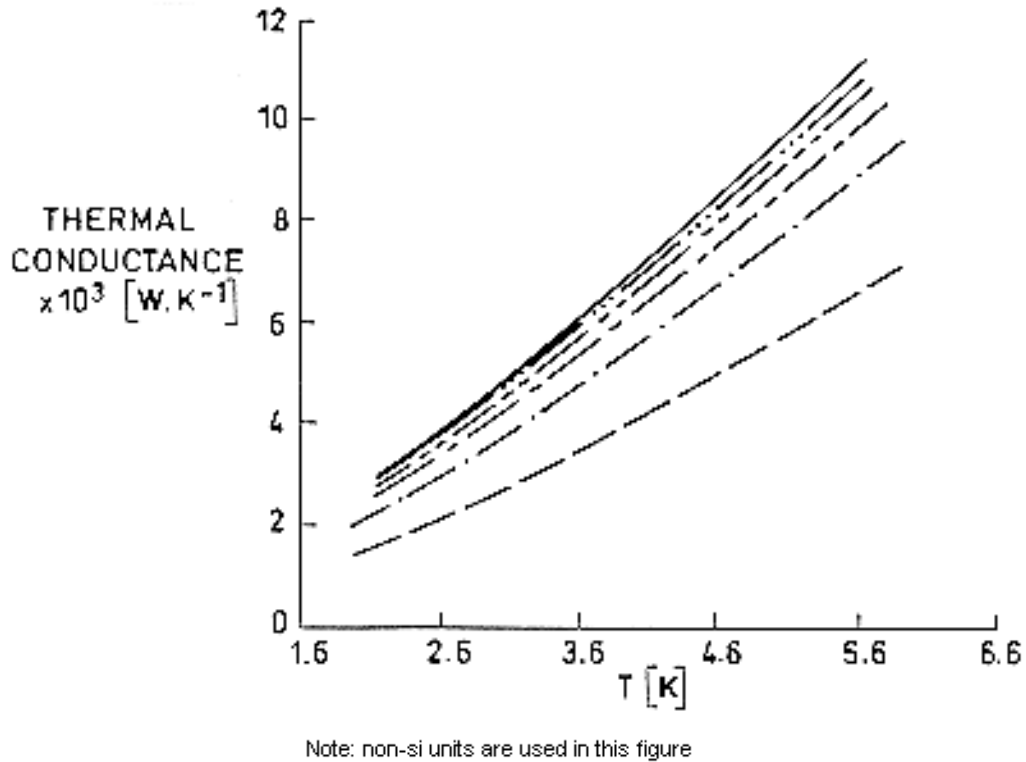


Figure 5-28: 1,6 μm brass sample pair applied force comparison.

Key as in Figure 5-24.

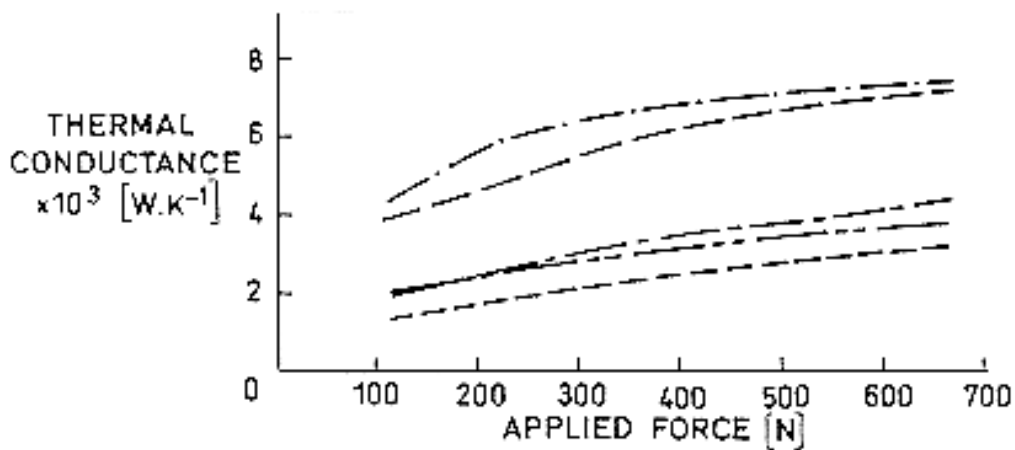
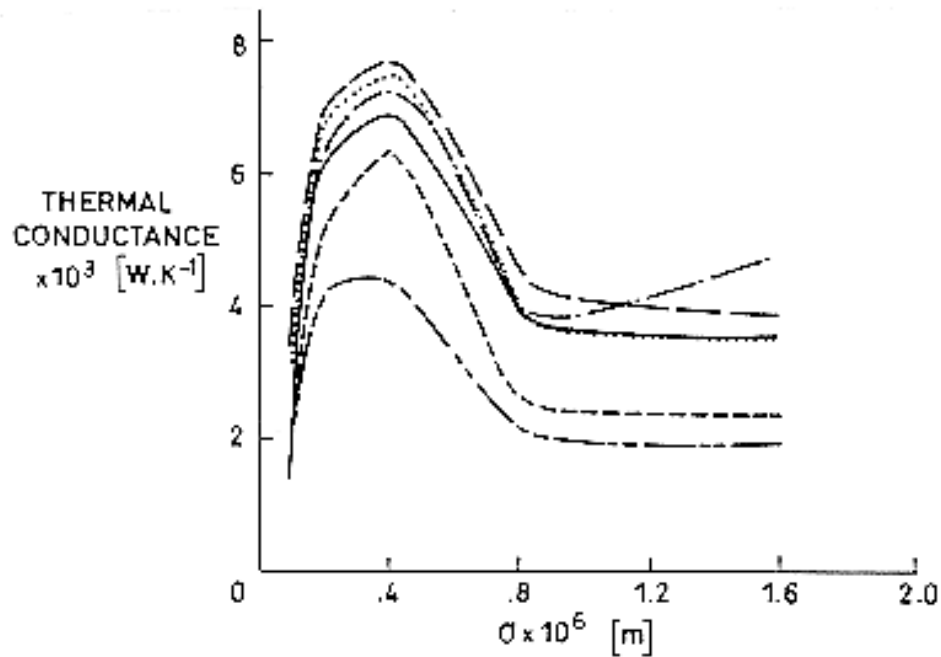


Figure 5-29: Brass sample pairs, 4,2 K surface finish comparison. Short dashed line: 0,1 μm ; long dashed line: 0,2 μm ; dashed-dotted line: 0,4 μm ; long-short dashed line: 0,8 μm ; long-double short dashed line: 1,6 μm .



Note: non-si units are used in this figure

Figure 5-30: Brass sample pairs, 4,2 K surface finish comparison. Long-double short dashed line: 112 N; short dashed line: 224 N; dashed-dotted line: 336 N; dotted line: 448 N; long dashed line: 560 N; solid line: 670 N.

From Salerno, Kittel, Books, Spivak & Marks (1986) [42].

SPECIMENS: Two different cylinders, OFHC Cu.

Radius, $r_1 = 6,35 \times 10^{-3}$ m, $r_2 = 5,10 \times 10^{-3}$ m

Length, $L_1 = 8,89 \times 10^{-3}$ m, $L_2 = 10,2 \times 10^{-3}$ m

Ambient pressure, $< 7 \times 10^{-3}$ Pa.

Contact at liquid helium temperature.

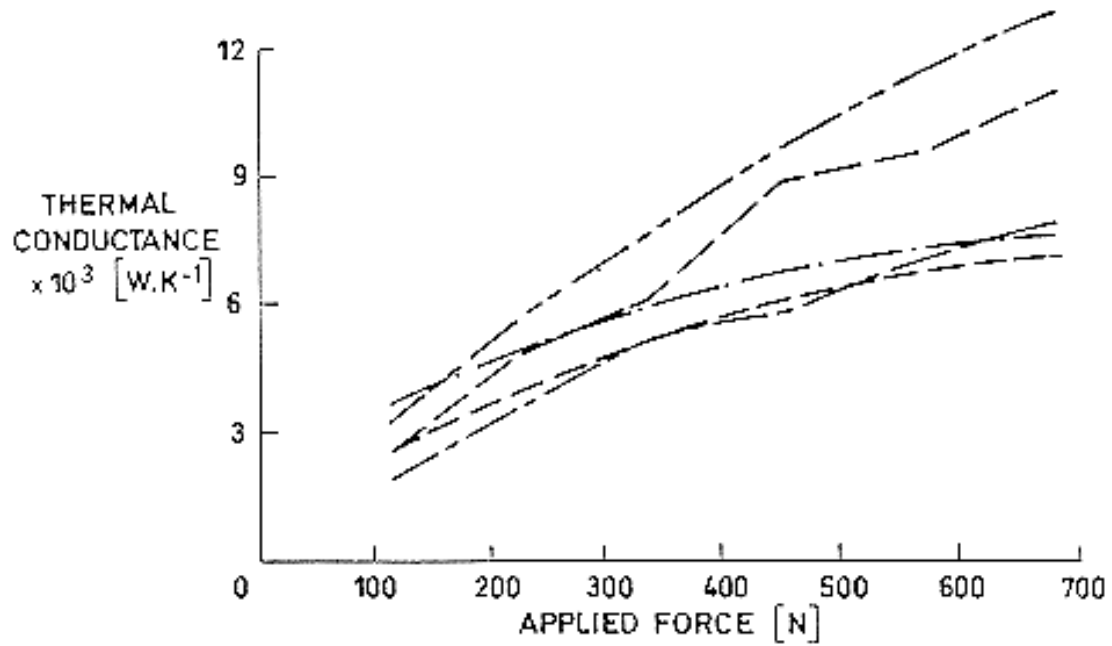


Figure 5-31: γ copper sample pairs, 4,2 K surface finish comparison. Key as in Figure 5-30.

From Salerno, Kittel, Books, Spivak & Marks (1986) [42].

SPECIMENS: Two rotating horizontal cylinders.

Outer diameter, 9×10^{-2} m

Length, 15×10^{-2} m

Inner diameter of upper cylinder, 6×10^{-2} m

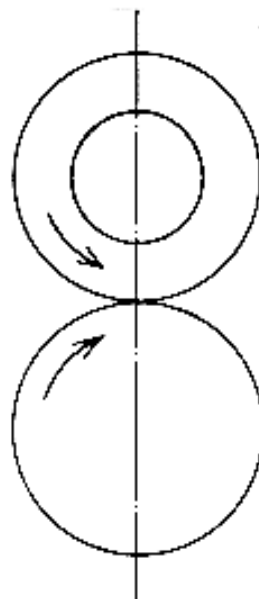
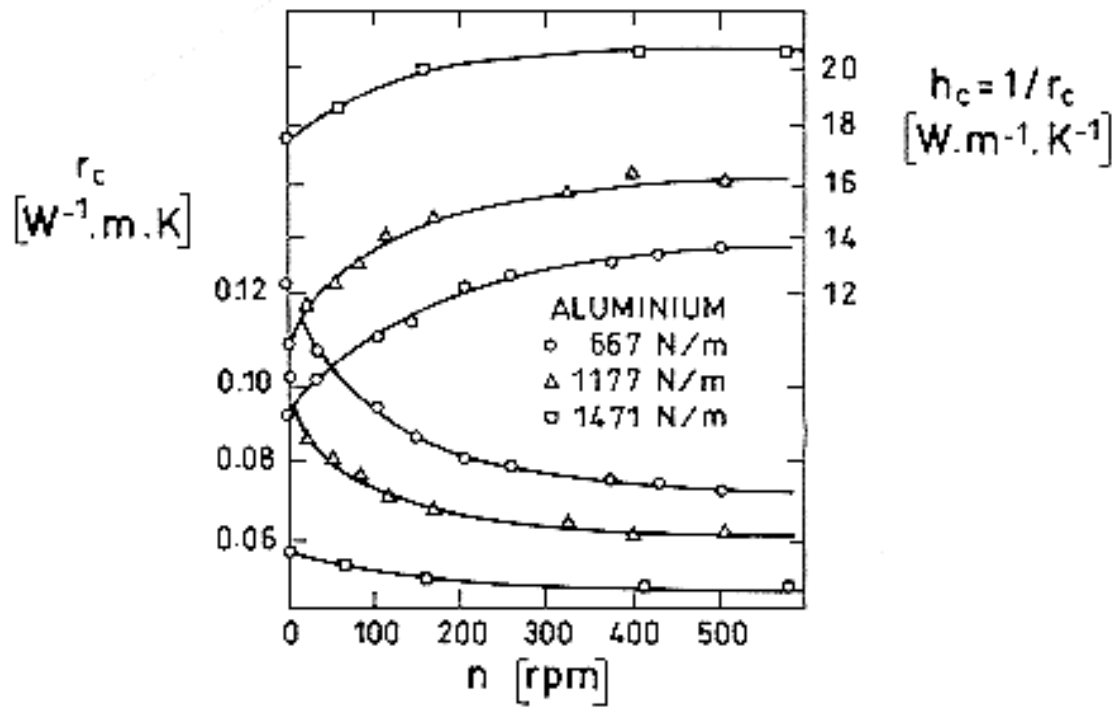


Figure 5-32: Physical model of two rotating cylinders contacted to each other.

From Yamazaki, Shimizu & Tsuchida (1987) [49].

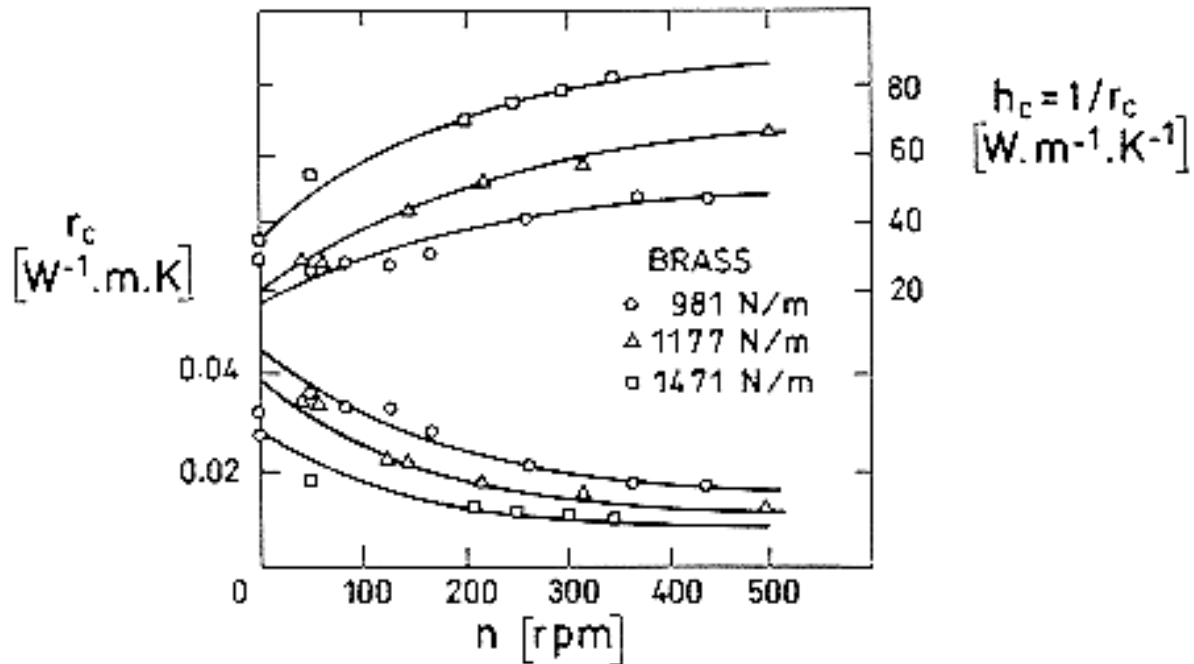
Aluminium



Note: non-si units are used in this figure

Figure 5-33: Contact thermal resistance after applied high contact pressure vs. rotating speed.

Brass



Note: non-si units are used in this figure

Figure 5-34: Contact thermal resistance after applied high contact pressure vs. rotating speed.

SPECIMENS: Two rectangular plates, Al 6061-T6.

Dimensions, 0,127 x 0,1778 x 0,0254 m

Ambient Pressure, $< 0,133 \times 10^{-2}$ Pa

RMS surface roughness

Plate A, $0,42 \times 10^{-6}$ m

Plate B, $0,48 \times 10^{-6}$ m

Load distribution

Four sets of load distribution plates were constructed. Each set consisted of two plates, one pin plate and one plate using conical shaped springs. The pin plate had a series of ceramic pins, located at each load point, of:

$$\phi = 0,635 \times 10^{-2} \text{ m}$$

$$L = 0,525 \times 10^{-2} \text{ m}$$

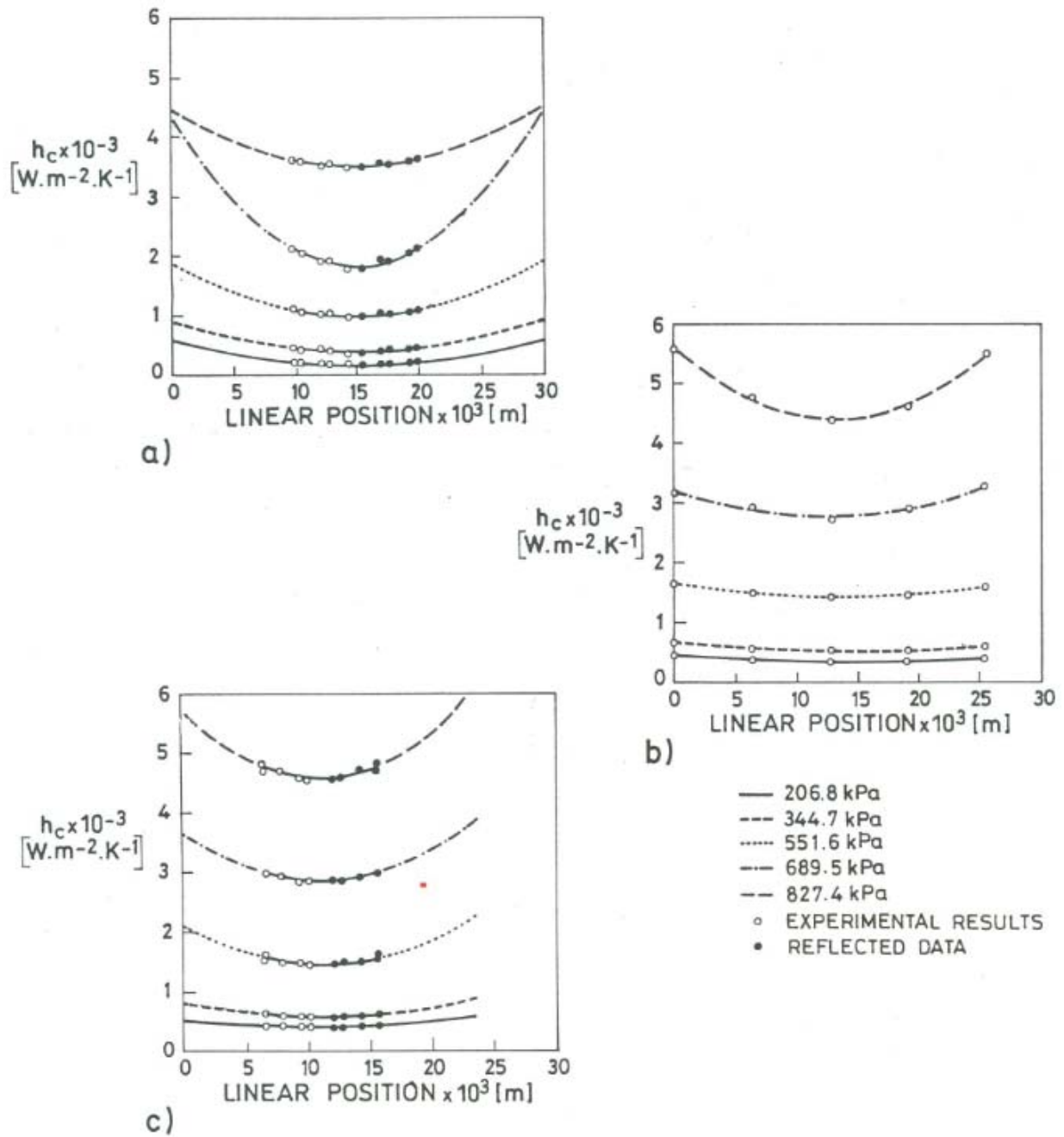
Measured thermal conductivity, k [$\text{W.m}^{-1}.\text{K}^{-1}$]

$$k = 111,94 + 0,226T, T [\text{K}]$$

Table 5-1: Load configuration thermal contact conductance data

Distance from pin x 10 ³ [m]	h _c [W.m ⁻² .K ⁻¹]				
	Interface Pressure x 10 ⁻³ [Pa]				
	206,8	344,7	551,6	689,5	827,4
	4 x 6 Array				
9,76	211,30	441,53	1089,25	2113,28	3618,08
10,42	200,60	419,48	1047,33	2023,66	3577,83
12,02	182,49	430,61	1012,15	1891,66	3547,53
12,74	167,50	402,98	1028,59	1932,11	3528,53
14,24	164,93	358,54	961,70	1773,41	3486,10
	5 x 7 Array				
0,00	459,29	666,26	1658,48	3172,15	5565,53
6,35	388,84	586,13	1522,06	2941,49	4797,40
12,70	372,22	557,29	1460,36	2754,54	4430,41
19,05	394,85	577,84	1515,45	2950,62	4656,66
25,40	460,97	653,08	1651,65	3324,30	5561,58
	6 x 8 Array				
6,54	422,58	627,78	1541,03	2992,30	4796,92
6,60	455,32	628,83	1632,38	2993,34	4710,84
7,94	427,48	611,72	1513,62	2935,71	4708,50
9,43	426,11	600,00	1513,07	2860,76	4594,37
10,16	435,04	584,81	1477,62	2880,97	4563,58

 NOTE Mean interface temperature 294 ± 6 K; all pressure values ± 10⁴ Pa.



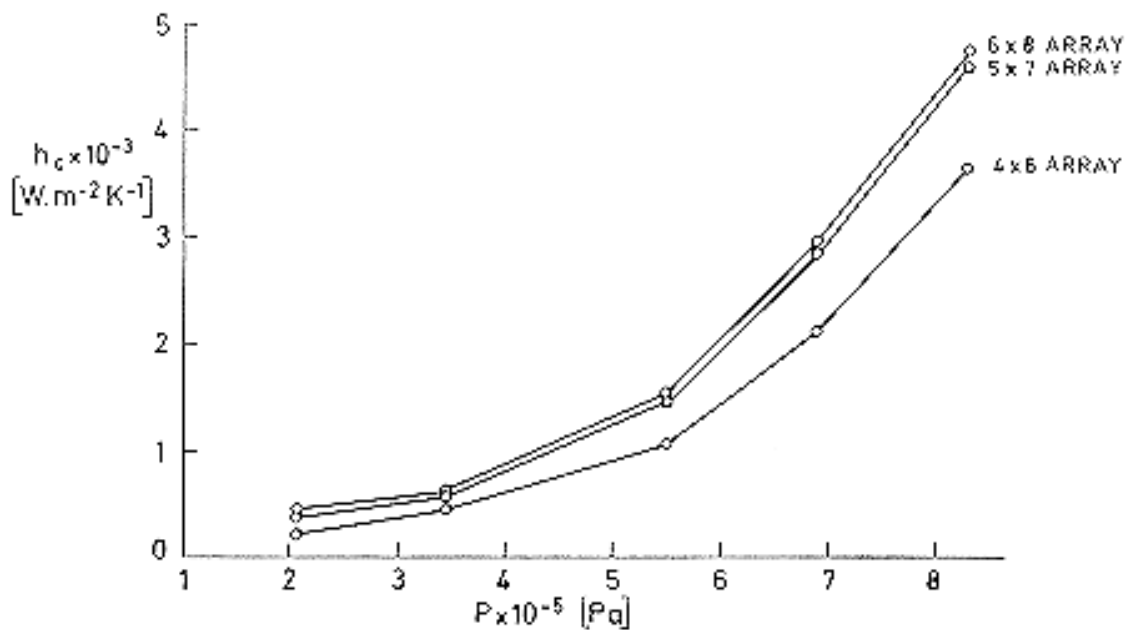
Note: non-si units are used in this figure

Figure 5-35: Thermal contact conductance as a function of position for: (a) 4 x 6 load array; (b) 5 x 7 load array; c) 6 x 8 load array. From Peterson and Fletcher (1992) [37].

Table 5-2: Integrated load configuration test thermal contact conductance values

Apparent pressure $\times 10^{-3}$ [Pa]	h_c [$W.m^{-2}.K^{-1}$]		
	4 x 6 Array	5 x 7 Array	6 x 8 Array
206,8	215,04	381,80	443,07
344,7	447,82	571,96	622,10
551,6	1090,79	1492,85	1564,81
689,6	2127,66	2844,85	2970,43
827,4	3620,85	4594,67	4729,86

Note Assuming symmetry around each load point and defining a unit cell as the region bounded by the midway between each load point, the expressions of thermal contact conductance as a function of radial distance from the loading points were integrated and then multiplied by the total number of load points to obtain the overall plate conductance.


Figure 5-36: Integrated thermal contact conductance. From Table 5-2.

5.2.1.2 Two different materials

SPECIMENS: Two cylinders, Fe - 19 Cr - 10 Ni (SS 304) and Al - 4,3 Cu - 1,5 Mg - 0,6 Mn (Al 2024-T4).

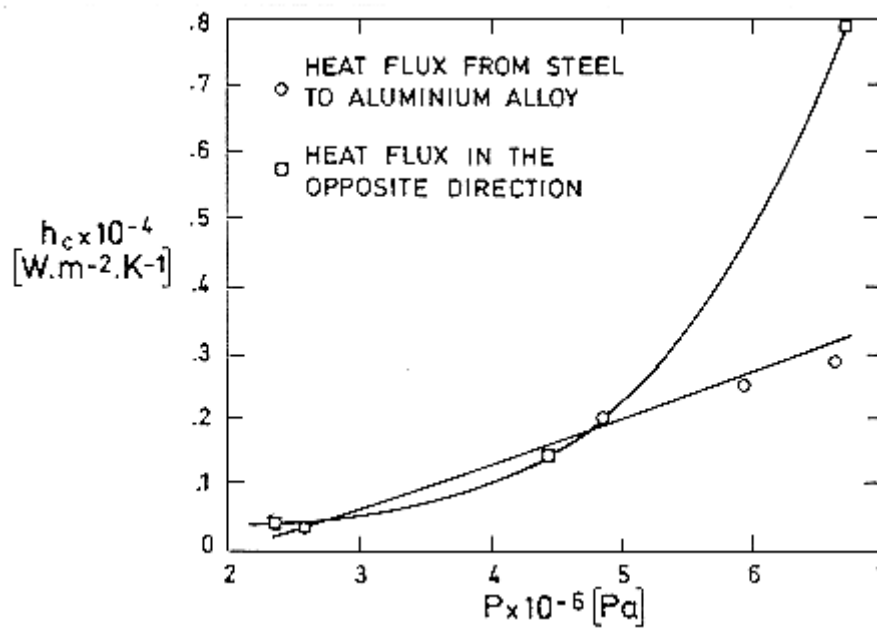
Radius, $b = 2,54 \times 10^{-2}$ m.

Flatness Deviation, $FD = -1,3 \times 10^{-6}$ and $+6,4 \times 10^{-6}$ m.

Roughness Deviation, $RD = 0,3 \times 10^{-6}$ and $0,2 \times 10^{-6}$ m.

Mean Temperature, $T_m = 302$ to 321 K.

Ambient Pressure, $p = 1,33 \times 10^{-2}$ Pa.



Note: non-si units are used in this figure

Figure 5-37: Plot of contact conductance vs. contact pressure. Notice the directional effect on contact conductance. From Fried & Kelley (1966) [24].

SPECIMENS: Two cylinders, Al 2024 - T4 and Stainless-steel 304.

Surface roughness, $0,038 - 1,60 \times 10^{-6}$ m (RMS)

Flatness deviations, $0,457 - 91,4 \times 10^{-6}$ m

Ambient pressure, $1,33 \times 10^{-3}$ Pa

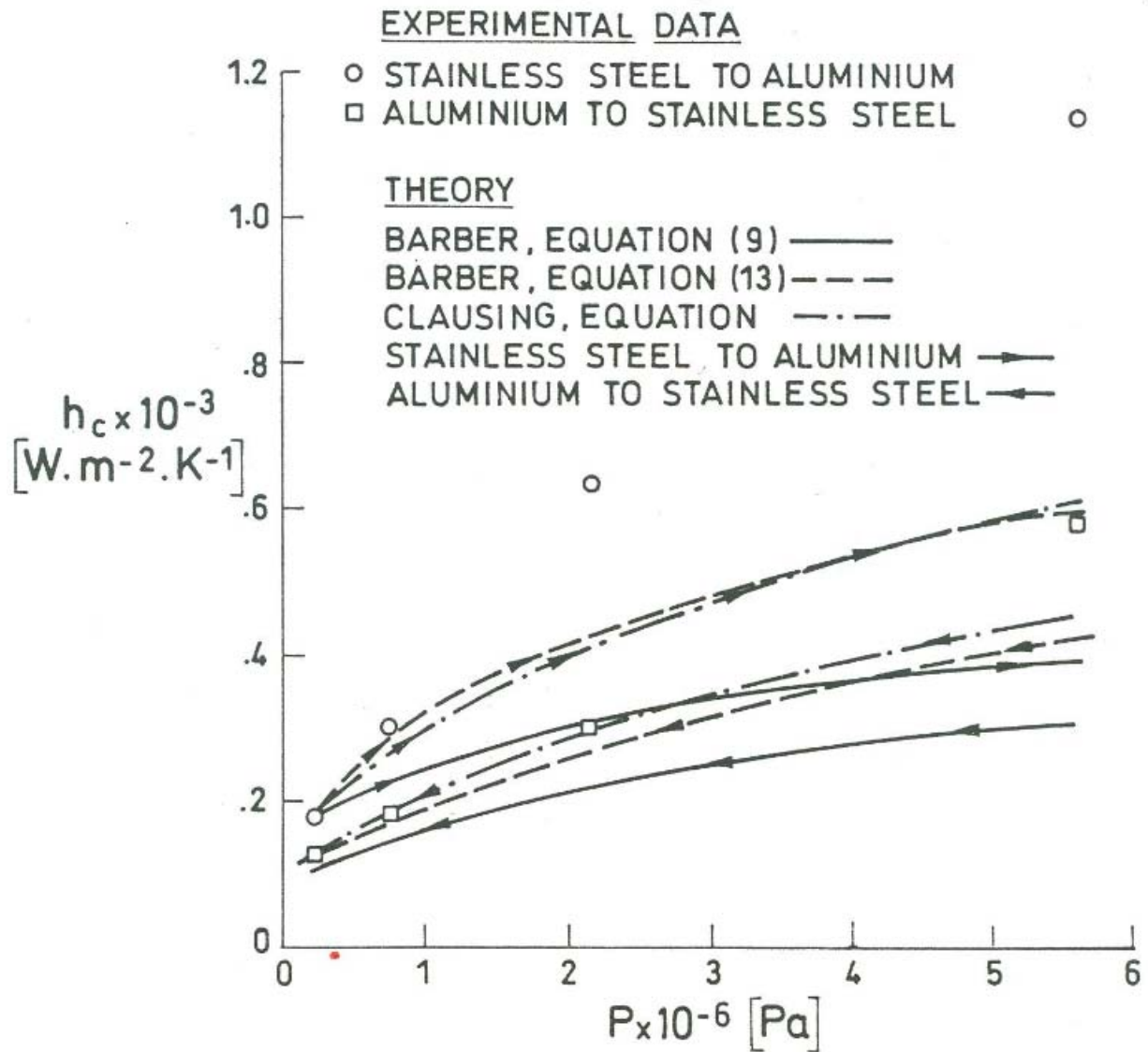


Figure 5-38: Thermal contact conductance vs. interfacial pressure for Al 2024-T4/SS 304 contacts: experimental data and theoretical results.

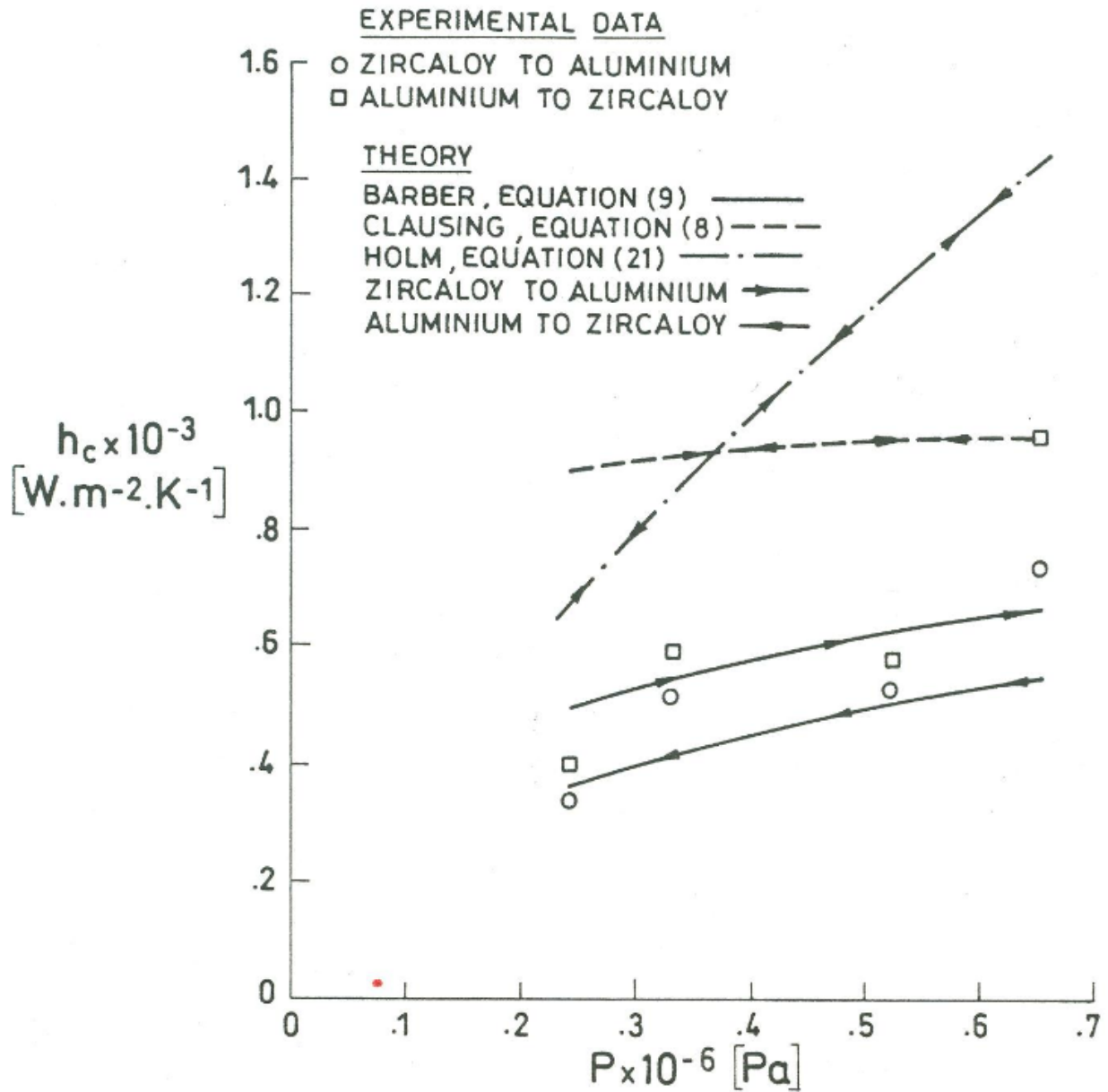
From Somer, Miller & Fletcher (1979) [45].

SPECIMENS: Two cylinders, Al 2024 - T4 and Zircaloy-2.

Surface roughness, 0,038 - 1,60 x 10⁻⁶ m (RMS)

Flatness deviations, 0,457 - 91,4 x 10⁻⁶ m

Ambient pressure, 1,33 x 10⁻³ Pa



Note: non-si units are used in this figure

Figure 5-39: Thermal contact conductance vs. interfacial pressure for Al 2024-T4/Zircaloy-2 contacts: experimental data and theoretical results.

From Somer, Miller & Fletcher (1979) [45].

SPECIMENS: Two cylinders, Stainless-steel 304 and Zircaloy-2.

Surface roughness, 0,038 - 1,60 x 10⁻⁶ m (RMS)

Flatness deviations, 0,457 - 91,4 x 10⁻⁶ m

Ambient pressure, 1,33 x 10⁻³ Pa

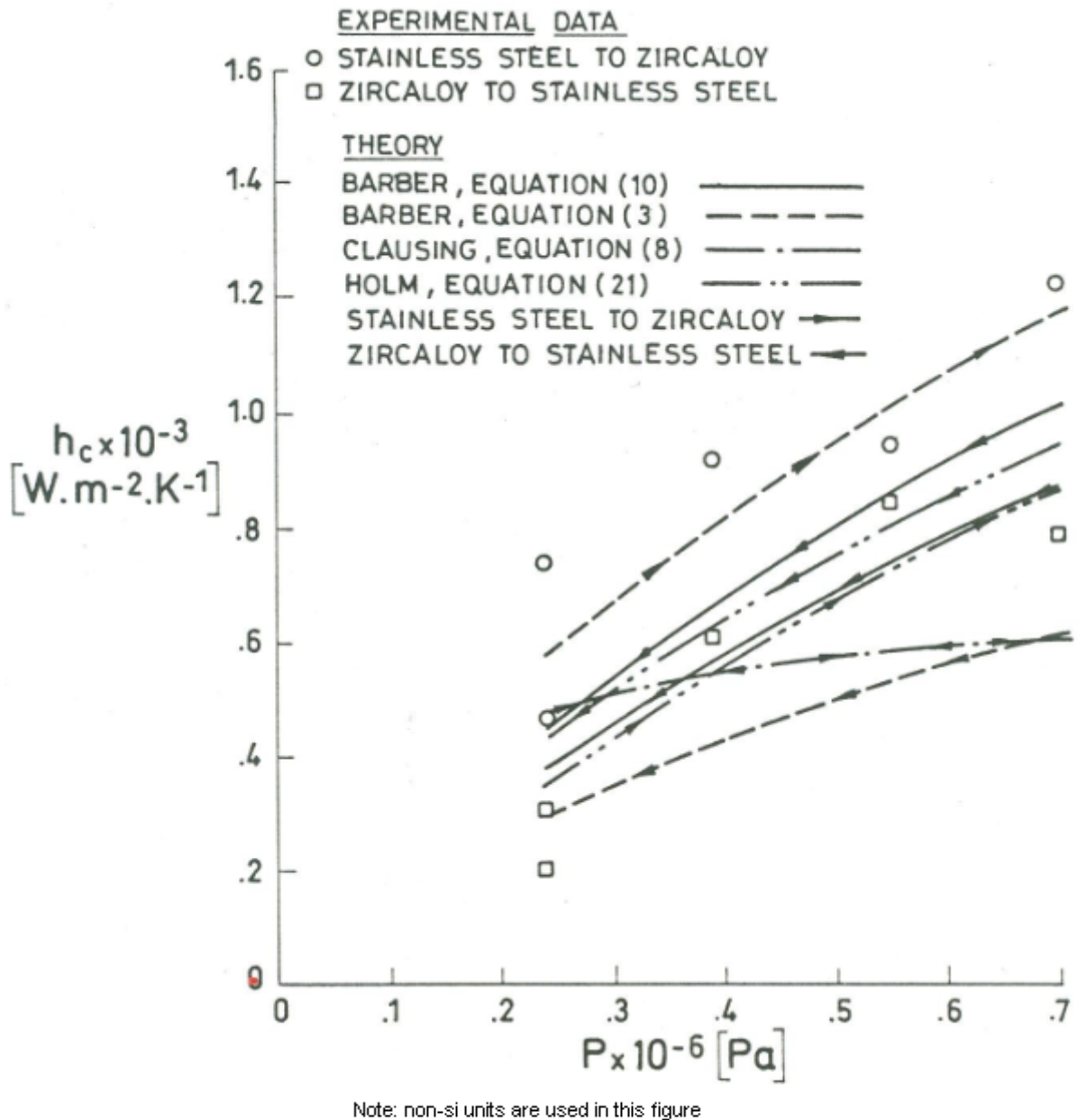


Figure 5-40: Thermal contact conductance vs. interfacial pressure for SS 304/Zircaloy-2 contacts: experimental data and theoretical results.

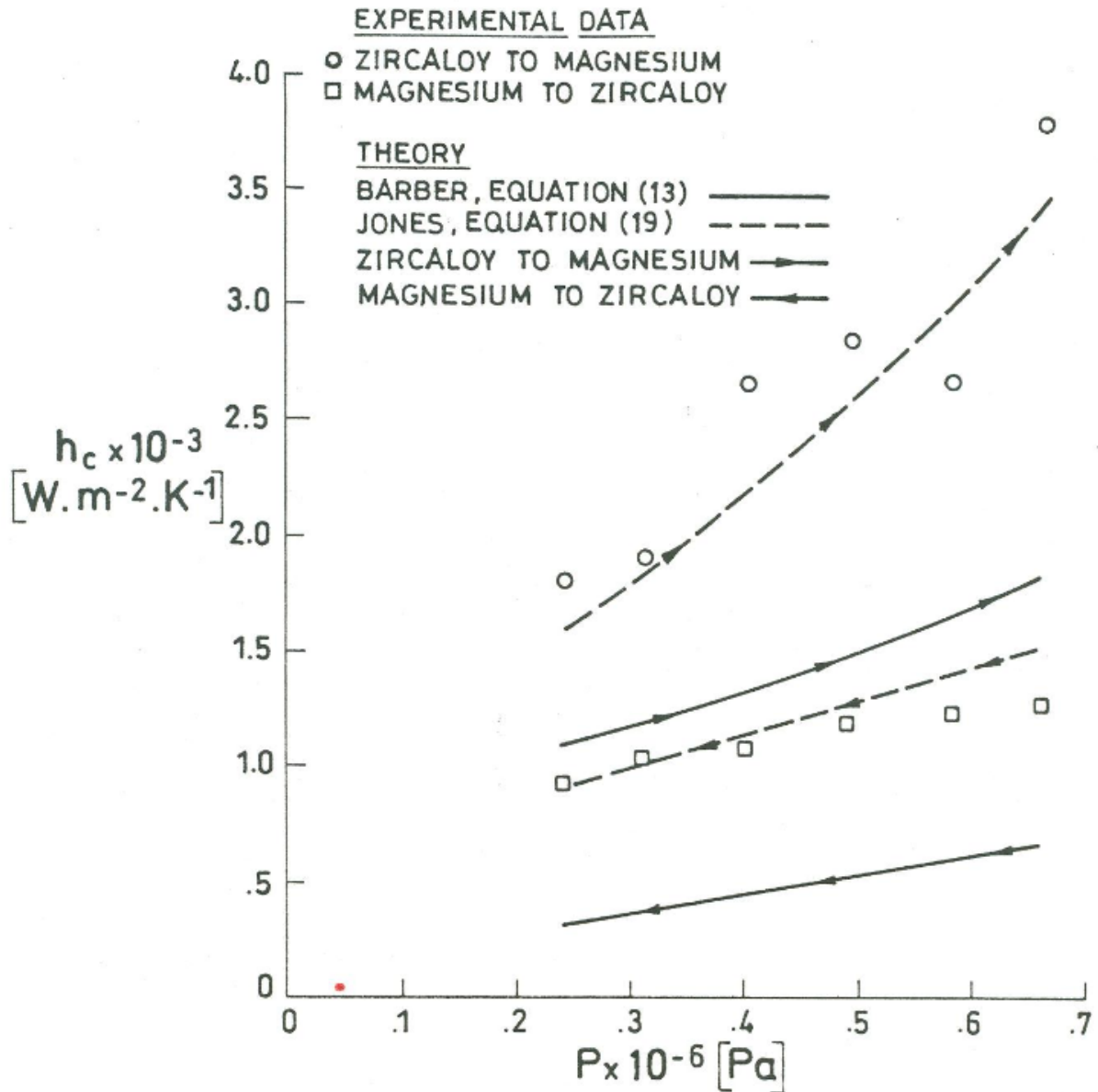
From Somer, Miller & Fletcher (1979) [45].

SPECIMENS: Two cylinders, Magnesium AZ31B and Zircaloy-2.

Surface roughness, 0,038 - 1,60 x 10⁻⁶ m (RMS)

Flatness deviations, 0,457 - 91,4 x 10⁻⁶ m

Ambient pressure, 1,33 x 10⁻³ Pa



Note: non-si units are used in this figure

Figure 5-41: Thermal contact conductance vs. interfacial pressure for Mg AZ31B/zircaloy-2 contacts: experimental data and theoretical results.

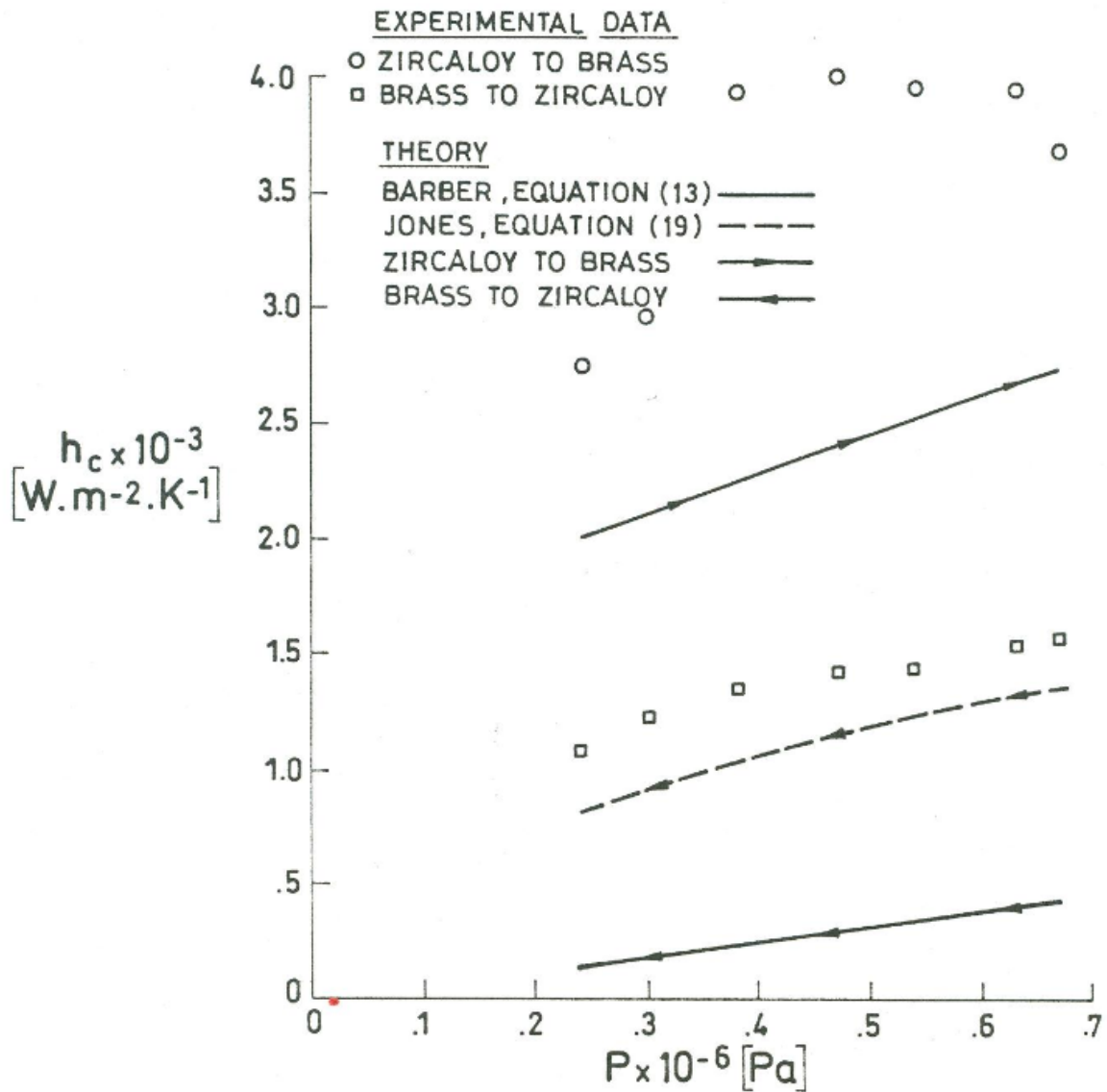
From Somer, Miller & Fletcher (1979) [45].

SPECIMENS: Two cylinders, Brass 271 and Zircaloy-2.

Surface roughness, 0,038 - 1,60 x 10⁻⁶ m (RMS)

Flatness deviations, 0,457 - 91,4 x 10⁻⁶ m

Ambient pressure, 1,33 x 10⁻³ Pa



Note: non-si units are used in this figure

Figure 5-42: Thermal contact conductance vs. interfacial pressure for Brass 271/Zircaloy-2 contacts: experimental data and theoretical results.

From Somer, Miller & Fletcher (1979) [45].

SPECIMENS: Two cylinders, Al 2024 - T4 and Stainless-steel 304

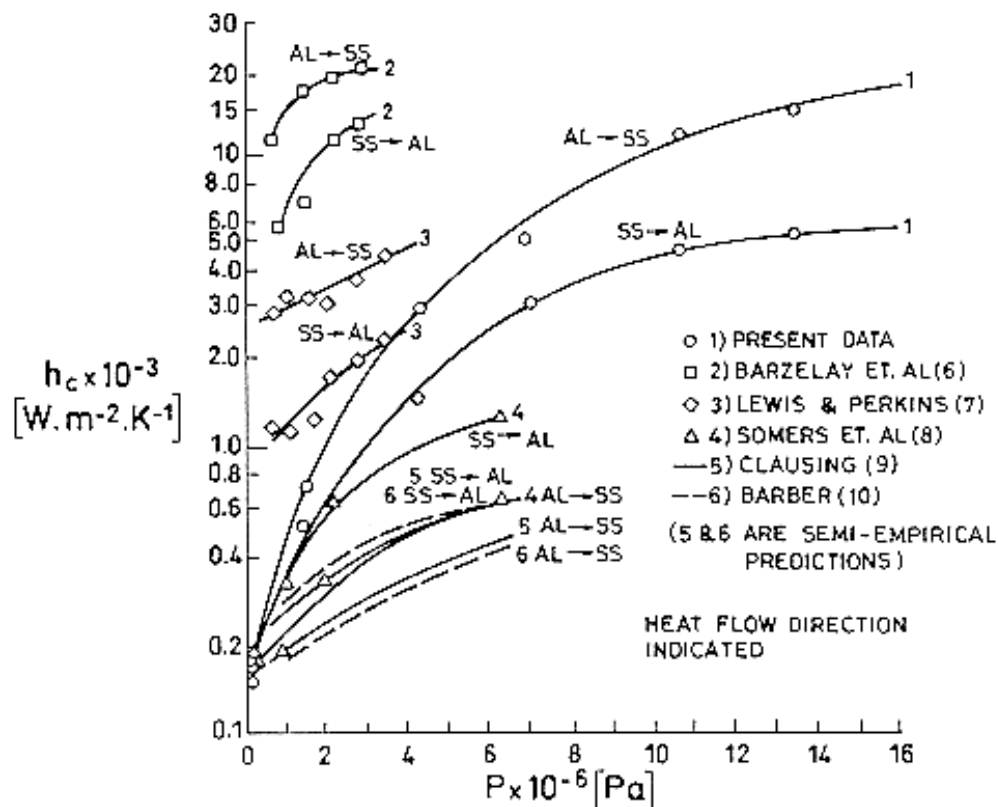
Radius, $1,77 \times 10^{-2}$ m

Ambient pressure, $1,33 \times 10^{-3}$ Pa

Table 5-3: Parameters of Samples Used in Tests Shown in Figure 5-43.

Curve	Investigator	Flatness [μm]		Roughness [μm]		Mean Interface Temperature [K]	
		Al	SS	Al	SS	SS-Al	Al-SS
1	Padgett & Fletcher (1982) [35]	2,1	2,2	0,513	0,256	351	468
2	Barzelay et al. (1955) *	5,1	5,1	0,25 to 3,1		363 to 473	
3	Lewis & Perkins (1968) *	0,81	0,61	0,81	0,61	329	386
4	Somers et al. (1978) [45] *	79,9	95,9	0,165	0,064	293	363
5	Clausing (1966) [7] *	79,9	95,9	0,165	0,064	293	363
6	Barber (1971) *	79,9	95,9	0,165	0,064	293	363

NOTE * Referenced by Padgett & Fletcher (1982) [35].

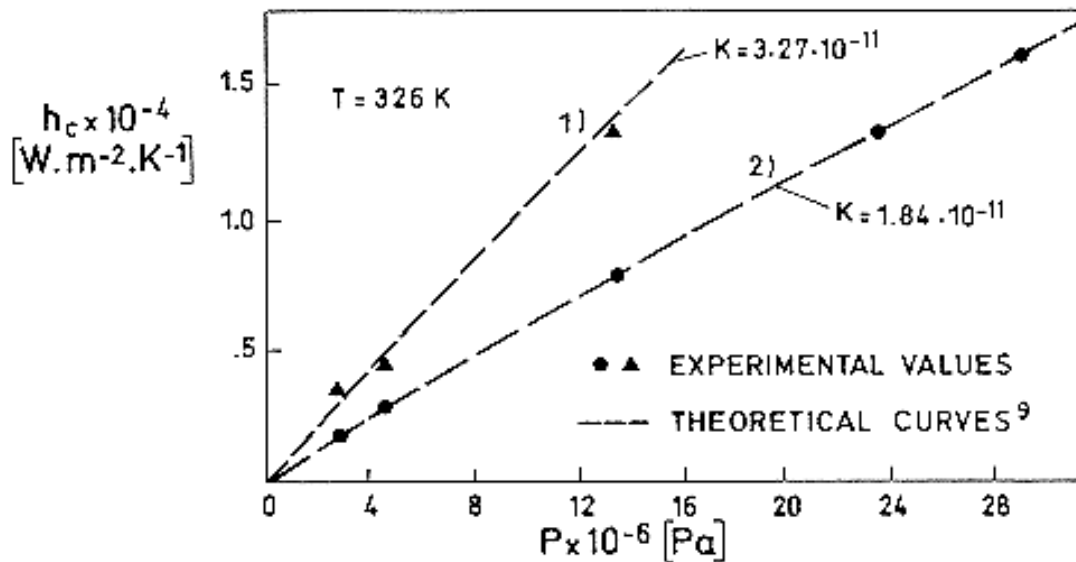

Figure 5-43: Variation of contact conductance with apparent interface pressure for Al 2024-T4/SS 304 metal surfaces at different mean junction temperatures.

From Padgett & Fletcher (1982) [35].

SPECIMENS: Two cylinders, (1) Al-alloy 6061-T6 and Stainless-steel AISI4340; (2) Stainless-steel AISI4340 and Cu UNI 2528

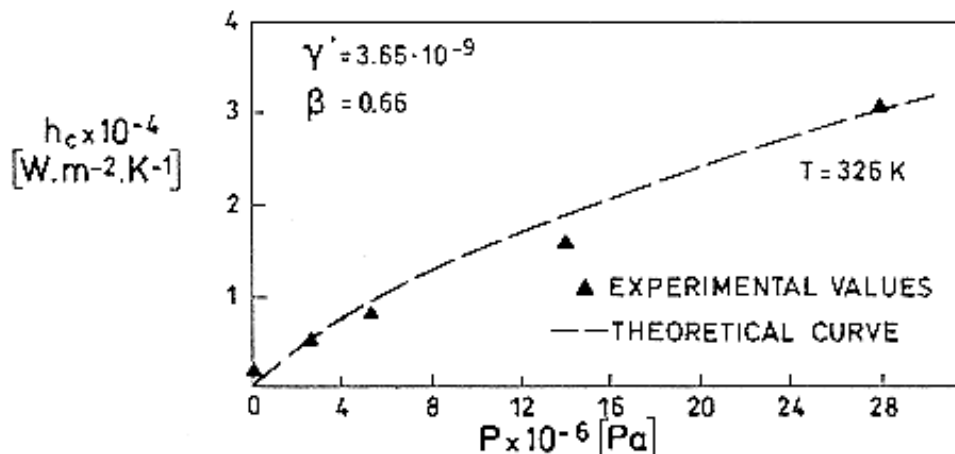
Radius, $0,10 \times 10^{-2}$ m

Thickness, $1,55 \times 10^{-2}$ m



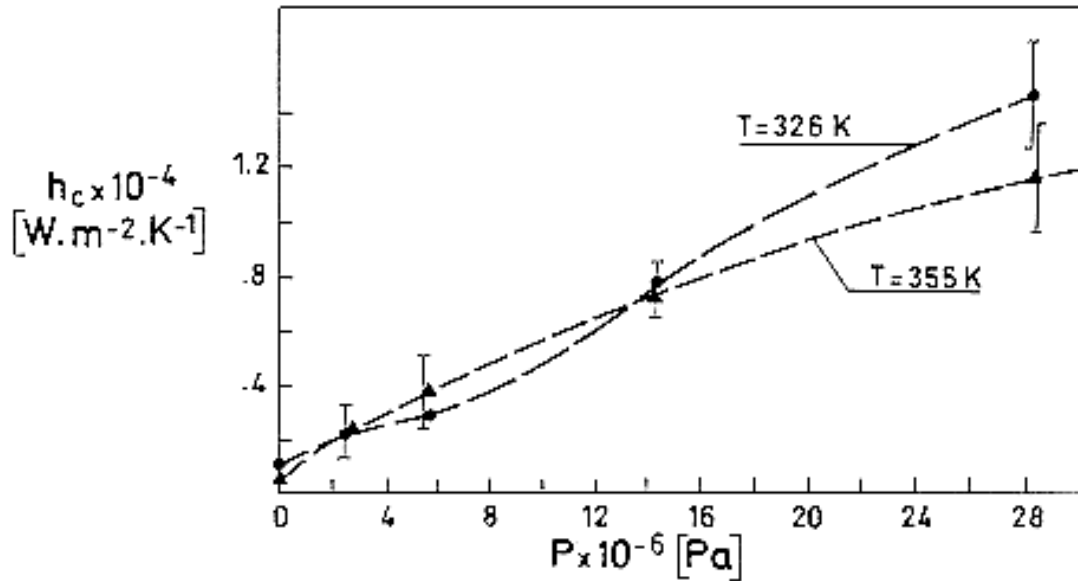
Note: non-si units are used in this figure

Figure 5-44: Thermal contact conductance vs. contact pressure. Theoretical curve: $h_c = KP^{0,93}$. (1) SS-Al, $K = 3,27 \times 10^{-11}$. (2) SS-Cu, $K = 1,84 \times 10^{-11}$.



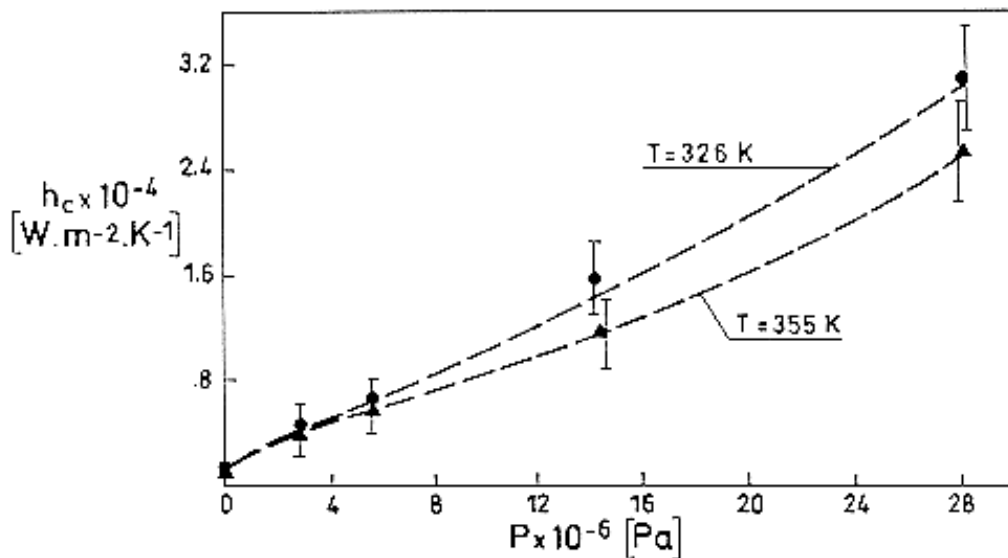
Note: non-si units are used in this figure

Figure 5-45: Comparison between experimental and theoretical values for SS/Al interface. Theoretical curve: $h_c = 3,65 \times 10^{-9} P^{0,66}$



Note: non-si units are used in this figure

Figure 5-46: Comparison between experimental and theoretical values for SS/Cu interface.



Note: non-si units are used in this figure

Figure 5-47: Comparison between experimental and theoretical values for SS/Al interface.

From Marchetti, Testa & Torrisi (1988) [31].

SPECIMENS: Two cylinders,

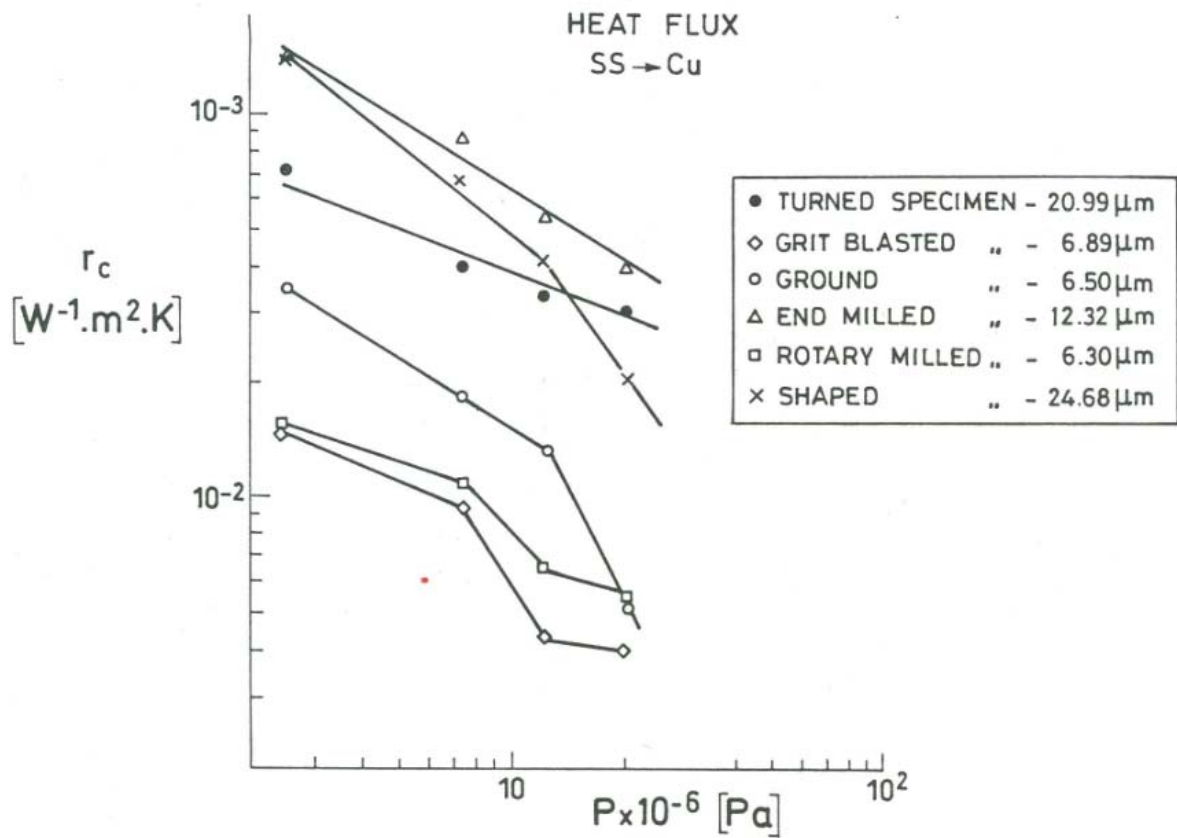
Commercially pure copper, $\alpha/k = 0,044 \times 10^{-6} \text{ W}^{-1}.\text{m}$

Stainless-steel EN58B, $\alpha/k = 1,165 \times 10^{-5} \text{ W}^{-1}.\text{m}$

Diameter, $25 \times 10^{-3} \text{ m}$

Length, $28 \times 10^{-3} \text{ m}$

Ambient pressure, $1,33 \times 10^{-3}$ Pa



Note: non-si units are used in this figure

Figure 5-48: Thermal contact resistance vs. applied pressure for SS to Cu specimens (RMS roughness values as indicated).

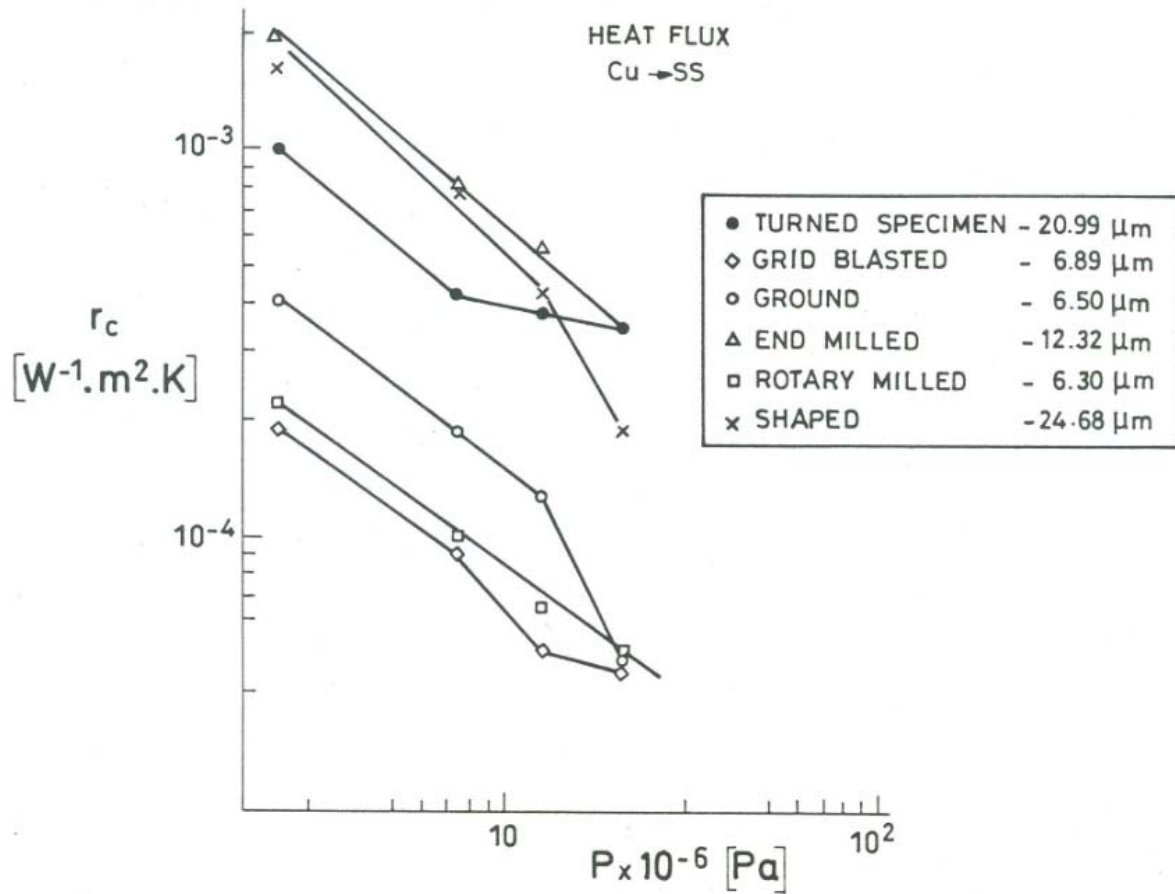
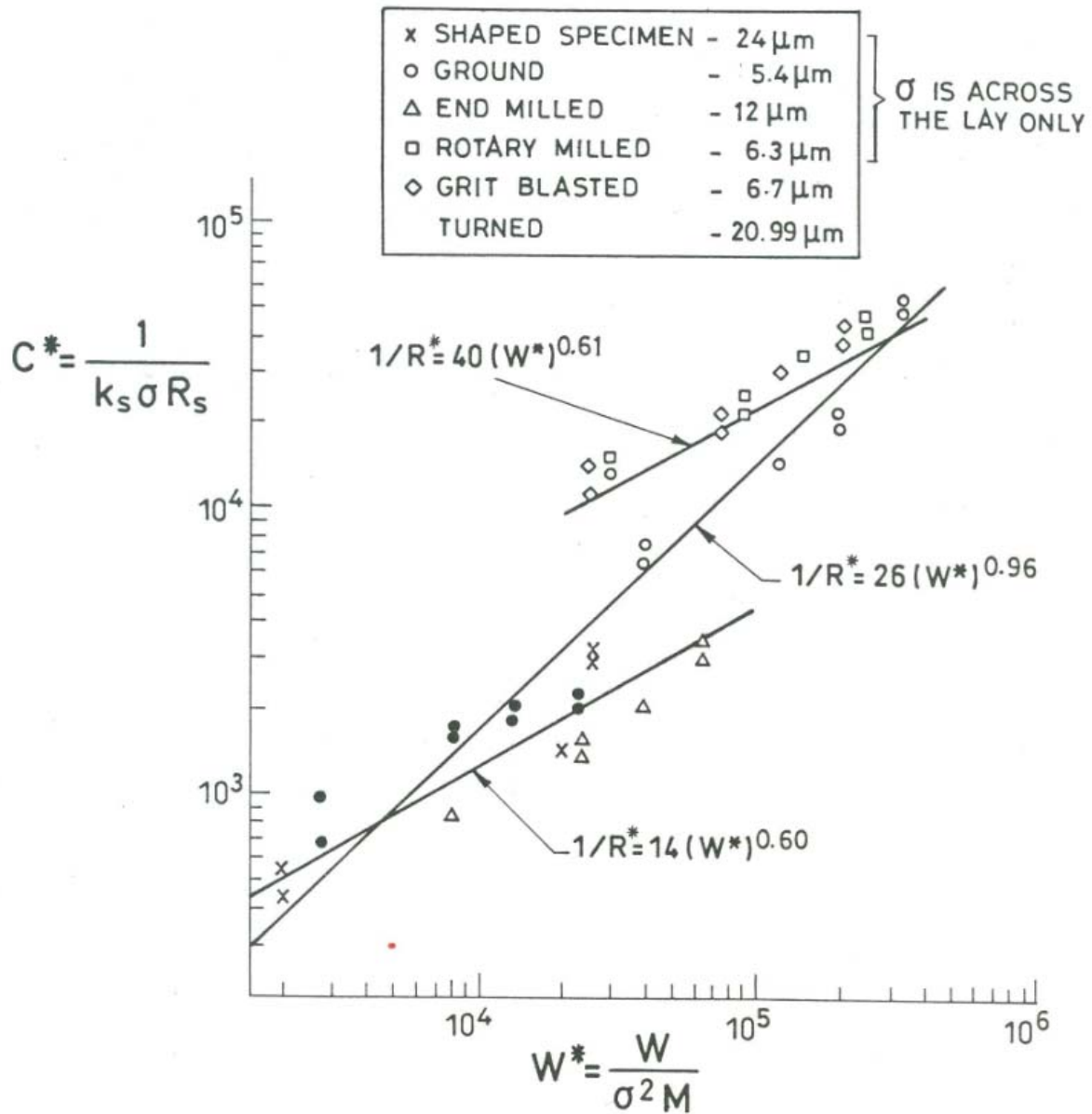
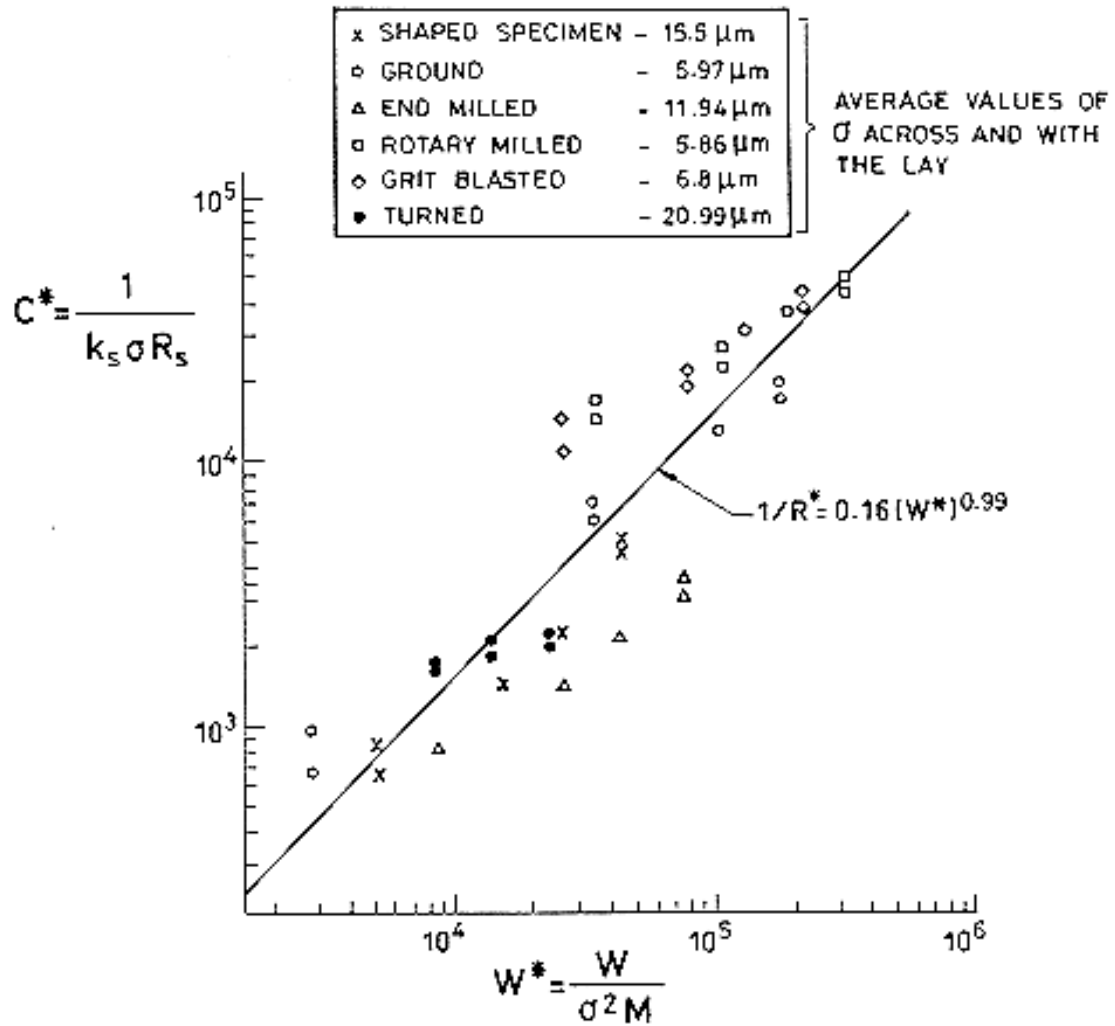


Figure 5-49: Thermal contact resistance vs. applied pressure for Cu to SS (RMS roughness values as indicated).



Note: non-si units are used in this figure

Figure 5-50: Dimensionless correlation of contact resistances between machined SS specimens pressed against copper optical-flats (surface finishes of the SS specimens as indicated).



Note: non-si units are used in this figure

Figure 5-51: Dimensionless correlation as for Figure 5-50 but for different surface finishes of the SS specimens.

From Edmonds, Jones & Probert (1980) [10].

5.2.1.3 Multilayered joints

SPECIMENS: Multilayered metallic sheets, Al 3004

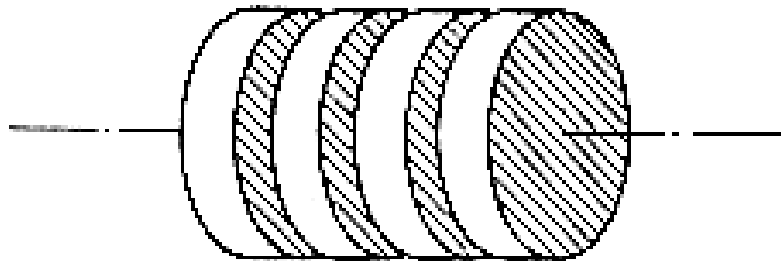
Radius, $1,27 \times 10^{-2}$ m

Ambient pressure, $< 0,133 \times 10^{-2}$ Pa

Aluminum sheet surface characteristics

Thickness $\times 10^3$ [m]	RMS surface roughness $\times 10^{-6}$ [m]	
	$3,036 \pm 0,013$	Side 1
Side 2		17,0
$0,305 \pm 0,013$	Side 1	22,5
	Side 2	23,5

Schematic of the junction



Measured thermal conductivity, k [$\text{W}\cdot\text{m}^{-1}\cdot\text{K}^{-1}$]

$$k = 147,76 + 0,15469 T \quad (280 \text{ K} < T < 420 \text{ K})$$

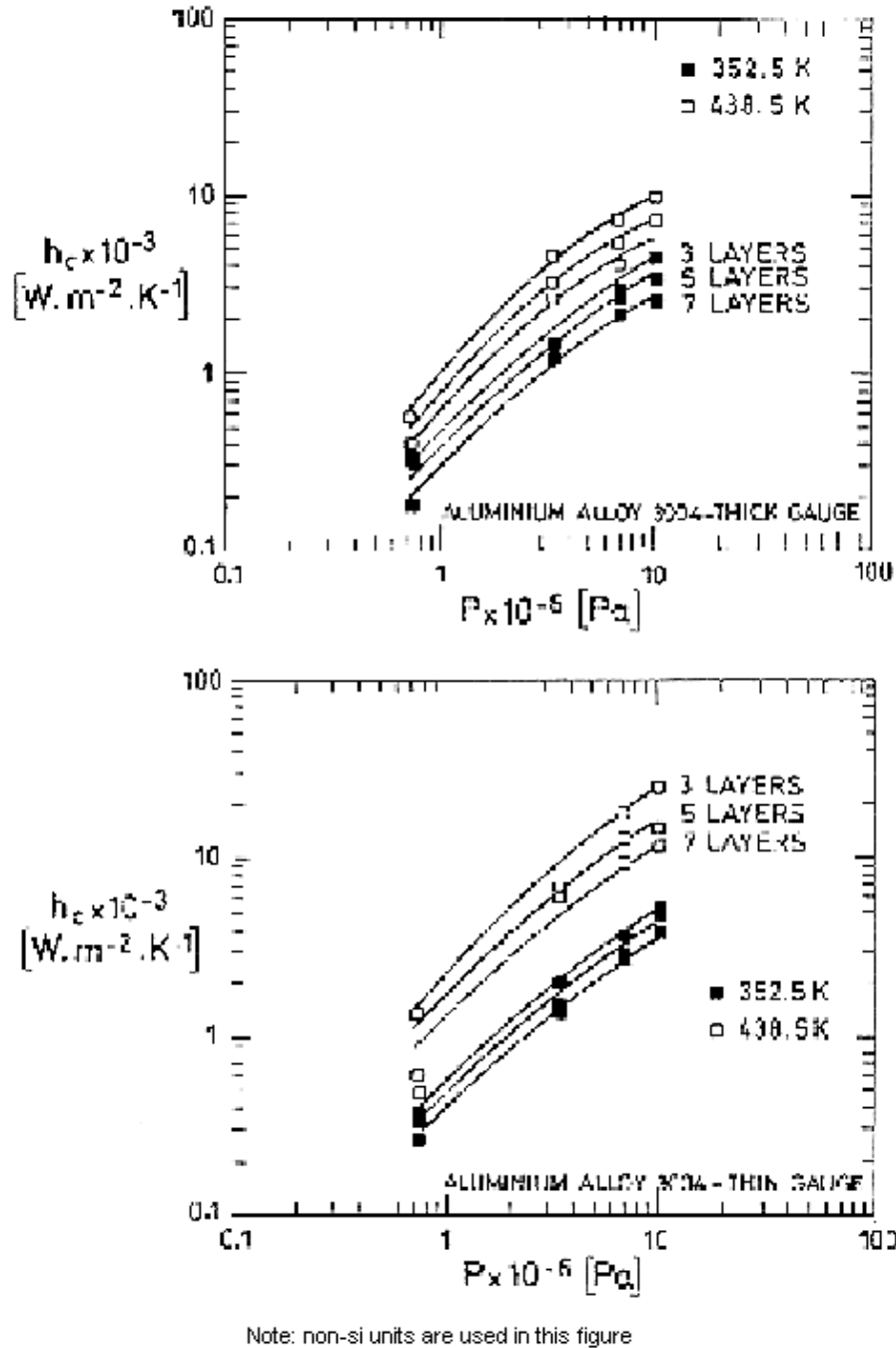


Figure 5-52: Overall thermal conductance as a function of apparent contact pressure and mean junction temperature.

5.2.1.4 Bolted joints

SPECIMENS: Two plates, Al 6061-T6

Dimensions, 0,50 x 0,75 m

Thermal plate, $t = 2,54 \times 10^{-2}$ m

$\sigma = 3,2 \times 10^{-6}$ m (rms)

Attachment technique: Bolted plate

77 steel bolts $\phi = 5 \times 10^{-3}$ m, length = 15×10^{-3} m

Spaced on a $0,070 \times 0,070$ m matrix pattern.

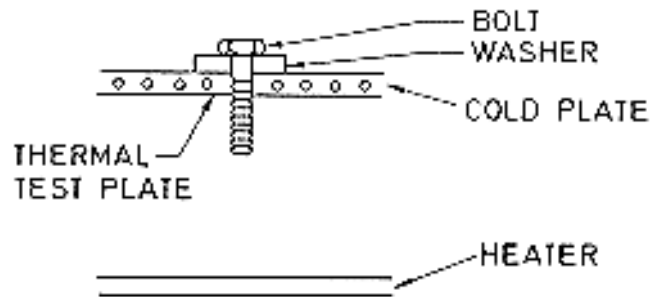
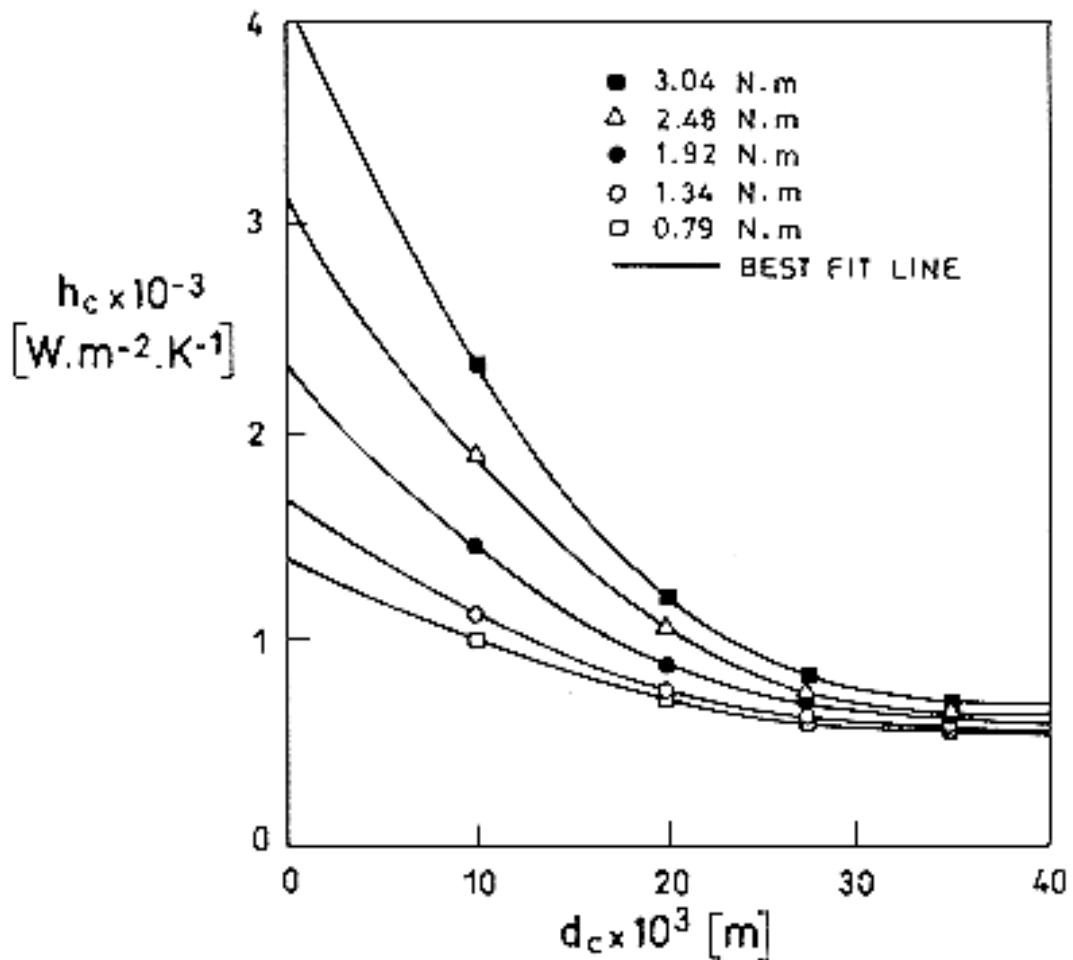


Figure 5-53: Joint Configuration.



Note: non-si units are used in this figure

Figure 5-54: Thermal contact conductance as a function of distance from center of bolt. From Peterson, Stanks & Fletcher (1991) [39].

Table 5-4: Integrated thermal contact conductance values.

Torque [N.m]	h_c [$W.m^{-2}.K^{-1}$]
0,79	855
1,35	985
1,92	1139
2,48	1331
3,04	1589

NOTE Assuming symmetry around each bolt hole and defining a unit cell as a 70 x 70 mm region with the bolt hole located in the center, the equations (obtained by a least squares curve fit technique from data of Figure 5-53) were integrated to obtain the individual bolt conductance. The average contact conductance in each case can be calculated by dividing these numbers by the area of unit cell.

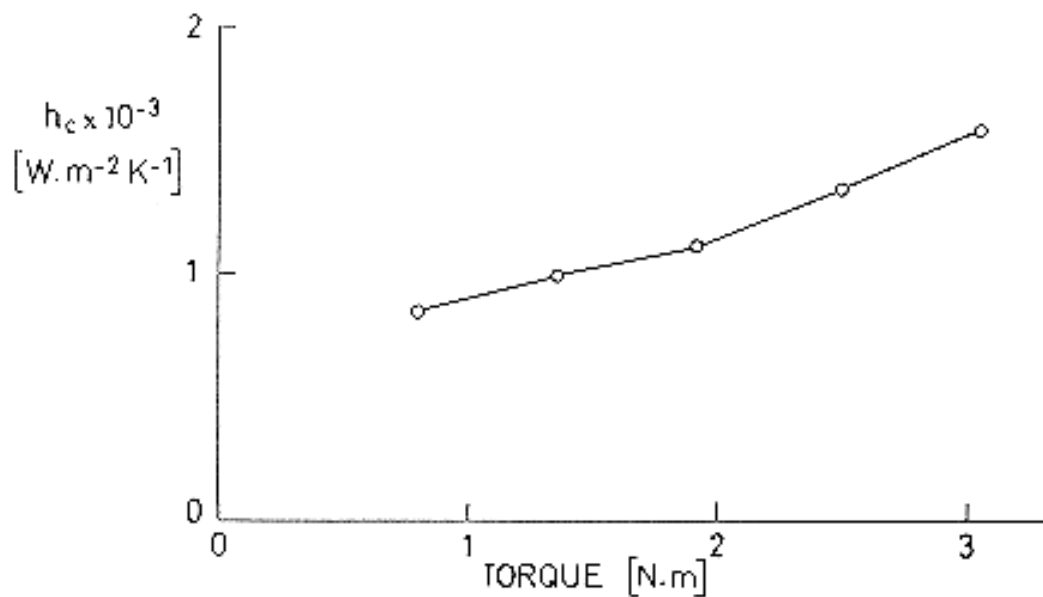


Figure 5-55: Integrated thermal contact conductance. From Table 5-4.

5.2.2 Metal-composite joints

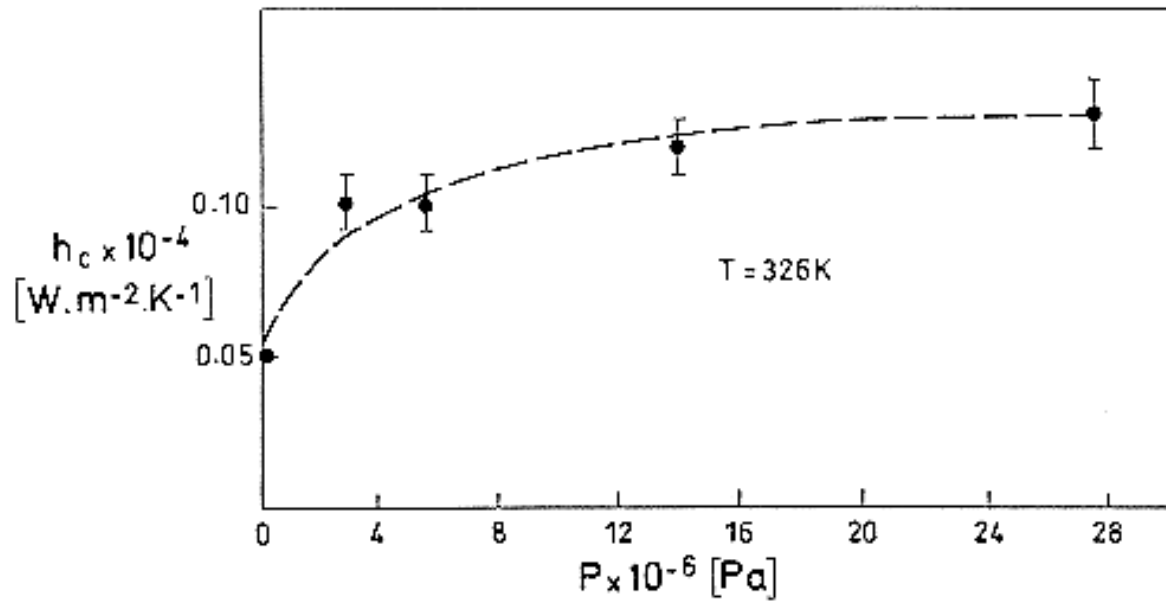
SPECIMENS: Two disks,

Stainless-steel AISI 4340 (1) and Graphite-epoxi-laminate (2)

Stainless-steel AISI 4340 (1) and Glass-epoxi-laminate (3)

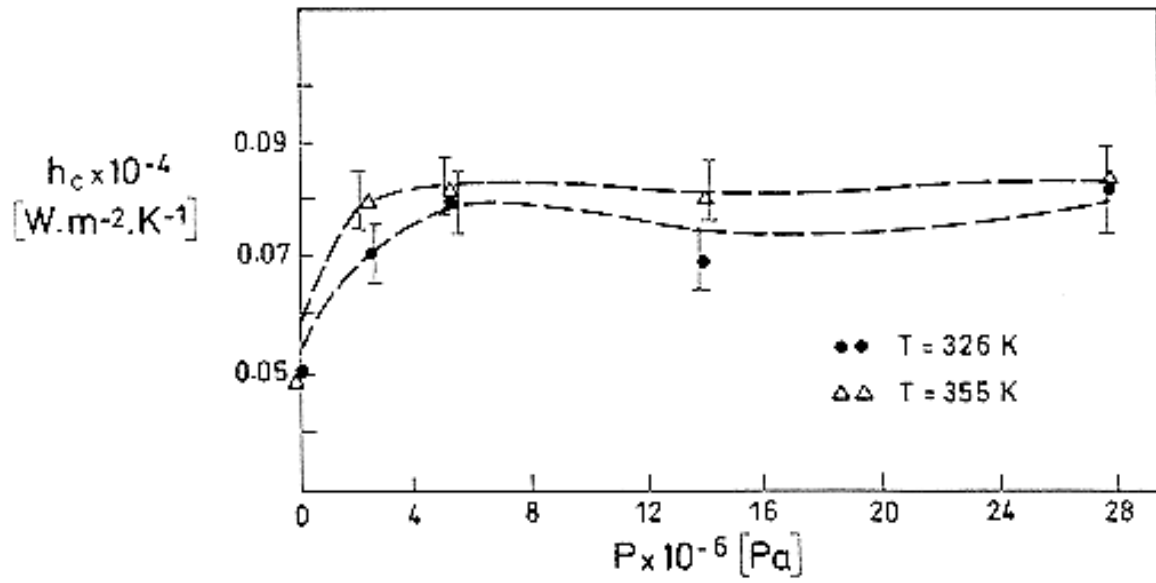
Diameter, $2,10 \times 10^{-2}$ m

Thickness, (1) $0,10 \times 10^{-2}$ m; (2) $0,20 \times 10^{-2}$ m; (3) $0,17 \times 10^{-2}$ m



Note: non-si units are used in this figure

Figure 5-56: Stainless-steel and Graphite-epoxi-laminate.



Note: non-si units are used in this figure

Figure 5-57: Stainless-steel and glass-epoxy-laminate.

From Marchetti, Testa & Torrisi (1988) [31].

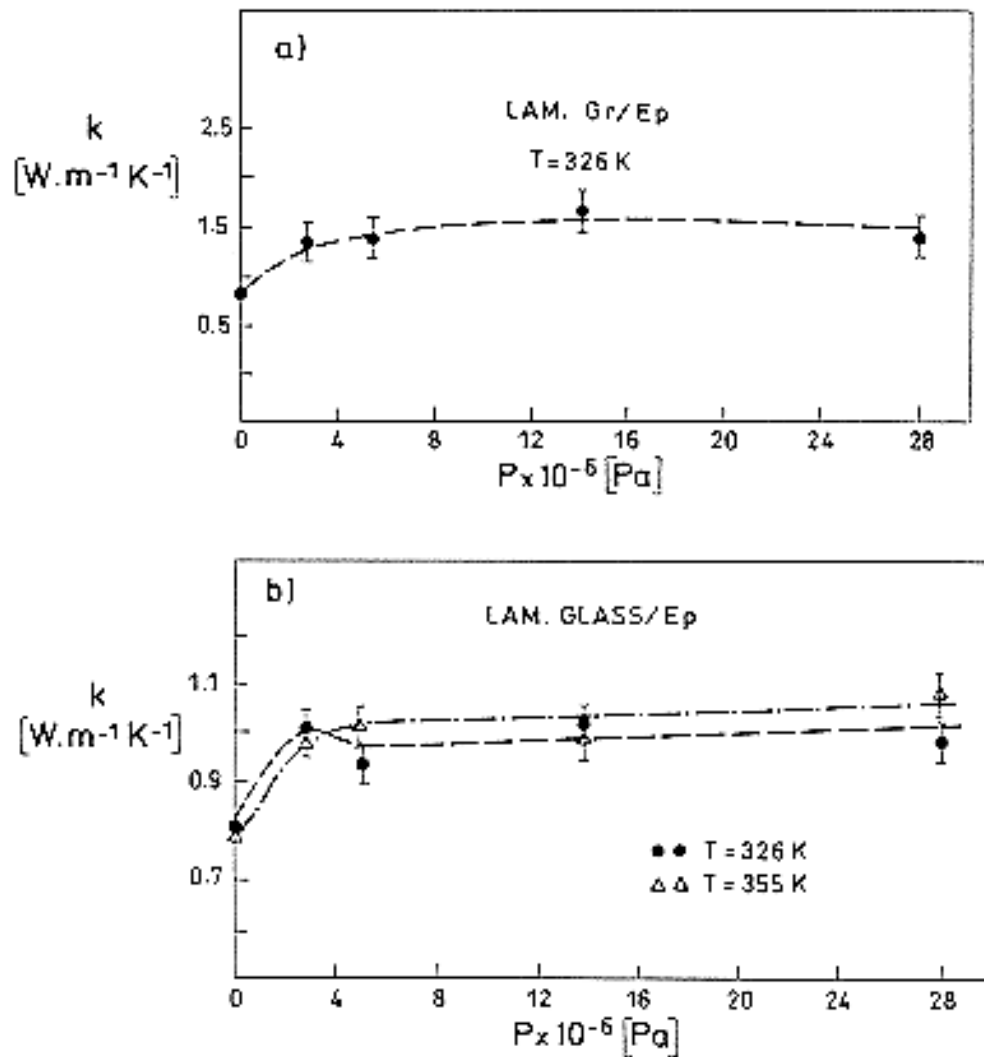
5.2.3 Composite-composite joints

SPECIMENS: Two disks,

Graphite-epoxy-laminate (1) and Glass-epoxy-laminate (2).

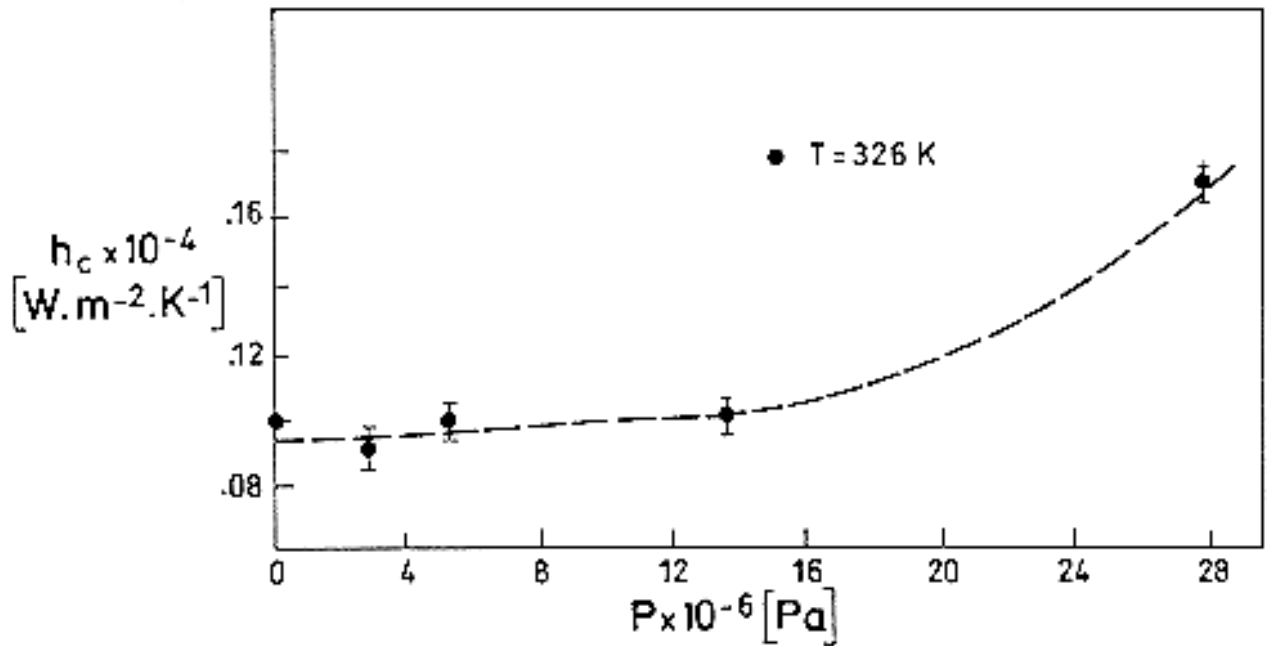
Diameter, $2,10 \times 10^{-2}$ m

Thickness, (1) $0,20 \times 10^{-2}$ m; (2) $0,17 \times 10^{-2}$ m



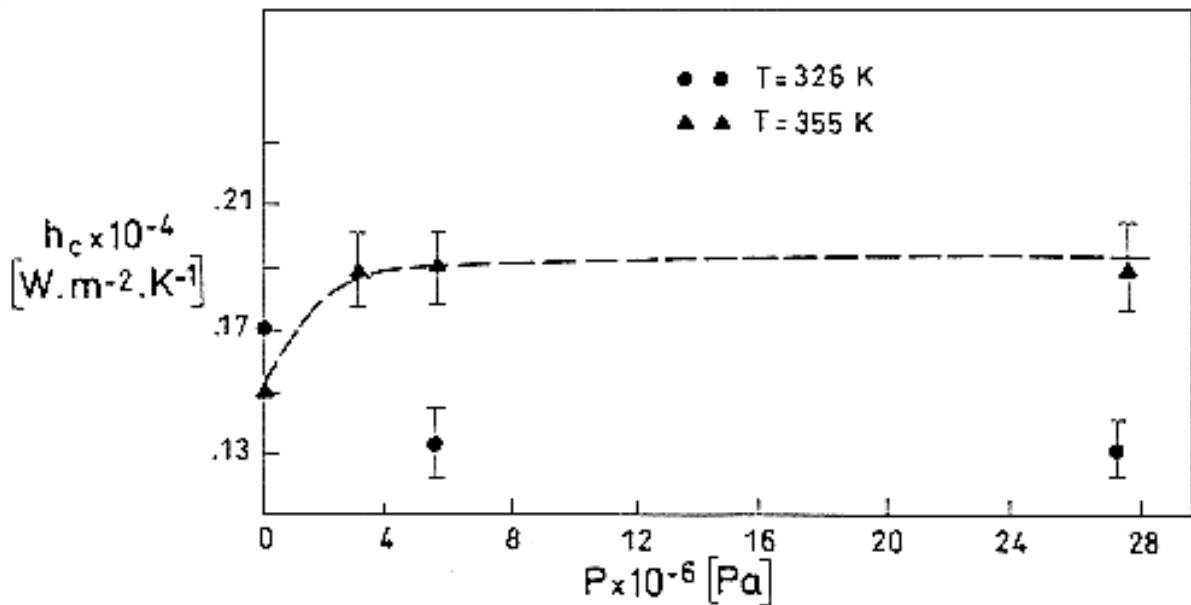
Note: non-si units are used in this figure

Figure 5-58: Experimental values of thermal transverse conductivity a) Graphite-epoxy-laminate. b) Glass-epoxy-laminate.



Note: non-si units are used in this figure

Figure 5-59: Graphite-epoxy-laminate and graphite-epoxy-laminate.



Note: non-si units are used in this figure

Figure 5-60: Glass-epoxy-laminate and glass-epoxy-laminate.

From Marchetti, Testa & Torrisi (1988) [31].

5.3 Interfacial materials between metals

5.3.1 Metallic foils between metals

5.3.1.1 Similar metals

FILLER: Indium Foil, 99,99 percent pure.

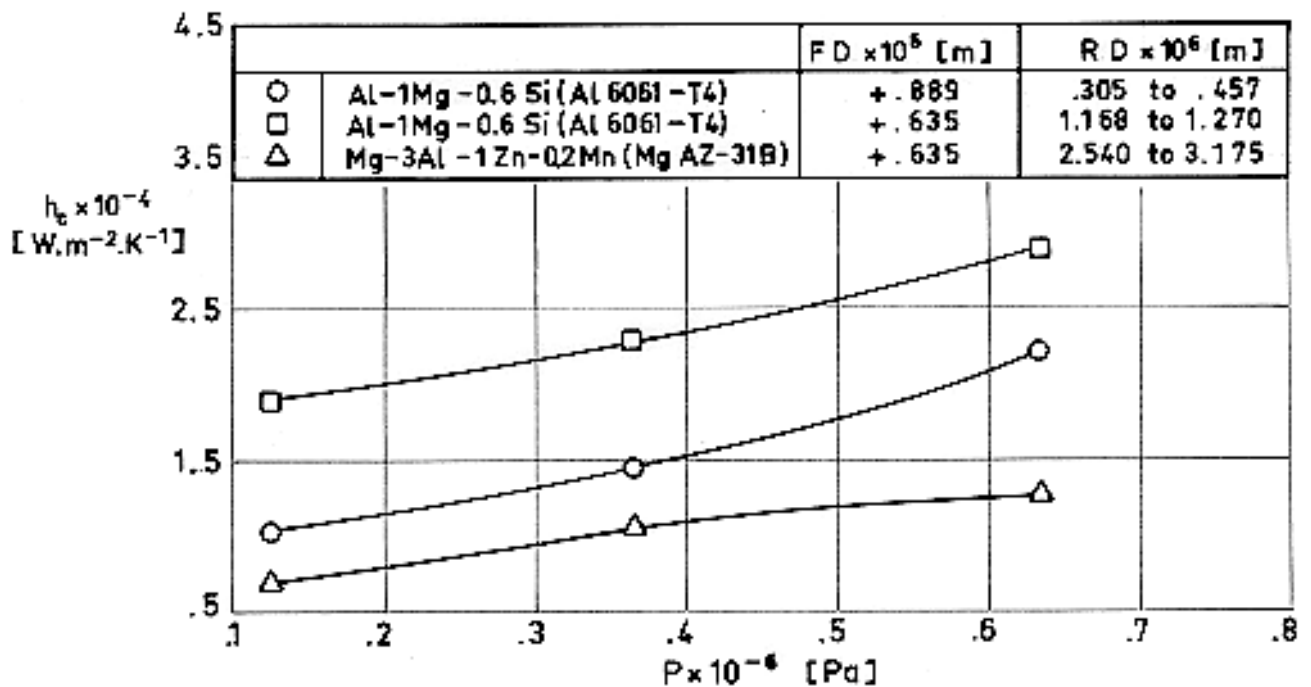
Density, $\rho = 7310 \text{ kg.m}^{-3}$

Initial Thickness, $t = 2,5 \times 10^{-5} \text{ m}$.

SPECIMENS: Two cylinders as indicated below.

Radius, $b = 1,27 \times 10^{-2} \text{ m}$.

Ambient Pressure, $p = 1,33 \times 10^{-3} \text{ Pa}$.



Note: non-si units are used in this figure

Figure 5-61: Plot of contact conductance vs. contact pressure. From Cunnington (1964) [9].

Cost of the filler: 1300 SF.kg^{-1} (Fluka).

FILLERS: Lead, Tin, Aluminium, Copper

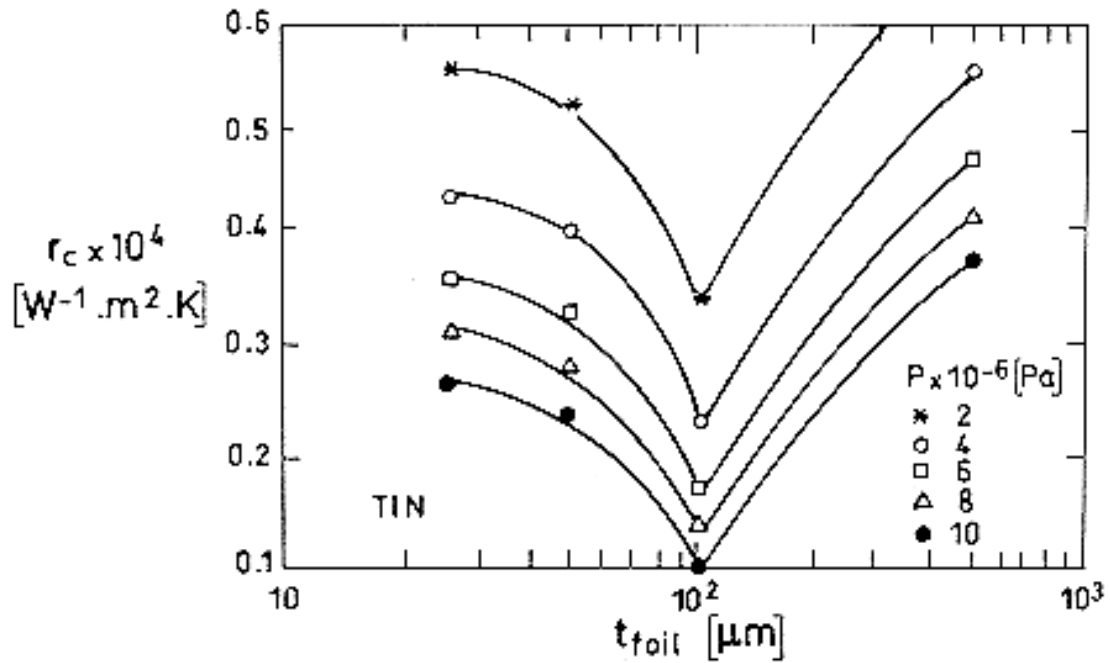
SPECIMENS: Two cylinders, Armco Iron.

Diameter, $25 \times 10^{-3} \text{ m}$

Length, $38 \times 10^{-3} \text{ m}$

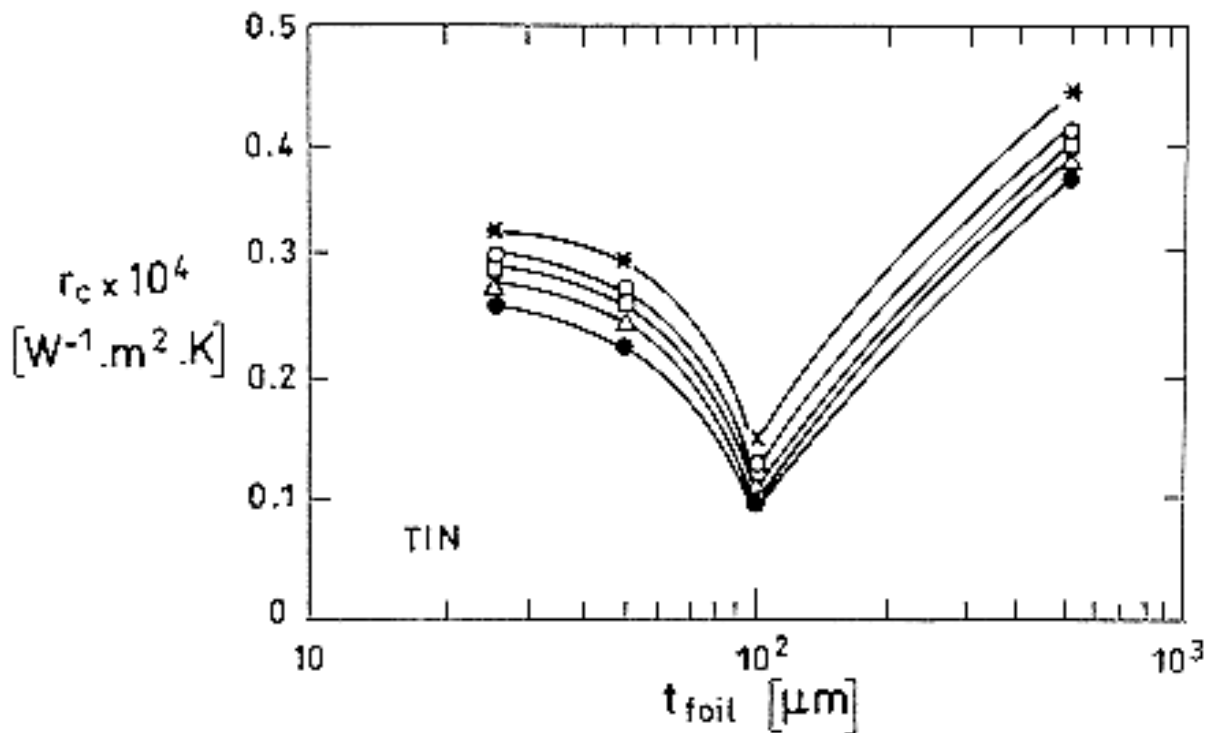
One surface optically flat and the other lathe turned such that a continuous spiral was produced.

Ambient pressure.



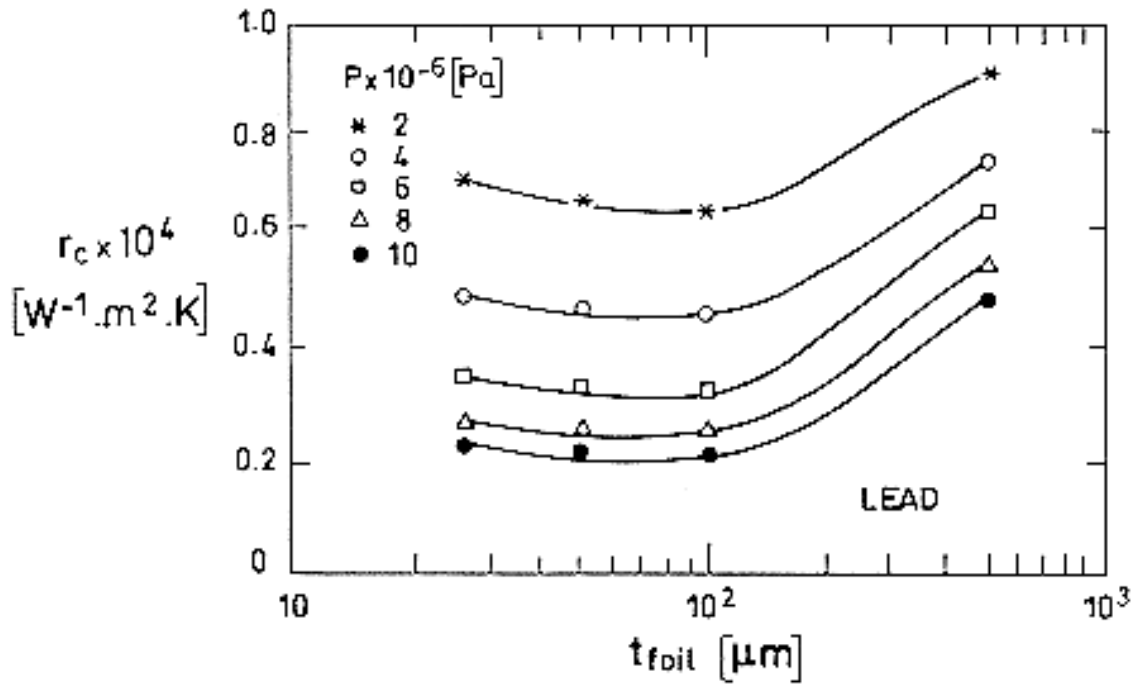
Note: non-si units are used in this figure

Figure 5-62: Loading resistance with tin.



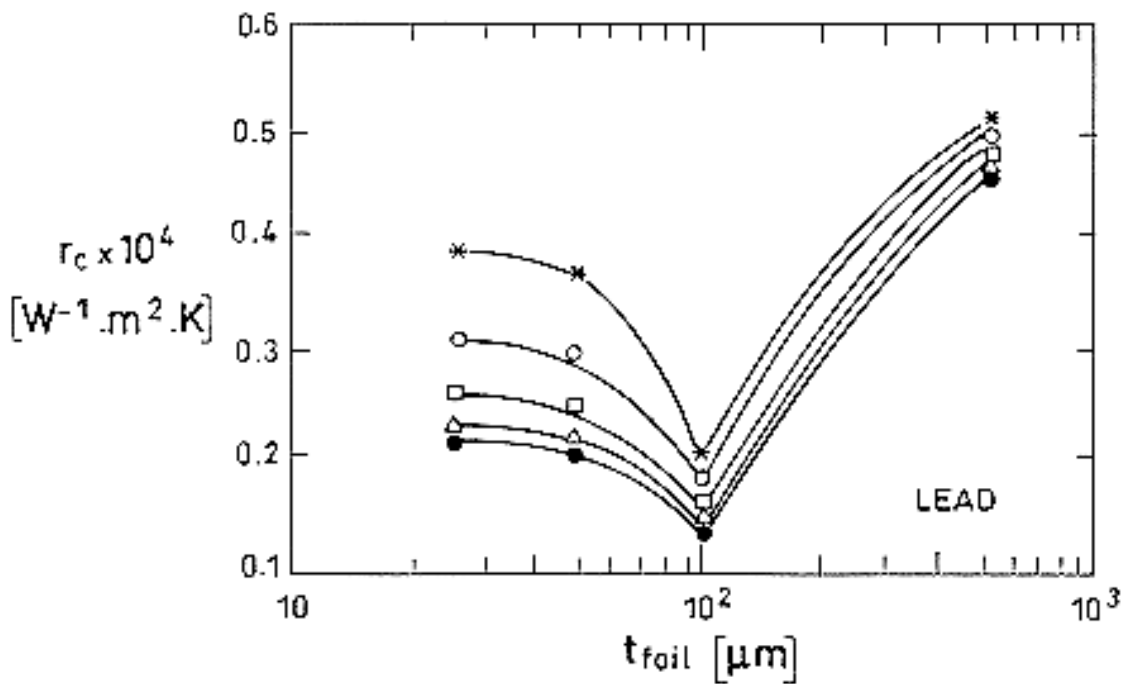
Note: non-si units are used in this figure

Figure 5-63: Unloading resistance with tin.



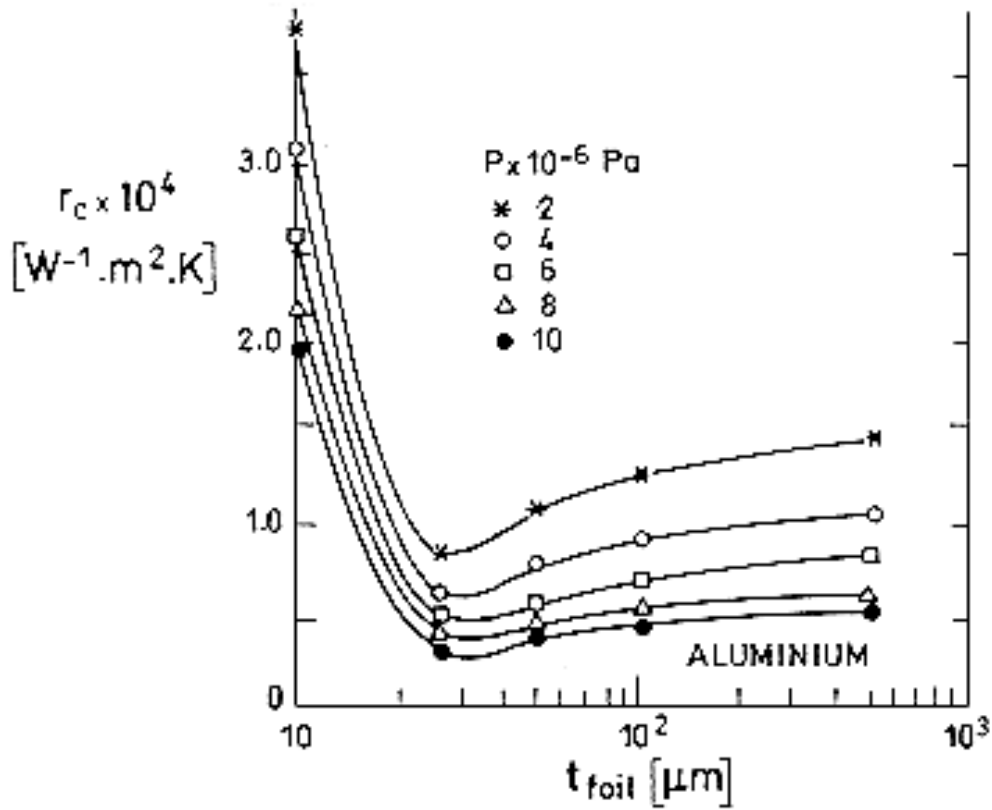
Note: non-si units are used in this figure

Figure 5-64: Loading resistance with lead.



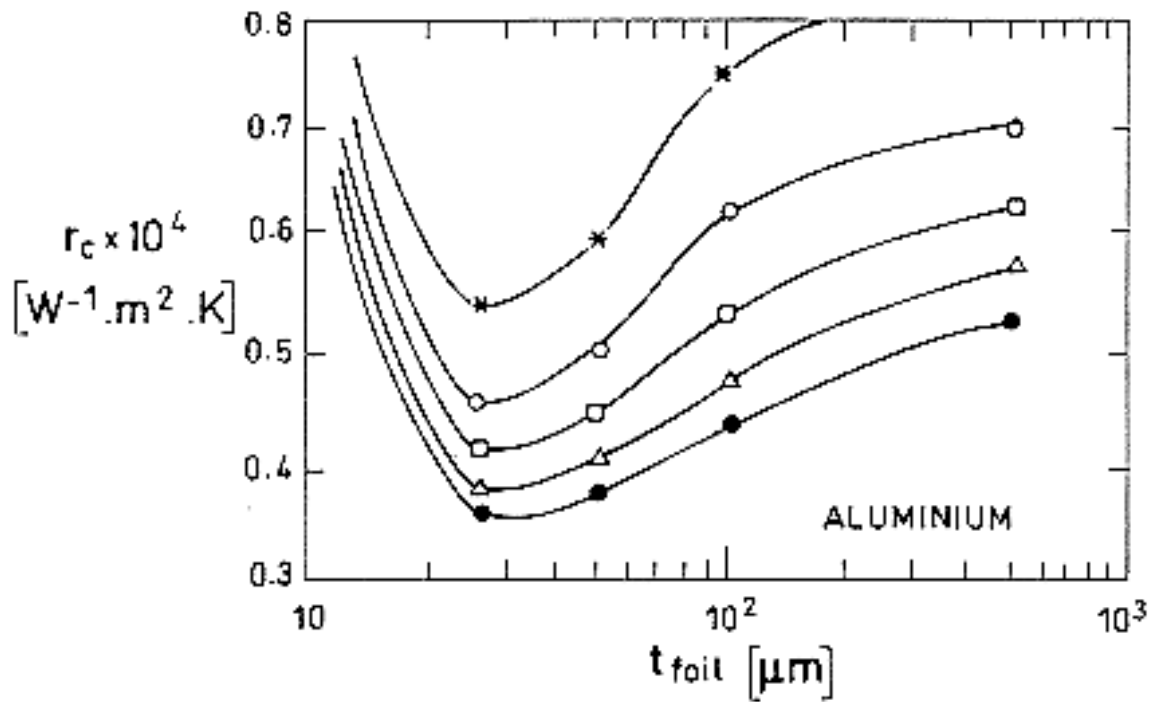
Note: non-si units are used in this figure

Figure 5-65: Unloading resistance with lead.



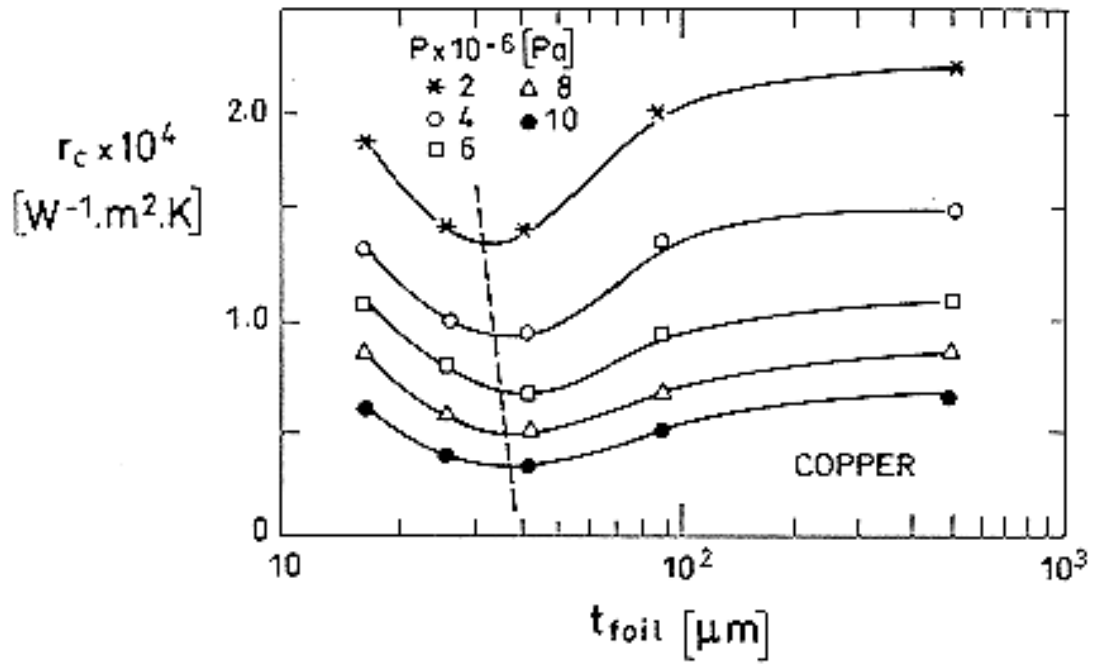
Note: non-si units are used in this figure

Figure 5-66: Loading resistance with aluminium.



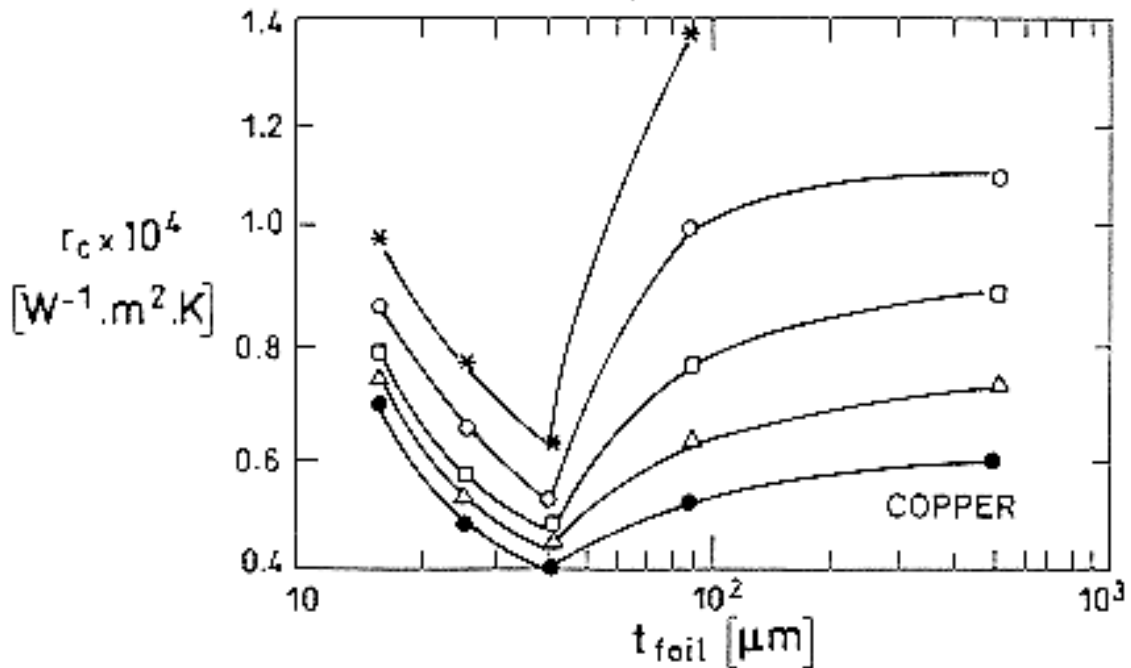
Note: non-si units are used in this figure

Figure 5-67: Unloading resistance with aluminium.



Note: non-si units are used in this figure

Figure 5-68: Loading resistance with copper.



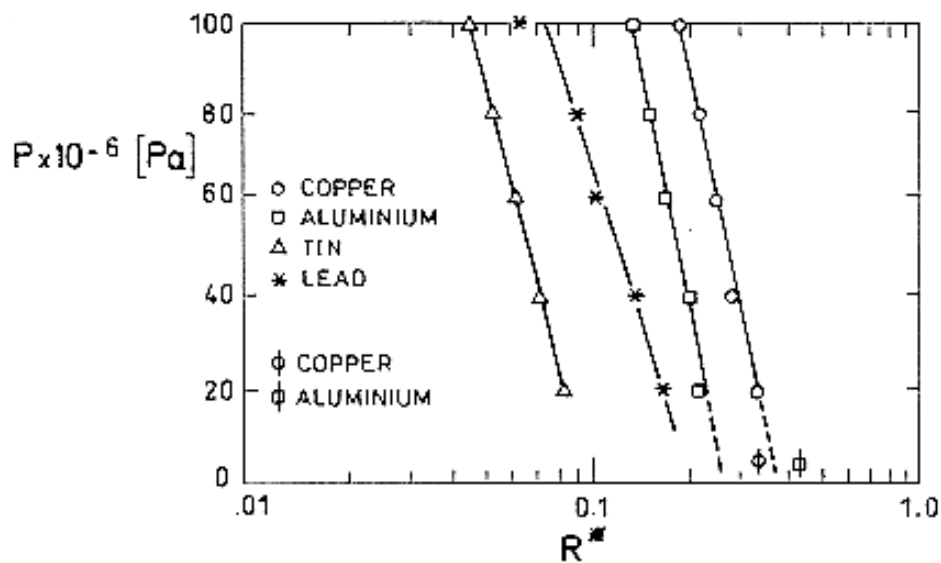
Note: non-si units are used in this figure

Figure 5-69: Unloading resistance with copper.

EMPIRICAL CORRELATION: $\ln R^* = C + m \text{ Pa}$

$R^* = R_m / R_b = R_{\text{optimum thickness}} / R_{\text{bare joint}}$ (dimensionless minimum resistance)

Material	C	m
Tin	-2,30	-0,0074
Lead	-1,60	-0,0100
Aluminium	-1,46	-0,0042
Copper	-0,98	-0,0072



Note: non-si units are used in this figure

Figure 5-70: Dimensionless minimum resistance to bare joint resistance.

From Yovanovich (1973) [50] and Koh & John (1965).

FILLERS:

Layer of indium, Thickness, 2,5 μm

Molybdenum disulfide coating (Moly-Tiolub-1175), Thickness, 1,25 μm

Teflon impregnated anodized coating (Hard-Tuf X20), Thickness, 1,25 μm

SPECIMENS: Two rectangular plates, Al 6061-T6

Dimensions, 0,127 x 0,1778 x 0,0254 m

Ambient Pressure, $< 0,133 \times 10^{-2}$ Pa

RMS surface roughness

Specimen set 1 (Indium)

Plate A, $0,33 \times 10^{-6}$ m

Plate B, $0,37 \times 10^{-6}$ m

Specimen set 2 (Moly-Tiolub-1175)

Plate A, $0,44 \times 10^{-6}$ m

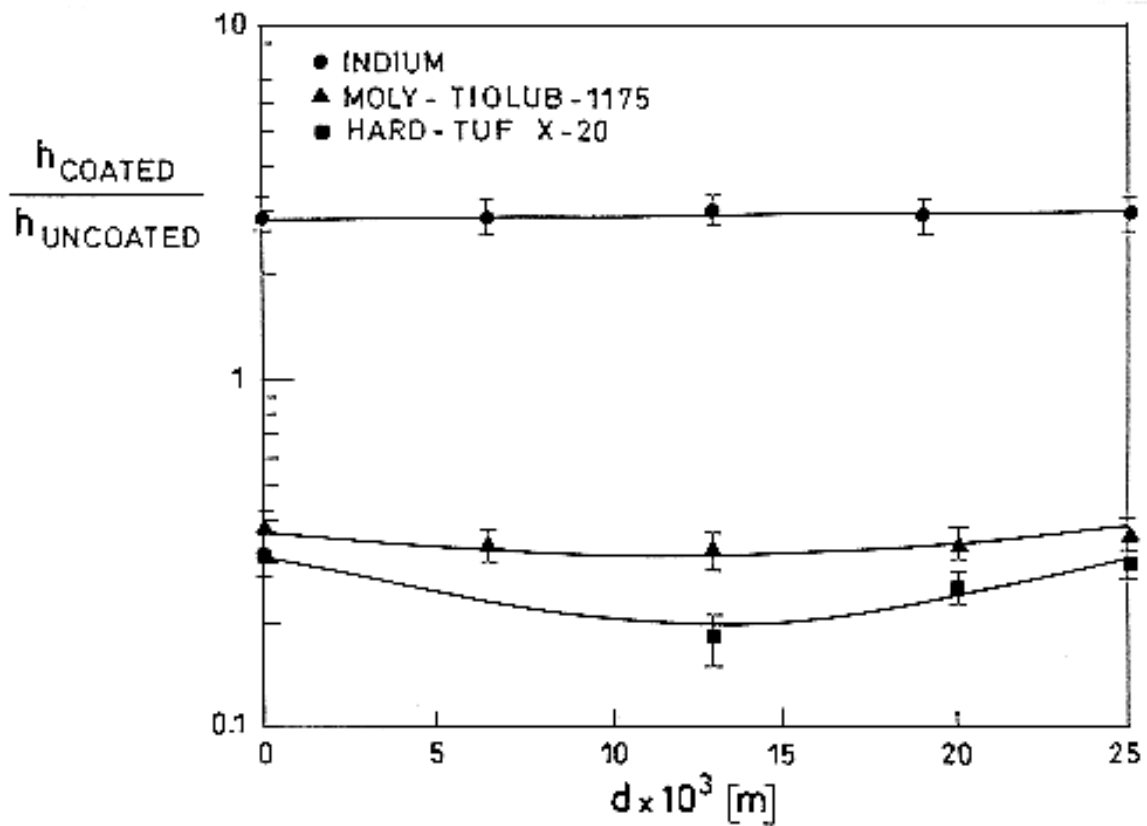
Plate B, $0,42 \times 10^{-6}$ m

Specimen set 3 (Hard-Tuf X20)

Plate A, $0,37 \times 10^{-6}$ m

Plate B, $0,42 \times 10^{-6}$ m

Load distribution: See the description of two rectangular plates of Al 6061-T6 in clause 5.2.1.1. Case 5 x 7 load array.



Note: non-si units are used in this figure

Figure 5-71: Dimensionless thermal contact conductance for specimen sets 1, 2 and 3 as a function of the distance from a load point. $P_{contact} = 689,5 \times 10^3$ Pa. Values for $h_{uncoated}$ from Table 5-1 (clause 5.2.1.1). From Peterson and Fletcher (1992) [37].

5.3.1.2 Bolted joints

FILLER: Metallic foils.

Foil type	Thickness $\times 10^6$ [m]	Hardness $\times 10^{-6}$ [kg.m ⁻²]	Thermal Conductivity [W.m ⁻¹ .K ⁻¹]
Aluminium	30	27,0	204
Copper	40	80,0	384
Lead	75	4,0	35
Tin	100	5,3	60

SPECIMENS: Two plates, Al 6061-T6

Dimensions, 0,50 x 0,75 m

Thermal test plate, $t = 2,54 \times 10^{-2}$ m, $\sigma = 3,2 \times 10^{-6}$ m (rms)

Attachment technique: Bolted plate

77 steel bolts, $\phi = 5 \times 10^{-3}$ m, length = 15×10^{-3} m

Spaced on a 0,070 x 0,070 m matrix pattern.

Joint configuration: See Figure 5-53 (clause 5.2.1.4)

Table 5-5: Thermal contact conductance data.

Radius $\times 10^3$ [m]	Torque [N.m]	h_c [W.m ⁻² .K ⁻¹]				
		Bare	Lead	Tin	Aluminum	Copper
11,76	0,79	989	2897	1480	1003	931
	1,92	1324	3879	1962	1459	1301
	3,04	2221	6603	3303	2493	2211
19,51	0,79	646	2214	951	701	621
	1,92	838	2395	1221	920	816
	3,04	1126	3541	1603	1251	1103
27,21	0,79	502	1879	742	536	501
	1,92	602	2131	836	659	603
	3,04	756	2546	1126	829	714
35,00	0,79	459	1513	693	741	421
	1,92	559	1841	818	602	546
	3,04	631	2113	926	713	641

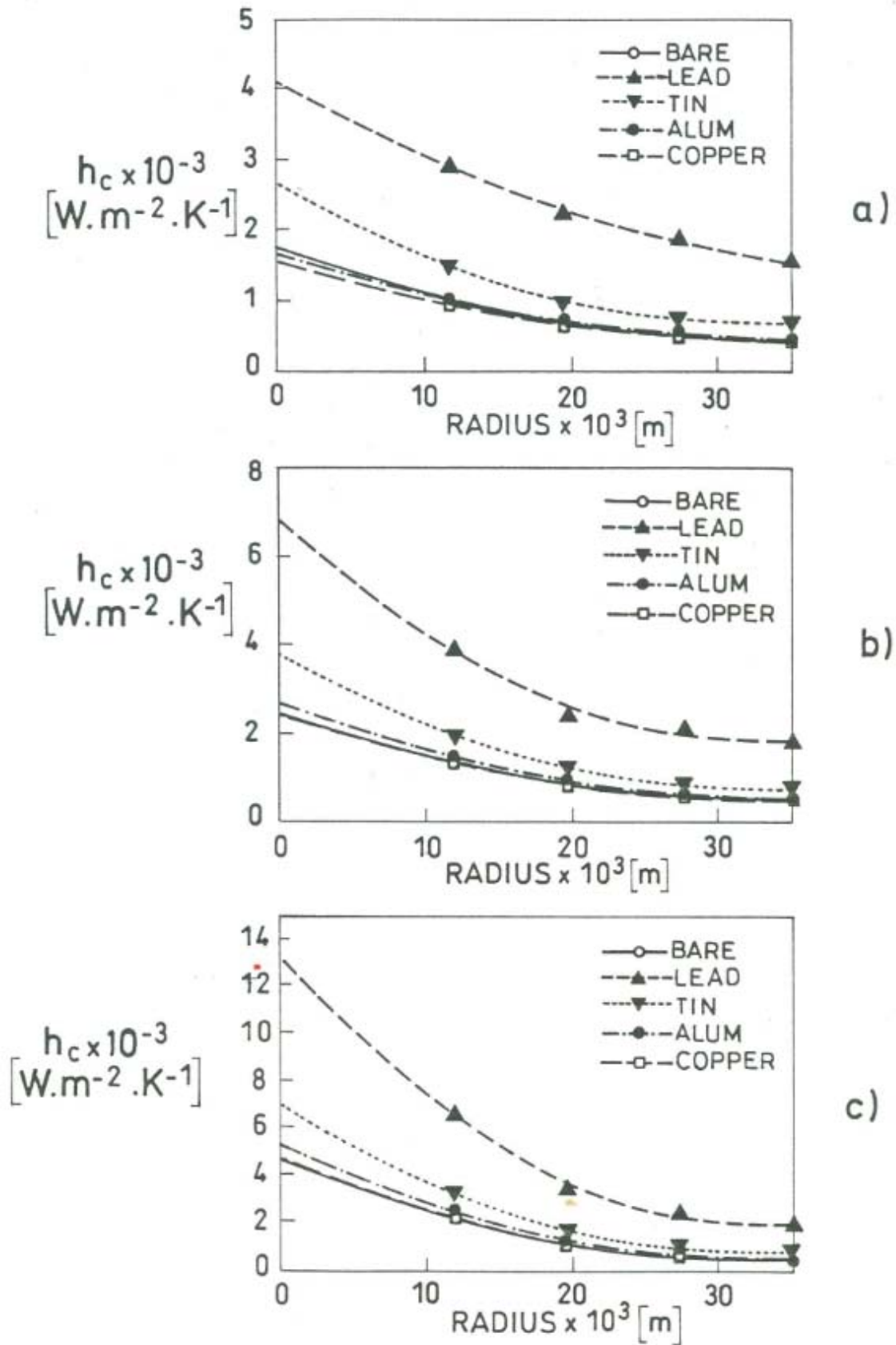
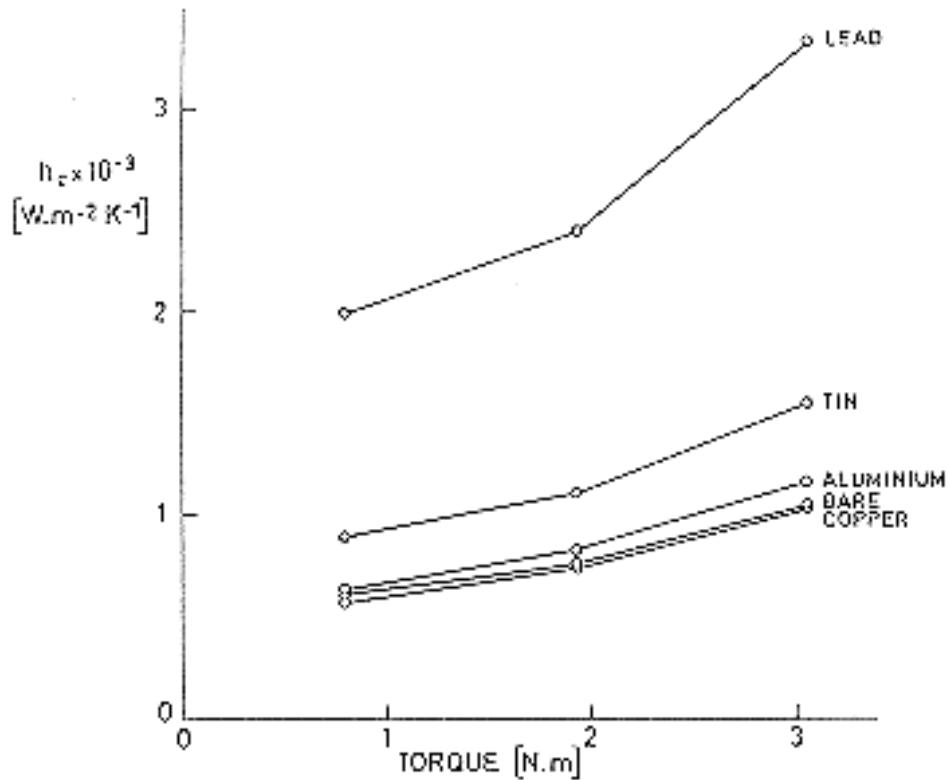


Figure 5-72: Thermal contact conductance variation: a) 0,79 N.m; b) 1,92 N.m; c) 3,04 N.m. From Peterson & Fletcher (1991) [37].

Table 5-6: Integrated thermal contact conductance values.

Torque [N.m]	h_c [W.m ⁻² .K ⁻¹]				
	Bare	Lead	Tin	Aluminium	Copper
0,79	603	1993	899	629	573
1,92	764	2396	1110	835	751
3,04	1050	3323	1544	1173	1037

NOTE Assuming symmetry around each bolt hole and defining a unit cell as a 70 x 70 mm region with the bolt hole located in the center, the equations (obtained by a least squares curve fit technique from data of Figure 5-72) were integrated to obtain the individual bolt conductance. The average contact conductance in each case can be calculated by dividing these numbers by the area of unit cell.


Figure 5-73: Integrated thermal contact conductance. From Table 5-6.

5.3.2 Metallic oxide powders between similar metals

FILLER: Rutile powder.

SPECIMENS: Two cylinders, Fe - 19 Cr - 10 Ni. (SS 304).

Radius, $b = 1,27 \times 10^{-2}$ m.

Flatness Deviation, $FD = +0,508 \times 10^{-6}$ to $+0,635 \times 10^{-6}$ m.

Roughness Deviation, $RD = 0,076 \times 10^{-6}$ to $0,152 \times 10^{-6}$ m.

Mean Temperature, $T_m = 387$ K.

Ambient Pressure, $p = 1,33 \times 10^{-3}$ Pa.

Table 5-7: Values of contact conductance vs. contact pressure.

$p \times 10^{-3}$ [Pa]	h_c [W.m ⁻² .K ⁻¹]
627	128
2137	271

From Gyrog (1970) [26]

Cost of the filler: 2,5 US \$.kg⁻¹.

5.3.3 Porous metallic materials between similar metals.

Understanding of the data in this clause requires some familiarity with the following concepts concerning porous materials.

The porosity, ϕ , of a porous material is the fraction of the bulk volume of the material occupied by voids.

Filters may be rated according to its degree of filtration. A filter rated, for example, $r = 25 \times 10^{-6}$ m., will, when new and clean, stop 98 per cent of the particles measuring 25×10^{-6} m or more while operating under its designed flow conditions.

Filter Rating, in m, should not be mixed up with Filtration Rate, which is the volume of liquid passing through a unit area of the filter medium in a unit time, for a given pressure loss. This rate is measured in m.s⁻¹.

FILLER: Porous Copper.

Porosity, $\phi = 0,8$

Fiber Diameter, $d = 0,4 \times 10^{-4}$ m.

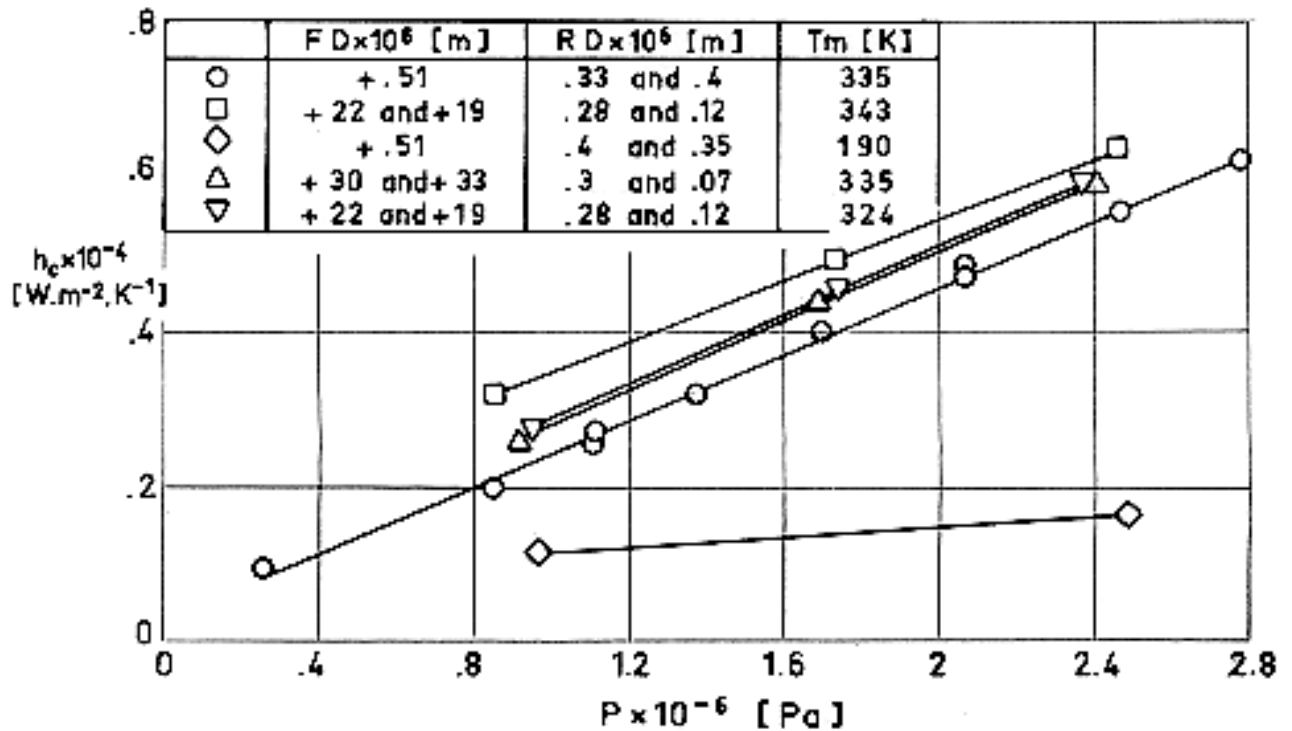
Filter Rating, $r = 0,145 \times 10^{-3}$ m.

Initial Thickness, $t = 0,66 \times 10^{-3}$ m.

SPECIMENS: Two cylinders, Al - 4,3 Cu - 1,5 Mg - 0,6 Mn. (Al 2024-T4).

Radius, $b = 1,27 \times 10^{-2}$ m.

Ambient Pressure, $p = 1,33 \times 10^{-3}$ Pa.



Note: non-si units are used in this figure

Figure 5-74: Plot of contact conductance vs. contact pressure for different surface finishes and mean temperatures. From Miller & Fletcher (1973) [32].

The filler is an structure of sintered metallic fibers. In this particular case it has been manufactured by Huyck Metals Co., USA.

Cost of the filler:

FILLER: Porous Nickel.

Porosity, $\phi = 0,8$

Fiber Diameter, $d = 0,12 \times 10^{-4}$ m.

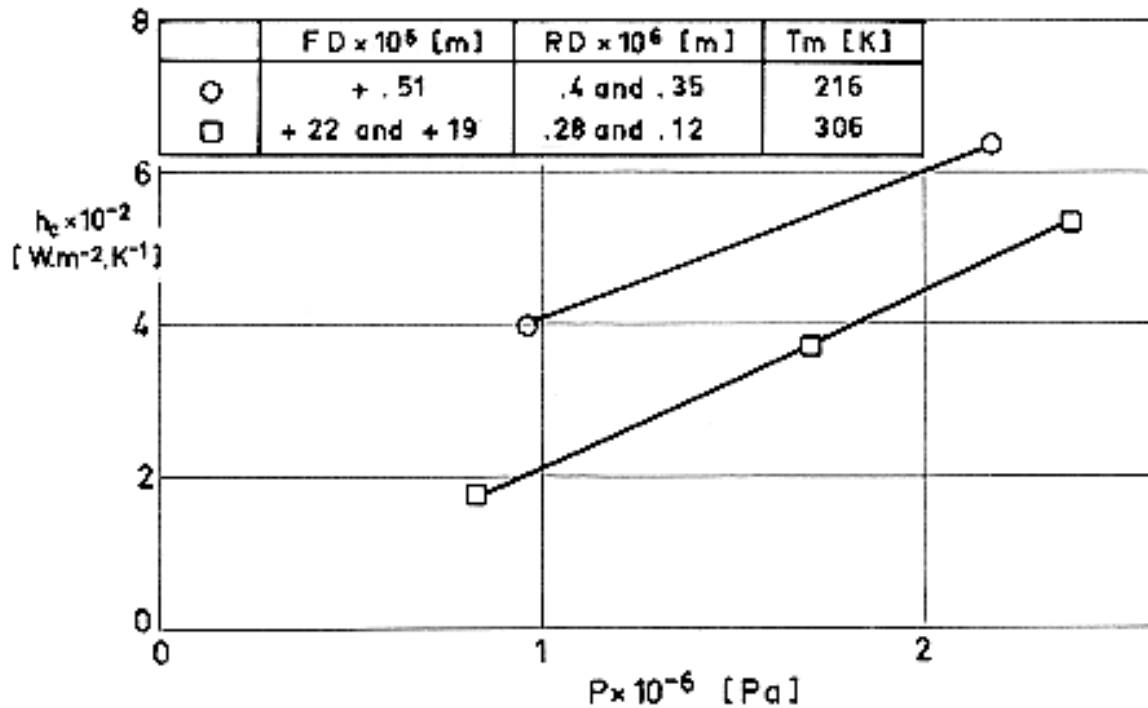
Filter Rating, $r = 0,6 \times 10^{-4}$ m.

Initial Thickness, $t = 2,05 \times 10^{-3}$ m.

SPECIMENS: Two cylinders, Al - 4,3 Cu - 1,5 Mg - 0,6 Mn. (Al 2024-T4).

Radius, $b = 1,27 \times 10^{-2}$ m.

Ambient Pressure, $p = 1,33 \times 10^{-3}$ Pa.



Note: non-si units are used in this figure

Figure 5-75: Plot of contact conductance vs. contact pressure for different surface finishes and mean temperatures. From Miller & Fletcher (1973) [32].

The filler is a structure of sintered metallic fibers. In this particular case it has been manufactured by Huyck Metals Co., USA.

Cost of the filler:

FILLER: Porous Fe - 16 Cr (SS 430).

Porosity, $\phi = 0,68$ and $0,80$

Fiber Diameter, $d = 0,43 \times 10^{-4}$ and $0,45 \times 10^{-4}$ m.

Filter Rating, $r = 1 \times 10^{-4}$ and $1,5 \times 10^{-4}$ m.

Initial Thickness, $t = 1,67 \times 10^{-3}$ and $1,62 \times 10^{-3}$ m.

SPECIMENS: Two cylinders, Al - 4,3 Cu - 1,5 Mg - 0,6 Mn. (Al 2024-T4).

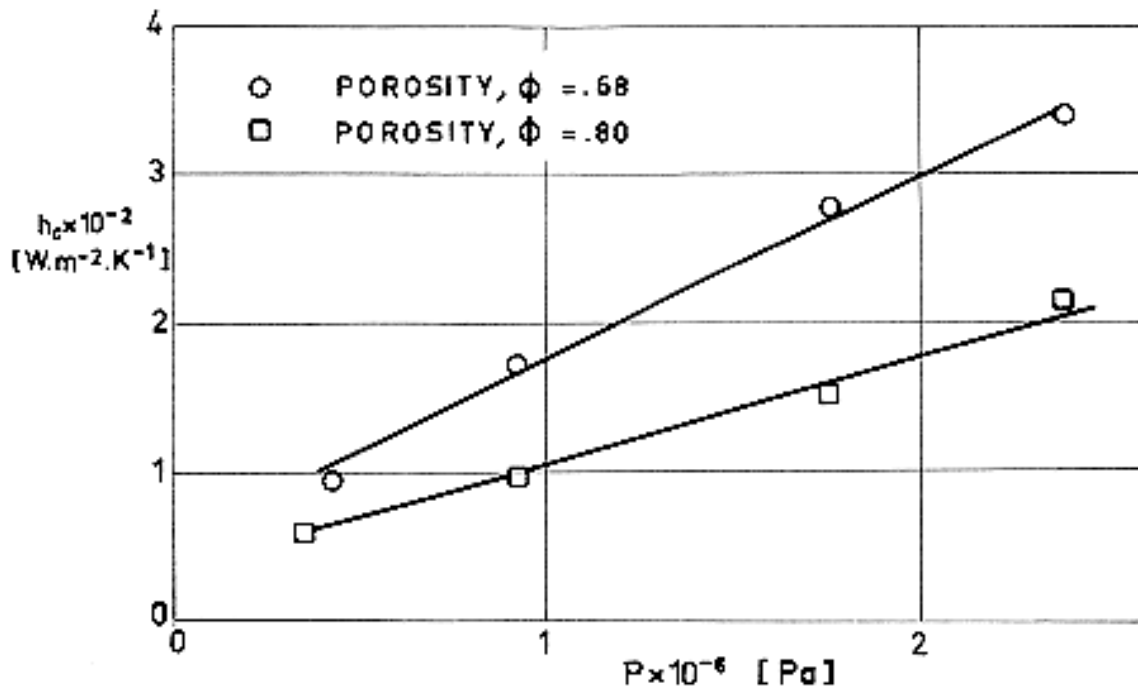
Radius, $b = 1,27 \times 10^{-2}$ m.

Flatness Deviation, $FD = +0,30 \times 10^{-4}$ and $+0,33 \times 10^{-4}$ m.

Roughness Deviation, $RD = 0,30 \times 10^{-6}$ and $0,07 \times 10^{-6}$ m.

Mean Temperature, $T_m = 341$ K.

Ambient Pressure, $p = 1,33 \times 10^{-3}$ Pa.



Note: non-si units are used in this figure

Figure 5-76: Plot of contact conductance vs. contact pressure for different porosities. From Miller & Fletcher (1973) [32].

The filler is a structure of sintered metallic fibers. In this particular case it has been manufactured by Huyck Metals Co., USA.

Cost of the filler:

FILLER: Stainless Steel 149 $\times 10^{-6}$ m. Mesh Screen.

Density, $\rho = 8009 \text{ kg.m}^{-3}$

Initial Thickness, $t = 2,29 \times 10^{-3}$ m.

SPECIMENS: Two cylinders, Fe - 19 Cr - 10 Ni. (SS 304).

Radius, $b = 1,27 \times 10^{-6}$ m.

Flatness Deviation, $FD = +0,508 \times 10^{-6}$ to $+0,635 \times 10^{-6}$ m.

Roughness Deviation, $RD = 0,076 \times 10^{-6}$ to $0,152 \times 10^{-6}$ m.

Mean Temperature, $T_m = 236$ to 418 K.

Ambient Pressure, $p = 1,33 \times 10^{-3}$ Pa.

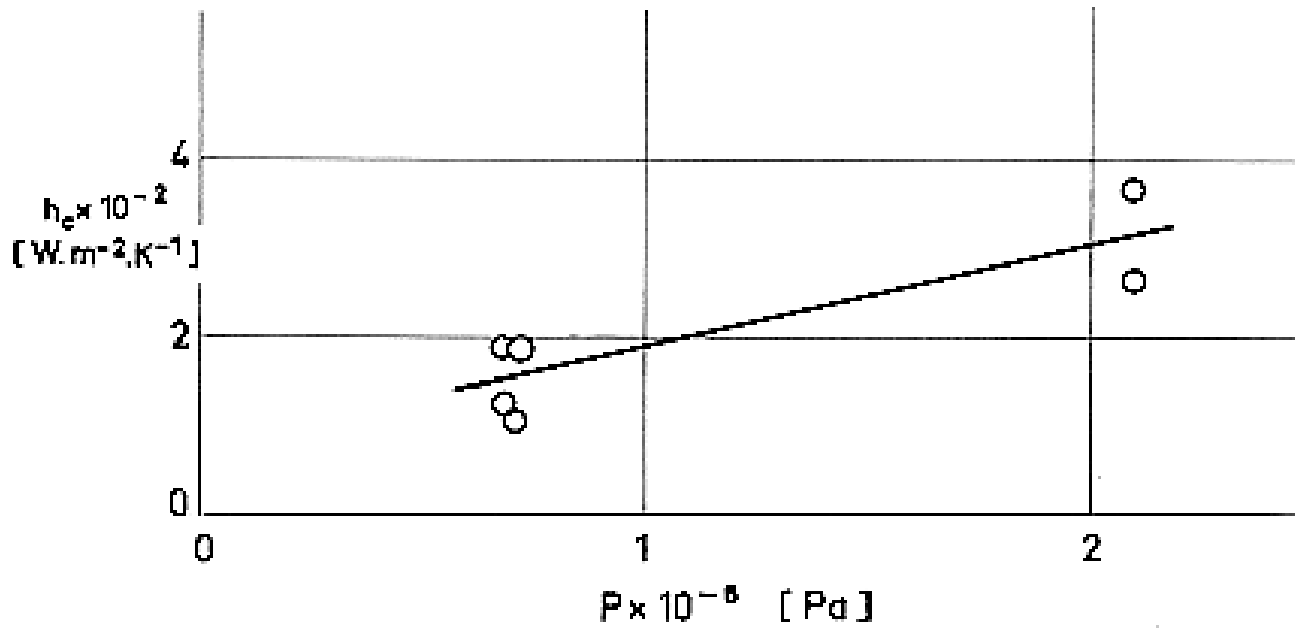


Figure 5-77: Plot of contact conductance vs. contact pressure. From Gyrog (1970) [26].

Cost of the filler: 20 US \$.m⁻²

FILLER: Stainless Steel 2x10⁻³ m. Mesh Screen.

Density, $\rho = 8009 \text{ kg} \cdot \text{m}^{-3}$

Initial Thickness, $t = 1,27 \times 10^{-3} \text{ m}$.

SPECIMENS: Two cylinders, Fe - 19 Cr - 10 Ni. (SS 304).

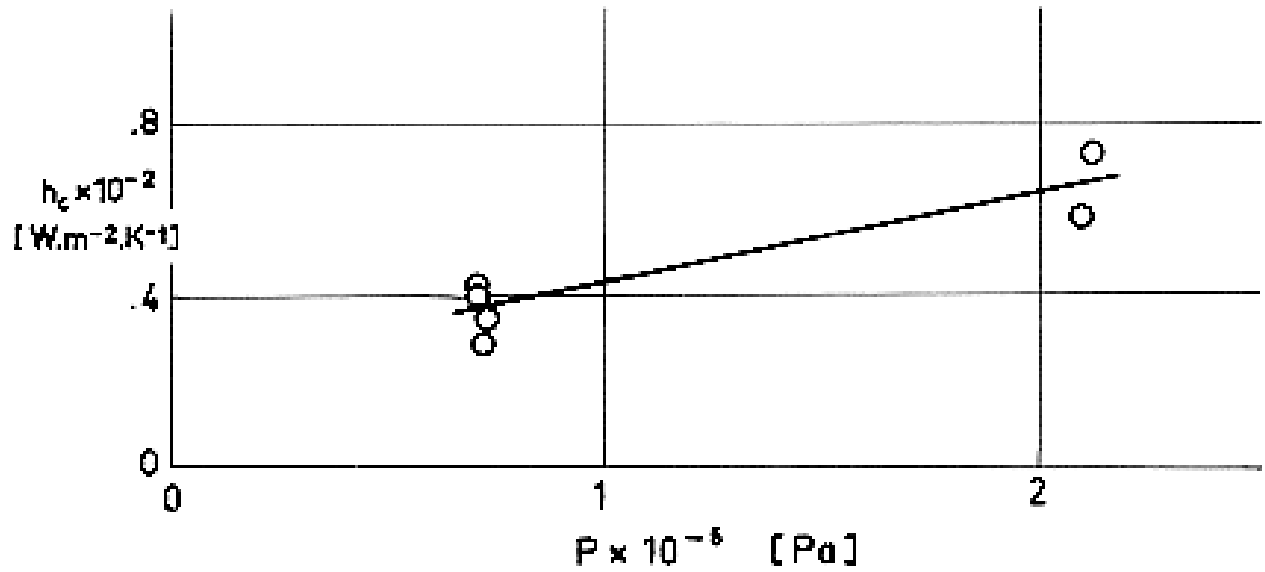
Radius, $b = 1,27 \times 10^{-2} \text{ m}$.

Flatness Deviation, $FD = +0,508 \times 10^{-6} \text{ to } +0,635 \times 10^{-6} \text{ m}$.

Roughness Deviation, $RD = 0,076 \times 10^{-6} \text{ to } 0,152 \times 10^{-6} \text{ m}$.

Mean Temperature, $T_m = 219 \text{ to } 385 \text{ K}$.

Ambient Pressure, $p = 1,33 \times 10^{-3} \text{ Pa}$.



Note: non-si units are used in this figure

Figure 5-78: Plot of contact conductance vs. contact pressure. From Gyrog (1970) [26].

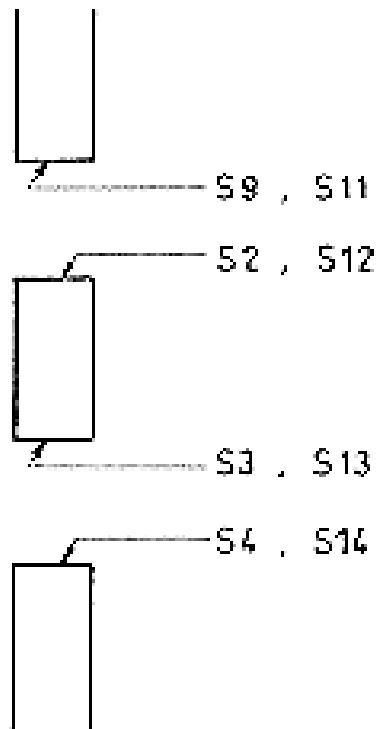
Cost of the filler: 11 US \$.m⁻²

FILLERS:

Material	Porosity %	Initial Thickness $\times 10^3$ [m]
Copper	80	0,660
Nickel	80	2,06
HCR	86	1,60
430 Stainless Steel	68	1,68
430 Stainless Steel	80	1,63
316L Stainless Steel	30	1,57
316L Stainless Steel	50	1,68
316L Stainless Steel	58	2,31

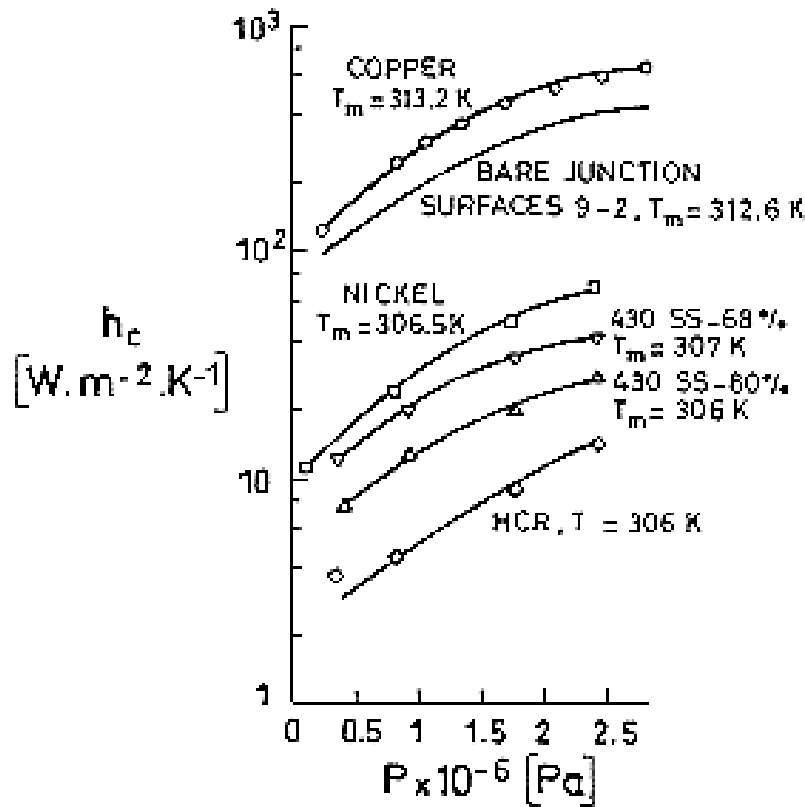
SPECIMENS: Three cylinders, Al 2024 - T4.

Diameter, $2,54 \times 10^{-2}$ m



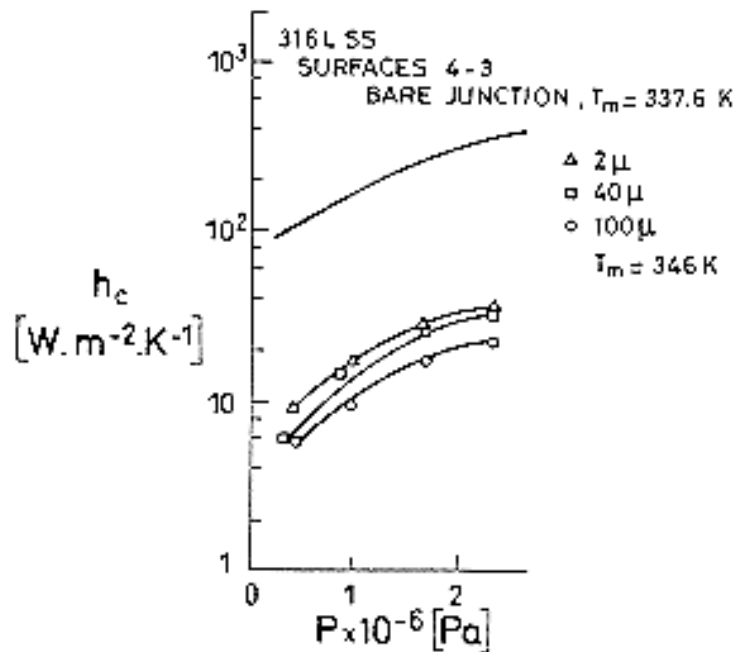
Surface	Flatness deviation $\times 10^6$ [m]	Roughness deviation $\times 10^6$ [m]
S9 ^a	19,05	0,127
S2 ^a	22,22	0,279
S3 ^a	30,48	0,305
S4 ^a	32,64	0,076
S11 ^b	0,508	0,406
S12 ^b	0,508	0,356
S13 ^b	0,508	0,330
S14 ^b	0,508	0,406

- a. Dome-shaped surface.
- b. Nominally flat surface.



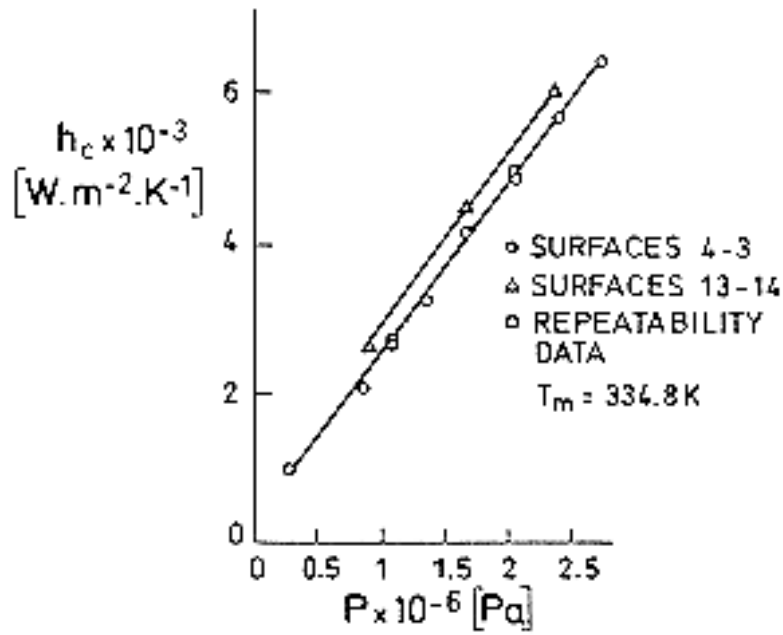
Note: non-si units are used in this figure

Figure 5-79: Comparison of thermal conductance of fiber metals with aluminium bare junction conductance, $T_m = 307$ K.



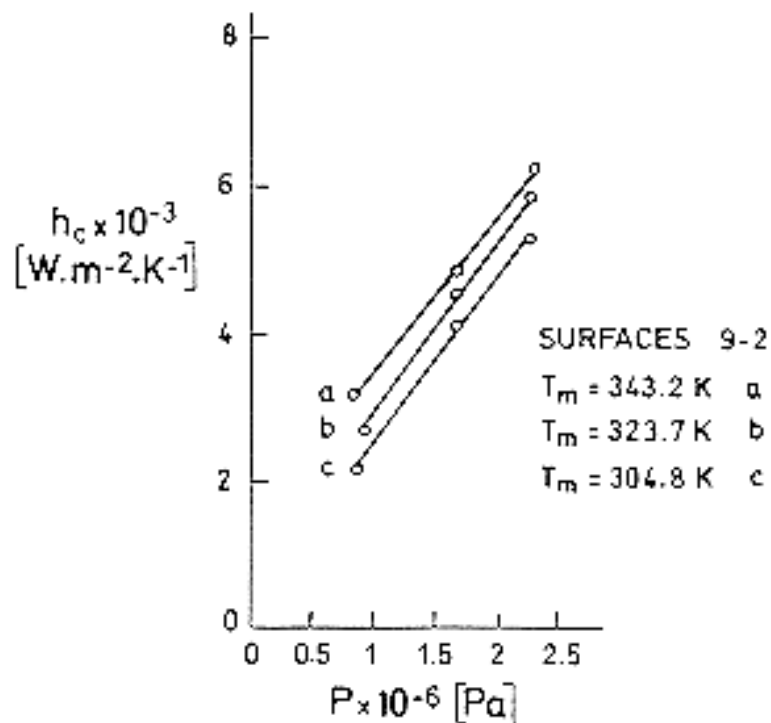
Note: non-si units are used in this figure

Figure 5-80: Comparison of thermal conductance of powder metals with aluminium bare junction conductance, $T_m = 342$ K.



Note: non-si units are used in this figure

Figure 5-81: Effect of surface finish on thermal conductance with a porous copper interstitial material.



Note: non-si units are used in this figure

Figure 5-82: Effect of mean junction temperature on thermal conductance with a porous copper interstitial material.

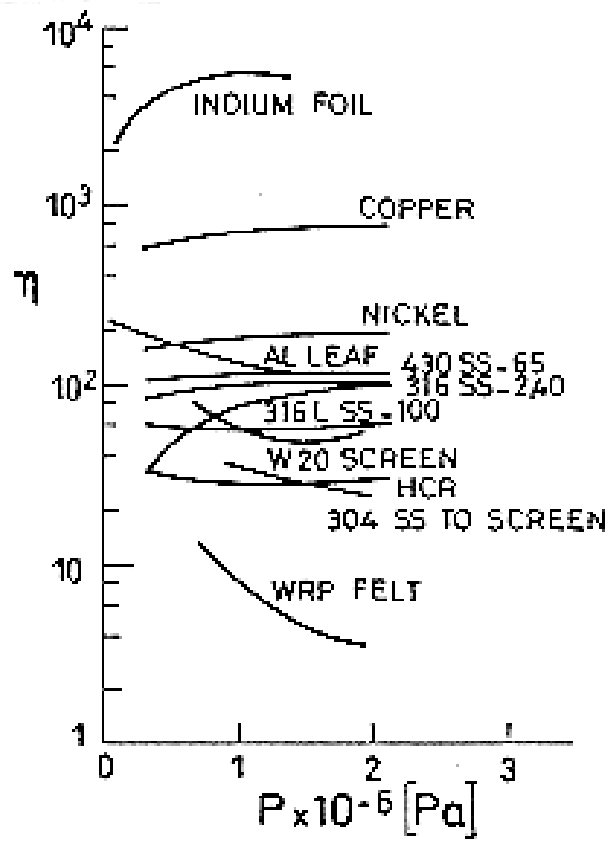
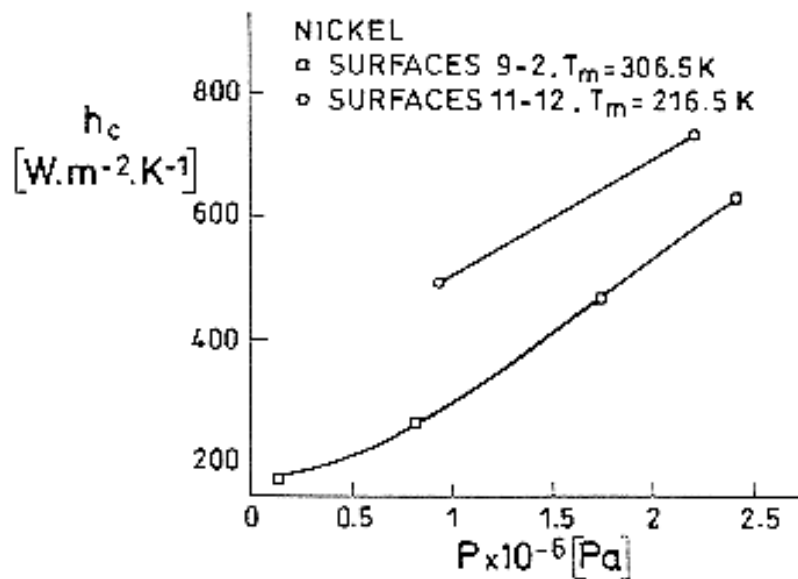
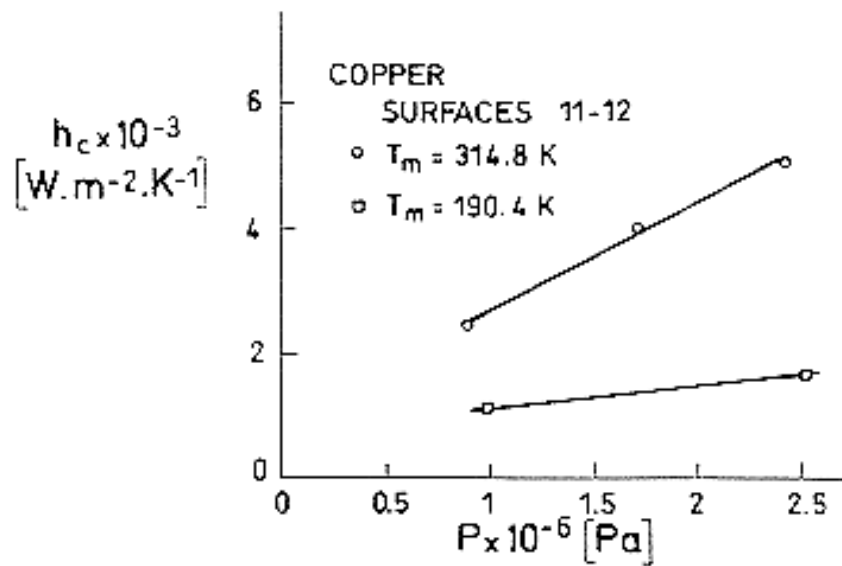


Figure 5-83: Dimensionless effectiveness parameter for porous metals and selected thermal control materials.



Note: non-si units are used in this figure

Figure 5-84: Effects of surface finish and temperature conductance with a porous nickel interstitial material.



Note: non-si units are used in this figure

Figure 5-85: Effects of mean junction temperature on thermal conductance with a porous copper interstitial material.

From Miller & Fletcher (1974) [33].

5.3.4 Insulating spacers between similar metals

FILLER: Asbestos Board

Density, $\rho = 2178 \text{ kg.m}^{-3}$

Initial Thickness, $t = 3,38 \times 10^{-3} \text{ m}$.

Appearance after thermal test: No apparent effect

SPECIMENS: Two cylinders, Al - 4,3 Cu - 1,5 Mg - 0,6 Mn. (Al 2024).

Radius, $b = 1,27 \times 10^{-2} \text{ m}$.

Flatness Deviation, $FD = +0,635 \times 10^{-6} \text{ m}$.

Roughness Deviation, $RD = 0,127 \times 10^{-6} \text{ m}$.

Mean Temperature, $T_m = 366 \text{ K}$.

Ambient Pressure, $p = 1,33 \times 10^{-3} \text{ to } 1,33 \times 10^{-4} \text{ Pa}$.

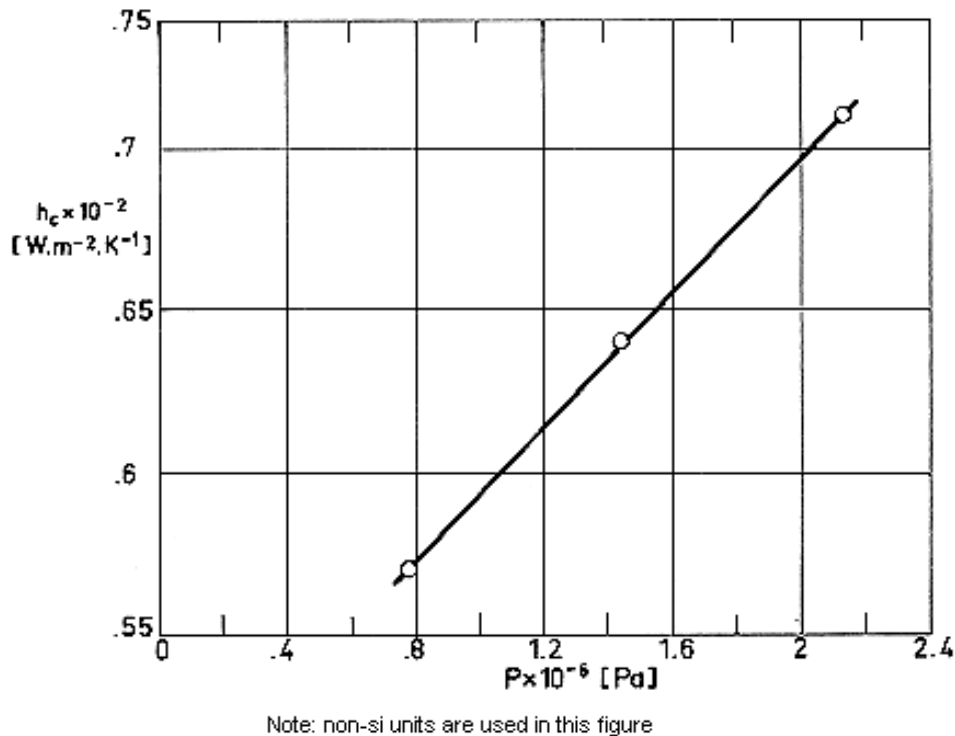


Figure 5-86: Plot of contact conductance vs. contact pressure. From Fletcher, Smuda & Gyrog (1969) [20].

Cost of the filler: 1 US \$.kg⁻¹, 7 US \$.kg⁻² (on basis of density).

FILLER: Asbestos Tape (No. 2074)

Density, $\rho = 880 \text{ kg} \cdot \text{m}^{-3}$

Initial Thickness, $t = 1,67 \times 10^{-3} \text{ m}$.

Appearance after thermal test: No apparent effect

SPECIMENS: Two cylinders, Al - 4,3 Cu - 1,5 Mg - 0,6 Mn. (Al 2024).

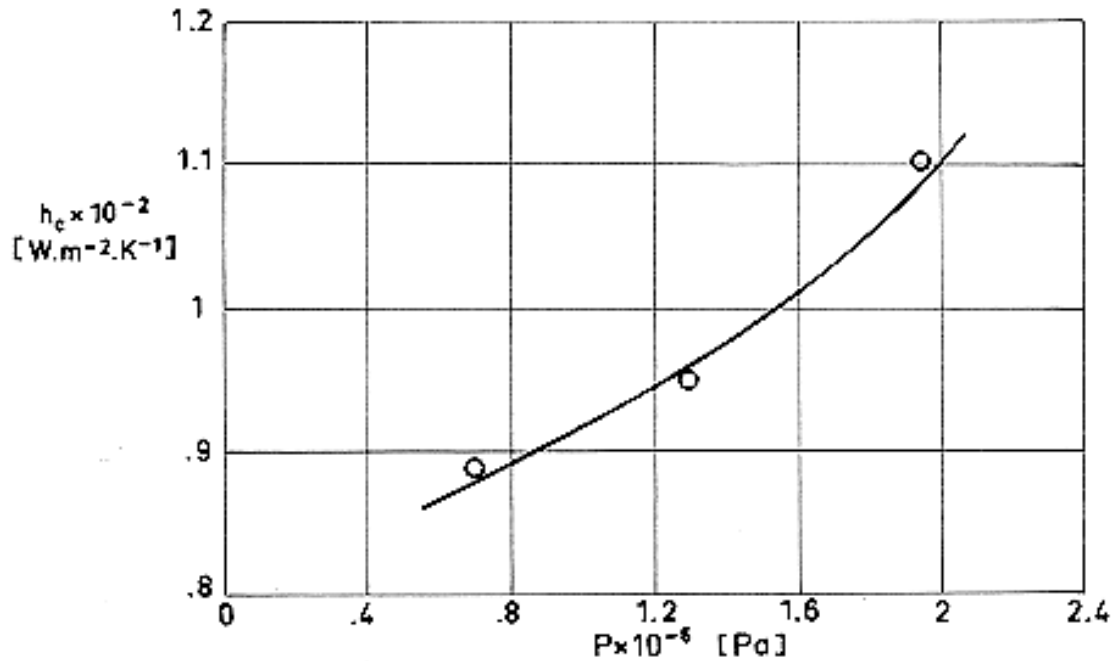
Radius, $b = 1,27 \times 10^{-2} \text{ m}$.

Flatness Deviation, $FD = +0,635 \times 10^{-6} \text{ m}$.

Roughness Deviation, $RD = 0,127 \times 10^{-6} \text{ m}$.

Mean Temperature, $T_m = 369 \text{ K}$.

Ambient Pressure, $p = 1,33 \times 10^{-3} \text{ to } 1,33 \times 10^{-4} \text{ Pa}$.



Note: non-si units are used in this figure

Figure 5-87: Plot of contact conductance vs. contact pressure. From Fletcher, Smuda & Gyrog (1969) [20].

Asbestos Tape (No. 2074 is produced by Atlas Asbestos Co. USA.

Cost of the filler: 1 US \$.kg⁻¹, 2 US \$.kg⁻² (on basis of density).

FILLER: Carbon Paper (F-907)

Density, $\rho = 144 \text{ kg.m}^{-3}$

Thickness, t , as given by the following compression test data:

$p \times 10^{-3}$ [Pa]	0	690	1380	2070
$t \times 10^{-3}$ [m]	1,19	0,43	0,33	0,25

Appearance after thermal test: Slightly compressed

SPECIMENS: Two cylinders, Al - 4,3 Cu - 1,5 Mg - 0,6 Mn. (Al 2024).

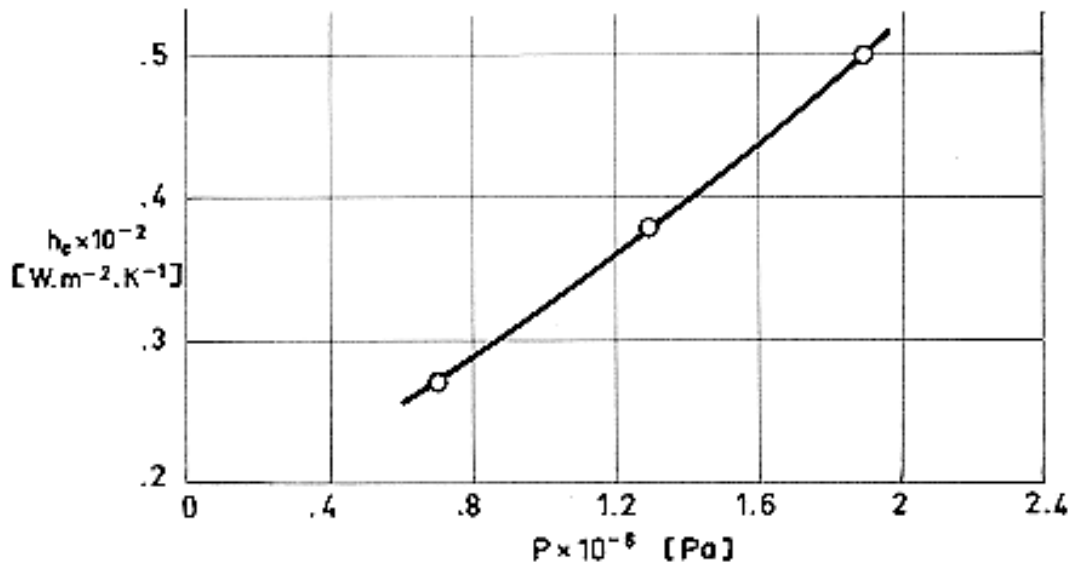
Radius, $b = 1,27 \times 10^{-2}$ m.

Flatness Deviation, $FD = +0,635 \times 10^{-6}$ m.

Roughness Deviation, $RD = 0,127 \times 10^{-6}$ m.

Mean Temperature, $T_m = 365$ K.

Ambient Pressure, $p = 1,33 \times 10^{-3}$ to $1,33 \times 10^{-4}$ Pa.



Note: non-si units are used in this figure

Figure 5-88: Plot of contact conductance vs. contact pressure. From Fletcher, Smuda & Gyrog (1969) [20].

Paper F-907 is a product of Fiberite Corp. USA.

Cost of the filler:

FILLER: Ceramic Paper (970-J)

Density, $\rho = 192 \text{ kg} \cdot \text{m}^{-3}$

Thickness, t , as given by the following compression test data:

$p \times 10^{-3}$ [Pa]	0	690	1380	2070
$t \times 10^{-3}$ [m]	2	0,86	0,71	0,64

Appearance after thermal test: Slightly deformed.

SPECIMENS: Two cylinders, Al - 4,3 Cu - 1,5 Mg - 0,6 Mn. (Al 2024).

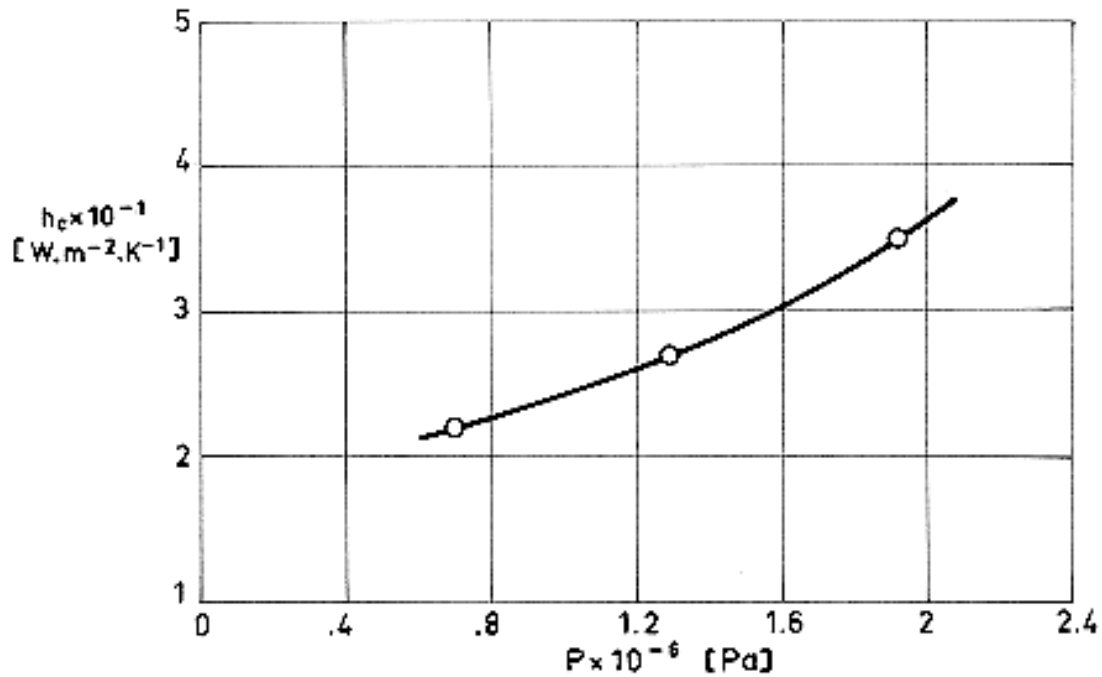
Radius, $b = 1,27 \times 10^{-2} \text{ m}$.

Flatness Deviation, $FD = +0,635 \times 10^{-6} \text{ m}$.

Roughness Deviation, $RD = 0,127 \times 10^{-6} \text{ m}$.

Mean Temperature, $T_m = 366 \text{ K}$.

Ambient Pressure, $p = 1,33 \times 10^{-3}$ to $1,33 \times 10^{-4} \text{ Pa}$.



Note: non-si units are used in this figure

Figure 5-89: Plot of contact conductance vs. contact pressure. From Fletcher, Smuda & Gyrog (1969) [20].

Paper 970 is made of Fiberfrax, which is a fiber composed mainly of Alumina and Silica. Fiberfrax is a Trade Name of Carborundum Co. USA.

Cost of the filler: 14 US \$.m⁻²

FILLER: Laminate T-30-LR

Density, $\rho = 801 \text{ kg.m}^{-3}$

Initial Thickness, $t = 3,33 \times 10^{-3} \text{ m}$.

Appearance after thermal test: No apparent effect

SPECIMENS: Two cylinders, Al - 4,3 Cu - 1,5 Mg - 0,6 Mn. (Al 2024).

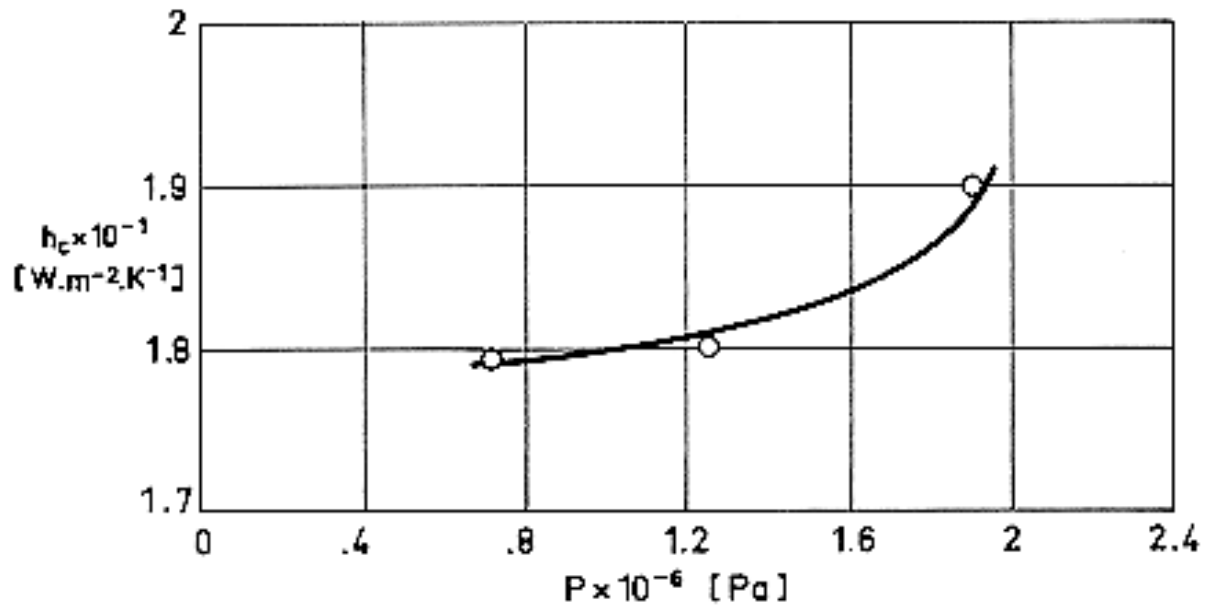
Radius, $b = 1,27 \times 10^{-2} \text{ m}$.

Flatness Deviation, $FD = +0,635 \times 10^{-6} \text{ m}$.

Roughness Deviation, $RD = 0,127 \times 10^{-6} \text{ m}$.

Mean Temperature, $T_m = 365 \text{ K}$.

Ambient Pressure, $p = 1,33 \times 10^{-3} \text{ to } 1,33 \times 10^{-4} \text{ Pa}$.



Note: non-si units are used in this figure

Figure 5-90: Plot of contact conductance vs. contact pressure. From Fletcher, Smuda & Gyrog (1969) [20].

T-30-LR is a laminate of impregnated Fiberfrax; which is a fiber composed mainly of Alumina and Silica. Fiberfrax is a Trade Name of Carborundum Co., USA.

Cost of the filler:

FILLER: Laminate T-30-LR

Density, $\rho = 801 \text{ kg} \cdot \text{m}^{-3}$

Initial Thickness, $t = 3,15 \times 10^{-3} \text{ m}$.

SPECIMENS: Two cylinders, Fe - 19 Cr - 10 Ni. (SS 304).

Radius, $b = 1,27 \times 10^{-2} \text{ m}$.

Flatness Deviation, $FD = +0,508 \times 10^{-6} \text{ to } +0,635 \times 10^{-6} \text{ m}$.

Roughness Deviation, $RD = 0,076 \times 10^{-6} \text{ to } 0,152 \times 10^{-6} \text{ m}$.

Ambient Pressure, $p = 1,33 \times 10^{-3} \text{ Pa}$.

Table 5-8: Values of contact conductance as a function of contact pressure and mean temperature.

$p \times 10^{-3}$ [Pa]	T_m [K]	h_c [$\text{W} \cdot \text{m}^{-2} \cdot \text{K}^{-1}$]
738	377	29
745	374	16
717	369	13
731	365	8
703	370	8
717	369	10

From Gyorog (1970) [26].

T-30-LR is a laminate of impregnated Fiberfrax; which is a fiber composed mainly of Alumina and Silica. Fiberfrax is a Trade Name of Carborundum Co., USA.

Cost of the filler:

FILLER: Mica (bonded)

Density, $\rho = 208 \text{ kg} \cdot \text{m}^{-3}$

Initial Thickness, $t = 0,5 \times 10^{-4} \text{ m}$.

Appearance after thermal test: Slightly deformed.

SPECIMENS: Two cylinders, Al - 4,3 Cu - 1,5 Mg - 0,6 Mn. (Al 2024).

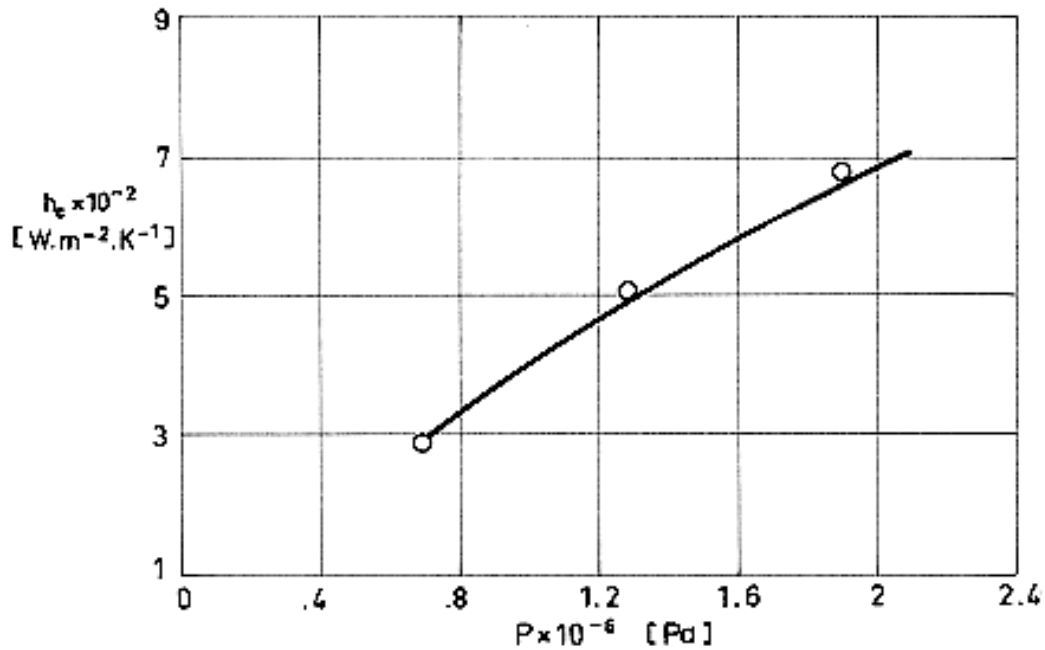
Radius, $b = 1,27 \times 10^{-2} \text{ m}$.

Flatness Deviation, $FD = +0,635 \times 10^{-6} \text{ m}$.

Roughness Deviation, $RD = 0,127 \times 10^{-6} \text{ m}$.

Mean Temperature, $T_m = 376 \text{ to } 385 \text{ K}$.

Ambient Pressure, $p = 1,33 \times 10^{-3} \text{ to } 1,33 \times 10^{-4} \text{ Pa}$.



Note: non-si units are used in this figure

Figure 5-91: Plot of contact conductance vs. contact pressure. From Fletcher, Smuda & Gyrog (1969) [20].

Cost of the filler: 2,5 US \$.kg⁻¹, 0,5 US \$.kg⁻² (on basis of density).

FILLER: Mica

Density, $\rho = 208 \text{ kg} \cdot \text{m}^{-3}$

Initial Thickness, $t = 0,7 \times 10^{-4} \text{ m}$.

Appearance after thermal test: Slightly deformed.

SPECIMENS: Two cylinders, Fe - 19 Cr - 10 Ni. (SS 304).

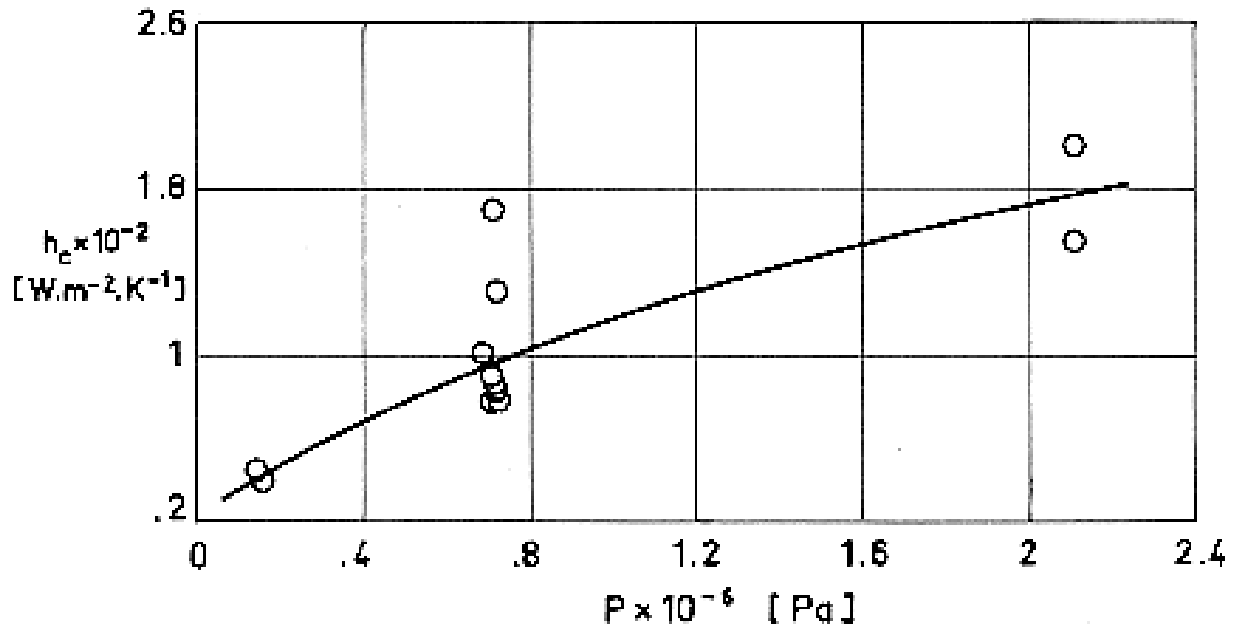
Radius, $b = 1,27 \times 10^{-2} \text{ m}$.

Flatness Deviation, $FD = +0,508 \times 10^{-6} \text{ to } +0,635 \times 10^{-6} \text{ m}$.

Roughness Deviation, $RD = 0,076 \times 10^{-6} \text{ to } 0,152 \times 10^{-6} \text{ m}$.

Mean Temperature, $T_m = 351 \text{ to } 401 \text{ K}$.

Ambient Pressure, $p = 1,33 \times 10^{-3} \text{ Pa}$.



Note: non-si units are used in this figure

Figure 5-92: Plot of contact conductance vs. contact pressure. From Gyrog (1970) [26].

Cost of the filler: 2,5 US \$.kg⁻¹, 0,5 US \$.kg⁻² (on basis of density).

FILLER: Pluton B-1 Cloth

Density, $\rho = 1394 \text{ kg} \cdot \text{m}^{-3}$

Initial Thickness, $t = 3,16 \times 10^{-3} \text{ m}$.

Appearance after thermal test: Slightly compressed.

SPECIMENS: Two cylinders, Al - 4,3 Cu - 1,5 Mg - 0,6 Mn. (Al 2024).

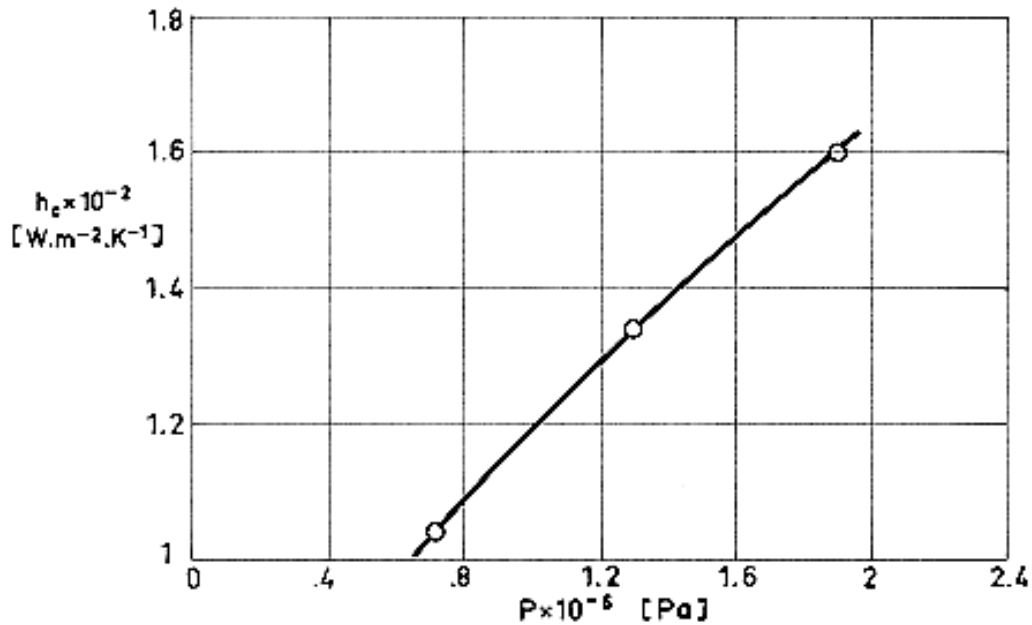
Radius, $b = 1,27 \times 10^{-2} \text{ m}$.

Flatness Deviation, $FD = +0,635 \times 10^{-6} \text{ m}$.

Roughness Deviation, $RD = 0,127 \times 10^{-6} \text{ m}$.

Mean Temperature, $T_m = 362 \text{ to } 364 \text{ K}$.

Ambient Pressure, $p = 1,33 \times 10^{-3} \text{ to } 1,33 \times 10^{-4} \text{ Pa}$.



Note: non-si units are used in this figure

Figure 5-93: Plot of contact conductance vs. contact pressure. From Fletcher, Smuda & Gyrog (1969) [20].

Cost of the filler:

FILLER: Pyroid

Density, $\rho = 2595 \text{ kg.m}^{-3}$

Initial Thickness, $t = 2,95 \times 10^{-3} \text{ m}$.

Appearance after thermal test: No apparent effect.

SPECIMENS: Two cylinders, Al - 4,3 Cu - 1,5 Mg - 0,6 Mn. (Al 2024).

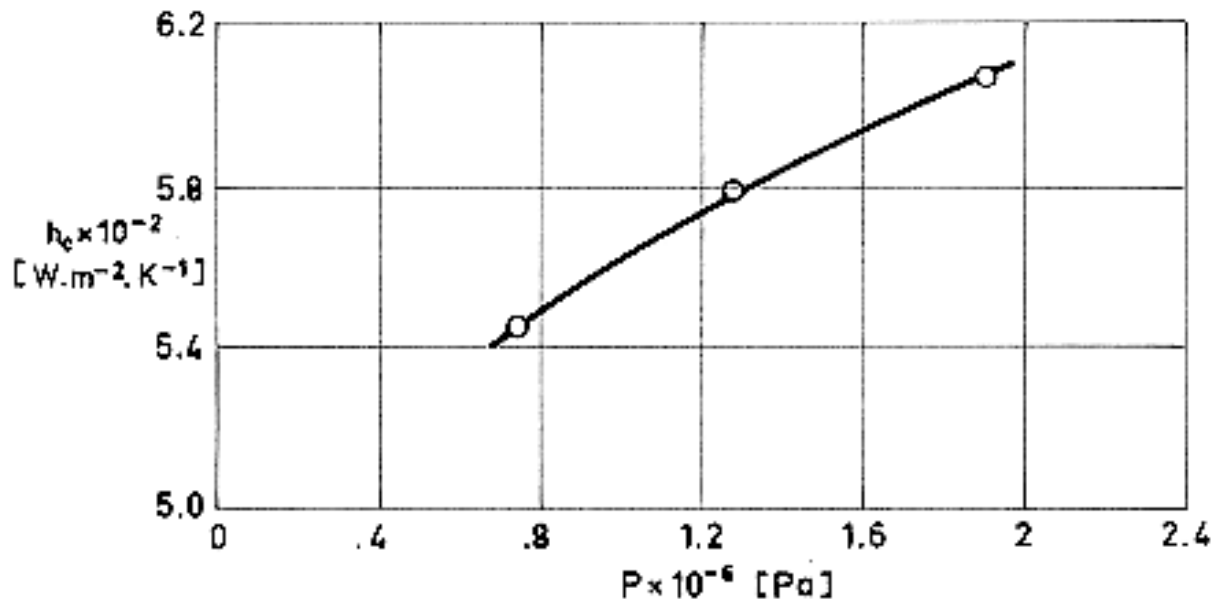
Radius, $b = 1,27 \times 10^{-2} \text{ m}$.

Flatness Deviation, $FD = +0,635 \times 10^{-6} \text{ m}$.

Roughness Deviation, $RD = 0,127 \times 10^{-6} \text{ m}$.

Mean Temperature, $T_m = 376 \text{ to } 378 \text{ K}$.

Ambient Pressure, $p = 1,33 \times 10^{-3} \text{ to } 1,33 \times 10^{-4} \text{ Pa}$.



Note: non-si units are used in this figure

Figure 5-94: Plot of contact conductance vs. contact pressure. From Fletcher, Smuda & Gyrog (1969) [20].

Cost of the filler:

FILLER: Pyrotex 23RPD

Density, $\rho = 1396 \text{ kg} \cdot \text{m}^{-3}$

Initial Thickness, $t = 2,84 \times 10^{-3} \text{ m}$.

SPECIMENS: Two cylinders, Fe - 19 Cr - 10 Ni. (SS 304).

Radius, $b = 1,27 \times 10^{-2} \text{ m}$.

Flatness Deviation, $FD = +0,508 \times 10^{-6} \text{ to } +0,635 \times 10^{-6} \text{ m}$.

Roughness Deviation, $RD = 0,076 \times 10^{-6} \text{ to } 0,152 \times 10^{-6} \text{ m}$.

Ambient Pressure, $p = 1,33 \times 10^{-3} \text{ Pa}$.

Table 5-9: Values of contact conductance as a function of contact pressure and mean temperature.

$p \times 10^{-3}$ [Pa]	T_m [K]	h_c [$W \cdot m^{-2} \cdot K^{-1}$]
648	393	69
2137	394	78

From Gyrog (1970) [26]

Pyrotex 23RPD is the Trade Name of an asbestos reinforced plastic from International Raybestos Manhattan Co., USA.

Cost of the filler:

FILLER: Silica paper

Density, $\rho = 160 \text{ kg.m}^{-3}$

Thickness, t , as given by the following compression test data:

$p \times 10^{-3}$ [Pa]	0	690	1380	2070
$t \times 10^{-3}$ [m]	1,24	0,43	0,30	0,27

Appearance after thermal test: Discoloring, considerably compressed.

SPECIMENS: Two cylinders, Al - 4,3 Cu - 1,5 Mg - 0,6 Mn. (Al 2024).

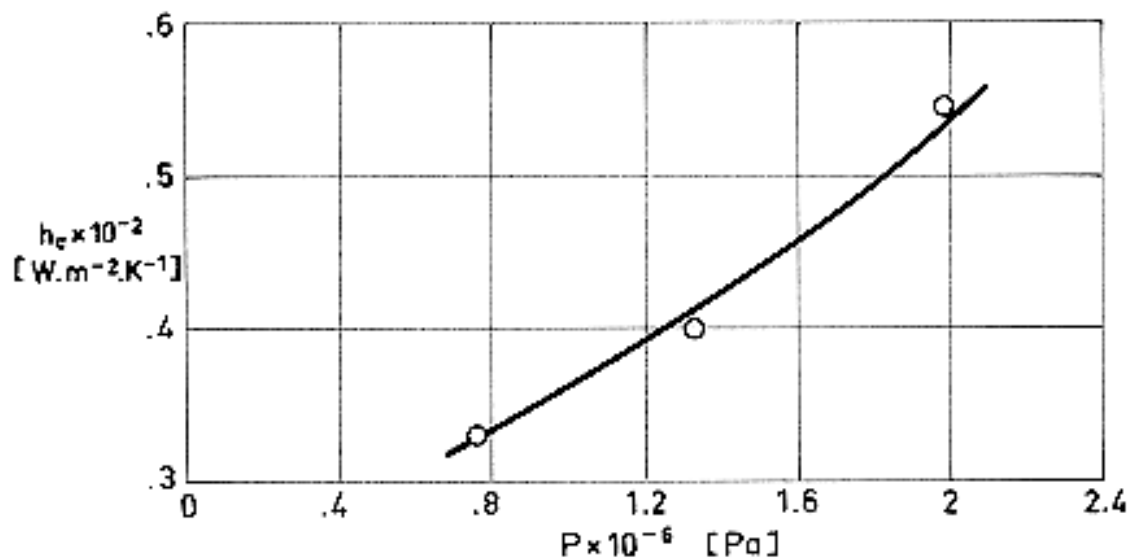
Radius, $b = 1,27 \times 10^{-2} \text{ m}$.

Flatness Deviation, $FD = +0,635 \times 10^{-6} \text{ m}$.

Roughness Deviation, $RD = 0,127 \times 10^{-6} \text{ m}$.

Mean Temperature, $T_m = 366 \text{ K}$.

Ambient Pressure, $p = 1,33 \times 10^{-3}$ to $1,33 \times 10^{-4} \text{ Pa}$.



Note: non-si units are used in this figure

Figure 5-95: Plot of contact conductance vs. contact pressure. From Fletcher, Smuda & Gyrog (1969) [20].

Silica paper is a product of Fiberite Corp., USA.

Cost of the filler:

FILLER: Teflon (TFE) Sheet

Density, $\rho = 160 \text{ kg.m}^{-3}$

Initial Thickness, $t = 0,5 \times 10^{-4} \text{ m}$.

Appearance after thermal test: No apparent effect.

SPECIMENS: Two cylinders, Al - 4,3 Cu - 1,5 Mg - 0,6 Mn. (Al 2024).

Radius, $b = 1,27 \times 10^{-2}$ m.

Flatness Deviation, $FD = +0,635 \times 10^{-6}$ m.

Roughness Deviation, $RD = 0,127 \times 10^{-6}$ m.

Mean Temperature, $T_m = 398$ to 401 K.

Ambient Pressure, $p = 1,33 \times 10^{-3}$ to $1,33 \times 10^{-4}$ Pa.

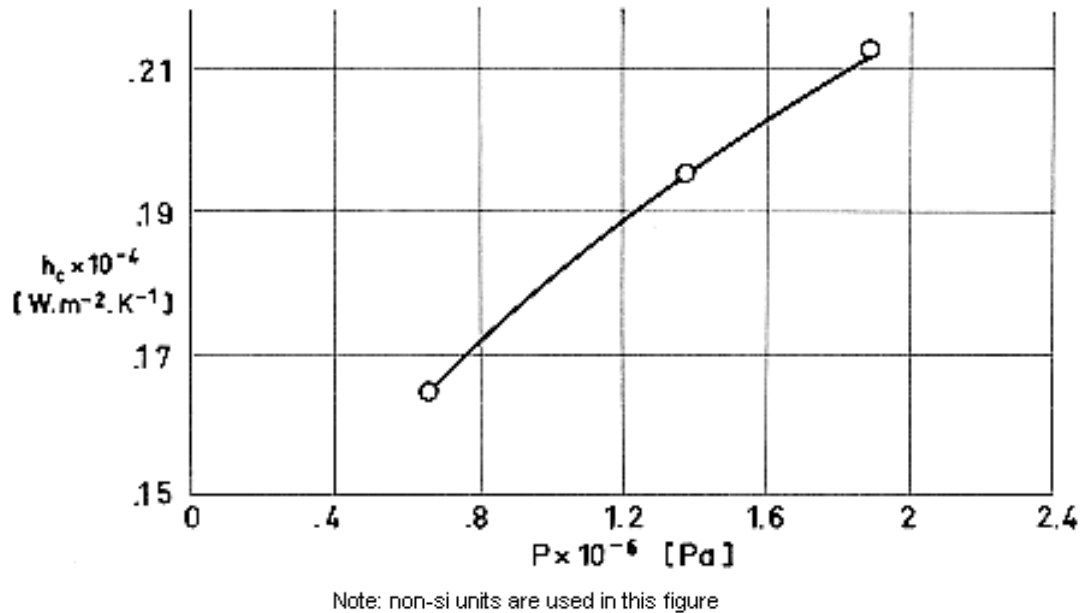


Figure 5-96: Plot of contact conductance vs. contact pressure. From Fletcher, Smuda & Gyrog (1969) [20].

Teflon polytetrafluoroethylene (TFE) is a Trade Name of E.I. DuPont de Nemours Co., Inc. USA.

Cost of the filler: 20 US \$.kg⁻¹, 0,16 US \$.kg⁻² (on basis of density).

FILLER: Teflon (TFE) Sheet

Density, $\rho = 160$ kg.m⁻³

Initial Thickness, $t = 3,07 \times 10^{-3}$ m.

SPECIMENS: Two cylinders, Fe - 19 Cr - 10 Ni. (SS 304).

Radius, $b = 1,27 \times 10^{-2}$ m.

Flatness Deviation, $FD = +0,508 \times 10^{-6}$ to $+0,635 \times 10^{-6}$ m.

Roughness Deviation, $RD = 0,076 \times 10^{-6}$ to $0,152 \times 10^{-6}$ m.

Ambient Pressure, $p = 1,33 \times 10^{-3}$ Pa.

Table 5-10: Values of contact conductance as a function of contact pressure and mean temperature.

$p \times 10^{-3}$ [Pa]	T_m [K]	h_c [$W \cdot m^{-2} \cdot K^{-1}$]
731	414	162
717	390	163
2110	392	170

From Gyrog (1970) [26].

Teflon polytetrafluoroethylene (TFE) is a Trade Name of E.I. DuPont de Nemours Co., Inc. USA.

Cost of the filler: 20 US \$. kg^{-1} , 9,6 US \$. kg^{-2} (on basis of density).

FILLER: Textolite

Initial Thickness, $t = 1,57 \times 10^{-3}$ m.

SPECIMENS: Two cylinders, Fe - 19 Cr - 10 Ni. (SS 304).

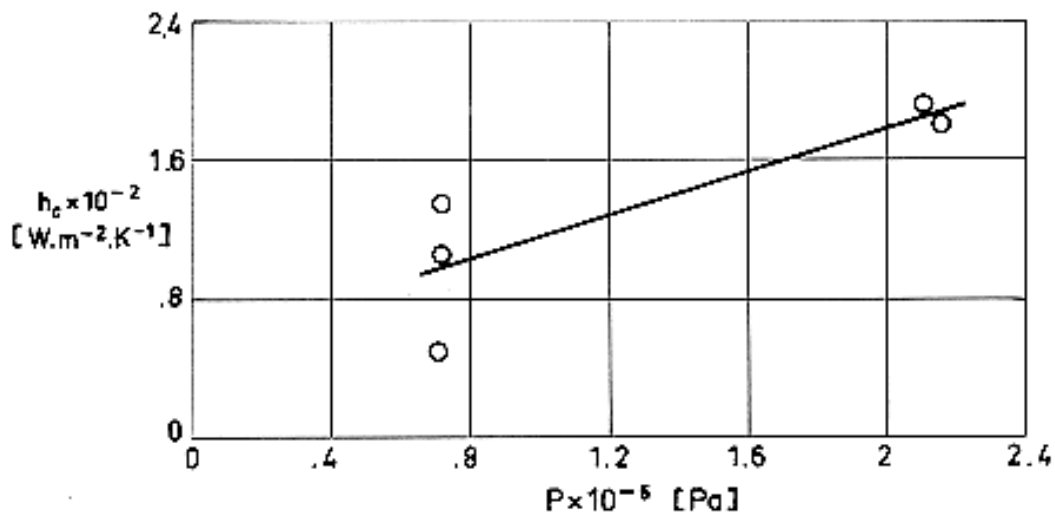
Radius, $b = 1,27 \times 10^{-2}$ m.

Flatness Deviation, $FD = +0,508 \times 10^{-6}$ to $+0,635 \times 10^{-6}$ m.

Roughness Deviation, $RD = 0,076 \times 10^{-6}$ to $0,152 \times 10^{-6}$ m.

Mean Temperature, $T_m = 386$ to 393 K.

Ambient Pressure, $p = 1,33 \times 10^{-3}$ Pa.



Note: non-si units are used in this figure

Figure 5-97: Plot of contact conductance vs. contact pressure. From Gyrog (1970) [26].

Textolite, Trade Name of General Electric Co. USA, is a phenol formaldehyde laminated compound.

Cost of the filler:

FILLER: WRP-X-AQ Felt

Density, $\rho = 288 \text{ kg.m}^{-3}$

Thickness, t , as given by the following compression test data

$p \times 10^{-3}$ [Pa]	0	690	1380	2070
$t \times 10^{-3}$ [m]	4,47	2,33	1,93	1,72

Appearance after thermal test: Slightly compressed

SPECIMENS: Two cylinders, Al - 4,3 Cu - 1,5 Mg - 0,6 Mn. (Al 2024).

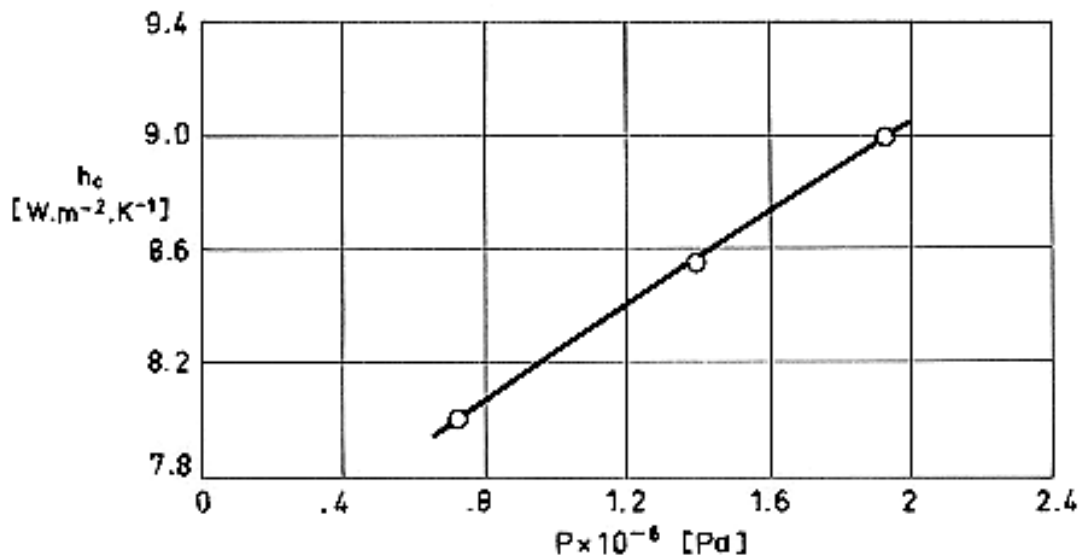
Radius, $b = 1,27 \times 10^{-2}$ m.

Flatness Deviation, $FD = +0,635 \times 10^{-6}$ m.

Roughness Deviation, $RD = 0,127 \times 10^{-6}$ m.

Mean Temperature, $T_m = 357$ K.

Ambient Pressure, $p = 1,33 \times 10^{-3}$ to $1,33 \times 10^{-4}$ Pa.



Note: non-si units are used in this figure

Figure 5-98: Plot of contact conductance vs. contact pressure. From Fletcher, Smuda & Gyrog (1969) [20].

Cost of the filler:

5.3.5 Fluids between metals

5.3.5.1 Similar metals

FILLER: DC-340 Grease

Density, $\rho = 2300 \text{ kg.m}^{-3}$

SPECIMENS: Two cylinders as indicated below.

Radius, $b = 1,27 \times 10^{-2} \text{ m}$.

Ambient Pressure, $p = 1,33 \times 10^{-3} \text{ Pa}$.

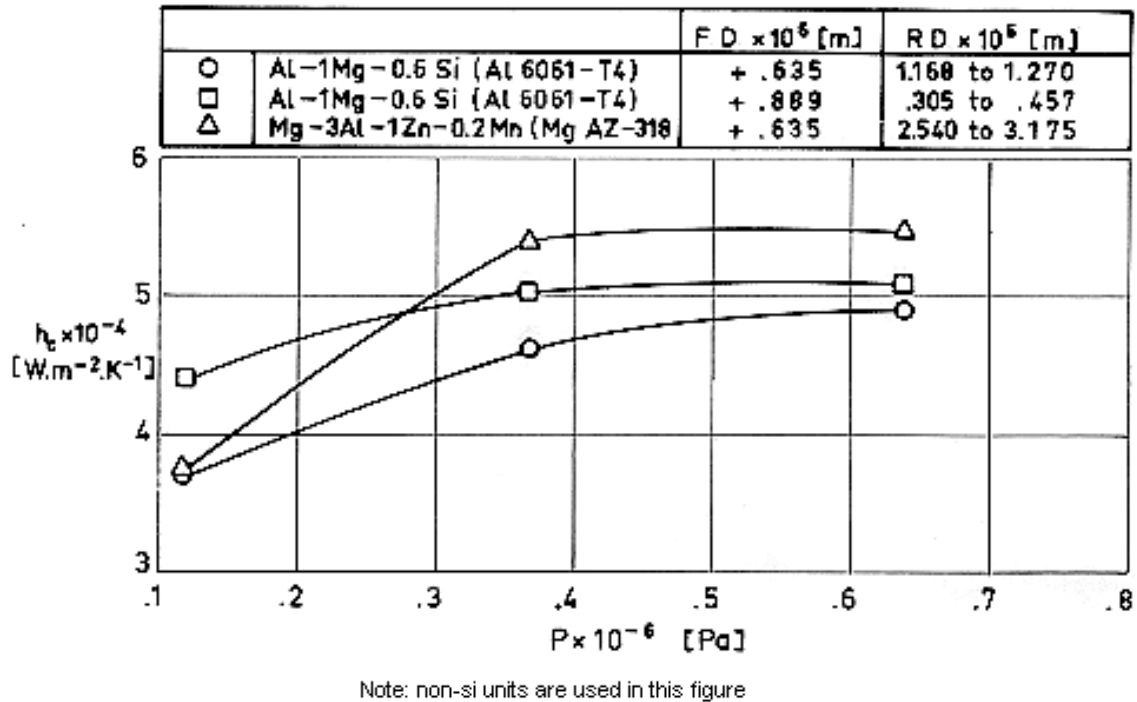


Figure 5-99: Plot of contact conductance vs. contact pressure. From Cunnington (1964) [9].

DC-340 is a silicone heat transfer compound, heavily filled with metal oxides. It is produced by Dow-Corning. USA.

Cost of the filler: 10 US \$.kg⁻¹

FILLER: Silicone Vacuum Grease

Density, $\rho = 1000 \text{ kg.m}^{-3}$

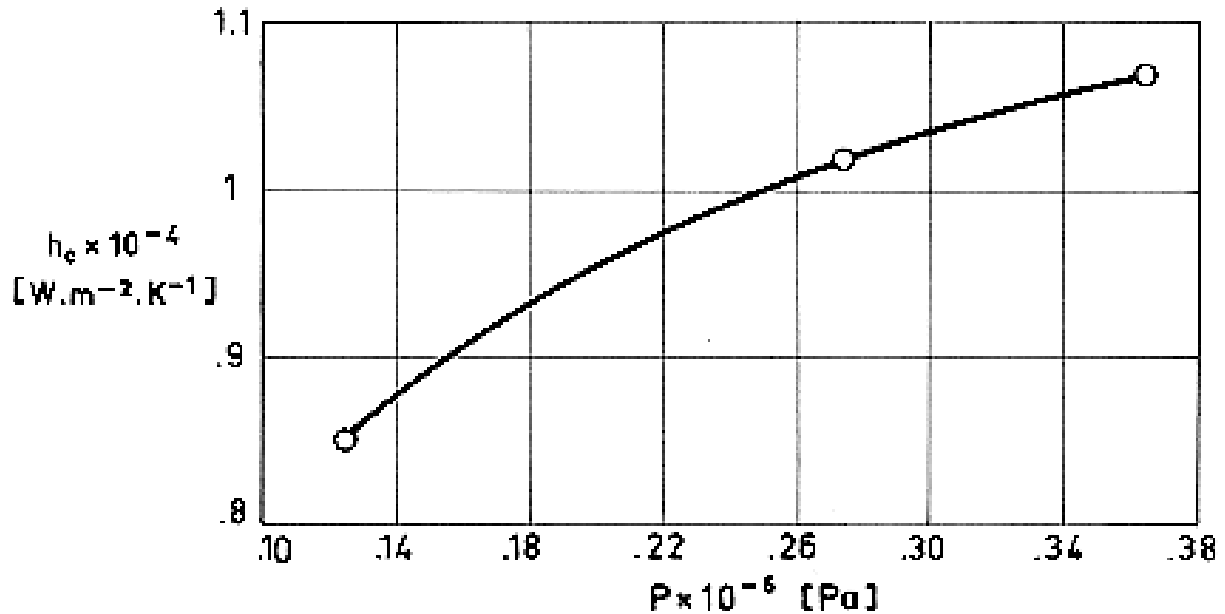
SPECIMENS: Two cylinders, Mg - 3 Al - 1 Zn - 0,2 Mn. (Mg AZ-31B).

Radius, $b = 1,27 \times 10^{-2} \text{ m}$.

Flatness Deviation, $FD = +0,635 \times 10^{-6} \text{ m}$.

Roughness Deviation, $RD = 2,54 \text{ to } 3,175 \times 10^{-6} \text{ m}$.

Ambient Pressure, $p = 1,33 \times 10^{-3} \text{ Pa}$.



Note: non-si units are used in this figure

Figure 5-100: Plot of contact conductance vs. contact pressure. From Cunnington (1964) [9].

The filler is a stiff, non-melting, silicone material that maintains its consistence over a temperature range 233 to 533 K. It is produced by Dow-Corning, USA.

Cost of the filler: 25 US \$.kg⁻¹

FILLER: Alloy consisting of an eutectic compositium of bismuth, lead, tin, indium and cadmium (320 K melting point alloy).

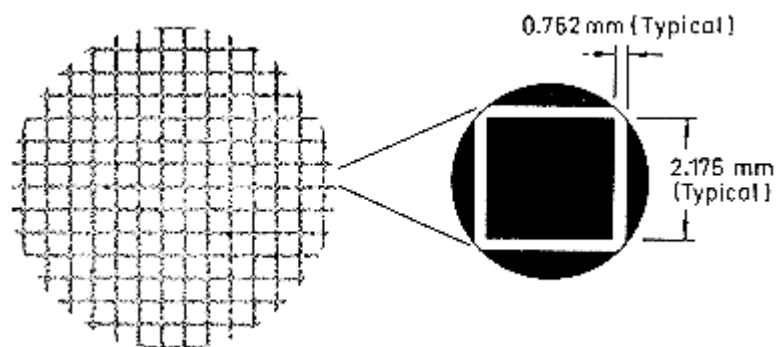
SPECIMENS: Two disks, Al 6061 - T6.

Diameter, $7,62 \times 10^{-2}$ m

Roughness, $3 - 3,8 \times 10^{-6}$ m (RMS); $1,5 - 2 \times 10^{-6}$ m (RMS) ; $0,25 - 0,38 \times 10^{-6}$ m (RMS)

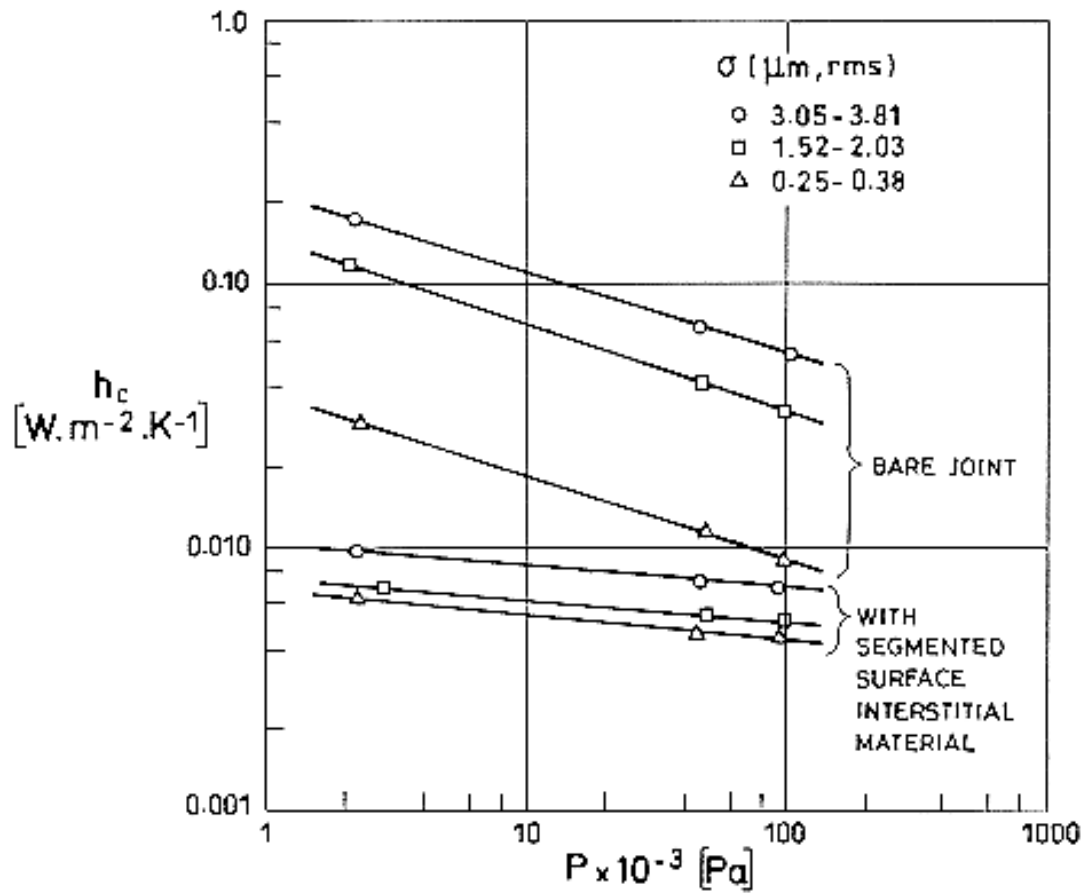
Flatness, $\pm 0,5 \times 10^{-6}$ m

Thickness, 10^{-3} m



Note: non-si units are used in this figure

Figure 5-101: Photograph of segmented surface test specimen.



Note: non-si units are used in this figure

Figure 5-102: Thermal contact resistance values for Al 6061-T6 with and without segmented surface interstitial material (one atmosphere).

From Cook, Token & Calkins (1982) [8].

5.3.5.2 Dissimilar metals

JOINT: Compound cylinders

FILLER: Air.

SPECIMENS: Inner cylinder (A): 2011 - T351 Alclad

Outer cylinder (B): 304 Stainless steel

	A	B
I.D. x 10 ³ [m]	22,23	59,16
O.D. x 10 ³ [m]	59,16 - 59,19	72,52
$\sigma \times 10^6$ [m]	3,05 - 4,83 ^a	1,27 - 1,65 ^a
	0,762 - 0,940 ^b	1,27 - 1,65 ^b
m^c	0,096 - 0,12 ^a	0,08 ^a
	0,03 ^b	0,08 ^b

a. Sample set 1 and 2

b. Sample set 3 and 4

c. effective absolute surface slope

Sample set characteristics

	$\sigma_A \times 10^6$ [m]	m	$\sigma_B \times 10^6$ [m]	m
SS1	3,048	0,096	1,270	0,08
SS2	4,826	0,12	1,650	0,08
SS3	0,762	0,03	1,270	0,08
SS4	0,940	0,03	1,650	0,08

NOTE Sample set 1 (SS1): test 1 data with minimum roughness of specimens.

Sample set 2 (SS2): test 1 data with maximum roughness of specimens.

Sample set 3 (SS3): test 2 data with minimum roughness of specimens.

Sample set 4 (SS4): test 2 data with maximum roughness of specimens.

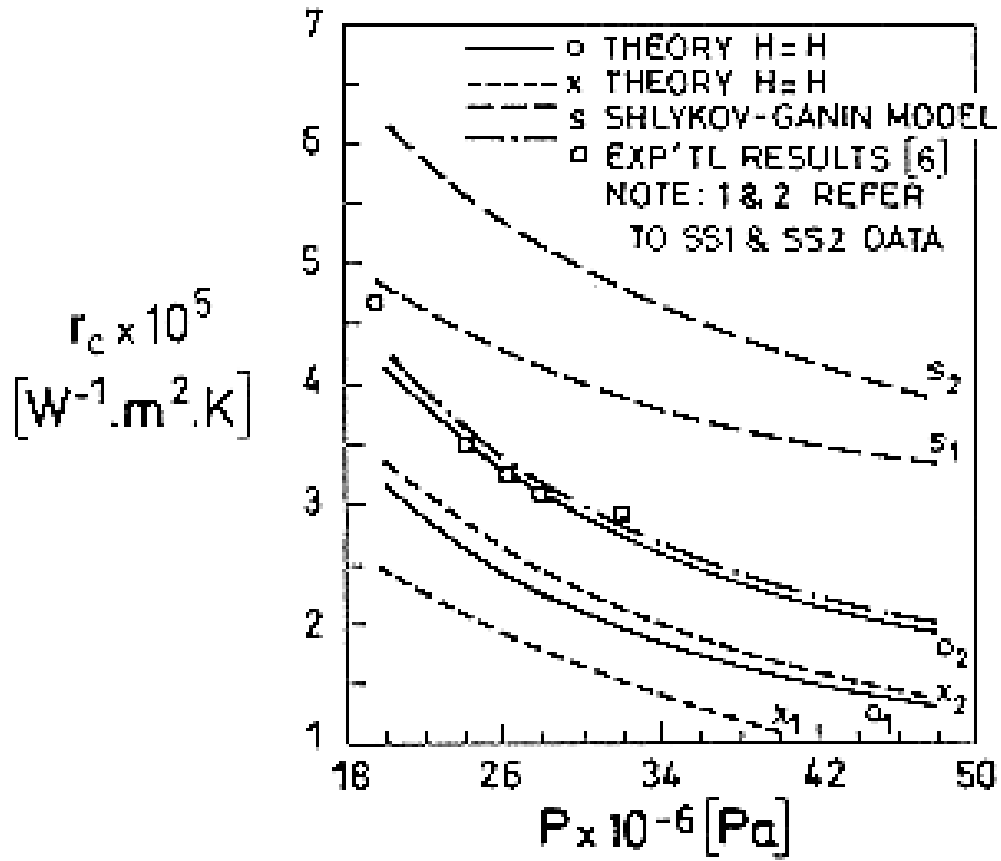


Figure 5-103: Comparison between models and experimental results for SS1 and SS2.

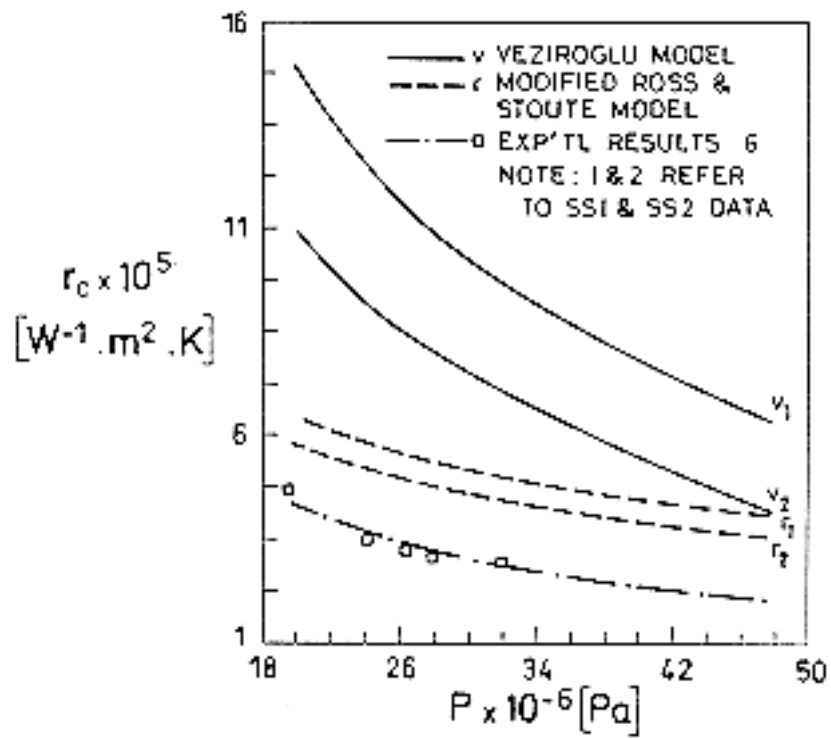


Figure 5-104: Comparison between models and experimental results for SS1 and SS2.

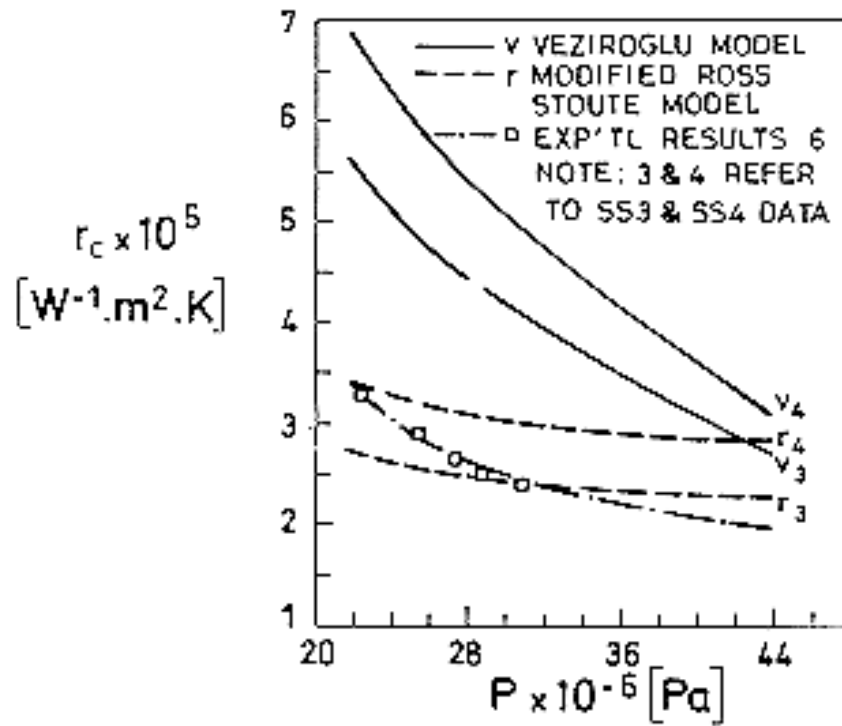


Figure 5-105: Comparison between models and experimental results for SS3 and SS4.

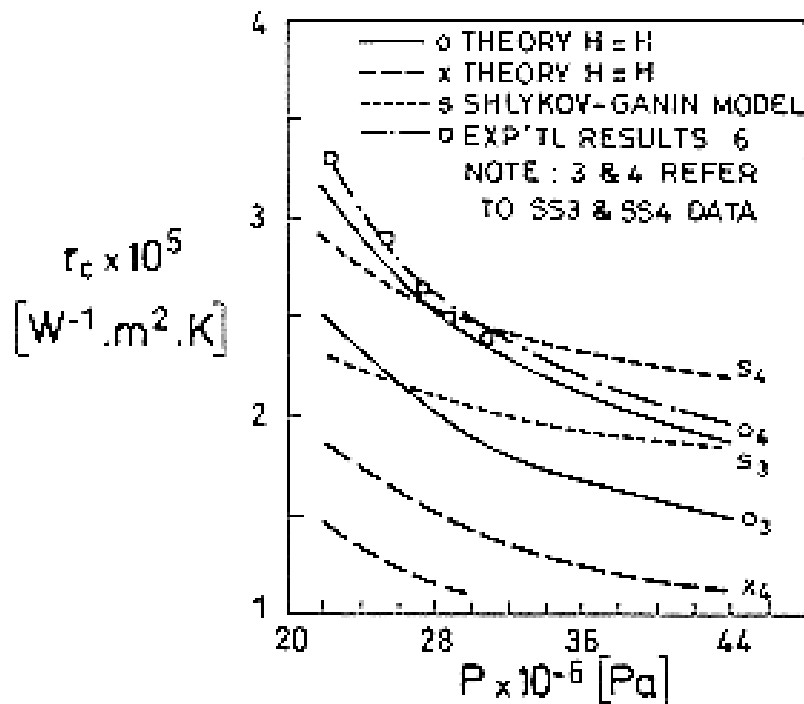
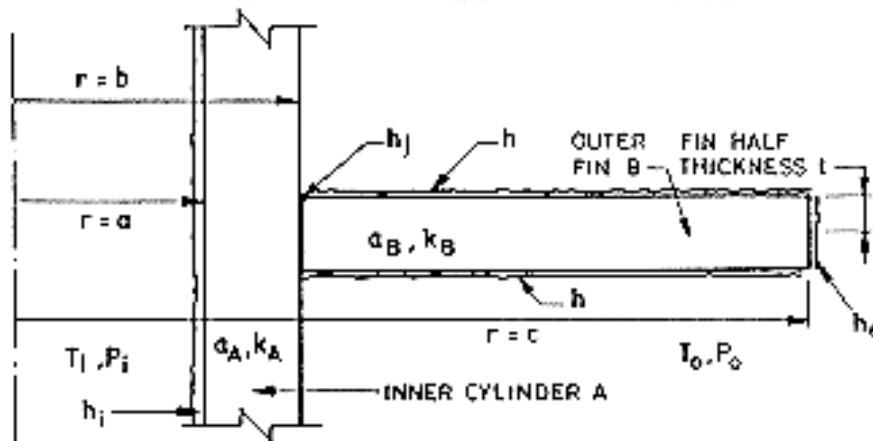


Figure 5-106: Comparison between models and experimental results for SS3 and SS4.

From Lemczyk & Yovanovich (1987) [30] and Hsu & Tam (1979) [30].

JOINT: Tube/Fin system



$$a = 4.458 \times 10^{-3} \text{ m}$$

$$b = 4.763 \times 10^{-3} \text{ m}$$

$$c = 1.905 \times 10^{-2} \text{ m}$$

$$t = 7.62 \times 10^{-5} \text{ m}$$

Note: non-si units are used in this figure

$$a = 4,458 \times 10^{-3} \text{ m}$$

$$b = 4,763 \times 10^{-3} \text{ m}$$

$$c = 1,905 \times 10^{-2} \text{ m}$$

$$t = 7,62 \times 10^{-5} \text{ m}$$

FILLER: Air

SPECIMENS: Copper tube (A) and Aluminium fin (B)

	A	B
k [W.m ⁻¹ .K ⁻¹]	380	154,9
h [W.m ⁻² .K ⁻¹]	100	100
Bi		$4,92 \times 10^{-5}$

THEORETICAL ANALYSIS

(A) Cylinder:

$$\log \frac{h_c A}{\sigma k m} = C \log \frac{PA}{\sigma^2 M} + D \quad [5-4]$$

 Solution $T_A(r) = C_1 + C_2 \ln r$

(B) One-dimensional fin:

$$\nabla^2 T_A = 0 \quad , \quad (T_A = T_A(r)) \quad [5-5]$$

Solution

$$\frac{1}{r} \frac{d}{dr} \left[r \frac{d\theta}{dr} \right] - \frac{h}{kt} \theta = 0 \quad , \quad \theta = T_B(r) - T_o \quad [5-6]$$

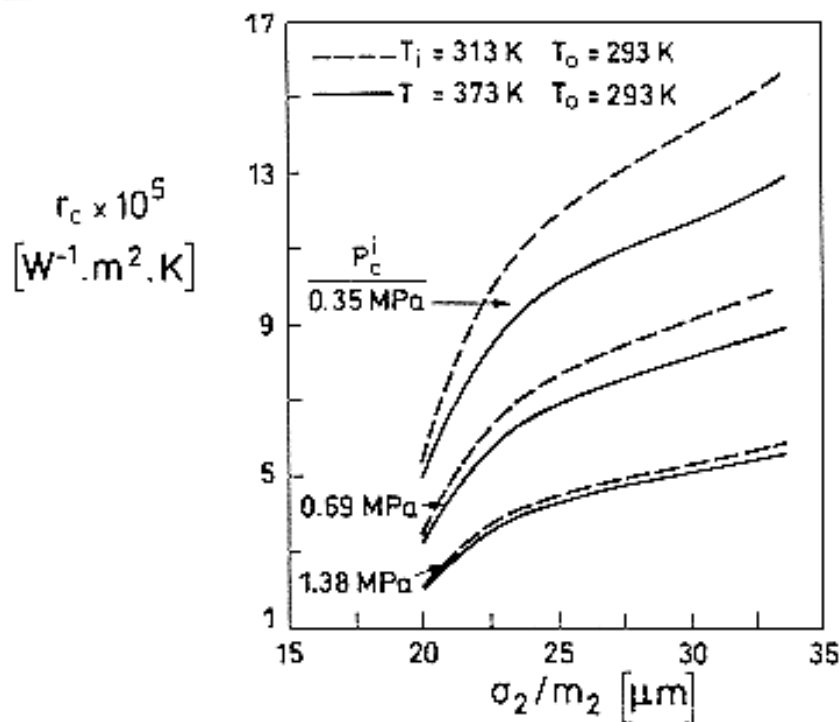
Boundary conditions:

$$T_B(r) = T_o + C_3 I_o \left(\sqrt{Bi} \frac{r}{t} \right) + C_4 K_o \left(\sqrt{Bi} \frac{r}{t} \right) \quad [5-7]$$

$$r = a \quad , \quad h_i (T_A - T_i) = k_A \frac{dT_A}{dr} \quad (\text{with convection}) \quad [5-8]$$

$$r = b \quad , \quad k_A \frac{dT_A}{dr} = h_j [T_B - T_A] \quad [5-9]$$

$$r = b \quad , \quad k_A \frac{dT_A}{dr} = k_B \frac{dT_B}{dr} \quad [5-10]$$



Note: non-si units are used in this figure

Figure 5-107: Effect of variation of initial contact pressure on joint resistance for the edge tube/fin system. $h_o = 0, h_e = 0, P_i = 0, P_o = 0, T_i = 313 \text{ K}, T_o = 293 \text{ K}, T_i = 373 \text{ K}, T_o = 293 \text{ K}.$

From Lemczyk & Yovanovich (1987) [30].

5.3.6 Elastomeric spacers between similar metals

Elastomeric materials are used as gaskets because of their superior environmental resistance, excellent sealing capability and durability through repeated loadings. These materials contain fillers to improve their mechanical or thermophysical properties.

The enclosed table, reproduced from Fletcher & Miller (1973) [18], shows the relevant characteristics of the elastomers used to obtain the joint conductance data presented in the following page.

Code	Name	Material	Filler	Density [kg.m ⁻³]	Temperature Range [K]	Thick t×10 ³ [m]
N1		Neoprene Rubber		1350	244-366	2,92
IP1	D84-1 ^a	Flouro- carbon	Carbon black	1875	233-533	2,08
IP2	EXN-117-3 ^a	Nitrile	Graphite, Talc	1450	233-422	1,98
IP3	SIL-181-3 ^a	Silicone	Diatomaceous earth	1340	219-533	2,05
IP4	R36-1 ^a	Nitrile	Carbon black, Organic peroxide	1215	244-394	2,36
IP5	4658-2 ^a	Poly- acrilate	Silica, Alumina Complex	1360	255-450	1,90
C1	1224 ^b	Silicone	Silver flakes	3250	218-473	0,76
C2	1215 ^b	Silicone	Silver coated copper powder	3650	218-398	0,71
C3	X-4044-3 ^b	Silicone	Inorganic-dielectric, thermally conductive material	1750	218-473	0,43
TW1	CONCIL R350 ^c	Silicone	Silver flakes	1700	222-450	0,74
TW2	CONCIL R600 ^c	Silicone	Silver flakes	1800	222-450	0,71
TW3	CONCIL G450 ^c	Silicone	Silver coated inert particles	1700	200-478	0,74
TW4	CONCIL G750 ^c	Silicone	Silver coated inert particles	1800	200-478	0,76

- a. International Packing Corporation, Bristol, New Hampshire 03222.
- b. Chomerics, 77 Dragon Court, Woburn, Massachusetts 01810.
- c. Technical Wire Products, Inc., 129 Dermody Street, Cranford, New Jersey 07016.

SPECIMENS: Three cylinders, Al - 4,3 Cu - 1,5 Mg - 0,6 Mn. (Al 2024-T4).

Two identical contacting junctions placed as sketched.

Radius, $b = 1,27 \times 10^{-2}$ m.

Surface	FD $\times 10^{-6}$ [m]	RD $\times 10^{-6}$ [m]
S1	+0,51	0,40
S2	+0,51	0,35
S3	+0,51	0,33
S4	+0,51	0,40

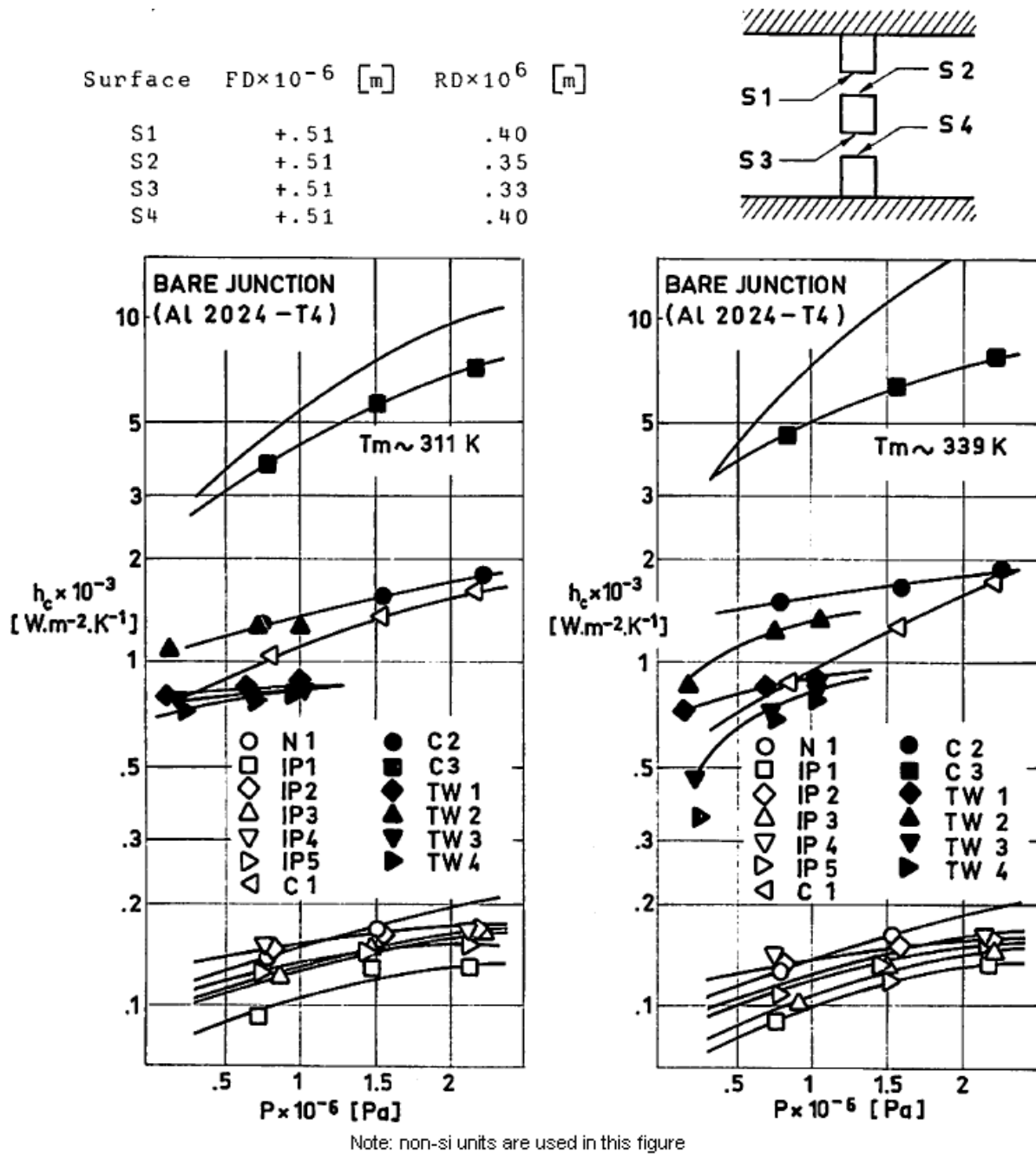


Figure 5-108: Plot of contact conductance vs. contact pressure for various elastomeric materials at two mean temperatures. From Fletcher & Miller (1973) [18].

5.3.6.1 Elastomeric thermal fillers

In this clause thermal fillers designed by Chomerics Co. are described.

CHO-THERM products are thermally conductive interface materials designed for transferring heat from electronic components to heat sinks. Most CHO-THERM products also provide electrical isolation at the interface sites. They offer many improvements over the older combinations of mica pads and silicone grease.

Composition. One-component thermal interface materials consist of a thermoset elastomeric binder containing a dispersed highly thermally conductive ceramic filler. The elastomer binder is typically a silicone molding resin cured at high temperatures and high pressure. Urethane elastomers have been introduced for use where silicone cannot be tolerated due to possible contamination. The ceramic fillers are added to the elastomer to increase its thermal conductivity. Typical fillers are boron nitride, aluminium oxide and magnesium oxide. This mixture is generally reinforced with fiberglass cloth or with polyimide or polyester dielectric film, which make the material highly resistant to tear and cut-through.

Thermal Conductivity. The thermal conductivity is determined by the materials composition, i.e., the type and ratio of thermal filler to elastomeric binder, and by the relative amount of reinforcing glass fiber or dielectric film.

In homogeneous materials, thermal conductivity is independent of physical dimensions. Unreinforced materials can be considered homogeneous and the thermal conductivity is independent of thickness. All reinforced materials are non-homogeneous in that the reinforcing layer is a poor thermal conductor compared to the outer elastic layers which are good thermal conductors. As sample thickness is increased, the reinforcing layer remains constant while the elastomeric layer expands. The ratio of good conductor to poor conductor increases, and the apparent, or total, thermal conductivity increases with increasing material thickness.

Values reported in different literature should be used with caution unless the test method is clearly stated. Thermal conductivity is difficult to measure for thin, interface materials. Many test methods cannot distinguish between contact resistance and the sample resistance, leading to unrealistically low values. Other methods based on calculations from "TO-3 Thermal Impedance Data" may seriously overestimate thermal conductivity. The values reported here are based on a guarded heater flat plate test method developed and published by Chomerics. This test is consistent with the methodology of several ASTM thermal conductivity test methods, but introduces the required modifications to correctly measure thin films of high thermal conductivity.

Thermal Impedance. Thermal interface materials can reduce contact resistance by conforming to two rough mating surfaces and eliminating air gaps. Because these elastomeric materials are highly loaded with hard ceramic fillers, they are relatively stiff and require pressure to make them "flow" into the surface irregularities and reduce contact resistance.

The contact resistance is high at low pressures due to poor mating. As pressure is increased, the material begins to flow into the surface irregularities and the contact resistance decreases.

The pressures needed for achieving minimum thermal impedance are easily accommodated in practice. In fact, secure attachment of components to heat sinks usually requires the same magnitude of force holding the component to the sink. However, recent developments, such as surface mount applications, require that good thermal contacts be made with minimum applied pressure. A new approach is required for applications in which an interface material will conform at very low pressures.

Suitable materials for such applications have been developed based on a precise balance of pliancy and thermal conductivity, by careful adjustment of filler level and binder elasticity.

Dielectric Strength. Measured according to ASTM D149, dielectric strength is defined as the AC voltage required to cause a breakdown on the insulating material being tested. The results are reported as the Dielectric Breakdown Voltage for a given thickness or as Dielectric Strength in volts/mil.

Measurements using ASTM D149 yield values obtained under controlled test conditions and may not accurately reflect actual field performance. Factors such as corona discharge, frequency, temperature and humidity can significantly affect the long term insulating characteristics of a material.

Volume Resistivity. Volume resistivity as determined by ASTM D257 is a measure of bulk electrical resistance. This property shows a strong inverse dependence on humidity and temperature. It is not unusual for volume resistivity to change by a factor of 10^5 - 10^6 when exposed to > 90% humidity. Increasing temperatures yield similar, though not such drastic changes. These changes are completely reversible. When conditions are returned to normal, the volume resistivity also returns to the original value.

Elastomeric Properties. Thermal interface materials exhibit properties consistent with highly filled elastomers, such as compression deflection, stress relaxation, and compression set. Each property has a major impact on the long term effectiveness of an interface material.

Compression Deflection. A solid elastomer, as opposed to a foam, is not compressible, but will yield when a load is applied. Under a compressive load, the material will undergo a deflection of the part as a whole. The magnitude of the deformation is proportional to the load up to the elastic limit (the point at which the material ruptures and can no longer recover).

Stress Relaxation. If an elastomer is subject to a compressive load it first undergoes compression deflection while the load is applied. This is followed by a slow relaxation process whereby the initial stress begins to decay; this stress decay is brought about by macromolecular rearrangement within the elastomer. The point, or % stress loss, is dependent on several factors including the nature of the elastomer and the level of loading.

Compression Set. If an elastomer is subject to a compressive load for an extended time, a part of the deflection becomes permanent and will not be recoverable when the load is removed. This behavior is important only in designs where the interface material is unloaded and reloaded occasionally during its service life.

Chemical Resistance. Interface materials may come into short term contact with solvents either in cleaning operations or through unintentional exposure to coolants, fuels or lubricants. Contact with any number of solvents will cause swelling of the exposed areas of elastomer interface materials. The severity of the swelling will depend on the type of solvent, duration of exposure and the type of elastomer. Generally, solvents such as ketones, halogenated hydrocarbons and esters cause more swelling than alcohols or aromatics.

While the elastomer is swollen its resistance to abrasion is reduced and care should be taken not to damage the material. The swelling phenomenon is reversible and the interface material returns to its normal state as the solvent evaporates. All physical, electrical and thermal properties remain the same as before the exposure.

For applications in which frequent and long term exposure to aliphatic and aromatic hydrocarbons are expected, a fluoro-silicone-based product is recommended.

FIBERGLASS REINFORCED SILICONES

The thermal interface materials in this family consist of a silicone elastomer binder with boron nitride or aluminium oxide as the thermally conductive filler. They are reinforced with glass cloth which makes them resistant to tear and cut-through. The family also includes a fluorosilicone material that resists hydrocarbons and other solvents which can be damaging to silicone.

CHO-THERM 1679, 1671, 1678 (boron nitride products) provide the highest thermal and electrical performance available in one-component interface materials. They are ideal replacements for two-component, greased beryllium oxide systems, particularly in aerospace and other high reliability environments. CHO-THERM 1679 is designed for use where the lowest possible thermal impedance is required. CHO-THERM 1678 possesses thermal properties approaching those of CHO-THERM 1671, but provides only moderate electrical isolation.

CHO-THERM 1674 elastomer is a low-cost, aluminium oxide-filled silicone interface product designed for applications which require moderate thermal and electrical performance.

CHO-THERM 1677, based on a fluorosilicone binder is ideal for use in environments prohibiting the use of thermal grease.

CHO-THERM 1661 thermal interface products have similar thermal characteristics to CHO-THERM 1671 products, but are somewhat more pliable because they are not reinforced with glass cloth.

Typical properties	1679	1671	1677	1674	1678	1661	Test Method
Binder	Silicone	Silicone	Fluorosilicone	Silicone	Silicone	Silicone	-
Filler	Boron Nitride	Boron Nitride	Boron Nitride	Aluminium Oxide	Boron Nitride	Boron Nitride	-
Thermal Conductivity [W.m ⁻¹ .K ⁻¹]	2,72	2,39	2,09	1,17	1,88	3,77	Chomerics Test Method No. 28
Thermal Impedance x10 ⁴ [W ⁻¹ .m ² .K]	0,97-1,16	1,16-1,42	2,45-2,70	1,93-2,19	1,42-1,54	1,54-1,80	Typical Flat Plate Test Values
Voltage Breakdown Rating [VAC]	4000	4000	4000	25000	2500	4000	ASTM D149
Thickness x10 ⁴ [m]	2,54±0,51	3,81±0,51	5,08±1,02	2,54±0,51	2,54±0,51	5,08±0,76	-
Maximum Use Temperature [K]	213 to 473	213 to 473	213 to 473	213 to 473	213 to 473	213 to 473	-
Tensile Strength [MPa]	6,89	6,89	2,76	10,34	6,89	1,38	ASTM D412
Tear Strength x10 ⁻³ [N.m ⁻¹]	17,51	17,51	10,51	17,51	17,51	1,75	ASTM D624
Elongation [%]	10	2	10	2	10	2	ASTM D412
Hardness	95	90	85	90	90	90	ASTM D2240

Typical properties	1679	1671	1677	1674	1678	1661	Test Method
(shore A)							
Specific Gravity	1,55	1,55	1,70	2,20	1,60	1,60	ASTM D7922
Volume Resistivity [ohm.m]	10x10 ¹²	10x10 ¹²	10x10 ¹²	2x10 ¹²	10x10 ¹²	10x10 ¹²	ASTM D257
Color	Yellow	White	White	Blue	Red	White	-

FILM REINFORCED SILICONES

The CHO-THERM materials in this family are reinforced with polyimide film which gives them superior dielectric strength and durability. The filler in these silicone products is boron nitride or magnesium oxide.

CHO-THERM 1698 thermal interface materials are boron nitride filled to give outstanding thermal conductivity. Polyimide film provides excellent cut-through resistance and a dielectric voltage breakdown of 6000 VAC. Maximum use temperature is 473 K.

CHO-THERM 1694 thermal interface elastomers contain magnesium oxide for good thermal conductivity and to promote longer tool life than that obtained with more abrasive aluminium oxide fillers. Reliable thermal performance is provided up to 473 K. These products have the same high durability and dielectric strength as CHO-THERM 1698.

Typical Properties	1698	1694	Test Method
Binder	Silicone	Silicone	-
Filler	BN	MgO	-
Carrier	Polyimide	Polyimide	-
Thermal conductivity [W.m ⁻¹ .K ⁻¹]	0,628	0,419	Chomerics Test Method No. 28
Thermal Impedance x10 ⁴ [W ⁻¹ .m ² .K]	1,61	2,26	Typical Flat Plate Test Values
Voltage Breakdown Level [VAC]	6000	6000	ASTM D149
Thickness x10 ⁴ [m]	1,27±0,25	1,27±0,25	-
Maximum Use Temperature [K]	213 to	213 to	-
Tensile Strength [MPa]	20,68	20,68	ASTM D412
Tear Strength x10 ⁻³ [N.m ⁻¹]	26,67	26,67	ASTM D624

Typical Properties	1698	1694	Test Method
Elongation [%]	10	10	ASTM D412
Hardness (Shore A)	90	90	ASTM D2240
Specific Gravity	1,50	2,20	ASTM D792
Volume Resistivity [ohm.m]	1 x 10 ¹²	1 x 10 ¹²	ASTM D257
Color	Copper	Brown	-

FILM REINFORCED URETHANES

The urethane binder in this family of CHO-THERM materials allows conformal coating without the dewetting problems (e.g. migration and bubbling) common to applying a conformal coat over silicone. These products use boron nitride or magnesium oxide as their thermally conductive filler. Their excellent dielectric strength and exceptional durability are provided by a polyimide or polyester layer which gives superior resistance to tear and cut through from burrs on heat sinks. Polyimide film prevents dielectric voltage breakdown up to 6000 VAC. Polyester film protects up to 4000 VAC.

CHO-THERM 1688 thermal interface elastomers are ideal for applications requiring very low thermal impedance and superior resistance to cut through. Their excellent thermal conductivity results from their boron nitride filler. Dielectric voltage breakdown is 6000 VAC.

CHO-THERM 1684 thermal interface elastomers are designed for applications needing moderate thermal performance with superior cut through resistance. The magnesium oxide filler provides good thermal conductivity and promotes longer tool life than does more abrasive aluminium oxide. Dielectric breakdown is 6000 VAC.

CHO-THERM 1682 elastomers feature the same urethane binder and magnesium oxide thermal filler as CHO-THERM 1684 materials, but have an economical polyester dielectric layer. Voltage breakdown is 4000 VAC.

Typical Properties	1688	1684	1682	Test Method
Binder	Urethane	Urethane	Urethane	-
Filler	BN	MgO	MgO	-
Carrier	Polyimide	Polyimide	Polyester	-
Thermal conductivity [W.m ⁻¹ .K ⁻¹]	0,628	0,419	0,419	Chomerics Test Method No. 28
Thermal Impedance x10 ⁴ [W ⁻¹ .m ² .K]	1,61	2,26	2,58	Typical Flat Plate Test Values
Voltage Breakdown Level [VAC]	6000	6000	4000	ASTM D149

Typical Properties	1688	1684	1682	Test Method
Thickness x10 ⁴ [m]	1,27±0,25	1,27±0,25	1,27±0,25	-
Maximum Use Temperature [K]	213 to 423	213 to 423	213 to 423	-
Tensile Strength [MPa]	20,68	20,68	24,13	ASTM D412
Tear Strength x10 ⁻³ [N.m ⁻¹]	26,27	26,27	35,03	ASTM D624
Elongation [%]	10	10	30	ASTM D412
Hardness (Shore A)	90	90	100	ASTM D2240
Specific Gravity	1,50	2,20	2,20	ASTM D792
Volume Resistivity [ohm.m]	1 x 10 ¹²	1 x 10 ¹²	1 x 10 ¹²	ASTM D257
Color	Yellow	Tan	Ivory	-

THERMAL CONDUCTIVITY WITHOUT ELECTRICAL ISOLATION

CHO-THERM 1646 pads offer the best available thermal performance, without the use of grease, in applications where no dielectric strength is required. The low thermal impedance of CHO-THERM 1646 materials approximates that of thermal grease.

One-component CHO-THERM 1646 pads eliminate the need for grease dispensing equipment or the labor-intensive brush-on process. CHO-THERM 1646 materials consist of boron nitride-filled silicone coated on one side to 50 x 10⁻⁶ m aluminium. Acrylic pressure sensitive adhesive is on the other side of the aluminium.

Typical Properties	1646	Test Method
Binder	Silicone	-
Filler	Boron Nitride	-
Carrier	Aluminium	-
Thermal Impedance x 10 ⁵ [W ⁻¹ .m ² .K]	9,67	Typical Flat Plate Test Values
Thickness x10 ⁴ [m]	1,27	-
Maximum Use Temperature [K]	213 to	-
Tensile Strength [MPa]	34,47	ASTM D412
Tear Strength x10 ⁻³ [N.m ⁻¹]	30,65	ASTM D624
Color	White/Silver	-

5.4 Outgassing data

Outgassing data, consisting of total weight loss (TWL) and volatile condensable materials (VCM), of several materials included in this part, are presented in the following table.

Table 5-11: Outgassing Data of Several Materials

MATERIAL	% TWL	% VCM	CURE TIME [h]	CURE TEMP. [K]	ATMOSPHERE
Aluminium DH 354 ¹	0,42	0,01	–	350	–
Aluminium oxide ¹	0,39	0,01	–	–	–
Carbon fiber ¹	0,58	0,02	–	–	–
Carbon fiber HTS ¹	0,60	0,00	–	–	–
Ceramic 9440 ¹	5,24	0,00	–	–	–
DC-340 Grease ²	0,35	0,11	–	273	–
DC-340 Grease ²	0,84	0,31	24	298	AIR
Laminate AS-4/1908 ³ Epoxi-Graphite	0,11	0,01	2	394	–
Laminate Epoxi-Fiberglass ³ Type II Classe Grade 2	0,28	0,01	–	–	–
Laminate T 300/934 ⁴ Graphite/Epoxi	0,58	0,00	–	–	–
Neoprene ²	3,01	1,72	–	273	–
PTFE (teflon, halon, fluon, ⁴ host flon)	0,05	0,00	–	–	–
Renker tin oxide x 50 µm ⁴ kapton-aluminium	1,12	0,00	–	–	–
Silicone high vacuum ² grease	1,52	0,34	–	273	–
Silver filled silicone ²	0,261	0,055	–	273	–
Silver filled silicone ²	0,048	0,023	24	450	AIR
Textolite 11546 ¹	0,38	0,01	90	348	–

MATERIAL	% TWL	% VCM	CURE TIME [h]	CURE TEMP. [K]	ATMOSPHERE
Textolite GIOFR4 ¹	0,44	0,01	–	–	–

¹ From ESA RD01 Rev. 3 (1992) [12].

² From Campbell, Marriott & Park (1973) [5].

³ From Campbell & Marriott (1987) [4].

⁴ From ESA PSS-01-701, Issue 1, Rev 2 (1990) [11].

Bibliography

- [1] Al-Astrabadi, F.R., O'Callaghan, P.W., Probert, S.D., "Thermal Contact Resistance Dependence on Surface Topography", AIAA, June 4-6, 1979.
- [2] Al-Astrabadi, F.R., O'Callaghan, P.W., Probert, S.D., Jones, A.M., "Thermal Contact Conductance Correlation for Stacks of Thin Layers in High Vacuums", *Journal of Heat Transfer*, Vol. 99-C, No. 1, Feb. 1977, pp. 139-142.
- [3] Andrews, R.V., "Solving Conductive Heat Transfer Problems with Electrical-Analogue Shape Factors", *Chemical Engineering Progress*, Vol. 51, No. 2, Feb. 1955, pp. 67-71.
- [4] Campbell, Jr., W.A., Marriott, R.S., "Outgassing Data for Selecting Spacecraft Materials", NASA RP 1124, Rev., 1987.
- [5] Campbell, Jr., W.A., Marriott, R.S., Park, J.J., "Compilation of Outgassing Data for Spacecraft Materials", NASA TN D-7362, Sep. 1973.
- [6] Cetinkale, T.N., Fishenden, M., "Thermal Conductance of Metal Surfaces in Contact", *Proceedings International Conference of Heat Transfer*, Inst. Mech. Eng., London 1951, pp. 271-275.
- [7] Clausing, A.M., Chao, B.T., "Thermal Contact Resistance in a Vacuum Environment", *Journal of Heat Transfer*, Vol. 87-C, No. 2, May 1965, pp. 243-251.
- [8] Cook, R.S., Token, K.H., Clakins, R.L., "A Novel Concept for Reducing Thermal Contact Resistance", AIAA 82-0886, June 7-11, 1982.
- [9] Cunnington, Jr., G.R., "Thermal Conductance of Filled Aluminium and Magnesium Joints in a Vacuum Environment", ASME Paper No. 64-WA/TH-40, 1964.
- [10] Edmonds, M.J., Jones, A.M., Probert, S.D., "Thermal Contact Resistance for Hard Machined Surfaces Pressed Against Relatively Soft Optical Flats", 1980.
- [11] ESA, "Data for Selection of Space Materials", ESA PSS-01-701, Issue 1, rev. 2, 1990.
- [12] ESA, "Outgassing and Thermo-optical Data for Spacecraft Materials", ESA RD01, Rev. 3, 1992.
- [13] Faulkner, R.C., Andrews, R.V., "Shape factors in Multiple-Pipe Systems", *Amer. Inst. Chem. Engrs. (AIChE) Journal*, Vol. 1, No. 4, Dec. 1955.
- [14] Fenech, H., Rohsenow, W.M., "Prediction of Thermal Conductance of Metallic Surfaces in Contact", *Journal of Heat Transfer*, Vol. 85-C, No. 1, Feb. 1963, pp. 15-24.
- [15] Fenech, H., Rohsenow, W.M., "Thermal Conductance of Metallic Surfaces in Contact", U.S. Atomic Energy Commission, Report NYO 2316, May 1959.
- [16] Fletcher, L.S., Blanchard, D.G., Kinneau, K.P., "Thermal Conductance of Multilayered Metallic Sheets", *Journal of Thermophysics and Heat Transfer*, Vol. 7, pp. 120-126, 1993.

- [17] Fletcher, L.S., Gyrogo, D.A., "Prediction of Thermal Contact Conductance between Similar Metal Surfaces", in "Progress in Astronautics and Aeronautics", Vol. 24, J.W. Lucas, Ed., MIT Press, Cambridge, Mass., 1970, pp. 273-288.
- [18] Fletcher, L.S., Miller, R.G., "Thermal Conductance of Gasket Materials for Spacecraft Joints", AIAA Paper No. 73-119, Jan. 1973.
- [19] Fletcher, L.S., Miller, R.G., "Thermal Conductance of Gasket Materials for Spacecraft Joints", Progress in Astronautics and Aeronautics, Vol. 35, 1974.
- [20] Fleycher, L.S., Smuda, P.A., Gyrogo, D.A., "Thermal Contact Resistance of Selected Low-Conductance Interstitial Materials", AIAA Journal, Vol. 7, No. 7, July 1969, pp. 1302-1309.
- [21] Fried, E., "Study of Interface Thermal Contact Conductance - Summary Report", General Electric Report 66SD4471, July 1966.
- [22] Fried, E., "Study of Interface Thermal Control Conductance", Summary Report, General Electric Doc. 65SD4395, 1965.
- [23] Fried, E., Atkins, H.L., "Interface Thermal Conductance in a Vacuum", Journal of Spacecraft and Rockets, Vol. 2, No. 4, July-Aug. 1965, pp. 591-593.
- [24] Fried, E., Kelley, M.J., "Thermal Conductance of Metallic Contacts in a Vacuum", in "Progress in Astronautics and Aeronautics", Vol. 18, G.B. Heller, Ed., Academic Press, New York, 1966, pp. 697-718.
- [25] Griggs, E.I., Pitts, D.R., Goyal, A.B., "Conductive Shape Factors for a Circular Cylinder Centered in a Rectangular Slab Having One and Two Adiabatic Surfaces", Journal of Heat Transfer, Vol. 95-C, No. 1, Feb 1973, pp. 129-130.
- [26] Gyrogo, D.A., "Investigation of Thermal Isolation Materials for Contacting Surfaces", in "Progress in Astronautics and Aeronautics", Vol. 24, J.W. Lucas, Ed., MIT Press, Cambridge, Mass., 1970, pp. 310-336.
- [27] Henry, J.J., Fenech, H., "The Use of Analog Computer for Determining Surface Parameters Required for Prediction of Thermal Contact Conductance", Journal of Heat Transfer, Vol. 86-C, No. 4, Nov. 1964, pp. 543-551.
- [28] Kutateladze, S.S., Borishanskii, V.M., "A Concise Encyclopaedia of Heat Transfer", Arthur, Pergamon Press, Oxford, 1966, Chap. 4, pp. 36-44.
- [29] Laming, L.C., "Thermal Conductance of Machined Metal Contacts", Proceedings International Conference on Developments in Heat Transfer, ASME, Part I, 1961, pp. 65-76.
- [30] Lemczyk, T.F., Yovanovoch, M.M., "Heat Transfer Engineering", Vol. 8, No. 2, Apr. 1987, pp. 35-48.
- [31] Marchetti, M., Testa, P., Torrisi, F.R., "Measurements of Thermal Conductivity and Thermal Control Resistance in Composite Materials for Space", ESA Journal, Vol. 12, No. 3, 1988.
- [32] Miller, R.G., Fletcher, L.S., "Thermal Contact Conductance of Porous Materials in a Vacuum Environment", AIAA Paper No. 73-747, July 1973.
- [33] Miller, R.G., Fletcher, L.S., "Thermal Contact Conductance of Porous Metallic Materials in a Vacuum Environment", Progress in Astronautics and Aeronautics, Vol. 35, 1974.
- [34] O'Callaghan, P.W., Probert, S.D., "Correlations for Thermal Conductance in Vacuo", Journal of Heat Transfer, Vol. 95-c, No. 1, Feb. 1973, pp. 141-142.

- [35] Padgett, D.L., Fletcher, L.S., "The Thermal Conductance of Dissimilar Metals", AIAA 82-0885, 1982.
- [36] Parker, J.D., Boggs, J.H., Blick, E.F., "Introduction to Fluid Mechanics and Heat Transfer", Addison-Wesley Publishing Company, Inc., Reading Mass. 1969, Chap. 14, pp. 427-431.
- [37] Peterson, G.P., Fletcher, L.S., "Heat Transfer Enhancement Techniques for Space Station Cold Plates", Journal of Thermophysics and Heat Transfer, Vol. 5, pp. 423-428, 1991.
- [38] Peterson, G.P., Fletcher, L.S., Blackler, D., "Thermal Performance of Thermal Pad Contact Heat Exchangers", Journal of Thermophysics and Heat Transfer, Vol. 6, pp. 69-76, 1992.
- [39] Peterson, G.P., Stacks, G., Fletcher, L.S., "Thermal Conductance of Two Space Station Cold Plate Attachment Techniques", Journal of Thermophysics and Heat Transfer, Vol. 5, pp. 246-248, 1991.
- [40] Ramavhandra Murthy, Ramavhandran, A., "Shape Factors in Conduction Heat Transfer", British Chemical Engineering, Vol. 12, No. 5, 1967, pp. 730-731.
- [41] Roess, L.C., "Theory on Spreading Conductance", Appendix to "Thermal Resistance Measurements of Joints Formed between Stationary Metal Surfaces", by N.D. Weills & E.A. Ryder. Transactions of the ASME, Vol. 71, No. 3, 1949.
- [42] Salerno, L.J., Kittel, P., Books, W.F., Spivak, A.L., Marks, Jr., W.G., "Thermal Conductance of Pressed Brass Contacts at Liquid Helium Temperatures", Cryogenics, Vol. 26, No. 4, Apr. 1986.
- [43] Scollon, T.R., Carpitella, M.J., "Long Life Reliability Thermal Control Systems Study Data Handbook", Prepared under Contract NAS 8-26252 by Space Systems Organization, General Electric Co., 1970.
- [44] Shlykov, Yu.P., Ganin, Ye.A., "Thermal Resistance of Metallic Contacts", International Journal of Heat and Mass Transfer, Vol. 7, No. 8, Aug. 1964, pp. 921-929.
- [45] Somer, R.R., Miller, J.W., Fletcher, L.S., "Thermal Contact Conductance of Dissimilar Metals", in "Thermophysics and Thermal Control", 1979.
- [46] Sunderland, J.E., Johnson, K.R., "Shape Factors for Heat Conduction through Bodies with Isothermal or Convective Boundary Conditions", Trans. Of the Amer. Soc. of Heating, Refrigeration and Air-Conditioning Engrs. (ASHRAE), Vol. 10, 1964, pp. 237-241.
- [47] Thomas, T.R., Probert, S.D., "Correlations for Thermal Contact Conductance in Vacuo", Journal of Heat Transfer, Vol. 94-C, No. 2, May 1972, pp. 276-281.
- [48] Veziroglu, T.N., Williams, A., Kabac, S., Nayak, P., "Prediction and Measurement of the Thermal Conductance of Laminated Stacks", March 1979.
- [49] Yamazaki, S., Shimizu, A., Tschida, A., "Contact Thermal Resistance between Two Rotating Horizontal Cylinders", in "Heat Transfer and Fluid Flow in Rotating Machinery", 1987.
- [50] Yovanovich, M.M., "Effect of Foils upon Joint Resistance: Evidence of Optimum Thickness", Progress in Astronautics and Aeronautics, Vol. 31, 1973.
- [51] Yovanovich, M.M., "Thermal Conductance of Turned Surfaces", Progress in Astronautics and Aeronautics, Vol. 29, 1972.